eman ta zabal zazu

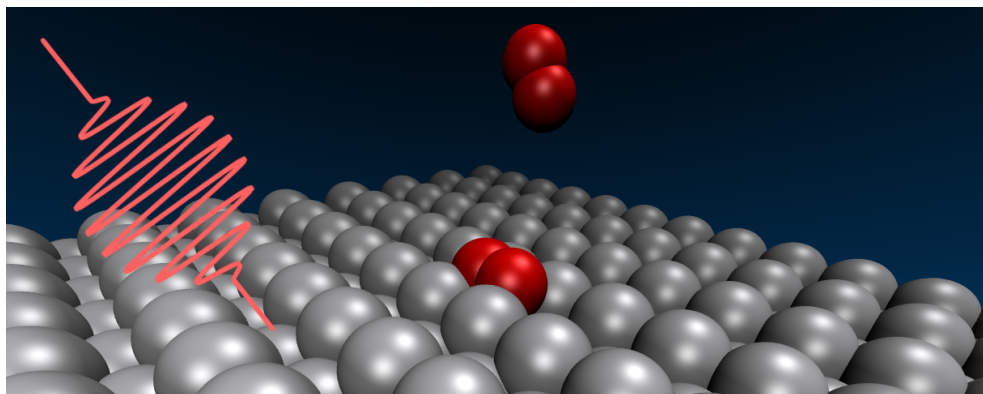Universidad Euskal Herriko
del País Vasco Unibertsitatea

Dynamics of diatomic molecules on metal surfaces: O_2/Ag(110) and CO/Ru(0001)

THESIS

submitted to the University of the Basque Country
for the degree of

DOCTOR IN PHYSICS

Ivor Lončarić

Donostia - San Sebastián, 2016

eman ta zabal zazu

Universidad
del País Vasco   Euskal Herriko
Unibertsitatea

Dynamics of diatomic molecules on metal surfaces: O_2/Ag(110) and CO/Ru(0001)

THESIS

submitted to the University of the Basque Country
for the degree of

DOCTOR IN PHYSICS

Ivor Lončarić

Supervisor :

Joseba Iñaki Juaristi Oliden

Donostia - San Sebastián, 2016

Contents

Acknowledgements

Publications

Publications covered in this thesis

1. **I. Lončarić**, M. Alducin, and J. I. Juaristi, *Dissociative dynamics of O_2 on Ag(110)*, Physical Chemistry Chemical Physics 17 (14), 9436-9445 (2015), doi: 10.1039/C4CP05900J

2. **I. Lončarić**, M. Alducin, P. Saalfrank, and J. I. Juaristi, *Femtosecond-laser-driven molecular dynamics on surfaces: Photodesorption of molecular oxygen from Ag (110)*, Physical Review B 93, 014301 (2016), doi: 10.1103/PhysRevB.93.014301

3. **I. Lončarić**, M. Alducin, P. Saalfrank, and J. I. Juaristi, *Femtosecond laser pulse induced desorption: A molecular dynamics simulation*, Nuclear Instruments and Methods in Physics Research Section B: Beam Interactions with Materials and Atoms 382, 114 (2016), doi: 10.1016/ j.nimb.2016.02.051

4. **I. Lončarić**, M. Alducin, and J. I. Juaristi, *Molecular dynamics simulation of O_2 adsorption on Ag(110) from first principles electronic structure calculations*, Physical Chemistry Chemical Physics 18, 27366 (2016), doi: 10.1039/C6CP05199E

5. **I. Lončarić**, M. Alducin, and J. I. Juaristi, *Search for an appropriate exchange-correlation functional to describe O_2 on Ag(110)*, in preparation

6. **I. Lončarić**, J. I. Juaristi, G. Füchsel, and P. Saalfrank, *Sticking of CO to Ru(0001) is determined by rotational anisotropy*, in preparation

Other publications

- V. Despoja, **I. Lončarić**, D. J. Mowbray, and L. Marušić, *Quasiparticle spectra and excitons of organic molecules deposited on substrates: G_0W_0-BSE approach*

applied to benzene on graphene and metallic substrates, Physical Review B 88, 235437 (2013), doi: 10.1103/PhysRevB.88.235437

- **I. Lončarić** and V. Despoja, *Benchmarking van der Waals functionals with non-contact RPA calculations on graphene-Ag (111)*, Physical Review B 90, 075414 (2014), doi: 10.1103/PhysRevB.90.075414

- R. Scholz, G. Floß, P. Saalfrank, G. Füchsel, **I. Lončarić**, and J. I. Juaristi, *Femtosecond-laser induced dynamics of CO on Ru(0001): Deep insights from a hot-electron friction model including surface motion*, Physical Review B 94, 165447 (2016), doi: 10.1103/PhysRevB.94.165447

Introduction

Heterogeneous catalysis has a tremendous impact on our society and it would be difficult to imagine our world without it. Catalytic reactions annually produce goods worth trillions of euros and in developed countries catalysis contributes to around 25% of the gross national product [1]. Global energy demand issues are well known, and, by definition, catalysts reduce energy required for material production. Catalytic converters in vehicles convert pollutants in exhaust to safer substances. Catalytic production of ammonia (the so-called Haber-Bosch process) enabled dramatic increase of the agricultural production [2]. Already from these examples, it is clear that the improvement of the existing and development of the new catalysts is highly valuable.

In heterogeneous catalysis the molecules involved in the catalytic reaction are often in the gas phase and the catalyst is often a solid metal surface. Two such gas-surface systems that correspond to two important catalytic reactions will be explored in this thesis. The first one is the $O_2/Ag(110)$ system. Adsorption and subsequent dissociation of oxygen on a silver surface is the first step in the ethylene epoxidation catalytic reaction. Silver is the best and only catalyst currently in use for this reaction. Ethylene oxide (oxirane) is a very important industrial chemical (raw material) and its annual production in the world is measured in tens of millions of tones [3]. Most of ethylene oxide is used to produce antifreeze, polyester, and polyethylene terephthalate (PET), but a range of other products are also made of it. The second system studied in this thesis is CO/Ru(0001). Interaction of CO with transition metal surfaces is important due to its relevance for two catalytic reactions: oxidation of CO to CO_2 in catalytic converters and the Fischer-Tropsch process. Catalytic converters are a standard equipment in vehicles that use internal combustion engines. The exhaust gas of these engines contains carbon monoxide which is toxic to humans and other animals that use hemoglobin to carry oxygen form the respiratory organs. Therefore, it has to be converted to

non-toxic carbon dioxide by oxidization on a catalyst surface. Modern catalytic converters are commonly made of platinum, palladium and rhodium. Fischer-Tropsch process is a name for a number of reactions in which a mixture of CO and H_2 is converted into liquid hydrocarbons. The fuels produced in this way are of a very high quality. This process is especially useful when coal or natural gas is available but not crude oil [4]. Typical catalysts are iron, cobalt and ruthenium. In fact, ruthenium is the most active catalyst [5].

A large portion of the history of new catalyst development is based on the method of trial and error. Fortunately, the understanding of catalysis is rapidly increasing (see Ref. [6]) and rational design of catalysts could be possible. This rapid increase started several decades ago with the advent of surface science experimental methods. In particular, the so-called model catalysis could be studied [7]. The difficulty for understanding catalysis under real working conditions relies in the fact that it usually takes place at high temperatures and/or pressures and that often even the catalyst itself has a very complicated structure. Due to this complexity, the microscopic mechanisms are hard to capture. In contrast, model catalysis proceeds in well-defined conditions, *e.g.*, for gas metal system it involves ultrahigh vacuum and clean single crystal surfaces with a known structure. Such model systems offer an opportunity to identify the fundamental processes behind the catalytic reaction.

Experimental surface science techniques have enabled to understand many catalytic reactions [8]. One of the most notable examples is the understanding of the mechanism of ammonia synthesis for which Gerhard Ertl was awarded the Nobel Prize in chemistry. Several spectroscopic, diffraction, and microscopic methods are used to study catalysis. For example, scanning tunnelling microscopy can provide the position and the orientation of a single molecule on a surface. Particularly useful experiments are those that use supersonic molecular beams. They are generated by gas expansion through nozzles (very small holes). By changing temperature of the nozzle or by inserting (seeding) other gases one can choose the translational energy of the gas molecules. In the molecular beam experiments often the angle of incidence can be controlled. More advanced setups also allow controlling the initial vibrational and/or rotational state of the gas molecules. Molecular beam experiments allow to measure sticking (adsorption) probabilities of gas molecules to a surface as a function of all these magnitudes. This is clearly a very important information for catalysis system. Molecular beam apparatuses are often coupled with other techniques that measure properties of

the molecules adsorbed on a surface or scattered back from it [9].

A major boost to understanding reactions on surfaces is lately provided from first principles (*ab initio*) theoretical simulations, *i.e.*, simulations that are results of the laws of physics without empirical models or free parameters to fit to experimental results. Advent of these simulations came with the exponential growth of available computational resources [10] that enabled the solution of well-known but complex equations that govern gas surface interaction at the nanoscale. As it is shown in this thesis, in some cases such first principle calculations already can match experimental accuracy, but in others there is still plenty of room for improvement. Several successful examples of the application of first principles simulations on gas surface problems can be found in Refs. [9] and [11]. The potential of first principles modelling of catalysis is great. Usually it is much cheaper to perform theoretical than experimental studies, dangerous experiments are not dangerous when simulated, and one could imagine computers as new laboratories. One could also imagine that a screening of millions of materials can be performed until the best catalyst is found [12]. However, we are not there yet. Nowadays, it seems that the best we can get is to combine both experimental and first principles theoretical models to understand and develop new catalysts. Of course, the above stated goal should be pursued by developing more accurate and faster time to solution theoretical methods and constantly testing them with state of the art experiments. This thesis is a small contribution in this direction.

As mentioned above, a large amount of information on the gas surface interaction can be obtained from molecular beam experiments, especially when they are performed with molecules having well defined incidence (and possibly internal) energies scattering from well-defined flat surfaces. Based on the results of these experiments one can try to understand the underlying potential energy surface. However, it is often hard to make such link between the experimental results and microscopical details of the interaction, which is, on the other hand, available from theoretical modelling. Therefore, molecular dynamics simulations that are able to reproduce the molecular beam experiments are crucial to understand the microscopic details of the molecule-surface interactions. Looking from the opposite side, molecular beam experiments are also the best benchmarks for the theoretical models [13]. For these reasons a large portion of this thesis is devoted to the understanding of molecular beam experiments of the $O_2/Ag(110)$ and $CO/Ru(0001)$ systems based on first principles electronic structure calculations. It is common for both systems that several molecular beam and many

others experiments have been performed. However, a theoretical simulation that would reproduce these experiments is missing.

The Ag(110) surface constitutes a good case study to model an ethylene epoxidation catalyst since it shows even a higher reactivity than the high surface area catalysts used in industry [14, 15]. Therefore, this surface was used in many experiments that aimed to understand this catalytic reaction, and more specifically the oxygen-silver interaction. Dynamics of oxygen on flat silver surfaces is particularly rich as experiments have identified three distinct adsorption states: a physisorbed state, a molecularly chemisorbed state, and a dissociative state [16–18]. Due to this and apart from the technological applications, dynamics of the O_2/Ag(110) interaction is interesting from a fundamental point of view as a model gas-metal system with several adsorption states and a dissociation process. Although, simple models that can explain adsorption dynamics for this system have been proposed based on molecular beam experiments [19–22], still a full understanding is lacking. An ideal tool to achieve this are the molecular dynamics simulations based on first principles calculations which are performed in this thesis.

In contrast, typical simple models could not explain molecular beam experiments [23–25] of CO adsorption and scattering from Ru(0001). Measured adsorption probabilities are mostly in agreement with the conclusions of other experimental techniques that suggest that the CO interaction with Ru(0001) is characterized by a single deep chemisorption well. However, measured scattering properties surprisingly do not agree with this simple model. Therefore, in this thesis we also aim to microscopically explain molecular beam experiments of this system by theoretical simulations.

In addition to pressure and temperature, light can also be used to facilitate and/or control catalytic reactions on surfaces. Such heterogeneous photocatalysis often involves transition metal oxides or semiconductors, but metal nanoparticles are also becoming important photocatalysts [26–29]. A special class of light induced reactions at surfaces are those driven by femtosecond laser pulses. New reaction channels, not accessible with ordinary thermal activation can be activated with such pulses [30]. Pump-probe experiments can be also performed to obtain a time-resolved insight [31]. As above, a theoretical modelling is indispensable in order to understand laser induced reactions at a microscopical level. Therefore, in this thesis we also discuss how femtosecond laser induced dynamics of molecules on metal surfaces can be modelled and we apply these models to

the laser induced desorption of O_2 from Ag(110)[*].

As mentioned above, O_2 can be found in different adsorption states on this surface and, therefore, it is an interesting case study system. Our aim is to explore how the femtosecond laser induced dynamics depends on the properties of each adsorption state. Compared to the studies that use different gases and/or surfaces, the use of one system with different adsorption states is beneficial as the most influential factors can be more easily identified.

Apart from the modelling of systems important for the heterogeneous catalysis, it should be said that the theoretical methods employed in this thesis can be applied to a much broader class of system. For instance, they can find application in the field of nanotechnology, which is already changing the world, since they are suitable to study the interaction of molecules with nanostructured surfaces. Therefore, development of new theoretical methods, testing the existing ones and understanding their accuracy for any given system is of great importance.

This thesis is structured as follows:

- In chapter 2 the theoretical methods that are used in this thesis are introduced. Starting from the complete quantum description of a system, we gradually arrive to the models applied to the particular gas-surface systems. First the electronic and nuclear degrees of freedom are separated. Second, we make a discussion on the methods for solving the electronic structure problem which shows the superiority of the density functional theory over other methods. Next, the density functional theory is briefly reviewed, common approximations are introduced, and its use in practice is described. At this point we turn to the introduction of the potential energy surfaces, their construction and exploration. Next, we discuss the dynamics of the nuclear degrees of freedom on a potential energy surface and we make a transition from the quantum to classical dynamics. We also describe how to model surface movement when the potential energy surface only includes molecular degrees of freedom and how to include non-adiabatic effects in the dynamics calculation. Furthermore, we introduce "on the fly" molecular dynamics. Finally, we describe the modelling of femtosecond laser induced dynamics.

- Chapter 3 is the first chapter that deals with the O_2/Ag(110) system. There-

---

[*]The author also studied femtosecond laser induced dynamics of CO on Ru(0001). This study is not part of this thesis and its results can be found in Ref. [32].

fore, we include an overview of the relevant experimental and previous theoretical works on this system. Next, we describe the procedure for obtaining the potential energy surface for this system based on density functional theory calculations. In the following, we test the quality of the obtained potential energy surface, explore its properties, describe the adsorption wells, and identify the energy barriers to dissociation. These properties are related to the experimental ones.

- In chapter 4 we study the dissociative dynamics of O_2 on Ag(110) by performing molecular dynamics simulations on the frozen surface potential energy surface. In particular, dissociation probabilities as a function of the incidence energy are calculated for different incidence angles. These results are understood by following the trajectories that lead to dissociation and exploring the energy barriers to dissociation. Results are also discussed in relation to the molecular beam experiments.

- In chapter 5 surface movement is included in the molecular dynamics simulations to study the adsorption dynamics of O_2 on Ag(110). Simulations are performed using both the precalculated potential energy surface and "on the fly". The obtained adsorption probabilities are compared to the measurements of molecular beam experiments. Reasons for differences between the results of the simulations and the experiments are discussed based on calculations of transition energy barriers between different adsorption wells.

- Following the conclusions of previous chapter, in chapter 6 we explore whether other approximations for the exchange-correlation functional in density functional theory can reproduce molecular beam experiments better than the approximation used in previous chapters. We use several exchange-correlation functionals of increasing complexity to calculate the relevant properties of the O_2/Ag(110) interaction. This enables us to discuss the applicability of each of the functionals in the modelling of this system.

- Study of laser induced desorption of O_2 from Ag(110) is presented in chapter 7. After a brief introduction to the modelling of femtosecond laser induced dynamics, we calculate desorption yields and desorption rates as a function of the laser fluence for each adsorption well. Based on these results we discuss which channel, electron or phonon, dominates the desorption in

each case. In addition, we explore the effects of the initial surface temperature and laser pulse properties on the desorption yields from each of the adsorption wells.

- In chapter 8 we study the CO scattering and adsorption dynamics on Ru(0001). First, the relevant molecular beam experiments are reviewed and a potential energy surface is presented. Next, we perform molecular dynamics simulation on this potential energy surface including surface movement with the aim of reproducing the results of molecular beam experiments. In particular, the adsorption probabilities as a function of the incidence energy, and the angular and energy distributions of the scattered molecules are simulated. Based on these simulations we explain the results of molecular beam experiments which were considered surprising. We also study the vibrational deexcitation of the scattered molecules that are initially vibrationally excited. For each result, we discuss the importance of energy loss of the molecule to the surface movement and to the excitation of electron-hole pairs.

- The main results of the thesis are summarized in chapter 9 and an outlook for further research studies based on these results is given.

2

Theoretical methods

This chapter provides an introduction to the theoretical framework that is used through the thesis. In Sec. 2.1 a general introduction to molecule surface interaction modelling is given. Next, in Sec. 2.2 a brief description of the density functional theory (DFT) is presented, followed by Sec. 2.3 that deals with the construction and exploration of potential energy surfaces (PES). The following section describes molecular dynamics either on precomputed PES or "on the fly" (Sec. 2.4). Simulation of laser induced processes on metal surfaces is discussed in Sec. 2.5.

2.1 Modelling molecule surface interaction and dynamics

As noted in the introduction, through this thesis understanding of gas-surface dynamics will be based on first principles calculations, *i.e.*, calculations that do not depend on experimental observations. Therefore, we start with a general (non-relativistic) quantum description of a (molecule-surface) system that contains N electrons and M nuclei. The interaction between these particles is fully described by the Schrödinger equation*

$$i\frac{\partial}{\partial t}\Psi(\mathbf{r}_i, \mathbf{R}_j, t) = H\Psi(\mathbf{r}_i, \mathbf{R}_j, t), \tag{2.1}$$

where H is Hamiltonian acting on the many-body wave-function Ψ that depends on electron ($\mathbf{r}_i$) and nuclear coordinates ($\mathbf{R}_j$). The only fundamental interaction that is relevant to our system is the electrostatic interaction. Therefore, the Hamiltonian is composed of kinetic energy terms (T) and electrostatic potentials (V)

$$H = T_e + T_n + V_{ee} + V_{nn} + V_{ne}, \tag{2.2}$$

---

*This equation and all subsequent equations are given in (Hartree) atomic units (a.u.) [33], unless specified otherwise.

where T_e is the kinetic energy of the electrons

$$T_e = -\frac{1}{2}\sum_{i=1}^{N}\nabla_i^2, \tag{2.3}$$

T_n is the kinetic energy of the nuclei (with masses m_I)

$$T_n = -\frac{1}{2}\sum_{I=1}^{M}\frac{1}{m_I}\nabla_I^2, \tag{2.4}$$

V_{ee} is the (repulsive) electrostatic interaction of the electrons

$$V_{ee} = \sum_{i=1}^{N}\sum_{j>i}^{N}\frac{1}{|\mathbf{r}_i - \mathbf{r}_j|}, \tag{2.5}$$

V_{nn} is the (repulsive) electrostatic interaction of the nuclei (with atomic numbers $Z_{I,J}$

$$V_{nn} = \sum_{I=1}^{M}\sum_{J>I}^{M}\frac{Z_I Z_J}{|\mathbf{R}_I - \mathbf{R}_J|}, \tag{2.6}$$

and V_{ne} is the (attractive) electrostatic interaction of the nuclei and the electrons

$$V_{ne} = -\sum_{i=1}^{N}\sum_{J=1}^{M}\frac{Z_J}{|\mathbf{r}_i - \mathbf{R}_J|}. \tag{2.7}$$

This Hamiltonian does not take into account the spin explicitly and it should be added as an additional degree of freedom. The spin dependence will be introduced in the Sec. 2.2.1. The relativistic effects are commonly negligible for the valence electrons and for the core electrons they can be efficiently mitigated in our calculations as mentioned in Sec. 2.2.

Unfortunately, $3N + 3M$ degrees of freedom in Eq. (2.1) makes it extremely hard to solve. Even storing the high-dimensional wave function in present computer memory is achievable only for very few (light) atom systems. Therefore, any first principles simulation of a gas-surface system has to rely on several approximations.

Usually, the first approximation consists in the partition of the problem into electronic and nuclear degrees of freedom, the so-called Born-Oppenheimer approximation [34]. The justification for this common approximation is the fact that even the lightest atom (hydrogen) is $\sim$ 2000 times heavier than the electron, and the atoms we are dealing with are at least an order of magnitude heavier. Due to

this the electrons move much faster than the nuclei and from the electron frame of reference the nuclei look static. Therefore, as far as electrons are concerned the kinetic energy of the nuclei term T_n can be neglected and the coordinates of the nuclei $\mathbf{R}_j$ can be treated as parameters in Eq. (2.1). In this thesis electron dynamics is not of interest and the time-independent electronic Schrödinger equation (2.1) can be used

$$H_{el}\Psi_{el}(\mathbf{r}_i, \mathbf{R}_j) = (T_e + V_{ee} + V_{nn} + V_{ne})\Psi_{el}(\mathbf{r}_i, \mathbf{R}_j) = E_{el}(\mathbf{R}_j)\Psi_{el}(\mathbf{r}_i, \mathbf{R}_j), \qquad (2.8)$$

where E_{el} are the electronic energy levels (eigenvalues) of the system[†]. In the Born-Oppenheimer (also called adiabatic) approximation $E_{el}(\mathbf{R}_j)$ is then used as a potential for the nuclei. Typically, the nuclei move on the electronic ground state potential energy surface - PES. The corresponding Schrödinger equation for the nuclei motion is

$$i\frac{\partial}{\partial t}\Psi_n(\mathbf{R}_j, t) = \left(T_n + E_{el}(\mathbf{R}_j)\right)\Psi_n(\mathbf{R}_j, t). \qquad (2.9)$$

Although the validity of the Born-Oppenheimer approximation is not easy to prove, it is successfully used to describe almost all ground state material properties and thermal reactions. Therefore, most of the theoretical chemistry and solid state physics relies on this approximation. Nevertheless, there are several counterexamples. In particular, the Born-Oppenheimer approximation can break down in gas-surface dynamics on metal surfaces due to close lying electronic states in metals. Additionally, photo induced processes involve electronically excited states for which the Born-Oppenheimer assumptions are not valid. Theoretical methods that help in circumventing these problems are given in Secs. 2.4 and 2.5.

Practical usage of the Born-Oppenheimer approximation in gas-surface dynamics consists in employing Eq. (2.8) to obtain the PES on which the motion of atoms is propagated [see Eq. (2.9)]. Even though in this way Eqs. (2.8) and (2.9) have to be solved with a reduced number of degrees of freedom usually both of these equations are still computationally too expensive and further approximations have to be employed.

A range of first-principles methods have been developed to treat the electronic Schrödinger equation (2.8), in an approximative way: Hartree-Fock theory, Møller-Plesset perturbation theory, configuration interaction methods, cou-

---

[†]Note that V_{nn} does not depend on $\mathbf{r}_i$ and enters the equation just as a constant

pled clusters methods, quantum Monte Carlo methods, density functional theory, etc. [35]. Excluding the last two on the list, these methods are usually called quantum chemistry methods. Of these, some post Hartree-Fock methods can be refined to give very accurate energies (with errors in energies lower than "chemical accuracy" of 1 kcal/mol = 43 meV). Unfortunately, such accuracy comes with a large computational expense even for systems with a small number of atoms (up to 20). Few atom systems, on the other hand, are usually not enough to model substrates, especially metallic ones, as small clusters of atoms often do not represent the extended substrate well. Due to this, quantum chemistry methods are rarely chosen as a tool in modelling gas surface problems. In principle, high accuracy can be also achieved by the quantum Monte Carlo methods, but there are still many obstacles before these methods can be used in gas surface modelling. The main problem is again the computational effort needed to generate accurate results by reducing the statistical error present in these calculations. On these grounds, the method of choice in the state of the art gas surface modelling is the density functional theory that is also employed through this thesis. Its foundations and practical applications are discussed in next Sec. 2.2.

As noted above, even if the solution to the electronic problem is available, the propagation of all nuclear degrees of freedom in a typical system according to Eq. (2.9) is very difficult. Therefore, it is possible to treat only few (important) degrees of freedom. Frequently, quantum effects in the nuclear motion are completely neglected and the classical limit is used. This is the approach used here as discussed in Sec. 2.4.

2.2   Density functional theory

Many problems in electronic structure calculations arise from the fact that the system is described by a high dimensional ($3N$) many electron wave function. Hohenberg and Kohn have proven that a much simpler three dimensional object, the electron density ρ, uniquely characterizes a quantum mechanical system [36]. They have shown, in what is nowadays known as the first Hohenberg and Kohn theorem, that the potential that determines the electronic Hamiltonian H_{el} as in Eq. (2.8) is a unique functional of ρ. All physical information about the system is given by H_{el} and, according to the theorem, there is a one-to-one correspondence between H_{el} and ρ. Therefore, all physical information is also given by the elec-

tronic density. In particular, the energy of the system is then also a functional of the electron density [see Eq. (2.8)]

$$E[\rho] = T_e[\rho] + V_{ee}[\rho] + V_{ne}[\rho] = F_{HK}[\rho] + V_{ne}[\rho], \tag{2.10}$$

where $F_{HK}[\rho]$ is the Hohenberg-Kohn functional that is universal (independent of the system) and V_{ne} is the only system dependent term (also called the external potential).

The importance of Eq. (2.10) becomes apparent from the second Hohenberg-Kohn theorem in which they proved that the energy of the system is minimal for the ground state electronic density. This makes possible to use the variational principle to obtain the ground state electronic density and energy. Only a three dimensional function (electronic density) has to be varied in contrast to using the many body high dimensional wave function. It is important to note that, in principle, no approximations are made so far and that the Hohenberg-Kohn theorems provide exactly the same quantum mechanical ground state as the electronic Schrödinger equation (2.8). Unfortunately, the two theorems do not provide an expression for $F_{HK}[\rho]$. Therefore, this functional remains unknown and has to be approximated. In order to do so, it is useful to separate $F_{HK}[\rho]$ in three contributions

$$F_{HK}[\rho] = T_e[\rho] + V_{ee}[\rho] = T_e[\rho] + E_{H}[\rho] + G_{xc}[\rho], \tag{2.11}$$

where E_{H} is the classical electrostatic interaction energy of the electron density ρ (Hartree energy)

$$E_{H}[\rho] = \frac{1}{2} \int \frac{\rho(\mathbf{r})\rho(\mathbf{r}')}{|\mathbf{r} - \mathbf{r}'|} d\mathbf{r} d\mathbf{r}' \tag{2.12}$$

and G_{xc} is a functional that contains the quantum mechanical many-body effects. Although this functional is not known, one may try to make some reasonable approximations. However, the Hohenberg-Kohn theory is still impractical as the kinetic energy functional $T_e[\rho]$ is also unknown[‡].

To avoid problems with the kinetic energy functional a practical scheme was developed by Kohn and Sham [37]. They introduced an auxiliary non-interacting system with single particle orbitals ϕ_i that yield the electron density of the original many-body system

$$\rho(\mathbf{r}) = \sum_{i=1}^{N} \phi_i^*(\mathbf{r})\phi_i(\mathbf{r}). \tag{2.13}$$

[‡]In the so-called orbital free DFT the kinetic energy functional $T_e[\rho]$ is approximated and Eq. (2.10) is directly minimized. Nowadays this approach still gives results that are below the required accuracy for gas-surface problems.

It is easy to evaluate exactly the kinetic energy of non-interacting electrons T_s:

$$T_s = -\frac{1}{2} \sum_{i=1}^{N} \int \phi_i^*(\mathbf{r}) \nabla^2 \phi_i(\mathbf{r}) d\mathbf{r}. \tag{2.14}$$

The total kinetic energy of the system can be then separated in a non-interacting contribution T_s and an unknown component T_c that contains corrections due to the many-body effects. The latter is also a functional of the density (following the Hohenberg-Kohn first theorem) and together with G_{xc} constitutes the so-called exchange-correlation functional $E_{xc}[\rho] = G_{xc}[\rho] + T_c[\rho]$. The exchange-correlation functional contains everything that is unknown. The name comes from the fact that it contains the exchange interaction§ and many-body electron-electron correlation. If one would know the expression for it, DFT would be an exact theory. Therefore, the exchange-correlation functional is a central quantity in DFT. Its approximations are discussed in Sec. 2.2.1.

Taking into account the definitions above, the total energy functional can be written in the following form

$$E[\rho] = T_s[\rho] + V_{ne}[\rho] + E_H[\rho] + E_{xc}[\rho]. \tag{2.15}$$

Minimization of this equation leads to single-particle Schrödinger like equations, the so-called Kohn-Sham equations

$$\left(-\frac{1}{2} \nabla^2 + v_{ne} + v_H + v_{xc} \right) \phi_i(\mathbf{r}) = \epsilon_i \phi_i(\mathbf{r}), \tag{2.16}$$

where v_{ne}, v_H, and v_{xc} are functional derivatives with respect to the density of the corresponding energy functionals:

$$\begin{aligned} v_{ne} &= -\sum_{J=1}^{M} \frac{Z_J}{|\mathbf{r} - \mathbf{R}_J|}, \\ v_H &= \int \frac{\rho(\mathbf{r}')}{|\mathbf{r} - \mathbf{r}'|} d\mathbf{r}', \\ v_{xc} &= \frac{\delta E_{xc}[\rho(\mathbf{r})]}{\delta \rho(\mathbf{r})}. \end{aligned} \tag{2.17}$$

The eigenfunctions ϕ_i and eigenvalues ϵ_i of the Kohn-Sham equations (2.16) are called the Kohn-Sham orbitals and orbital (band) energies, respectively. These

---

§This interaction is due to the Pauli exclusion principle which requires that the total wave function for two identical fermions (in our case electrons) is antisymmetric with respect to the exchange of particles.

orbitals, in principle, do not have a specific physical meaning. However, in many cases they resemble well the quasiparticle eigenvalues of the interacting system (see Ref. [38]). The ground state total energy is given by the sum of the occupied band energies and the corrections to avoid double-counting contributions to the total energy

$$E = \sum_{i=1}^{N} \epsilon_i - E_{\mathrm{H}} + E_{\mathrm{xc}} - \int v_{\mathrm{xc}}(\mathbf{r})\rho(\mathbf{r})d\mathbf{r}. \tag{2.18}$$

Since functional derivatives (2.17) that enter the Kohn-Sham equations (2.16) depend on density and, thus, on ϕ_i through Eq. (2.13), the Kohn-Sham equations have to be solved self-consistently. Usually, one starts with an initial guess for the density to obtain the functional derivatives, often by combining individual densities of each atom. From here, Kohn-Sham equations are solved, the new density is obtained and the scheme is repeated until convergence is obtained. Solving the eigenvalue problem, that is the Kohn-Sham equations, is therefore the most computationally consuming part of density functional theory. The way in which these equations are solved in this thesis is explained in Sec. 2.2.2.

2.2.1 Exchange-correlation functionals

The local density approximation

Already in the paper of Kohn and Sham [37], the simplest approximation for the exchange-correlation functional was proposed. It is called the *local density approximation* (LDA) due to its purely local character. In this approximation, the contribution of each point in the space to the exchange-correlation energy is the one that corresponds to a homogeneous electron gas of the same density. The exchange-correlation functional can then be written as

$$E_{\mathrm{xc}}^{\mathrm{LDA}}[\rho(\mathbf{r})] = \int \rho(\mathbf{r})\varepsilon_{\mathrm{xc}}(\rho(\mathbf{r}))d\mathbf{r}, \tag{2.19}$$

where $\varepsilon_{\mathrm{xc}}$ is the exchange-correlation energy per electron of a homogeneous electron gas with the electron density ρ. $\varepsilon_{\mathrm{xc}}$ is usually split into exchange and correlation contributions, $\varepsilon_{\mathrm{xc}} = \varepsilon_{\mathrm{x}} + \varepsilon_{\mathrm{c}}$. The exchange energy of a homogeneous electron gas is exactly known (see *e.g.* Ref. [38])

$$\varepsilon_{\mathrm{xc}}(\rho) = -\frac{3}{4}\left(\frac{3\rho}{\pi}\right)^{\frac{1}{3}}. \tag{2.20}$$

The correlation part is not known analytically, but can be calculated accurately with quantum Monte Carlo methods [39]. In practice, results of these calculations are then parametrised to form a functional of the electron density. Most common parametrizations are those of Refs. [40–42].

Up to now spin degrees of freedom were omitted. However, for magnetized systems (*e.g.* oxygen molecule) they are important and have to be taken into consideration. DFT can be generalized to spin-dependent problems by solving the Kohn-Sham equations separately for the spin-up density $\rho^\uparrow$ and the spin-down density $\rho^\downarrow$ with an exchange-correlation functional that is a functional of both spin densities $E_{xc}[\rho^\uparrow, \rho^\downarrow]$ [38]. The spin dependent analogue of LDA is called the *local spin density approximation* (LSDA)

$$E_{xc}^{LSDA}[\rho^\uparrow(\mathbf{r}), \rho^\downarrow(\mathbf{r})] = \int \rho(\mathbf{r})\varepsilon_{xc}(\rho^\uparrow(\mathbf{r}), \rho^\downarrow(\mathbf{r}))d\mathbf{r}, \qquad (2.21)$$

where $\rho = \rho^\uparrow + \rho^\downarrow$.

Similarly as above, $\varepsilon_{xc}(\rho^\uparrow(\mathbf{r}), \rho^\downarrow(\mathbf{r}))$ is usually separated in exchange and correlation parts. For the exchange part, it can be shown that

$$E_{xc}[\rho^\uparrow, \rho^\downarrow] = \frac{1}{2}(E_x[2\rho^\uparrow] + E_x[2\rho^\downarrow]), \qquad (2.22)$$

where each of the contributions on the right hand side of the equation is that of an unpolarized system as defined above (exchange interaction exists only for identical particles). The correlation part is, like in the unpolarized case, more involved and again parametrizations of higher level calculations are used [40–42].

Despite their simplicity LDA and LSDA proved to be successful in simulating many bulk and surface systems [43]. On the other hand, for the systems with strongly varying densities, as in the case of gas-surface systems, L(S)DA usually does not perform very well. Often L(S)DA gives vastly overestimated binding energies and underestimated bond lengths. Therefore, the more advanced exchange-correlation functionals presented below are customarily employed for gas-surface problems.

The generalized gradient approximation

L(S)DA results can be improved if the exchange-correlation functional also explicitly depends on the gradient of the density. Such functionals are known as

the *generalized gradient approximation* (GGA) exchange-correlation functionals

$$E_{xc}^{GGA}[\rho^\uparrow, \rho^\downarrow] = \int \rho(\mathbf{r})\varepsilon_{xc}(\rho^\uparrow, \rho^\downarrow, \nabla\rho^\uparrow, \nabla\rho^\downarrow)d\mathbf{r}. \qquad (2.23)$$

Unlike the L(S)DA, for which the exchange-correlation energy in any point with a given density is fixed as discussed above, in GGA the exchange-correlation energy for given electron density and its gradient can be chosen rather freely. Therefore, many different GGA functional forms exist. In construction of GGAs two major approaches have been used [44]. The first approach is to use exact quantum mechanical constrains to derive the parameters in approximate functionals. The second approach is to fit the parameters to particular systems. The most famous example of the first approach is the PBE functional [45], the most used functional in the solid state physics community. This functional significantly improves the LDA results in many cases and it is relatively accurate for a broad range of systems. The most famous example of the second approach is the BLYP functional [46, 47] which is the most used GGA in theoretical chemistry. This functional gives a better description of molecules (*e.g.* more accurate atomization energies) compared to PBE, but on the other hand much worse description of solids. Due to this, PBE is customarily used for describing gas-surface systems and, in fact, it is also employed to obtain many results presented in this thesis. Another exchange-correlation functional frequently used for gas-surface problems is RPBE [48]. This functional was in fact constructed as a refinement of PBE functional with an intention of improving the overbinding of small molecules on transition metal surfaces. It is also used in parts of this thesis. Unfortunately, none of the functionals is guaranteed to work for a given system. Often, for instance, it is observed that RPBE is too repulsive, while PBE is too attractive at the same time, and that the mixing of these two functionals can provide the required accuracy [49]. Implementations and references for a large number of other GGA functionals can be found for example in Ref. [50]. Construction of new GGAs is still an active research field.

Meta-GGA

A natural step forward from GGAs are the so-called *meta-GGAs* which would also explicitly include the Laplacian of the density, or more often the kinetic energy density $\tau = \frac{1}{2}\sum_{i=1}^{N}|\nabla\phi_i|^2$,

$$E_{xc}^{meta-GGA}[\rho^\uparrow, \rho^\downarrow] = \int \rho(\mathbf{r})\varepsilon_{xc}(\rho^\uparrow, \rho^\downarrow, \nabla\rho^\uparrow, \nabla\rho^\downarrow, \tau^\uparrow, \tau^\downarrow)d\mathbf{r}. \qquad (2.24)$$

This additional component in the construction of the exchange-correlation functional provides an opportunity for a better incorporation of exact quantum mechanical constraints and also for fitting to a broader range of systems. Therefore, in principle, higher accuracy can be achieved with meta-GGAs compared to GGAs. For example, atomization energies of molecules and lattice constants of solids can be improved at the same time, while in GGAs often improvement of one of these properties worsens others. A popular such meta-GGA is TPSS [51]. A number of versatile and accurate meta-GGAs have been proposed by the group of Truhlar that are parametrized on high-quality benchmark databases [52]. Finally, it should be said that meta-GGAs still have not achieved widespread use, neither in general nor, more specifically, in gas-surface problems. This is certainly correlated with problems in achieving self-consistency with meta-GGAs and also with the fact that they are not always available in popular DFT codes. This might change in the near future [53].

Hybrid functionals

The Coulomb self interaction present in Eq. (2.12) should be exactly cancelled out by the corresponding exchange term. However, this is not the case in above presented exchange correlation functionals. This inconsistency is believed to be the reason for a large portion of the inaccuracy in GGA-DFT. On the other hand, the expression for the exact exchange is known

$$E_\text{x}^\text{exact} = -\frac{1}{2} \sum_{i,j} \int \frac{\phi_i^*(\mathbf{r})\phi_j^*(\mathbf{r}')\phi_i(\mathbf{r})\phi_j(\mathbf{r}')}{|\mathbf{r} - \mathbf{r}'|} d\mathbf{r}d\mathbf{r}'. \tag{2.25}$$

Therefore, one may try to improve the GGA-DFT results by using this expression instead of the above discussed approximations for exchange functionals. If one does so, in fact, the results worsen [54]. Nevertheless, exact exchange can be used to improve on GGA-DFT if a new exchange functional is constructed by mixing a portion of exact exchange with ordinary GGA exchange. Due to this mixing, such functionals are called *hybrid functionals*

$$E_\text{xc}^\text{hybrid} = aE_\text{x}^\text{exact} + (1-a)E_\text{x}^\text{GGA} + E_\text{c}^\text{GGA}, \tag{2.26}$$

where the parameter $a \in [0,1]$ defines the portion of exact exchange in the hybrid functional. Although physical meaning can be assigned to the parameter a (see *e.g.* Refs. [55, 56]) it is often tuned to produce results in good agreement with

experiments. A well known example of such functional is B3LYP [57, 58] which gives very good (much better than GGAs) energetics and structural properties of isolated molecular system. In fact, this is globally the most used functional and it has been already for years the workhorse of theoretical chemistry. Exact exchange can also be mixed with meta-GGAs to obtain even better energetics. Recent hybrid meta-GGAs of the Truhlar group [52] are some of the most accurate exchange correlation functionals for thermochemistry.

Despite the great success of hybrid functionals in chemistry of molecules, they are not that common in solid state physics, especially for metals. This is due to the fact that since the Coulomb potential has an infinite range and that the electrons in metals are delocalized, the evaluation of Eq. (2.25) is computationally very costly. Computational cost can be reduced by the so-called screened hybrid functionals in which the long range exact exchange contribution is replaced by its GGA counterpart and only the short range exact exchange contribution is explicitly used. A well known functional of this kind is HSE [59]. It has been shown that it gives similar results to the ones obtained with the unscreened hybrid functionals [60]. Due to its good accuracy for both solids and small molecules [60] it could be an attractive choice for gas-surface problems. However, difficulties (large computational effort) in evaluating the exact exchange, Eq. (2.25), are still hampering the use of hybrid functionals in dynamics studies of gas-surface interactions.

van der Waals functionals

An important shortcoming of all above mentioned functionals is that they can not, by construction, describe long range electronic correlations that give rise to the non-local van der Waals (vdW) interactions. A simple approach for circumventing this problem is adding a pairwise potential of the form $\frac{C_6^{i,j}}{|\mathbf{r_i}-\mathbf{r_j}|}$ between each of two atoms i, j in the system. The coefficients C_6 can be derived in different manners, giving rise to, *e.g.*, DFT-D2 [61] and vdW-TS [62] methods. More accurate vdW corrections have been proposed based on these works, see Refs. [63, 64]. These methods greatly improve the DFT description of weakly bound materials. A very significant progress was achieved by the introduction of the non-local correlation density functional vdW-DF [65]. Further refinements of vdW-DF functional, mostly by coupling to appropriate exchange functionals, provided very satisfying results for many systems (see reviews [66, 67]). Development of new

vdW methods in DFT (as the one of Ref. [68]) is an active research field. The introduction of a new vdW functional is always followed by the benchmark of its accuracy to available experimental data or/and higher level theories. The author also participated in one study of this kind [69].

2.2.2   Density funcitional theory in practice

Up to here the main ingredients of DFT have been presented and it has been shown that a standard DFT calculation reduces to solving the Kohn-Sham equations (2.16). Here we give a brief discussion on how these equations are solved in practice, with emphasis on the approach taken in this thesis (a much broader overview can be found in several books, *e.g.* see Ref. [38]). The first important step is the choice of the basis set that is used to represent the Kohn-Sham orbitals ϕ_i. Different basis functions are nowadays in use. Some of them are localized like Gaussian orbitals, Slater-type orbitals, Numerical Atomic Orbitals, etc. In other cases nonlocalized ones are used such as plane waves, real-space basis set, etc. Plane waves are particularly well suited for solid state systems due to their intrinsic periodicity. This is the basis set used in this thesis. Advantages of plane waves are their orthogonality, their independence on atomic positions, the easiness to control the completeness of the basis set and that fast algorithms exist to operate with them (most noticeably fast Fourier transform).

The potential in a solid is periodic and Bloch theorem applies [70]. This theorem states that the eigenstates (in our case Kohn-Sham orbitals) of a periodic potential can be written as

$$\phi_{i,\mathbf{k}}(\mathbf{r}) = u_{i,\mathbf{k}}(\mathbf{r})e^{i\mathbf{k}\cdot\mathbf{r}}, \tag{2.27}$$

where $\mathbf{k}$ is a wavevector in the first Brillouin zone and $u_{i,\mathbf{k}}$ is a function with the same periodicity ($\mathbf{R}$) as the potential,

$$u_{i,\mathbf{k}}(\mathbf{r}) = u_{i,\mathbf{k}}(\mathbf{r} + \mathbf{R}). \tag{2.28}$$

By expanding $u_{i,\mathbf{k}}$ in the plane wave basis set (Fourier series), Kohn-Sham orbitals can be written as

$$\phi_{i,\mathbf{k}}(\mathbf{r}) = \frac{1}{\sqrt{\Omega}} \sum_{\mathbf{G}} C_{i,\mathbf{k}}(\mathbf{G})e^{i(\mathbf{k}+\mathbf{G})\cdot\mathbf{r}}, \tag{2.29}$$

where $\mathbf{G}$ are reciprocal lattice vectors and $\frac{1}{\sqrt{\Omega}}$ is a normalization factor. Inserting Eq. 2.29 in the Kohn-Sham equations [Eq. (2.16)] one obtains a matrix equation

for the coefficients $C_{i,\mathbf{k}}$

$$\sum_{\mathbf{G}'} \left(\frac{1}{2} |\mathbf{k} + \mathbf{G}|^2 + v_{\text{eff}}(\mathbf{G} - \mathbf{G}') \right) C_{i,\mathbf{k}}(\mathbf{G}') = C_{i,\mathbf{k}}(\mathbf{G})\epsilon_{i,\mathbf{k}}, \qquad (2.30)$$

where $v_{\text{eff}} = v_{ne} + v_{\text{H}} + v_{\text{xc}}$.

Obviously, in practice (on computers) the number of plane waves that represent the wave function, Eq. (2.29), can not be infinite. Usually their number is conveniently expressed by a cut-off kinetic energy

$$\frac{1}{2}(\mathbf{k} + \mathbf{G}) \leq E_{\text{cut-off}}. \qquad (2.31)$$

To determine a suitable $E_{\text{cut-off}}$ one should perform several calculations with increasing $E_{\text{cut-off}}$ and stop when the property of the interest (*e.g.* energy) converges.

Continuous sampling of the first Brillouin zone is also computationally problematic. However, this sampling can be performed efficiently and accurately by discrete (and finite) **k**-point grids. Monkhorst and Pack [71] devised a particularly useful scheme for generation of **k**-point grids that will be used in this thesis.

The disadvantage of plane wave basis sets is the fact that a prohibitively large number of plane waves (large $E_{\text{cut-off}}$) are necessary to describe large oscillations of wave-functions close to the nuclei. However, core electrons described by these wave-functions almost do not participate in the interaction with the other atoms. Therefore, it is possible to remove these electrons from explicit consideration. This is the so-called *pseudopotential* approximation. The pseudopotential name comes from the fact that it replaces the strong Coulomb potential of a bare nucleus with a softer potential of a pseudo-atom. That pseudo-atom contains the nucleus, core electrons, and the interaction among them including relativistic effects. The pseudopotentials are constructed such that the potential and resulting pseudo-wave-function are as smooth as possible inside a cut-off radius r_c close to the nucleus and that they are exactly the same as the real potential and wave-function outside r_c. Early pseudopotentials were the so-called *norm-conserving* pseudopotentials [72, 73]. Although still useful today due to their simplicity, their required $E_{\text{cut-off}}$ is still usually too large. Considerably smaller cut-offs can be achieved by the so-called *ultrasoft* pseudopotentials [74]. Related, but more general approach is provided by the *projector-augmented waves* (PAW) method [75, 76] that also allows for calculation of all-electron observables. PAW pseudopotentials are used in most of the calculations presented in this thesis.

Plane wave DFT is intrinsically periodic in all three dimensions in contrast to the two dimensional periodicity of the surface or no periodicity of the gas molecules. Therefore, a *supercell* approach is used to treat such systems. For molecules on a surface, one should construct a supercell that is laterally large enough to avoid interactions between molecules in adjacent cells. The surface is represented by a slab which has to be thick enough to avoid interaction between the two surfaces of the slab. Between the slabs there should be a thick enough vacuum region that prevents the interaction between the slab and its image. In the construction of the supercell these factors have to be taken into account keeping the computational cost (number of atoms) as low as possible.

2.3   The potential energy surface

2.3.1   Construction of a potential energy surface

Previous Sec. 2.2 provided the theoretical and practical methods that are used in this thesis to solve the electronic structure problem which is needed to obtain the potential energy surface-PES on which the nuclear motion is propagated. As Eq. (2.8) depends on nuclear positions, as soon as they are changed the electronic structure problem has to be solved again. On the other hand, for a practical solution of the Schrödinger equation for the nuclei motion, Eq. (2.9), one usually needs a continuous PES. Therefore, solving consistently electronic and nuclear equations is problematic. Moreover, even in the methods where necessity of a continuous PES is circumvented, the computational time has to be taken into account. For one set of nuclear coordinates of a typical small molecule on a surface system, the time required to solve the electronic structure problem with plane-wave DFT, on a modern multicore CPU, is usually between several minutes to several hours (depending on the system). Although, this is fast in terms of a single point calculation, a dynamics study usually requires thousands of steps. In addition, often one has to sample the initial conditions of the molecule or model the surface movement (temperature effects) keeping the results statistically meaningful. This drastically enlarges the number of single point calculations and dynamics becomes intractable with modern computing power. Instead of performing a DFT calculation for each geometry it would be, therefore, very advantageous to have a parametrized PES for arbitrary geometries that is of the same quality as the DFT calculations themselves. This is in fact possible to achieve as

discussed in the following.

In order to obtain a continuous PES, first one performs a number of DFT calculations for a set of system geometries. Subsequently, based of these calculations, one parametrizes a PES that is valid for an arbitrary geometry. Different schemes for this parametrization have been devised, and development of new ones is an interesting field of research (see *e.g.* Ref. [11]). These schemes can be mostly divided in two categories, those with physical insight and purely mathematical ones. The former usually involve small number of physically justified parameters, but the required accuracy is often hard to achieve. Examples of such potentials used for gas surface problems include LEPS potential [77–80] and the embedded atom method [81, 82]. Purely mathematical schemes are usually more flexible, they can be (and have to be) fitted to a large number of parameters and often provide good accuracy. For gas surface problems the most used schemes are: the corrugation reducing procedure [83], the modified Shepard interpolation [84], and neural network interpolation [85]. The advantage of the latter two methods is that they can be in principle applied to any number of degrees of freedom. On the other hand, the corrugation reducing procedure is particularly suited for diatomic molecules on surfaces and it provides a very good accuracy as shown in several applications [9]. In fact, the accuracy can be systematically increased as desired by adding additional DFT data. A general problem in PES parametrizations by mathematical schemes is that the number of input DFT data points increases with the number of degrees of freedom that are considered. Therefore, it is common to only consider molecular degrees of freedom (that are the most relevant ones) and keep the surface degrees of freedom frozen; *frozen surface approximation*. This approach is also followed here. We treat only diatomic molecules (six degrees of freedom) so the PES in the frozen surface approximation is six dimensional (6D).

The corrugation reducing procedure (CRP) is the parametrization (interpolation) method used through this thesis. The main problem in the interpolation of a molecular potential near the surface is the fact that it is highly corrugated. This means that for a small variation in molecular coordinates there is a large variation in the potential. The idea behind CRP is to reduce this corrugation to reasonable levels so that conventional interpolation techniques can be employed. It has been observed that most of the corrugation in the potential of a molecule on a surface comes from the interaction of individual atoms with the surface. Therefore, in CRP one subtracts the potentials of individual atoms from the molecular

potential with the aim of obtaining a smoother function which can then be easily interpolated.

The procedure for a diatomic molecule is the following. Let us first define the coordinate system for a molecule on a surface. The geometry of the molecule relative to the surface can be described by the cartesian coordinates of the center of mass of the molecule (X, Y, Z), the interatomic distance (r), the angle between the molecular axis and normal to the surface (θ), and the angle between the projection of the molecular axis to the surface and the X axis (φ). Alternatively, the molecule can be described by the cartesian coordinates of each atom in the molecule $(X_A, Y_A, Z_A, X_B, Y_B, Z_B)$. The first step in the procedure is to calculate a set of DFT energies for a grid of geometries. To reduce the computational cost it is convenient to include the most symmetric molecular configurations. Inclusion of these configurations is additionally important as the adsorption wells and reaction barriers are often found there. Therefore, usually one chooses several most symmetric X, Y positions. For each of these positions, several orientations (θ, φ) are chosen. Finally, for each set (X, Y, θ, ϕ) a grid of (r, Z) values is chosen and for each $(X, Y, Z, r, \theta, \varphi)$ configuration the DFT calculation is performed. r is usually sampled from a value a little bit below vacuum equilibrium interatomic distance to a value where the molecule can be regarded as dissociated. Z is usually varied form close to the surface where the potential is repulsive to several angstroms away from the surface where the interaction of the molecule and the surface is negligible. Once the DFT points are calculated the three dimensional potentials of each atom in the molecule, $V_{A,B}^{3D}$, are subtracted from the 6D molecule-surface potential V^{6D} points obtained by DFT. In this way one obtains the interpolation function I^{6D}

$$
\begin{aligned}
I^{6D}(X, Y, Z, r, \theta, \varphi) = \quad & V^{6D}(X, Y, Z, r, \theta, \varphi) - \\
& V^{3D}(X_A, Y_A, Z_A) - V^{3D}(X_B, Y_B, Z_B) .
\end{aligned}
\tag{2.32}
$$

This interpolation function is usually smooth enough to be interpolated by standard numerical interpolation methods. Usually the following steps are used:

- For each calculated (X, Y, θ, ϕ) configuration one uses 2D cubic splines to interpolate the calculated (r, Z) grid of energy points.

- With the obtained values from the previous step one proceeds with the (θ, ϕ) interpolation for each (X, Y). Usually a Fourier interpolation is used with

basis functions (sines and cosines) that have the same symmetry as the system.

- In the last step, the remaining (X, Y) interpolation is performed. In this case one can again use a symmetry adapted Fourier expansion or 2D periodic cubic splines.

After interpolating I^{6D}, the V^{3D} values are again added to the interpolation function to obtain the intended continuous $V^{6D}(X, Y, Z, r, \theta, \varphi)$.

Apparently, in the CRP scheme also the individual atom potentials $V_{A,B}^{3D}$ have to be calculated. They are obtained in a similar way as V^{6D}. First, DFT energies are calculated for a grid of positions of each atom $(X_{A,B}, Y_{A,B}, Z_{A,B})$. Note that the number of points in this grid is much smaller than in the 6D case because only three degrees of freedom must be considered. Therefore, the computational cost of calculating the 3D potential $V_{A,B}^{3D}$ is relatively small. $V_{A,B}^{3D}$ is also corrugated. This corrugation is reduced by subtraction of one-dimensional pair potentials V^{1D} that depend on the distance between the individual atom and the surface atoms

$$
\begin{aligned}
I^{3D}(X_{A,B}, Y_{A,B}, Z_{A,B}) = {} & V_{A,B}^{3D}(X_{A,B}, Y_{A,B}, Z_{A,B}) \\
& - \sum_i^n V^{1D}\left(\sqrt{(X_{A,B} - X_i)^2 + (Y_{A,B} - Y_i)^2 + (Z_{A,B} - Z_i)^2}\right),
\end{aligned} \tag{2.33}
$$

where (X_i, Y_i, Z_i) are the positions of surface atoms and the sum includes surface atoms that are close enough to the isolated atom to give nonzero contributions. Usually for V^{1D} one uses the DFT derived potential for varying distances Z of an isolated atom that is positioned above the top site of the surface. Then, I^{3D} can be interpolated using 3D cubic splines. Once the interpolation is performed, the subtracted V^{1D} terms are again added.

At the end of the PES construction it is important to verify its accuracy by comparing it to DFT data not included in the interpolation grid. If necessary, accuracy of the CRP can be increased by adding more DFT points in the grid.

2.3.2 Exploring a potential energy surface

Once it is decided how to obtain the PES, one usually characterizes it by several important properties, namely, the geometries and binding energies of adsorption

states, vibrational modes of the molecule in these states, and the energy barriers between different adsorption states. Next, we discuss how to obtain these properties from the PES.

Adsorption wells

Usually, the most important property of the PES is the adsorption well of the molecule described by its adsorption (binding) energy. This is one of the quantities that is often measured in experiments, and, therefore, theoretical predictions can be benchmarked against this value. If only one adsorption well (the minimum of the PES) exists, it is relatively easy to obtain its value and the corresponding molecular coordinates. For this task one may use any of the well known local optimizers, *e.g.* the conjugate gradient method [86], the quasi-Newton method [87], FIRE [88], etc.

The situation is more complicated if in addition to the global minimum, there are one or more local minima. In this case one might use its knowledge of physics to wisely choose starting configurations and proceed as above. However, this might be prone to omissions. Having a parametrized PES that is fast to evaluate (see previous section) can be advantageous as one can easily visually explore large portions of the PES and identify possible adsorption wells. This is usually enough for the systems studied within this thesis. More general approaches for global optimization exist, such as basin hopping [89] and minima hopping algorithms [90].

Vibrational analysis

In addition to the well depth, molecular vibrational modes in the well are also interesting. On the one hand, they can be experimentally measured and, therefore, compared to theoretical values. On the other hand they provide information about the shape of the adsorption well.

Different methods can be used to obtain vibrational modes (see review [91]). In this thesis we use a very simple finite differences method. For vibrational analysis usually the harmonic approximation is employed in which the energy of the molecule (in a well) is expanded in a second order Taylor series

$$
\begin{aligned}
E(\mathbf{R}) = {} & E(\mathbf{R_0}) + (\mathbf{R} - \mathbf{R_0})^{\mathrm{T}} \nabla \{E(\mathbf{R_0})\} \\
& + \frac{1}{2}(\mathbf{R} - \mathbf{R_0})^{\mathrm{T}} \mathbf{H} \{E(\mathbf{R_0})\} (\mathbf{R} - \mathbf{R_0}),
\end{aligned}
\tag{2.34}
$$

where $\mathbf{R_0}$ are the molecular coordinates that correspond to the adsorption well, $\nabla\{E(\mathbf{R_0})\} = 0$ is the value of the gradient of the potential in the adsorption well that is exactly zero, and $\mathbf{H}\{E(\mathbf{R_0})\}$ is the Hessian of the potential at the adsorption well. The Hessian is a square matrix and its elements are the second-order partial derivatives of the potential evaluated at the adsorption well coordinates

$$H_{i,j}\{E(\mathbf{R_0})\} = \left.\frac{\partial^2 E(\mathbf{R})}{dR_i dR_j}\right|_{\mathbf{R}=\mathbf{R_0}}. \tag{2.35}$$

From Eq. (2.34), the Newton equation for each degree of freedom can be written as

$$M_i\ddot{R}_i = -\sum_j H_{i,j}\{E(\mathbf{R_0})\}R_j, \tag{2.36}$$

where M_i is the mass corresponding to the i-th degree of freedom. Assuming an oscillatory solution to this equation, $R_i(t) = R_i(0)e^{i\omega t}$, one obtains the eigenvalue equation, which written in matrix form reads

$$\omega^2\mathbf{R} = \mathbf{H}^m\{E(\mathbf{R_0})\}\mathbf{R}, \tag{2.37}$$

where $\mathbf{H}^m$ is the mass-weighted Hessian matrix, $H_{i,j}{}^m = \frac{H_{i,j}}{\sqrt{M_i * M_j}}$. Therefore, diagonalization of the matrix $\mathbf{H}^m$ provides the vibrational normal mode vectors and frequencies. Within the finite differences method, the Hessian matrix elements are obtained in terms of finite differences of the forces for configurations in which the atoms are displaced from their equilibrium positions by small (finite) values. At least one displacement per degree of freedom is needed to obtain the Hessian matrix

$$H_{i,j} = \frac{f_{R_i}(\Delta R_j)}{\Delta R_j}, \tag{2.38}$$

where f_{R_i} is the force on the i-th degree of freedom which arises from the displacement ΔR_j of j-th degree of freedom from the equilibrium position. To reduce the computational noise in the Hessian matrix, usually one uses more than one displacement. For example, the formula for Hessian elements with four displacements is [92]

$$H_{i,j} = \frac{-f_{R_i}(2\Delta R_j) + 8f_{R_i}(\Delta R_j) - 8f_{R_i}(-\Delta R_j) + f_{R_i}(-2\Delta R_j)}{12\Delta R_j}. \tag{2.39}$$

Nudged elastic band method

Usually one is also interested in energy barriers that are present in the PES. In fact, they are usually the most influential quantity for chemical reactions in general. Here we discuss the methods we use to search for an energy barrier on the minimum energy path between given initial and final states. For gas-surface systems the relevant energy barriers are the barrier between vacuum and the adsorption state, and the barrier between two adsorption states. A rudimentary method that one can use is the brute force search that explores all possible paths between two states and identifies the path with the lowest energy. Although, this method is very inefficient, evaluation of the PES is fast enough to allow for such method.

Several more sophisticated methods are available (see Refs. [93, 94]). In this thesis the so-called *nudged elastic band method* [95, 96] is used and here it is briefly discussed. This method is very efficient and guarantees that the minimum energy path between an initial and final state is found. Therefore, it became a standard tool in chemistry and surface science. In this method one makes a guess for the minimum energy path, which is divided in several "images". The image is a configuration of the molecule which is between the initial and the final state. Commonly, a first guess for the images is a linear interpolation of the coordinates of the initial and the final state. The idea of the method is to optimize these intermediate images along the reaction path. Each image is relaxed towards the lowest possible energy while maintaining equal spacing to the neighboring images. This constrained optimization is achieved by addition of spring forces between each image. Due to the minimum energy path discretization, the saddle point (barrier) is usually not exactly found. To circumvent this problem, the *climbing image nudged elastic band method* can be used. In this refinement of the original method, the image with the highest energy is driven toward the saddle point. To accomplish that, spring forces are removed for this image and the true force along the transition path is reversed. In this way, the barrier energy can be accurately calculated.

2.4 Molecular dynamics

As already mentioned at the end of Sec. 2.1, in this thesis the nuclear motion is modelled by classical molecular dynamics simulations. Transition from quantum to classical equations of motion is necessary if more than few (up to six) degrees

of freedom are considered. However, it is not straightforward to prove that the classical Newton equation is a good approximation for the Schrödinger equation for the nuclei, Eq. (2.9) [97]. A good starting point for the transition from quantum to classical equations of motion is the Ehrenfest theorem [98] that gives the time evolution of the expectation values of position $< \mathbf{R}_i >$ and momentum $< \mathbf{P}_i >$ operators

$$M_i \frac{d}{dt} < \mathbf{R}_i > = < \mathbf{P}_i >,$$
$$\frac{d}{dt} < \mathbf{P}_i > = < \nabla_i V(\mathbf{R}) > . \tag{2.40}$$

From these equations one could infer that the quantum mechanical expectation values obey the classical equations of motion[¶]. Therefore, if the wave-function that describes the nucleus is localized enough, it could be a reasonable approximation to solve the classical equations of motion. Usually, quantum effects are associated only with the lightest atoms, *i.e.* hydrogen. Even in the case of hydrogen interaction with the surfaces, comparative classical and quantum studies showed similar results [99, 100]. Quantum effects typically vanish exponentially with the mass (for example tunneling). The lightest atom that is studied in this thesis is carbon, which is already an order of magnitude heavier than the hydrogen atom, so quantum effects can be safely neglected.

2.4.1   Molecular dynamics on a potential energy surface

Once the 6D PES is constructed one can perform classical trajectory calculations using the Newton equation for the six molecular degrees of freedom

$$M_i \frac{d^2 \mathbf{R}_i}{dt^2} = -\nabla_i V^{6D}(\mathbf{R}_i, \mathbf{R}_j), \quad i \neq j, \tag{2.41}$$

where $i, j = $ A, B are the indexes of the atoms in the diatomic molecule. Several well-know integrators of this equation exist and can be used, *e.g.* (velocity) Verlet algorithm [101], Beeman algorithm [102], etc.

At the beginning of each trajectory calculations the initial conditions have to be set. First, let us discuss simulations of molecular beam experiments. In these simulations the molecule is initially positioned far from the surface, where the

---

[¶]This statement is not entirely true due to the fact that in general $< \nabla_i V(\mathbf{R}) > \neq \nabla_i V(< \mathbf{R} >)$, see discussion in Ref. [97].

interaction between the molecule and the surface is negligible. Molecular beam widths are much larger that the typical periodicity of the surface. Due to this, the lateral initial position of the molecule is usually sampled by a conventional Monte-Carlo method (each initial X_i, Y_i position has the same probability). The interatomic distance is chosen to be the equilibrium one in the vacuum (the one with the lowest energy). Orientations of the molecule are also sampled by a conventional Monte-Carlo method. Momenta of the center of mass of the molecule are chosen such that they reproduce the experimentally chosen incidence angle and incidence energy. The radial momentum and rotational momentum are often set to zero in classical calculations, but they can also be sampled according to the temperature of the beam.

On the other hand if one wants to simulate the dynamics of a molecule already adsorbed on the surface, the molecule is usually positioned in (one of) the adsorption well(s). Therefore, its initial coordinates are determined by the adsorption geometry and a sampling over degrees of freedom is not needed.

Classical equations neglect the vibrational zero point energy of the molecule. However, due to the strong bond of the atoms in typically studied diatomic molecules, this energy can be substantial, of the same order of magnitude as the translational energy. To reduce the effect of this shortcoming, one can perform the so-called quasi-classical calculations. In these calculations the interatomic distance and radial momenta are sampled in such way that the vibrational energy of the molecule corresponds to its zero point vibrational energy. This scheme usually improves the agreement between the classical and quantum calculations, as demonstrated for hydrogen in Refs. [99, 100].

2.4.2 The generalized Langevin oscillator model

We perform the dynamics on a 6D PES calculated within the frozen surface approximation which, in principle, does not allow to include the dynamical energy exchange between the molecule and the surface lattice. One successful model that is able to keep the accuracy of a DFT based PES and at the same time provides a reasonable description of the surface movement is the generalized Langevin oscillator (GLO) model [103–106]. In the GLO model, the surface motion is described in terms of a three dimensional (3D) harmonic oscillator of mass m_s with position vector $\mathbf{R}_s$ and associated diagonal 3×3 frequency matrix Ω^2. Energy dissipation and thermal fluctuations are modelled with the help of a ghost 3D os-

cillator with position vector $\mathbf{R}_g$. The mass and the associated frequency matrix for the ghost oscillator are also m_s and Ω^2. The equations of motion for the molecule and the surface and ghost oscillators, which are coupled by the coupling matrix Λ_{gs}, are the following,

$$M_i \frac{d^2\mathbf{R}_i}{dt^2} = -\nabla_i V^{6D}(\mathbf{R}_i - \mathbf{R}_s, \mathbf{R}_j - \mathbf{R}_s), \quad i \neq j, \tag{2.42}$$

$$m_s \frac{d^2\mathbf{R}_s}{dt^2} = -\nabla_s V^{6D}(\mathbf{R}_i - \mathbf{R}_s, \mathbf{R}_j - \mathbf{R}_s) - m_s\Omega^2\mathbf{R}_s + m_s\Lambda_{gs}\mathbf{R}_g, \tag{2.43}$$

$$m_s \frac{d^2\mathbf{R}_g}{dt^2} = -m_s\Omega^2\mathbf{R}_g + m_s\Lambda_{gs}\mathbf{R}_s - \eta_{ph}\frac{d\mathbf{R}_g}{dt} + \mathbf{Rf}^{ph}(T_{ph}). \tag{2.44}$$

The friction force $-\eta_{ph}\frac{d\mathbf{R}_g}{dt}$ models the energy dissipation from the interacting surface atoms to the bulk thermal bath. Following Ref. [104], the friction coefficient η_{ph} is calculated from the Debye frequency ω_D as $\eta_{ph} = m_s\pi\omega_D/6$. The random fluctuation force $\mathbf{Rf}^{ph}$, which models the heating of the surface atoms due to the thermal motion of the bulk atoms, is a Gaussian white noise with variance

$$Var(\mathbf{Rf}^{ph}(T_{ph})) = \sqrt{\frac{2k_B T_{ph}(t)\eta_{ph}}{\Delta t}}, \tag{2.45}$$

where Δt is the time integration step, k_B is the Boltzmann constant, and T_{ph} is the time-dependent phonon (surface) temperature. The friction and random fluctuation forces are linked by the fluctuation-dissipation theorem to ensure that the surface atoms are coupled to a thermal bath of temperature T_{ph}. The oscillator frequencies $(\Omega^2)_{ii} = 2\omega_i^2$ and coupling matrix elements $(\Lambda_{gs})_{ii} = \omega_i^2$ are obtained from the surface phonon frequencies ω_i $(i = x, y, z)$ at the edges of the surface Brillouin zone, as proposed in Refs. [105, 106].

2.4.3 Electronic friction

From what it has been stated above, it already became clear that the Born-Oppenheimer (adiabatic) approximation, in which the electrons react instantaneously to the nuclear motion, is a cornerstone of gas-surface dynamics. Nevertheless, the existence of a nonadiabatic energy dissipation upon adsorption of gas species (atomic or molecular) on metal surfaces through electron-hole pair excitations is well established [107, 108]. Several methods can be used to model this dissipation mechanism [109–113]. Among them, a method that has proven to be

both accurate and suitable to perform multidimensional molecular dynamics is the *local density friction approximation* (LDFA) [111]. In this model, electronic non-adiabatic dissipative effects are introduced in the dynamics equation of motion via a friction force proportional to the velocity of the atom

$$M_i \frac{d^2 \mathbf{R}_i}{dt^2} = -\nabla_i V(\mathbf{R}_i, \mathbf{R}_j) - \eta_{el,i}(\mathbf{R}_i) \frac{d\mathbf{R}_i}{dt}. \tag{2.46}$$

The friction coefficient η_{el} is obtained in terms of the scattering of electrons by an atom inside a homogeneous free electron gas (FEG) as

$$\eta_{el} = \frac{4\pi n}{k_F} \sum_{l=0}^{\infty} (l+1) \sin^2[\delta_l(k_F) - \delta_{l+1}(k_F)]. \tag{2.47}$$

In this equation, n is the FEG density and k_F is the Fermi momentum. The $\delta_l(k_F)$ are the scattering phase shifts evaluated at the Fermi level corresponding to the potential induced by the atom in the FEG, which is calculated within DFT. The friction coefficient of Eq. (2.47) has successfully been used to calculate the stopping power of atoms and ions in metal solids and surfaces [114–117]. Within the LDFA, the electronic density entering Eq. (2.47) is chosen at each point of the trajectory as that of the bare surface at the position of the atomic nuclei $n(\mathbf{R}_i)$. The latter can be easily obtained from a DFT calculation. The LDFA has been applied to study the effect of electronic excitations in the dynamics of atoms and molecules on metal surfaces [111, 118–123].

Dynamics with electronic friction can be easily coupled with the GLO model, Eqs. (2.43) and (2.44), by replacing $\mathbf{R}_i$ with $\mathbf{R}_i - \mathbf{R}_s$ in Eq. (2.46).

2.4.4 Ab-initio molecular dynamics

Complementary to the dynamics on a 6D PES is *ab-initio* molecular dynamics (AIMD). Advantages of the 6D PES dynamics lie in the fact that it is very fast, which allows to obtain a large number of trajectories and, thus, statistically meaningful results. Disadvantages are that surface atoms are frozen and that the PES construction can be cumbersome. In contrast, AIMD allows the equal treatment of all degrees of freedom, not only those of the molecule, but also those of the surface atoms. Additionally, AIMD calculations require a rather simple set-up and a limited time of human work. However, this comes with a rather large computational cost and it is often hard to obtain good statistics.

The idea of AIMD is to use DFT to calculate forces on the atoms "on the fly", *i.e.*, at each step in the dynamics. A convenient scheme to evaluate the forces $\mathbf{F}_{\mathbf{R}_i}$ on the nucleus in DFT is given by the Hellmann-Feynman theorem [124]

$$\mathbf{F}_{\mathbf{R}_i} = - <\phi|\nabla_{\mathbf{R}_i} H_{el}|\phi> . \tag{2.48}$$

Note that only the electrostatic terms in H_{el}, Eq. (2.8), explicitly depend on nuclear coordinates $\mathbf{R}_i$, so once the ground state electronic density is obtained by DFT, forces can be calculated using classical electrostatics. The computational cost of evaluation of Eq. (2.48) is very small compared to a total DFT calculation.

Except for the changes in the force evaluations, the dynamics calculation set-up, *e.g.* initial conditions for the molecule, are the same as in 6D PES dynamics. Obviously, the GLO model is not needed in this case, the surface atoms can also move and, thus, the molecule can transfer its energy to the surface. One can apply a thermostat [125] to the surface atoms to explore temperature effects. The molecular dynamics with electronic friction can be used in the same way in AIMD as with the 6D PES dynamics [121].

2.5   Hot electrons

The scattering of metal surface electrons on the atoms of the molecule is responsible for the energy loss of the molecule moving close to the surface, as discussed above. This is the situation encountered at relatively low temperatures of surface electrons. At high surface electron temperatures, many electron-hole pairs are already excited, and the reverse process in which molecule takes energy from the electronic system becomes important. One way of obtaining the high surface electron temperatures in metals is by laser excitation in the ultra-violet (UV), visible (VIS), and near infra-red (NIR) spectral range. Therefore, if a molecule is adsorbed on a metal surface it is possible to induce its movement by shining an intense laser light on the surface.

The response of a metal surface to the excitation generated by an ultra short laser pulse can be described by the so called *two temperature model* (2TM) [126]. In this model, the equilibration between the electron and lattice heat baths with temperatures T_{el} and T_{ph}, respectively, is described by the following coupled diffusion equations,

$$C_{el}\frac{\partial T_{el}}{\partial t} = \frac{\partial}{\partial z}\kappa\frac{\partial T_{el}}{\partial z} - g(T_{el} - T_{ph}) + S(z,t), \tag{2.49}$$

$$C_{ph}\frac{\partial T_{ph}}{\partial t} = g(T_{el} - T_{ph}), \tag{2.50}$$

where C_{el} is the the electron heat capacity, C_{ph} is the phonon heat capacity, κ is the electron thermal conductivity, g is the electron-phonon coupling constant, and $S(z,t)$ is the laser source term. In the regime of intense laser pulses, metal electrons are rapidly heated to several thousands K due to the low electron heat capacity C_{el} of metals. The formed hot electrons can either diffuse to the bulk [first term in the right hand side of Eq. (2.49)] or transfer heat to the lattice phonons [term $g(T_{el} - T_{ph})$ in Eqs. (2.49) and (2.50)]. The heat source term $S(z,t)$ is calculated for a metal film of thickness d by

$$S(z,t) = \frac{I(t)e^{-\alpha z}}{1 - e^{-\alpha d}}, \tag{2.51}$$

where $I(t)$ is the adsorbed fraction of a laser pulse intensity and α^{-1} is the optical penetration depth. The latter is calculated from the laser wavelength λ and the imaginary part of the refractive index of the surface k as $\alpha^{-1} = \lambda/(4\pi k)$.

Following Ref. [127], the laser-induced dynamics of the adsorbed molecule is modelled using a Langevin equation for each atom i in the molecule,

$$M_i\frac{d^2\mathbf{R}_i}{dt^2} = -\nabla_i V(\mathbf{R}_i, \mathbf{R}_j) - \eta_{el,i}(\mathbf{R}_i)\frac{d\mathbf{R}_i}{dt}$$
$$+ \mathbf{R}\mathbf{f}_i^{el}(T_{el}, \eta_{el,i}(\mathbf{R}_i)), \quad i \neq j. \tag{2.52}$$

This equation is the same as Eq. (2.46) with the addition of a fluctuating (random) force $\mathbf{R}\mathbf{f}_i^{el\,\|}$. This fluctuating force is due to scattering of heated electrons with the adsorbate. $\mathbf{R}\mathbf{f}_i^{el}$ can be connected through the fluctuation-dissipation theorem to the electronic friction force via the electronic temperature T_{el} [127]. Here, $\mathbf{R}_i^{el}$ is modelled by a Gaussian white noise with variance

$$Var(\mathbf{R}_i^{el}(T_{el})) = \sqrt{\frac{2k_B T_{el}(t)\eta_{el,i}}{\Delta t}}. \tag{2.53}$$

$^\|$This term is usually negligible for the typical thermal surface temperatures used in gas-surface experiments and, therefore, it can safely be neglected, as in Eq. (2.46). However, this term gives a large contribution in case of the high T_{el} that are obtained in the wake of the laser excitation, particularly, for adsorbates embedded in high electron density regions of the surface.

Potential energy surface for O$_2$ on Ag(110)

3.1 Introduction: current research status of the O$_2$ on Ag(110) system

Interaction of oxygen with silver surfaces is a paradigmatic example of the gas-surface dynamics as it features three adsorption states depending on the surface temperature: a physisorbed state, a molecularly chemisorbed state and a dissociatively chemisorbed state. Moreover, silver is the most important catalyst in the ethylene epoxidation, where oxygen dissociation on the surface is a first step. Among all the low index surfaces, the Ag(110) is particularly interesting as it is the most reactive toward dissociation. Therefore, this system was a subject of comprehensive research both from the experimental and theoretical point of views. In spite of it, O$_2$ adsorption dynamics on Ag(110) is still not fully understood. A model for the adsorption dynamics has been proposed on the basis of molecular beam experiments [19–22]. However, up to date no theoretical work has succeeded in reproducing those experiments.

Aforementioned molecular beam experiments [19–22] have investigated the dependence of the initial sticking probability on the surface temperature. For all studied surface temperatures (T_s = 80–500 K), the system shows a similar sticking probability curve as a function of the molecule incidence energy $S_0(E_i)$. At low surface temperatures (T_s = 80–200 K) the sticking probabilities at a given incidence energy hardly depend on T_s. At higher T_s, the sticking probabilities decrease with increasing T_s, their value at $T_s \approx 350$ K being around one half of the value at low temperatures. At low T_s and normal incidence, the sticking curve

---

This chapter is based on publications 1 and 4.

$S_0(E_i)$ measured by the method of King and Wells, rises from $\approx 10^{-2}$ at the lowest incidence energy of 0.1 eV to ≈ 0.5 at incidence energies of 0.6–0.7 eV, and slightly decreases afterwards [19, 22]. It is well established (as discussed below) that at $T_s > 150$–200 K the adsorbed oxygen molecules are dissociated. This leads to the conclusion that the molecular beam experiments are measuring the sticking probabilities of the molecularly chemisorbed oxygen at low surface temperatures and the sticking probabilities of the dissociatively chemisorbed oxygen at higher surface temperatures. In fact, electron energy loss spectroscopy (EELS) was used to measure the sticking probabilities by monitoring the vibrational frequency assigned to a O-O stretch mode of the chemisorbed molecule at low surface temperatures ($T_s \approx 100$ K) and by monitoring a O-Ag mode of the dissociated molecule at high surface temperatures ($T_s \approx 300$ K) [19]. After a calibration to the results obtained with the King and Wells method, the EELS sticking probabilities are reported to be in the range of 10^{-4}–10^{-3} at the lowest beam incidence energy of 88 meV. No direct dissociation at $T_s = 83$ K was measured even for the largest incidence energy of 0.62 eV.

The model for the adsorption dynamics is based on all this information. Due to the similarities of the sticking curves for molecular and dissociative adsorption, it has been concluded that the molecular chemisorption acts as a precursor to dissociation [19]. The latter only happens if the surface temperature is high enough ($T_s > 150$–200 K). The decrease of the sticking probability with increasing T_s is explained by the competing partial desorption of some of the chemisorbed molecules. Within this assumption, one can obtain the difference between the barrier for desorption and the barrier for dissociation, which amounts to ≈ 0.1 eV [17, 19, 22]. Effects of the physisorbed state on the adsorption dynamics at the studied temperatures ($T_s = 80$–500 K) have been disregarded due to the measured low sticking probabilities at low incidence energies [19].

The aim of this and three next chapters is to understand the dynamics of the above described processes on the basis of first principles electronic structure calculations. In doing so we will refer to other types of experiments also performed in this system that provide further insight in the adsorption process.

Using temperature programmed desorption (TPD) several desorption peaks have been observed to appear depending on the surface temperature at which O$_2$ is deposited [17, 22, 128–138]. More specifically, if O$_2$ is deposited at room temperature only one peak is identified around 580 K that is attributed to the recombinative desorption of the dissociatively chemisorbed state [22, 128–131, 133]. An ad-

ditional peak appears at 160–190 K when O$_2$ is dosed at $T_s = 120$–140 K [17, 130–132]. Beside these two peaks, a further peak at 100–120 K is observed when O$_2$ is deposited on the surface at even lower temperatures $T_s = 75$–90 K [134–136, 138]. Both peaks at 160–190 K and 100–120 K, are attributed to the molecularly chemisorbed states. Furthermore, the peak around 160–190 K is not observed in the zero coverage limit and, as recently argued, is attributed to the interaction of hot O atoms (which originate from the dissociation process) and a molecularly chemisorbed species [138]. When the molecule is deposited at very low surface temperatures ($T_s < 30$ K) several peaks attributed to the physisorbed state arise that depend on the surface coverage. More precisely, for the lowest coverages a broad peak at 50 K is observed that splits in two peaks at 46 K and 59 K with increasing coverage up to one monolayer. At coverages larger than one monolayer an additional peak at 38 K is measured [134–137]. Interestingly, when depositing O$_2$ at such low surface temperatures, the desorption peak at 100–120 K is still measured while the peaks at 160–190 K and 580 K are not. This leads to the conclusion that the physisorbed state can be converted into the molecularly chemisorbed species that desorbs at 100–120 K. However, it can not be converted into the other molecularly chemisorbed species (characterized by the peak at 160–190 K) that is prepared by dosing at higher surface temperatures and that is the precursor to the dissociated state [134–136, 139].

In addition to TPD measurements, EELS can also be used to distinguish the adsorption states which are prepared by dosing O$_2$ at different surface temperatures. At $T_s > 200$ K only one loss peak at 40 meV, corresponding to the O-Ag vibration, is measured [19, 131, 140]. At lower surface temperatures $T_s = 70$–120 K, for which the molecularly chemisorbed state is populated, two vibrational frequencies at 30 meV and 80 meV are measured, which are attributed to the O$_2$-Ag and O-O vibrations, respectively [19, 131, 134–136, 140]. The disappearance of the peak at 80 meV and the appearance of the peak at 40 meV as the surface temperature is increased allowed Vattuone *et al.* [140] to establish $T_s = 143$ K as the surface temperature at which chemisorbed molecules dissociate. EELS measurements at $T_s = 15$ K show a peak arising from the O-O stretch vibration of the physisorbed state at 194 meV and a peak at 85 meV attributed to the molecularly chemisorbed species [134–136]. From the EELS study of the angular distributions in resonance electron scattering it was concluded that the physisorbed state lies parallel to the surface with the molecular axis oriented in the [001] direction. Additionally, from the EELS resonance energy, the physisorption height is estimated

to be $Z = 2.5 \pm 0.3$ Å [136, 141, 142].

A near-edge x-ray-absorption fine-structure (NEXAFS) study of oxygen adsorbed at $T_s = 90$ K showed that the molecules adsorb parallel to the surface oriented in the $[1\bar{1}0]$ direction with an estimated O-O distance of 1.47 ± 0.05 Å [143, 144]. The NEXAFS study of the molecules deposited at $T_s = 25$ K (physisorbed state) suggests that the molecules adsorb parallel to the surface but oriented in the [001] direction [18].

Angle-resolved photoemission spectroscopy (ARPES) measurements, together with the application of selection rules, have allowed to deduce that the physisorbed molecule, which was prepared at $T_s = 25$ K with sticking probabilities close to one, lies parallel to the surface while the chemisorbed molecule, which was prepared at $T_s = 110$ K, lies parallel to the surface and oriented along the $[1\bar{1}0]$ direction [16, 145].

However, using ESDIAD (electron stimulated desorption ion angular distribution) and measuring angular distributions of O^+ when chemisorbed O_2 molecules, prepared at a temperature $T_s = 80$ K, were present at the surface, showed that the desorbed O^+ ions were preferentially emitted towards the [001] direction. This suggested that the [001] was the favoured orientation for the chemisorbed state [146]. Additionally, ESDIAD of the physisorbed state, prepared at $T_s = 33$ K, identified two molecular orientations, along the [001] and the $[1\bar{1}0]$ directions [137].

The system was also studied by the scanning tunneling microscope (STM) [147–152]. STM images of adsorbed O_2 prepared by depositing it on the surface at $T_s = 40$–75 K revealed two different molecularly chemisorbed species, both found on the hollow site of Ag(110), but with two different orientations, [001] and $[1\bar{1}0]$ [148, 150]. Vibrational frequencies of the molecularly chemisorbed molecule oriented along the [001] direction measured by inelastic electron tunneling spectroscopy (IETS) performed with STM are found to be 82 meV for the O-O stretch mode and 38 meV for the antisymmetric O_2-Ag mode [148]. Unfortunately, STM experiments for molecules deposited at very low surface temperature ($T_s = 13$ K) could not provide information about the position and orientation of the physisorbed molecule. The reason was that the physisorbed molecules seemed to diffuse across the surface until encountering an impurity to form an island [150].

A number of theoretical works have been devoted to the study of the O_2/Ag(110) system [153–166]. Semi-local density functional theory (DFT) calculations of Gravil *et al.* [153–155] found the adsorption positions of the two

chemisorbed states in agreement with the STM measurements [150]. The measured vibrational modes of the chemisorbed states are also reasonably well described by DFT calculations using different semi-local exchange-correlation functionals [155, 157, 159, 160]. Furthermore, STM-IETS experiments [148] were successfully simulated on the basis of semi-local DFT results [156–158]. Calculations of Gravil *et al.* also predicted a physisorbed state at the long bridge site with the molecular axis oriented along the [001] direction. This site is accompanied by another physisorbed state at the short bridge site with the molecular axis oriented along the [1$\bar{1}$0] direction according to recent DFT calculations [159].

Aforementioned DFT calculations were focused on specific configurations of the molecule on the surface and give information about adsorption positions, adsorption energies, and energy barriers to dissociation. Still, full understanding of the complex interaction of the oxygen molecule with the Ag(110) surface at DFT level can only be achieved by performing trajectory calculations. Dynamics of this system has been previously studied using a model LEPS (London-Eyring-Polanyi-Sato) potential by Pazzi *et al.* [161, 162] with modest success. This approach enables to evaluate large numbers of trajectories but introduces empiricism in the potential. On the other hand, as discussed in previous chapter, if the surface is kept frozen a full (six) dimensional high quality potential energy surface-PES can be constructed by interpolating a grid of DFT energies. Thousands of trajectories can then be evaluated on this PES providing reliable statistics. This methodology has been already used to study dynamics of oxygen on the Ag(100) [167] and the Ag(111) [168, 169] surfaces, but a similar study on the more reactive Ag(110) is missing. With this aim in this chapter we construct such DFT-PES and examine its features. Dynamics on this PES is then discussed in next chapters.

3.2 Calculation of the adiabatic potential energy surface

As pointed out in Ch. 2, the interaction of the O_2 molecule and the frozen Ag(110) surface is fully described by a 6D PES that only depends on the position of the two O atoms over the surface. Here, we show the procedure we use to construct the continuous 6D PES of O_2/Ag(110). We use the *corrugation reducing procedure* (CRP) [83] to interpolate a set of 25 376 energies that are calculated with

spin-polarized density functional theory (DFT) for chosen O_2–Ag(110) geometries. The DFT calculations are performed with the *Vienna Ab initio Simulation Package* (VASP) [170, 171] using an energy cut-off of 400 eV in the plane-wave basis set. We apply the projector augmented-wave method (PAW) [75, 76] to describe the electron–core interaction. The exchange-correlation energy is described by the Perdew-Burke-Ernzerhof (PBE) functional [45].

The molecule-surface interaction can be modelled by the plane-wave basis set code only by using a supercell due to the implicit periodicity of this approach. Therefore the first step of any calculation is to construct such supercell. We start by finding the Ag lattice constant a with DFT-PBE. With this purpose we perform a series of energy calculations for different a and the one with the lowest energy corresponds to the silver bulk lattice constant. The calculated $a = 4.16$ Å compares well with the experimental value of 4.09 Å [172]. The Ag(110) surface is modelled by a supercell consisting of a five-layer thick slab with 14 layers of vacuum and a (2×3) surface unit cell. As discussed below, the use of such a large supercell is necessary in the ulterior calculations of the O_2/Ag(110) DFT energies to avoid undesirable interactions among the periodically repeated molecules. The Brillouin-zone of the supercell is sampled with a $4 \times 4 \times 1$ Monkhorst-Pack grid of special **k**-points [71]. Partial occupancies are determined by the Methfessel-Paxton method [173] of order 1 with a smearing width of 0.2 eV. Keeping the middle layer frozen we allow relaxation of the other two layers from each side of the slab. As a result, the distance between the first and second layers reduces by -7.8%, and the distance between the second and third layers increases by $+3.6\%$. These results should be compared with the experimental values of -7.8% and $+4.3\%$ [174].

Next, we calculate the binding energy, the bond length and the vibrational quanta of the O_2 molecule located in the middle of the vacuum region. At this position, there is no interaction between the molecule and the surface and the potential energy only depends on the O_2 interatomic distance r. Thus, after calculating the DFT energies for various r, we obtain from a simple spline interpolation the values of 5.88 eV for the binding energy (neglecting the zero point energy, ZPE) and 1.23 Å for the bond length. The vibrational quanta of 0.18 eV is calculated from the same potential energy $E(r)$ by solving numerically the radial Schrödinger equation. The results for the equilibrium bond length and vibrational quanta compare well with the corresponding experimental values of 1.21 Å and 0.19 eV [175]. Regarding the binding energy, our value is somewhat

higher than 5.12 eV, the experimental one [175]. This difference is consistent with the well known overestimation of the O_2 binding energy in vacuum at the DFT-GGA level [176]. Nevertheless, since adsorption energies and dissociation barriers close to the surface are obtained from total energy differences involving configurations with relatively low density gradients, this overestimation is largely cancelled, and therefore, it is not expected to affect much the dynamics in the interpolated potential energy surface. Importantly, our results for O_2 midway the two Ag slabs confirm the adequacy of the supercell size used in our calculations.

Due to the large number of DFT energies needed for the construction of the 6D PES, above listed specific choices of the size of the unit cell, the thickness of the Ag slab, the **k**-point mesh, etc., are chosen to give a good compromise between computational cost and accuracy. A careful convergence study presented in Appendix A shows that these choices do not affect the conclusions drawn in this thesis. We note, that in all the calculations special care has been taken to obtain correct spin densities as we have verified that potential energies of the system are strongly dependent on the spin state.
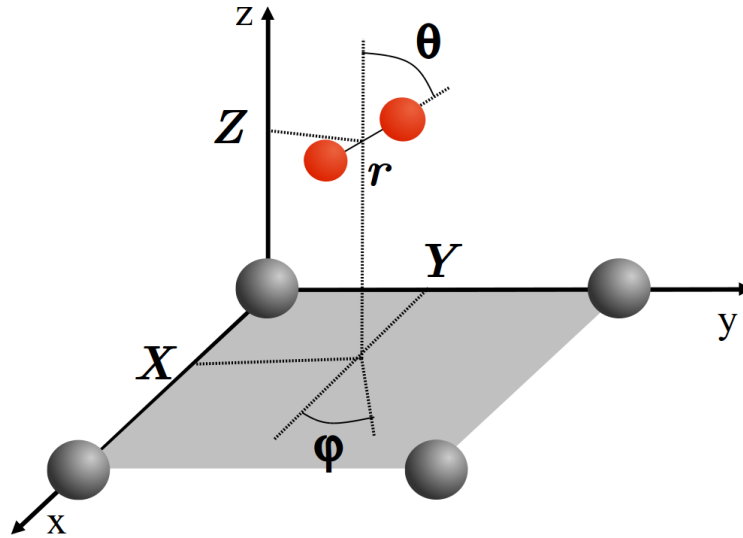
Figure 3.1: *Coordinate system used in our calculations: Ag atoms are in grey and the O atoms are in red. The x- and y-axis are parallel to the [001] and [1\bar{1}0] directions, respectively.*

After all these preliminary tests, we proceed to calculate the set of DFT energies that will be used to construct the 6D O_2/Ag(110) PES. In all the calculations the relaxed geometry of the surface is kept frozen. For practical reasons the reference zero potential energy is taken as that of the molecule in its equilibrium

bond length ($r_0 = 1.23$ Å) placed at 6.0 Å from the surface. At this distance the energy differs in less than 10 meV from the value obtained when the molecule is in the middle of the vacuum region, which justifies our choice. As explained in Ch. 2, we use a convenient coordinate system as the one depicted in Fig. 3.1, that includes: the cartesian coordinates that define the position of the center of mass of the molecule with respect to the surface (X,Y,Z), the O$_2$ interatomic distance r, and the polar and azimuthal angles (θ,φ) that define the orientation of the molecule. The DFT energy grid is constructed by computing two-dimensional (2D) (r,Z) cuts for different configurations of the O$_2$ molecule over the Ag(110) surface. Each configuration is defined by the center of mass coordinates (X,Y) and the O$_2$ orientation (θ,φ). In the 2D cuts r is varied from 0.93 Å to 2.53 Å in a non-equidistant grid of 13 points and Z is varied from 6.0 Å down to 0.0 Å in steps of 0.1 Å. The 2D cuts have been calculated for the five different (X,Y) positions shown by black circles in Fig. 3.2. Four of them correspond to the most symmetrical sites on the surface. The fifth one corresponds to a non-symmetrical
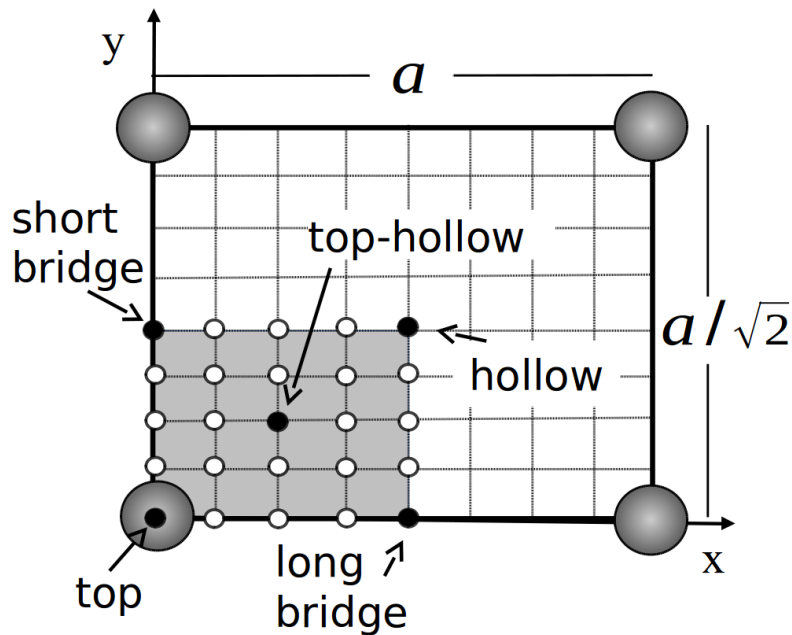
Figure 3.2: *Geometry of the Ag(110) surface. DFT calculations of the 3D O/Ag(110) PES have been performed for all sites marked by white and black circles. For O$_2$/Ag(110), DFT calculations have been performed for configurations with the molecular center of mass over the sites marked by black circles. The shaded area shows the irreducible surface unit cell.*

site that has been chosen in order to improve the quality of the CRP interpolation. For each site a different number of orientations have been considered. All in all, the 2D cuts have been calculated for the following 34 configurations:

- top site ($X = 0$, $Y = 0$) with seven orientations: $\theta = 0°$; $\theta = 45°$ with $\varphi = 0°$, 35.26°, 90°; $\theta = 90°$ with $\varphi = 0°$, 35.26°, 90°

- hollow site ($X = a/2$, $Y = a/(2\sqrt{2})$) with seven orientations $\theta = 0°$; $\theta = 45°$ with $\varphi = 0°$, 35.26°, 90°; $\theta = 90°$ with $\varphi = 0°$, 35.26°, 90°

- long-bridge site ($X = a/2$, $Y = 0$) with five orientations: $\theta = 0°$; $\theta = 45°$ with $\varphi = 0°$, 90°; $\theta = 90°$ with $\varphi = 0°$, 90°

- short-bridge site ($X = 0$, $Y = a/(2\sqrt{2})$) with five orientations: $\theta = 0°$; $\theta = 45°$ with $\varphi = 0°$, 90°; $\theta = 90°$ with $\varphi = 0°$, 90°

- top-hollow site ($X = a/4$, $Y = a/(4\sqrt{2})$) with ten orientations $\theta = 0°$; $\theta = 45°$ with $\varphi = 35.26°$, 90°, 144.74°, 215.26°, 270°, 324.74°; $\theta = 90°$ with $\varphi = 35.26°$, 90°, 144.74°.

To perform the 6D interpolation using the CRP [83] one also has to calculate the three dimensional (3D) PES of an atom interacting with the surface, in our case O with Ag(110). As described in Sec. 2.3, this 3D PES V^{3D} is then subtracted from the 6D PES V^{6D} to obtain the less corrugated function I^{6D} that can be accurately interpolated. After interpolating I^{6D}, the V^{3D} values are again added to the interpolation function to obtain the intended $V^{6D}(X, Y, Z, r, \theta, \varphi)$. A similar procedure is applied to obtain the requested $V^{3D}(X_{A,B}, Y_{A,B}, Z_{A,B})$ using in this case a one-dimensional (1D) O-Ag potential energy to reduce the corrugation of the 3D PES as prescribed in Sec. 2.3. Here, the atomic 3D O/Ag(110) PES is obtained from a grid of spin-polarized DFT energies that are calculated for the 25 sites illustrated by white and black circles in Fig. 3.2. For each site the distance of the atom to the surface is sampled from 6.0 Å to -1.2 Å in steps of 0.1 Å. After subtracting the 1D O-Ag potential the resulting 3D interpolation function is interpolated by the 3D cubic spline method (more information about the 3D atomic PES is given in Appendix B). The interpolation of I^{6D} is carried out in three steps. First, the (r,Z) interpolation is performed using the 2D cubic spline method. Subsequently, we interpolate over φ and θ using Fourier series expansions that take into account the symmetry of each particular site. Finally, the 2D cubic spline method is again

applied for the (*X,Y*) interpolation (a detailed explanation is given in Appendix B).
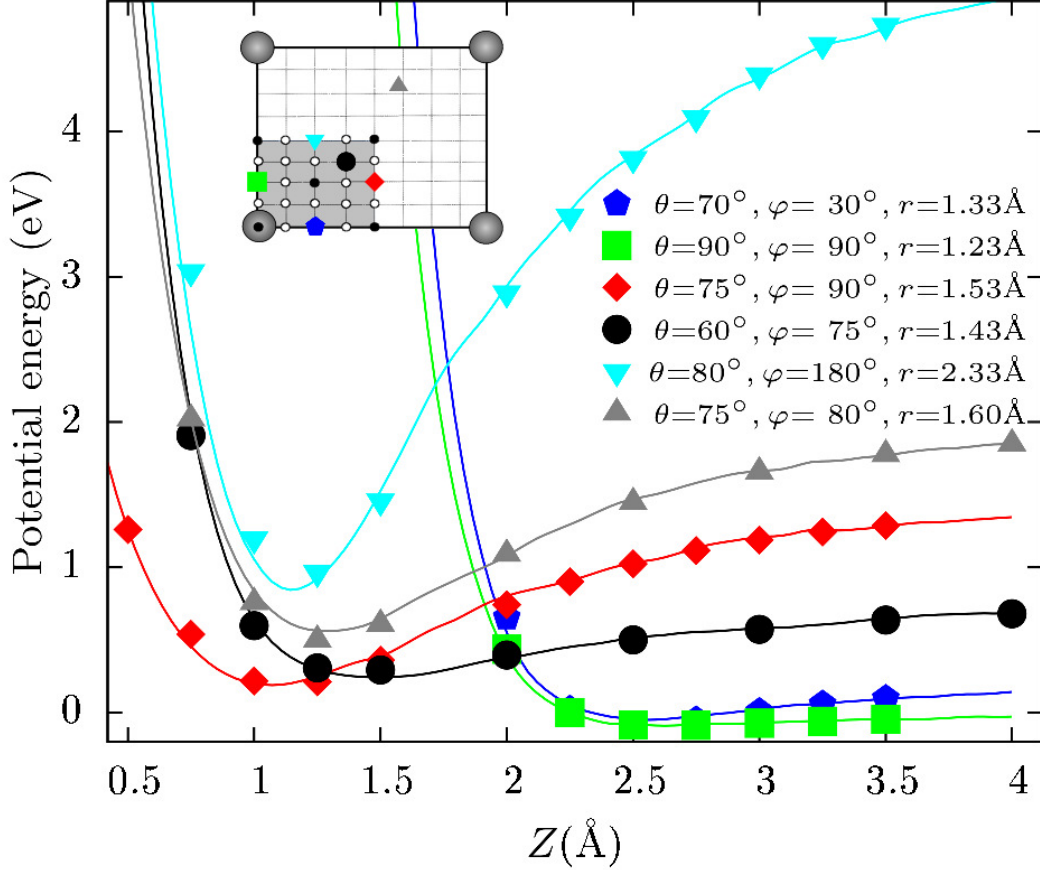
Figure 3.3: *Potential energy as a function of the O₂ center of mass height Z. The interpolated potential energies (lines) are compared with their corresponding DFT values (symbols) for different O₂ configurations (X, Y, r, θ, φ) not used in the interpolation procedure. The (X, Y) positions are marked on the Ag(110) cell by the corresponding symbols.*

In order to benchmark the accuracy of our interpolation we perform various tests using DFT data not included in the construction of the interpolation function. Comparisons of the DFT and interpolated values are shown in Figs. 3.3, 3.4, and 3.5. The tests shown in Fig. 3.3 are done for the configurations for which one would expect the largest interpolation errors, that is, for (*X, Y*)-positions located halfway the sites used in the construction of the 6D PES and for (*θ,φ*) orientations not used in the DFT energy set. Extreme examples of the accuracy reached in the typically sensitive (*θ,φ*) interpolations are shown in Figs. 3.4 and 3.5. The
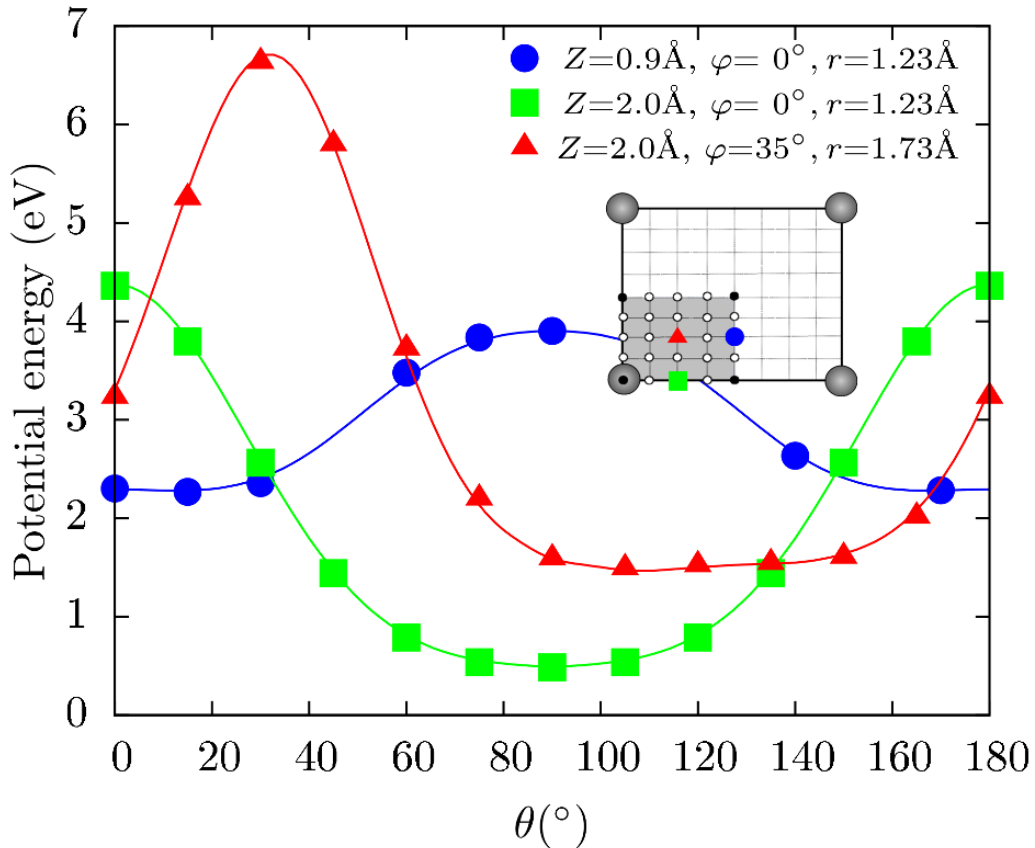
Figure 3.4: *Potential energy as a function of the O_2 polar angle θ. The interpolated potential energies (lines) are compared with their corresponding DFT values (symbols) for different O_2 configurations (X, Y, Z, r, φ) not used in the interpolation procedure. The (X, Y) positions are marked on the Ag(110) cell by the corresponding symbols.*

selected configurations correspond to those showing the largest interpolation errors. In general, we observe that interpolation errors are small (~ 50 meV) in the majority of the molecule configurational space. For a small number of configurations, the accuracy is in the range of ~ 100 meV when the molecule is close to the surface ($Z < 2$ Å), as can be seen in Fig. 3.5. However, errors in the important regions for the dynamics, such as adsorption sites and minimum energy barriers for reactions are kept below 20 meV. Errors are larger in highly repulsive regions (> 5 eV), but these regions are not probed in the dynamics of the molecule.

We have implemented our 6D PES as a calculator of energies and forces in the *Atomic Simulation Environment* (ASE) [177]. This tool give us the access to a range of methods applicable to our PES. In particular, we use ASE to calculate
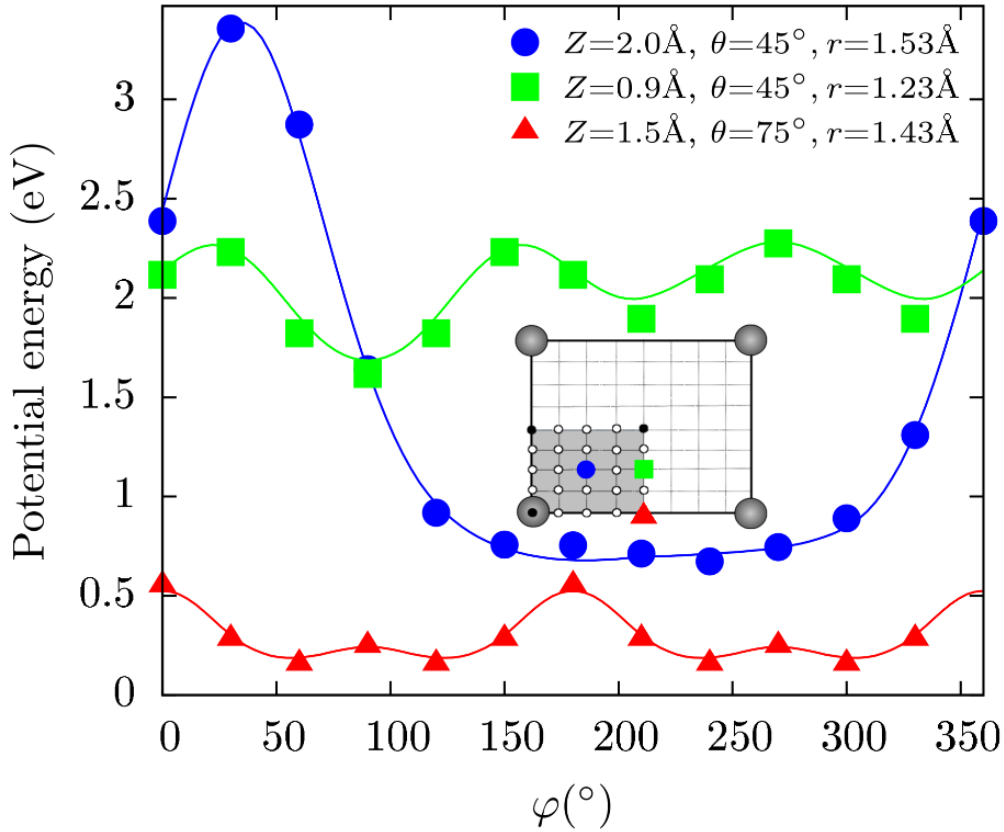
Figure 3.5: *Potential energy as a function of the O_2 azimuthal angle φ. The interpolated potential energies (lines) are compared with their corresponding DFT values (symbols) for different O_2 configurations (X, Y, Z, r, θ) not used in the interpolation procedure. The (X, Y) positions are marked on the Ag(110) cell by the corresponding symbols.*

vibrational modes of the molecule in the adsorption wells and energy barriers between adsorption states.

3.3 Features of the 6D potential energy surface

A selection of 2D (r, Z) cuts of the $O_2/Ag(110)$ PES is shown in Fig. 3.6. We choose these configurations because of their importance in either the dissociation or the O_2 adsorption processes. In the selected configurations the molecule center of mass is located at hollow, long-bridge, and short-bridge sites and with its axis oriented parallel to the surface ($\theta = 90°$) along the [001] ($\varphi = 0°$) and [1$\bar{1}$0] ($\varphi = 90°$) directions. Four of these configurations correspond to four distinctive adsorption
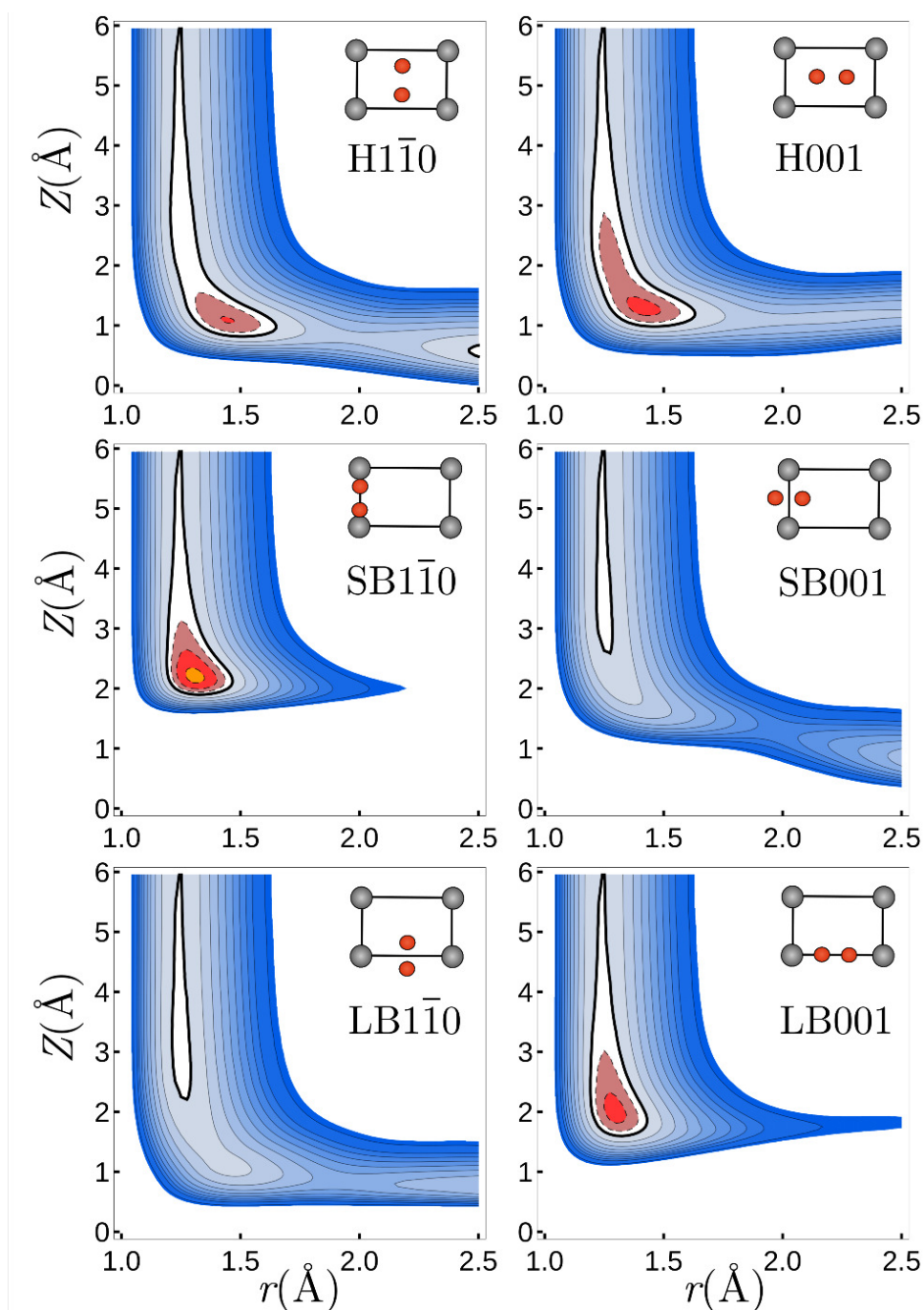
Figure 3.6: *(r, Z)-cuts of the O$_2$/Ag(110) 6D PES. The molecular orientation and position over the surface unit cell is schematically depicted in each contour plot. All molecules are positioned parallel to the surface (θ = 90°). Solid (dashed) contour lines correspond to positive (negative) values of the potential energy and separate intervals of 0.2 eV (0.1 eV). Thick solid lines correspond to zero potential energy.*

wells, namely, hollow [1$\bar{1}$0] (denoted as H110 in the following), hollow [001] (denoted H001), short-bridge [1$\bar{1}$0] (denoted SB110) and long-bridge [001] (denoted LB001). The same adsorption positions have been identified in Ref. [159] and, with the exception of SB110, in Refs. [153–155]. Although the other two configurations in Fig. 3.6, short-bridge [001] (denoted SB001) and long-bridge [1$\bar{1}$0] (denoted LB110), show also shallow minima in the 2D cuts, they do not correspond to adsorption wells because they are not minima in 6D. By performing global optimization using the minima hopping method (see Ch. 2.3.2), as implemented in ASE, we have verified that only the above listed four adsorption wells are present in our 6D PES. A remarkable feature of the 6D PES is the absence of energy barriers to access the adsorption wells, as shown in Fig. 3.6, in accordance with previous DFT results [153–155, 159]. The properties of each adsorption well are discussed in next Sec. 3.4.

Energy barriers to dissociation are also visible in Fig. 3.6. Our interpolated PES allows for a systematic exploration of the molecular configurational space to find the lowest energy barrier to dissociation*. Among all the configurations, the H110 and the H001 are the ones that present the minimum energy barriers to dissociation with a value of 0.36 eV. In both cases, they are late barriers that appear at an interatomic distance of 2.0 Å. The existence of a minimum energy barrier that the molecules have to overcome in order to dissociate is in agreement with the lack of direct dissociation events at low incidence energies reported in molecular beam experiments [19, 22]. It is worth to mention that even though the barriers for H110 and H001 are of the same height and located at the same interatomic distance, the shape of these barriers and the neighboring energy landscape differ significantly from each other, as observed in Fig. 3.6. In the H110 configuration, the potential energy decreases for $r > 2.0$ Å and it is already negative at our uttermost interatomic distance $r = 2.53$ Å. In contrast, for the H001 configuration, the potential energy remains almost constant for $r > 2.0$ Å. Previous DFT calculations give similar barrier heights [153–155, 159]. Figure 3.6 shows the existence of paths to dissociation also in the LB1$\bar{1}$0 and SB001 configurations but with higher

---

*We use a simple brute force method that consists in exploring the entire configurational space by making loops over a fine grid mesh of the six variables of the O$_2$/Ag(110) PES. More precisely, for each configuration defined by the set of coordinates $(X, Y, Z, \theta, \varphi)$ we find the maximum energy value when increasing r. In this way, we obtain the dissociation energy value for each configuration. By selecting the minimum of these energy values we obtain the minimum dissociation barrier and the corresponding coordinates define the transition state configuration.

energy barriers of $\sim$ 0.7 eV and $\sim$ 1.2 eV, respectively. It is worth to mention that the minimum barrier to dissociation in Ag(110) (0.36 eV) is much lower than the minimum barriers to dissociation found in the two other low-index silver surfaces (1.05 eV for Ag(100) [167] and 1.1 eV for Ag(111) [168]). This is consistent with the experimentally observed more reactive character of the Ag(110) surface [19, 20, 22, 178–181].

3.4   Properties of the adsorption wells

As discussed above, DFT-PBE predicts four different adsorption wells that are shown in Fig. 3.7. Table 3.1 lists the main properties of the adsorption wells,
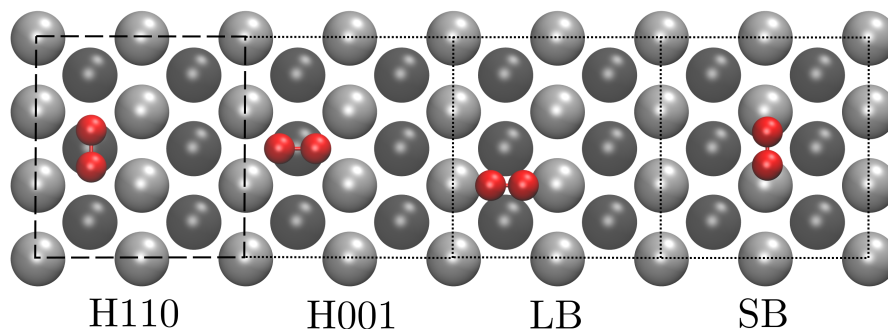
Figure 3.7: *Positions of the O_2 molecule (red atoms) in the four adsorption wells over the Ag(110) surface (first layer atoms are in light grey and second layer atoms are in dark grey). Each molecule is positioned in a 2×3 unit cell as that used in the calculation. From the left, the first unit cell is marked with dashed lines and the following ones with dotted lines.*

namely, the adsorption energy E_a, the distance of the molecular center of mass from the surface Z, the O-O interatomic distance r, the charge Q transferred from the surface to O_2, and the frequency ω of the O-O stretch mode, as given by the frozen surface PES and by VASP with the relaxed surface. The vibrational frequencies are obtained from the method of finite differences with 4 displacements for each degree of freedom (see Ch. 2.3.2) as implemented in VASP and ASE. Bader charge analyses are performed as prescribed in Refs. [182–184]. In the following we discuss the results we obtain for the properties of the wells in relation to available experiments and to previous calculations.

In general, the DFT-PBE values reported here are similar to the DFT values reported before by other authors [153–160]. However, we want to mention the

Table 3.1: *Properties of the adsorption wells: Binding energy (E$_a$), O$_2$-surface distance (Z), interatomic O-O distance (r), Bader excess charge of the molecule (Q), and vibrational frequency (ω). The first numbers are frozen surface values that are obtained using our 6D PES and the numbers in parenthesis are obtained when the surface is allowed to relax. The adsorption energy is given relative to the potential energy at Z = 6 Å.*

Well	E_a (eV)	Z (Å)	r (Å)	Q(e)	ω(meV)
H110	0.21(0.36)	1.09(1.01)	1.45(1.45)	(0.99)	94(92)
H001	0.24(0.36)	1.29(1.22)	1.42(1.42)	(0.95)	98(98)
SB	0.33(0.34)	2.20(2.17)	1.31(1.31)	(0.49)	143(143)
LB	0.24(0.25)	1.98(1.96)	1.29(1.30)	(0.49)	148(143)

importance of obtaining the correct magnetization (the one corresponding to the lowest energy) in the bridge wells, which in our experience is not readily obtained when using default VASP parameters (see Appendix A). This difficulty can lead to different results for the bridge sites, in particular for E_a, which explains the discrepancies with Ref. [160].

It is easy to relate the structural and the vibrational results for the hollow wells in Table 3.1 with several experimental results. The two adsorption wells at the hollow site characterized by the two different molecular orientations in the [001] and [1$\bar{1}$0] directions are consistent with STM measurements [148, 150]. These wells are also compatible with NEXAFS, ARPES, and ESDIAD measurements of the so-called chemisorbed species in which the molecule was found to lie parallel to the surface with both orientations. In these experiments, the [1$\bar{1}$0] orientation was predominantly observed when the molecule was deposited at $T_s > 80$ K, while the [001] orientation appeared when the chemisorbed molecule was transferred from the physisorbed state by heating the surface. The obtained interatomic distance in the H110 well of 1.45 Å agrees very well with the NEXAFS value of 1.47 ± 0.05 Å. The calculated O-O stretch vibrational frequencies are also similar to those measured by EELS and STM-IETS. In fact, very good agreement was obtained in previous works when the frequencies were calculated beyond the harmonic approximation [156, 157].

From the fact that in experiments different orientations of the chemisorbed molecule are obtained depending on the preparation procedure, the TPD peak at 160–190 K was identified with the H110 configuration and the TPD peak at 100–120 K with the H001 configuration [134, 138]. From TPD measurements, ad-

sorption energies can in principle be deduced. In line with this, previous works (see Refs. [154, 155, 159]) claimed that there is a good agreement between the DFT adsorption energy for the H110 well when comparing it with the adsorption energy of 0.4 eV obtained from the TPD data (characterized by a peak at 190 K) of Ref. [17]. However, this experimental value corresponds to a coverage of 0.5 monolayers (ML) and it has been shown that the adsorption energy deduced from TPD experiments reduces to 0.2 eV at a coverage of 0.2 ML [135]. At lower coverages the desorption yield was too small to allow measurements. In fact, it was recently argued that the peak at 190 K originates from desorption of a molecule induced by its collision with an O atom produced in the dissociation of a nearby molecule [138]. We are not aware of any analysis of the TPD peak at 100–120 K attributed to the H001 well. Due to all this, there are no reliable experimental values for the adsorption energy of the hollow wells to compare with. However, we note that the observed difference in the desorption temperatures would suggest a substantial difference in the adsorption energies for the two different orientations, whereas according to the DFT-PBE, the two hollow wells have a very similar adsorption energy.

The connection of the calculated bridge wells with experimental results is by no means straightforward. Due to their distance from the surface one could be tempted to assign them to measured physisorbed states. Moreover, the presence of two different wells in which the molecular axis is parallel to the surface but it is oriented along both the [1$\bar{1}$0] and [001] directions, respectively, also seems to fit well with the EELS, NEXAFS, ARPES and ESDIAD measurements discussed in Sec. 3.1. However, there are two major difficulties in doing so. DFT-PBE vibrational frequencies of the O-O stretch vibrations in the bridge wells are substantially lower, $\omega = 143$ meV, compared to $\omega = 194$ meV that is measured by high resolution EELS. The latter value is very similar to the one of the free O_2 molecule, which suggests a weak interaction with the surface. On the contrary, DFT-PBE predicts a charge transfer of 0.5 electrons from the surface to the molecule. The adsorption energy for the physisorbed state obtained from TPD measurements [135, 137] amounts to $E_a \approx 0.1$ eV, whereas DFT-PBE significantly overestimates these values as can be seen in Table 3.1 and in Appendix A. Moreover, the physisorbed molecules have a large mobility even at $T_s = 13$ K, so that stable STM images could not be obtained [150]. All these facts lead to the conclusion that if the bridge wells are describing physisorbed states, DFT-PBE strongly overbinds them. Consequences of this are discussed in more detail in Ch. 5.

3.5   Summary

In this chapter we have constructed the 6D PES of the O$_2$/Ag(110) system based on first principles electronic structure calculations (using PBE-DFT) . The need for such PES is apparent from the review of the current research status for this system that is given at the beginning of the chapter. In the construction of the PES we have used CRP to interpolate more than 25 000 DFT energy points. In this way, we have obtained a 6D PES that is fast to evaluate and at the same time accurate, as shown by the comparison to the DFT values not included in the interpolation.

Four adsorption wells are identified in the 6D PES which are accessible from vacuum without an energy barrier. These adsorption wells were also identified in previous DFT calculations. We have compared the properties of these wells to the available experimental results. Two adsorption wells are positioned on the hollow site of the surface and seem to be consistent with measured chemisorption states. The other two adsorption wells are positioned on the bridge sites of the surface, and have some similarities with measured physisorption states, although they are bounded to the surface more strongly than expected from the experiments.

We have also identified the energy barriers to dissociation. The lowest barrier to dissociation with a value of 0.36 eV measured from vacuum is positioned on the hollow site of the surface. This value is considerably lower than the one obtained for the Ag(100) and Ag(111) surfaces. This is consistent with the measured much higher reactivity of Ag(110).

4

Dissociative dynamics of O_2 on Ag(110)

The static analysis of the O_2/Ag(110) 6D PES performed in Ch. 3 that is focused on dissociation energy barriers and adsorption wells, although informative, can be misleading in the explanation of the reaction dynamics that is probed, *e.g.*, in molecular beam experiments. This is due to the fact that the actual reaction of the molecule with the frozen surface proceeds through a six-dimensional configurational space. In this chapter we study the dissociative dynamics of O_2 on Ag(110) by performing classical and quasi-classical trajectory calculations. In these calculations the adiabatic force acting on the molecule is calculated with the 6D PES described in the previous chapter and the surface is kept frozen.

Our study complements similar previous dynamics calculations of O_2 dissociation on Ag(100) [167] and Ag(111) [168]. Both of these studies found no dissociation for incidence energies below 1 eV. These results agree with very low dissociation probabilities on Ag(111) [178, 179] and Ag(100) [180] measured in molecular beam experiments for incident kinetic energies below 0.8 eV. The Ag(110) surface, on the other hand, is much more reactive toward O_2 dissociation (at lower incidence energies), as discussed in Ch. 3.1. This fits with a much lower minimum energy barrier to dissociation in our Ag(110) 6D PES compared with the ones observed in the corresponding 6D PESs for Ag(100) [167] and Ag(111) [168]. Consequences of such lower barrier for Ag(110) on dynamics are, thus, explored in this chapter.

In next Sec. 4.1 we list the most important details of the calculations. In Sec. 4.2 we present and discuss results of the trajectory calculations. The main conclusions of the chapter are summarized in Sec. 4.3.

This chapter is based on publication 1.

4.1 Computational details

We perform (quasi-)classical dynamics calculations on the 6D PES solving the Newton equation, Eq. (2.41). For each incidence condition determined by the initial kinetic energy E_i and the incidence polar angle Θ_i, a conventional Monte Carlo procedure is used to sample all possible initial O_2 orientations (θ, φ) and lateral positions (X, Y). Incidence azimuthal angle is also sampled by a Monte Carlo procedure. All trajectories start with the molecule at $Z = 6.0$ Å above the surface, where the potential energy is by definition zero for O_2 at its equilibrium bond length, $r_0 = 1.23$ Å. In the classical calculations, which neglect ZPE, the initial O_2 interatomic distance is precisely r_0. In the quasi-classical calculations, the ZPE or higher rovibrational energies are included in the initial conditions of the O_2 internal degrees of freedom by using the corresponding classical microcanonical distribution of r and its conjugate momentum p_r. In our case, the ZPE and higher rovibrational energies are obtained by solving the radial Schrödinger equation for the potential energy $E(r)$ that is calculated with the molecule halfway between two slabs. Newton equation is integrated using the Beeman algorithm [102] with a time step of 0.01 fs and a total integration time of 15 ps. We distinguish three possible outcomes of each trajectory: (i) reflection, if the molecule is scattered back and reaches the starting point $Z = 6.0$ Å with a positive velocity along the surface normal, (ii) dissociation, if the interatomic distance is larger than 2.5 Å (*i.e.* $r \geq 2r_0$) with positive radial velocity, and (iii) molecular trapping, if after the maximum integration time of 15 ps, the molecule is neither reflected not dissociated. Trapping events are negligible for the incident energies studied here $(E_i \geq 0.1$ eV).

4.2 Dissociation probabilities, reaction paths and vibrational efficiency in promoting dissociation

The initial dissociative sticking coefficient S_0, *i.e.*, the dissociative adsorption probability at zero coverage, as a function of the incidence energy E_i is shown in Fig. 4.1(a). Dissociation probabilities are evaluated for each incidence condition (E_i, Θ_i) from the outcome of 50 000 trajectories. In all cases the $S_0(E_i)$ curves show the characteristic behavior of an activated system, which is typically associated to the existence of energy barriers to dissociation. Let us first concentrate
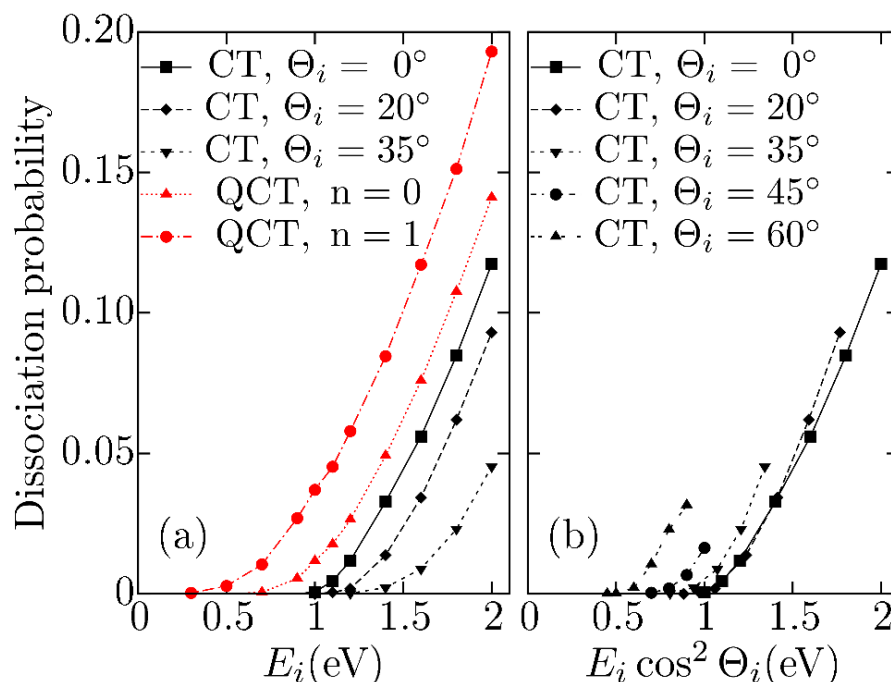
Figure 4.1: *Initial dissociative sticking coefficient S_0 as a function of (a) the initial kinetic energy E_i and (b) the initial normal energy $E_i \cos^2 \Theta_i$. Black curves: classical trajectory (CT) calculations performed for different incidence angles Θ_i. Red curves: quasi-classical trajectory (QCT) calculations performed at normal incidence ($\Theta_i = 0$) for the ground (n=0, ZPE) and the first excited (n=1) vibrational states.*

on the results obtained from the classical calculations at normal incidence. There are no dissociation events or, more precisely, the dissociation probability is lower than 2×10^{-5} for incident energies below 0.9 eV. This energy threshold for dissociation is considerably larger than the barrier for dissociation of 0.36 eV found for the H110 and H001 configurations. Such difference suggests that reaction takes place through a very reduced configurational space. Similar observations have been reported for N_2 dissociation on Fe(110) [185, 186]. Interestingly, the configurational space leading to O_2 dissociation on the Ag(100) [167] and also on the close-packaged Ag(111) [168] appears to be more accessible than on the more reactive Ag(110).

A better understanding of the dynamics leading to dissociation can be obtained by looking at Fig. 4.2. This figure shows the (X,Y) position of the dissociating and reflecting molecules when they first arrive at $Z = 3, 2, 1.5$, and 0.8 Å along the incoming part of the trajectory. We observe that for the incidence conditions of 1.5 eV and 0° all the molecules can arrive at $Z = 3$ Å with no noticeable
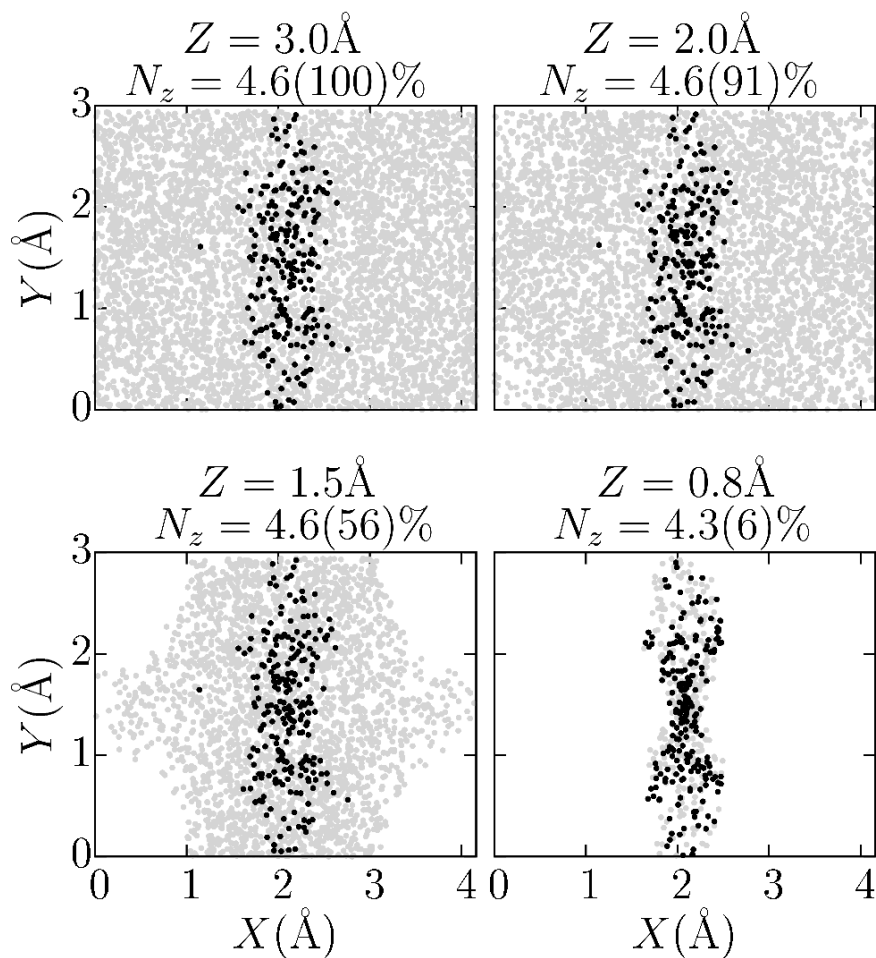
Figure 4.2: *Position of the O_2 center of mass over the surface unit cell when first reaching the height Z written above each panel. The dissociating and reflecting molecules are plotted by black and grey circles, respectively. On top of each panel, N_z denotes the fraction of dissociating molecules reaching Z, while the total percentage of molecules at each Z is written in parenthesis. Results are obtained from 5 000 trajectories for E_i= 1.5 eV and $\Theta_i = 0°$. 4.6% of the molecules are dissociated.*

lateral displacement. The reason is that up to this distance the PES is similarly attractive for all molecular configurations and, therefore, the lateral corrugation is negligible. Interestingly, the dissociating molecules are already located within a 1 Å wide strip that spans through long-bridge and hollow sites. At $Z = 2$ Å, 9% of the molecules are reflected and there are less molecules near top sites. Dissociating molecules remain more or less in the same (X,Y) positions. Depopulation of the top site (now very repulsive) becomes even more apparent when molecules reach $Z = 1.5$ Å. At this distance, almost half of the molecules are already re-

flected. Most of the molecules are already reflected before reaching $Z = 0.8$ Å. In fact more than 2/3 of the molecules that come that close to the surface will dissociate. At this distance, molecules are preferentially concentrated around the hollow site, but some of them still remain close to the long-bridge site.
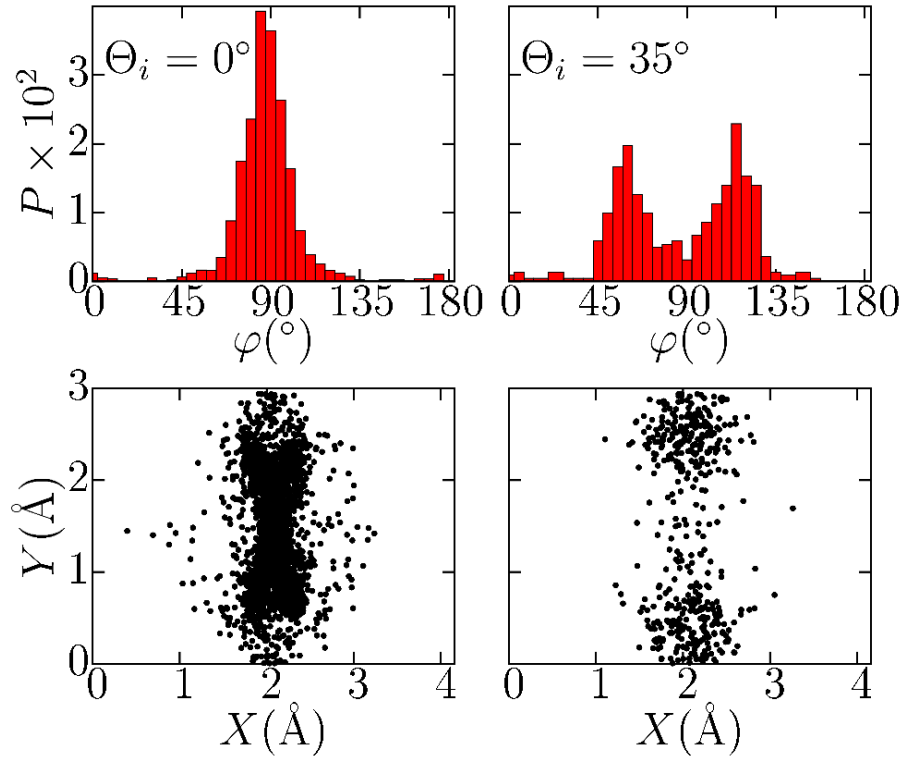
Figure 4.3: *Distribution of the azimuthal angle φ (top panels) and (X, Y)-positions of the O_2 center of mass (bottom panels) at the moment when the interatomic distance is maximal $r = 2.5$ Å. The φ-distributions are multiplied by 100. Results obtained from 50 000 trajectories for $E_i = 1.6$ eV and incidence angles $\Theta_i = 0°$ (left panels) and $\Theta_i = 35°$ (right panels).*

Next we analyze in more detail the position and orientation of the molecules at the instant of dissociation, *i.e.*, when its internuclear distance reaches 2.5 Å. Left panels of Fig. 4.3 show their corresponding φ-distribution and (X,Y) position for the incidence conditions, $E_i = 1.6$ eV and $\Theta_i = 0°$. The dissociated molecules are basically parallel to the surface with $\theta \approx 90° \pm 15°$ (not shown). It is apparent that molecules dissociate with their axis oriented close to the $[1\bar{1}0]$ direction ($\varphi \approx 90°$). Additionally, a larger number of molecules dissociate close to the hollow site than close to the long-bridge site. This behavior can be well understood with the help of Figs. 4.4 (a) and (b). These figures show the distribution on (X, Y)
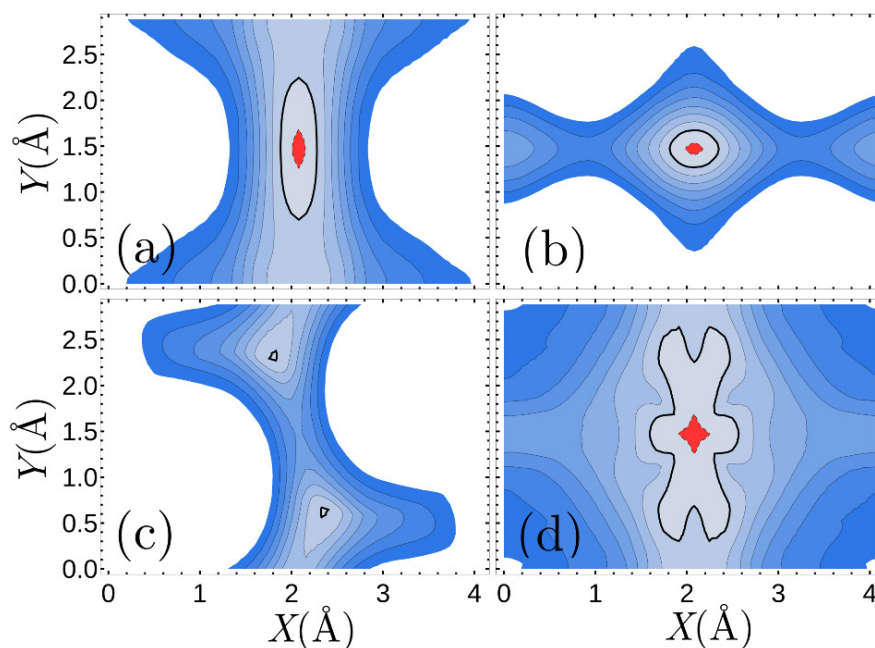
Figure 4.4: *Dependence of the minimum energy barriers to dissociation on the X, Y position of the center of mass of the molecule. In panels (a), (b) and (c) the minimum barrier is calculated in the two dimensional (r, Z) configurational space for the following molecular orientations: (a) $\theta = 90°$ and $\varphi = 90°$, (b) $\theta = 90°$ and $\varphi = 0°$, (c) $\theta = 90°$ and $\varphi = 60°$. In panel (d) the minimum barrier to dissociation is calculated in the four dimensional (r, Z, θ, φ) configurational space. Every contour line separates intervals of 0.2 eV. In the red area barriers are lower than 0.4 eV. The thick contour line corresponds to a value of 0.6 eV.*

of the minimum energy barriers to dissociation obtained in the (r, Z) configurational space when the molecule is oriented parallel to the surface ($\theta = 90°$) along the [1$\bar{1}$0] direction ($\varphi = 90°$) in Fig. 4.4(a) and along the [001] direction ($\varphi = 0°$) in Fig. 4.4(b)[*]. It is observed that the region with rather low barriers is much broader in the [1$\bar{1}$0] direction. This explains why molecules under normal incidence preferentially dissociate in this direction and not in the [001] direction although the minimum energy barrier heights are similar. Additionally, focusing on the [1$\bar{1}$0] direction, the fact that barriers are lower close to the hollow site explains why more molecules dissociate near the hollow site than close to the long-bridge site, where the energy barriers are around 0.3-0.4 eV larger. Figure 4.4(d) shows the

---

[*]To obtain these values a brute force method is used that consists in exploring the entire configurational space by making loops over a fine grid mesh of the desired variables in the O_2/Ag(110) PES.

distribution on (X, Y) of the minimum barriers to dissociation obtained in the (r, Z, θ, φ) configurational space. Interestingly, this distribution of barriers follows more closely than Fig. 4.4(a) the distribution of actual dissociation positions shown in the bottom-left panel of Fig. 4.3. This observation can be linked with the fact that dissociation also occurs for orientations different from $\varphi = 90°$ as shown in the φ-distribution of Fig. 4.3, though with lower probability.

Quasi-classical calculations performed at normal incidence are also shown in Fig. 4.1(a). Comparison with the classical results reveals that the dissociation probability $S_0(E_i)$ increases when the ZPE is included. In particular, the classical energy threshold for dissociation is reduced by more than 0.3 eV, even if the ZPE is 90 meV only. To explore in more detail the efficiency of the vibrational energy, we have also calculated $S_0(E_i)$ when the molecule is initially excited in the first vibrational state ($n = 1$). Compared with the quasi-classical results for the ground vibrational state ($n = 0$), we first observe that there is a further reduction in the energy threshold to dissociation of around 0.3 eV despite the added vibrational quanta amounts to 0.18 eV. Noticeably, the vibrational energy is more efficient than the translational energy in promoting dissociation for the E_i-range studied here. In other words, the same 0.18 eV added into E_i produces less dissociation: $S_0(E_i, n = 1) > S_0(E_i + 0.18, n = 0)$. Still, the dissociation path is the same as in the classical calculations, i.e the initial (X, Y)-positions of the dissociating O_2 are located in a narrow strip that spans through long-bridge and hollow sites. The obtained increase in the dissociation probability can, thus, be attributed to the better conversion of the incidence energy to radial momenta when the molecule already starts with a non-zero vibrational energy. As originally argued by Polanyi and Wong [187] for the simpler gas-phase reactions case, the reason of large vibrational efficiency in late barrier systems can be naively understood in terms of the typical elbow plots associated with a dissociation configuration (for instance, see the 2D cut of H1$\bar{1}$0 in Fig. 3.6). The vibrational motion starts being perpendicular to the reaction coordinate while the molecule approaches the surface, but it ends up running parallel to the reaction coordinate when the molecule reaches the surface. Thus, in a late barrier system, the vibrationally excited molecule arrives at the barrier with part of its energy already conveniently localized in the degree of freedom where the barrier appears, what facilitates the system to overcome it. Similar findings regarding the efficiency of the vibrational energy in dissociation has been reported for other late barrier systems [188–191].

In the following we analyze with classical calculations the dependence of

$S_0(E_i)$ on the polar incidence angle. Comparing the classical results shown in Fig. 4.1(a) for $\Theta_i = 0°$, $20°$, and $35°$, it is clear that $S_0(E_i)$ decreases as Θ_i increases. This decrease, however, does not follow a normal energy scaling, because we observe in Fig. 4.1(b) that for equal normal incidence energy ($E_i \cos^2 \Theta_i$), S_0 increases with Θ_i, *i.e.*, with the total energy E_i. A similar behavior was observed for N_2 dissociation on Fe(110) and explained in terms of the low energy barriers existing in the entrance channel [185]. However, since there are no entrance barriers to access the dissociating configurations in the O_2/Ag(110) PES, other factors should be causing the Θ_i-dependence in the present case as we discuss next.

When analyzing the dissociation dynamics under normal incidence in Fig. 4.2, we showed that in that case 6% of the molecules with initial energy of 1.5 eV arrive at $Z = 0.8$ Å before being reflected or dissociated. Additionally, 4.3% of the total number of molecules arrive at that distance and later dissociate. From a similar analysis for $\Theta_i = 35°$ and the same initial energy, we get that 3.5% of molecules arrive at $Z = 0.8$ Å, but that only 0.3% are dissociating molecules. This shows that the main difference between normal and off-normal incidence it is not the different number of molecules that arrive close to the surface, but the number of molecules that arriving close to the surface dissociate, 72% for $0°$ and only 9% for $35°$. The comparison between the configurational space at the instant of dissociation shown in Fig. 4.3 serves to highlight important differences between the dissociation conditions at normal and off-normal ($\Theta_i = 35°$) incidence. We observe that dissociation at the hollow site is strongly reduced for $\Theta_i = 35°$. In addition, the φ-distribution changes drastically from the preferential $\varphi = 90°$ obtained at normal incidence to an axis orientation close to $\varphi \approx 60°$ (or symmetrically $\varphi \approx 120°$). To understand this finding, we show in Fig. 4.4(c) the distribution in (X, Y) of the minimum energy barriers to dissociation in the (r, Z) configurational space for the molecule oriented parallel to the surface along the $\varphi = 60°$ direction. The figure shows that for this molecular orientation the minimum energy barriers for dissociation, with values around 0.6-0.8 eV, are located in the X, Y positions where molecules, under $\Theta_i = 35°$ incidence angle, dissociate (see Fig. 4.3). The values of these energy barriers are clearly higher than 0.36 eV, which is the value found at the hollow site for the minimum energy barrier. Indeed, the fact that for off-normal incidence dissociation takes place through reaction paths with higher energy barriers explains the lower dissociation probabilities. However, it remains to be understood why dissociation occurs preferentially at these positions and with this orientation for off-normal incidence.

In order to understand this fact, we plot in Fig. 4.5 the (X, Y) contour plot of the potential energy calculated as an average on Z within the range $Z = 2 - 4\,\text{Å}$ for different φ-orientations. In all cases, the molecule lies parallel to the surface
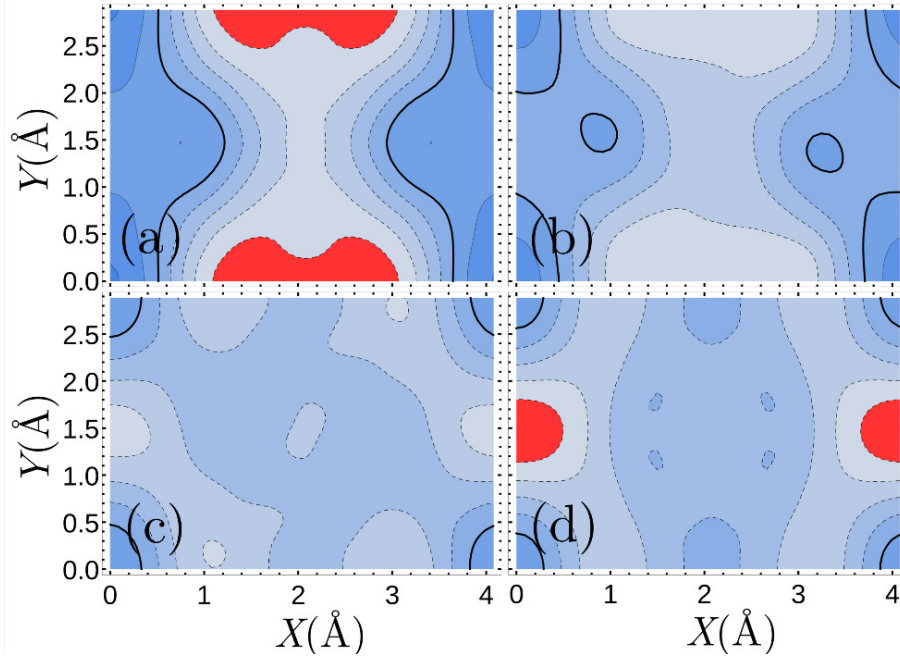
Figure 4.5: *Average on Z of the potential energies of the molecule as a function of the X, Y position of its center of mass for the equilibrium interatomic distance $r_0 = 1.23$ Å. The Z-range considered goes from $Z = 2$ Å up to $Z = 4$ Å. The molecule is oriented parallel to the surface ($\theta = 90°$) with: (a) $\varphi = 0°$, (b) $\varphi = 30°$, (c) $\varphi = 60°$, (d) $\varphi = 90°$. Every contour line separates intervals of 0.025 eV. In the red area the average potential energy is lower than -0.1 eV. The thick contour line corresponds to an average potential energy of 0 eV.*

($\theta = 90°$) with the gas-phase bond length $r_0 = 1.23$ Å. Off-normal incidence molecules, as they have initial parallel momenta, explore a large region of the X, Y configurational space at intermediate distances from the surface ($Z = 2 - 4$ Å). At these intermediate distances the O_2 interatomic distance is close to r_0. Therefore, the average potential energy provides a meaningful measure of the attractive or repulsive character of the PES along the incoming part of the trajectory. More precisely, Figs. 4.5(a) and (b) show that molecules with small azimuthal angle φ are attracted to broad areas around the long-bridge site. In fact, we have verified that this behavior is fulfilled for angles $\varphi = 0° \pm 45°$. For larger φ, the incident O_2 starts to be attracted to the short-bridge site as shown in Figs. 4.5(c) and (d).

Notice that the hollow site is not particularly attractive or repulsive at any φ. However, for the bridge sites there exist orientations ($\varphi = 0° \pm 45°$ for the long-bridge and $\varphi = 90° \pm 30°$ for the short-bridge) where the attractive parts of the PES are relatively broad in the (X, Y)-plane. Figures 4.4 and 4.5 together show that the most attractive regions for a given φ orientation present relatively high barriers for dissociation. The region near the long-bridge site with $\varphi \approx 60°$ (or symmetrically $\varphi \approx 120°$) represents a compromise between the attractiveness of the PES and the presence of not too high barriers to dissociation. This is the reason why this region is favored for dissociation under off-normal incidence. The figures also explain the lack of dissociation close to the short-bridge site. For the configurations for which the short-bridge region is attractive [Fig. 4.5(d)] the barriers to dissociation are very high [Fig. 4.4(a)].

It is worth to discuss our results in relation to the experimental findings. To this aim, we compare in Fig. 4.6 the experimental data of Ref. [22] with our classical results of the dissociative $S_0(E_i)$ obtained for normal incidence conditions. For completeness, we also show and compare the dissociative sticking coefficient obtained by similar adiabatic dynamics calculations on Ag(100) [167] and Ag(111) [168] to the experimental results of Ref. [180] and Ref. [192], respectively. We start noting that our results for dissociative adsorption show that the reactivity of O$_2$ on Ag(110) is much higher than the one obtained in the calculations for Ag(100) and Ag(111). This is apparent from the lower energy barrier obtained for dissociation, as explained above, but also from the actual values of the dissociation probabilities. For instance, at an initial energy of $E_i = 2.0$ eV and normal incidence we obtain a dissociation probability of $S_0 = 0.12$ in this surface, whereas in Ag(111) and Ag(100) the calculated dissociation probabilities for the same incidence conditions are $S_0 \approx 0.05$. These facts are consistent, at least qualitatively, with molecular beam experiments performed at a surface temperature of 300 K showing that the Ag(110) is the most reactive of the low-index (flat) Ag surfaces for O$_2$ dissociation [19, 22, 178, 180]. Nevertheless, we note that the dissociation measured in those experiments actually occurs for incidence energies below the barrier for dissociation analyzed here. In particular, the experimental initial sticking coefficient shows an activation energy of around 0.2 eV and takes values as high as $S_0 = 0.45$ for $E_i = 0.7$ eV and normal incidence. This discrepancy cannot be resolved by invoking non-adiabatic effects as was done to explain the dissociative adsorption of O$_2$ on aluminium surfaces [193, 194]. These effects generate energy barriers to dissociation in the entrance channel that would in general
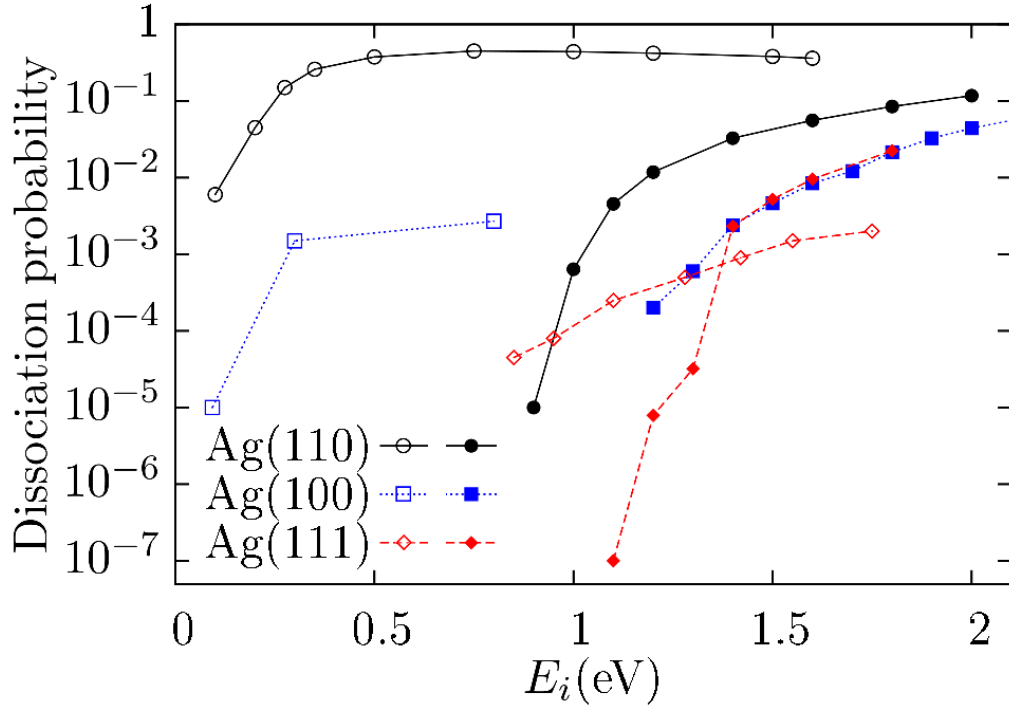
Figure 4.6: *Initial dissociative sticking coefficient S_0 as a function of the initial kinetic energy E_i at normal incidence ($\Theta_i = 0$). Comparison of experimental molecular beam results performed at surface temperatures $T_s \geq 300$ K (open symbols) and classical trajectory calculations (full symbols) for flat Ag surfaces. Black lines represent Ag(110) ([22], this work), blue lines represent Ag(100) ([180],[167]) and red lines represent Ag(111) ([192], [168]).*

further reduce the calculated sticking probability as compared to our adiabatic results, worsening, instead of improving, the comparison with the experimental data.

All this leads us to suggest that the quantitative disagreement between the theoretical and the experimental S_0 curves is probably related to the existence of two different dissociation mechanisms. As discussed in Refs. [19, 20, 22], the dependence of the experimental S_0 on the surface temperature indicates that the dissociation measured at these low E_i cannot be attributed to the direct mechanism found here, but to dissociation events preceded by molecular chemisorption. Hence, the analysis of adsorption at this energy regime would require to go beyond the frozen surface approximation to incorporate energy exchange channels between the molecule and the surface. This is the subject of the next chapter.

4.3 Summary

In summary, in this chapter we have studied the dynamics of the interaction between the O_2 molecule and the Ag(110) surface with especial emphasis on the dissociation process. We have performed classical and quasi-classical molecular dynamics simulations on top of the DFT-PES for different incidence kinetic energies and polar angles of the molecular beam, calculated the corresponding initial sticking coefficient and obtained information on the dissociation paths. Our classical dynamical calculations show that under normal incidence conditions, no dissociation event is obtained out of 50 000 trajectories for initial translational energies below 0.9 eV. This value contrasts with the calculated minimum energy barrier to dissociation of 0.36 eV that is found for O_2 over the hollow site and oriented parallel to the surface along the $[1\bar{1}0]$ direction ($\varphi = 90°$). Such an energy mismatch is an indication of the very reduced configurational space leading to dissociation in this system. In fact, we observe that the dissociating molecules remain located along a narrow strip linking hollow and long-bridge sites even for an incidence energy as high as 1.6 eV. Furthermore, most of them still dissociate through configurations close to the minimum-energy-barrier configuration. Interestingly, for off-normal incidence ($\Theta_i = 35°$) the configuration that dominates dissociation is closer to the long-bridge site with the orientation ($\theta \approx 90°, \varphi \approx 60°$). The fact that close to the long-bridge site the barrier to dissociation is larger (0.7 eV) than in the hollow site implies a much lower dissociation probability and a higher threshold energy for dissociation at off-normal incidence.

The quasi-classical calculations performed for normal incidence reveal the high efficiency of the vibrational energy in promoting dissociation. By including the zero-point-energy of only 90 meV, the classical activation energy of 0.9 eV is reduced to about 0.6 eV. Moreover a further reduction of ca. 0.3 eV is obtained for O_2 initially excited in the first vibrational state. The efficiency of the vibrational against the translational energy is confirmed when comparing the quasi-classical dissociation probabilities obtained for the ground and the first vibrational states.

Finally, we want to emphasize that our results for O_2 dissociation on Ag(110) are consistent with the absence of direct dissociation at low incidence energies reported by different molecular beam experiments [19, 20, 22]. For higher incidence energies, the authors suggest that direct dissociation is actually masked by the more efficient indirect dissociation process that proceeds through the chemisorp-

tion state. The analysis of molecular adsorption and of the associated indirect channels to dissociation requires the incorporation of energy interchange between the molecule and the surface which is studied in next chapter.

5

Molecular adsorption dynamics of O$_2$ on Ag(110)

Previous chapter discusses the dynamics of the direct dissociative adsorption process. No direct dissociation was found to occur below an incidence energy of 0.9 eV (0.6 eV including the vibrational zero point energy), even if the minimum energy barrier to dissociation amounts to 0.36 eV. As molecular beam experiments were not performed with such high incidence energies at surface temperatures below the one for which indirect dissociation occurs ($T_s < 150$ K), we were not able to perform a direct comparison between our results and the experimental data.

In this chapter we study the process of molecular adsorption and indirect dissociation which are still not understood theoretically. These processes can only be studied if there is an exchange of energy between the molecule and the surface. With this in mind, we include surface movement in the dynamics at two different levels of approximation. In the first case, we perform molecular dynamics using our 6D PES, allowing for energy exchange with the surface within the generalized Langevin oscillator (GLO) model [103–106]. We denote this model as PES+GLO. Additionally, we perform ab-initio molecular dynamics simulations (AIMD) allowing for surface atom movement. The rest of the chapter is organized as follows: in Sec. 5.1 the theoretical methods are described, PES+GLO dynamics is presented and discussed in Sec. 5.2, effects of surface relaxation are explored in Sec. 5.3 from a pure static analysis, while the subsequent full dimensional AIMD dynamics is presented and discussed in Sec. 5.4. Conclusions are drawn in Sec. 5.5.

This chapter is based on publication 4.

5.1 Computational details

On the basis of the 6D PES we perform classical trajectory calculations (that neglect zero point energy) in which the energy exchange between the molecule and the surface is simulated using the GLO model (see Ch. 2.4.2). Despite its simplicity, the GLO model can provide a reasonable description of surface temperature effects and of the energy exchange with the lattice [118, 169, 185, 186, 195]. The GLO equations for the Ag(110) surface are solved using $\omega_x = \omega_y = 3.7 \times 10^{-4}$ a.u. (atomic units) and $\omega_z = 2.9 \times 10^{-4}$ a.u. for the surface oscillator frequencies [196, 197], and $\eta_{ph} = 74.4$ a.u. for the friction coefficient of the ghost oscillators. All trajectories start with the center of mass (CM) of the molecule at $Z = 6$ Å from the surface with the equilibrium bond length, a configuration for which the potential energy is zero by definition, and with the CM momentum pointing normal towards the surface. The value of the momentum corresponds to a given initial incidence energy E_i. The initial lateral positions and orientations of the molecule are sampled by a Monte Carlo procedure. In accordance with the previous chapter, we distinguish the following possible outcomes for each trajectory calculation: (i) reflection, if the molecular CM reaches $Z = 6$ Å with a positive velocity along the surface normal, (ii) dissociation, if the interatomic O-O distance is larger than $r = 2.5$ Å, (iii) adsorption, if after the integration time of 15 ps the total energy (kinetic + potential) of the molecule is less than zero, and (iv) trapping, if none of the previous criteria is met. In this study, the occurrence of trapping events is negligible. As in the previous chapter, Newton equations are integrated using the Beeman algorithm [102] with the same time step of 0.01 fs and a total integration time of 15 ps.

Energy barriers between adsorption wells are calculated using the climbing-image nudged elastic band (CI-NEB) method as implemented in the *Transition State Tools for VASP* code [95, 96, 198, 199]. As discussed in Ch. 2.3.2, this method is able to accurately capture the maximum value of the barrier. We use the same method to search for barriers in the 6D PES with the help of the *Atomic Simulation Environment* (ASE) [177].

We also perform *ab initio molecular dynamics* (AIMD) calculations for a few incidence energies. In these calculations DFT is used to obtain Hellmann-Feynman forces at every step of the trajectory using the same initial conditions as in the PES+GLO trajectory calculations. In these AIMD simulations the four uppermost silver layers are allowed to move and no thermostat is applied to the surface (con-

stant energy calculation).

5.2 Dynamics on the precalculated potential energy surface

With the aim of understanding the molecular beam experiments described in Ch. 3.1 we perform GLO trajectory calculations on top of the 6D PES. All results presented below are obtained from 20 000 trajectories for each initial condition.

The upper panel in Fig. 5.1 shows the dissociation probability as a function of the incidence energy E_i for normal incidence conditions. Similarly to the results of previous chapter, in which the frozen surface was used, there are no dissociation events for incidence energies smaller than 0.9 eV. The dissociation probabilities are very much alike, regardless of the surface temperature. More importantly, we have checked that the obtained dissociation is still due to the direct process in which the molecule dissociates immediately upon the collision with the surface. In comparison to the case of the frozen surface, dissociation probabilities obtained within the GLO model are reduced. More precisely, at $E_i = 2$ eV the dissociation probability of 0.12 in the frozen surface calculation is reduced to 0.05 in the GLO model calculation. This decrease can be attributed to the loss of the molecule incidence energy to the surface movement that prevents the molecule from overcoming the energy barriers to dissociation.

The model that was proposed on the basis of molecular beam experiments [19] suggested that the measured dissociation probabilities at high T_s were the result of an indirect process in which the molecule first adsorbs on the surface and afterwards thermally dissociates if T_s is high enough. There are at least two reasons why our dynamics calculations cannot capture such a process: First, in our PES the minimum dissociation barrier is 0.36 eV above the vacuum level (defined as the energy at $Z = 6$ Å). For this reason, dissociation is a very unlikely process in the case in which the molecule has lost its initial kinetic energy and it has thermalized with the surface. Second, thermal dissociation could proceed on timescales much longer than our integration time. Therefore, it is reasonable to look at the nondissociative adsorption probability and identify it with the total dissociation probability at large T_s. In fact, this is the procedure employed in the interpretation of molecular beam experiments [19, 22].

The lower panel in Fig. 5.1 shows the nondissociative adsorption probability
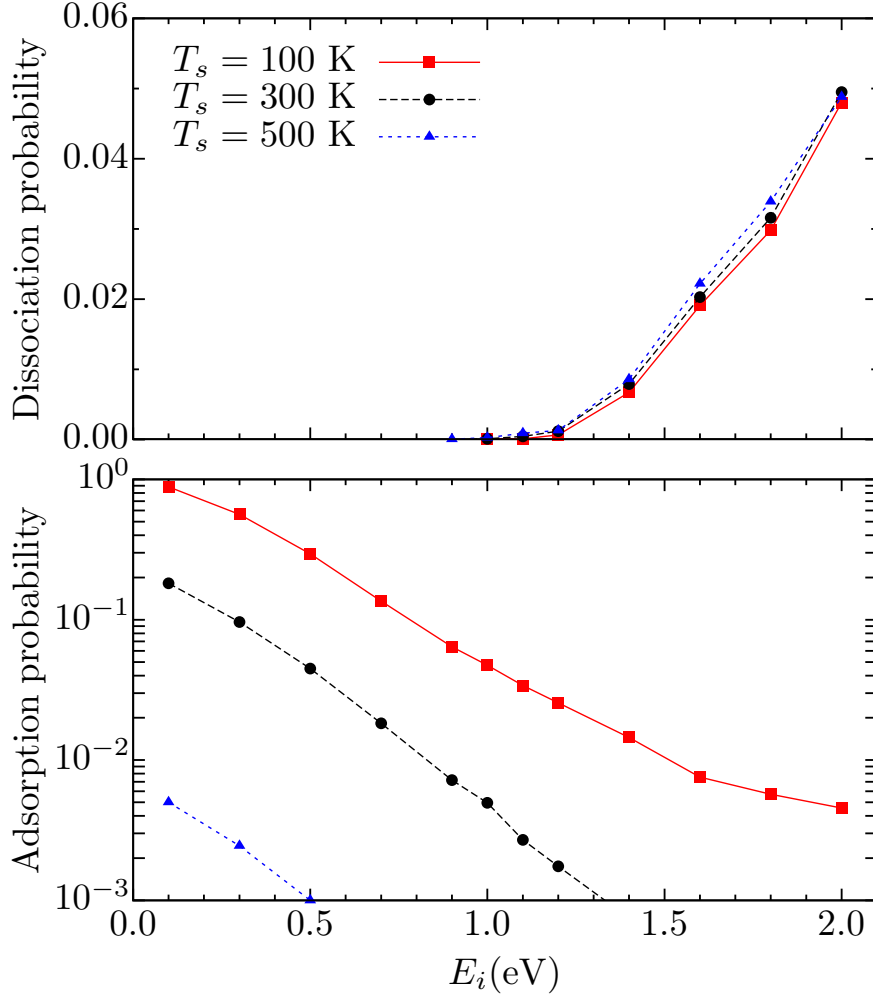
Figure 5.1: *Upper panel: Dissociation probability of O$_2$ on Ag(110) as a function of the initial incidence energy E_i for three different surface temperatures T_s under normal incidence conditions. Lower panel: Nondissociative adsorption probability (ordinate in logarithmic scale) as a function of the initial kinetic energy E_i for three different surface temperatures T_s under normal incidence conditions.*

as a function of the incidence energy E_i at surface temperatures of $T_s = 100$ K, 300 K, and 500 K and normal incidence conditions. To a good approximation, the adsorption probability decreases exponentially with E_i. At $T_s = 100$ K and low $E_i < 0.1$ eV almost all the molecules are adsorbed (around 90% for $E_i = 0.1$ eV), whereas the adsorption probability is already 10 times smaller at $E_i = 0.8$ eV. The adsorption probability also rapidly decreases with T_s, such that for $E_i = 0.3$ eV it is 0.56 at $T_s = 100$ K, 0.09 at $T_s = 300$ K, and 0.002 at $T_s = 500$ K. These results are clear signals of the adsorption process in a non-activated system. In fact, in the

DFT-PBE PES there are no energy barriers from vacuum to the adsorption wells, and the results, in this respect, are consistent.

We proceed by looking at the adsorption process in more detail. Figure 5.2 shows the positions and orientations of the adsorbed molecules for $T_s = 100$ K and 300 K (after an integration time of 15 ps). At $T_s = 100$ K the long bridge site
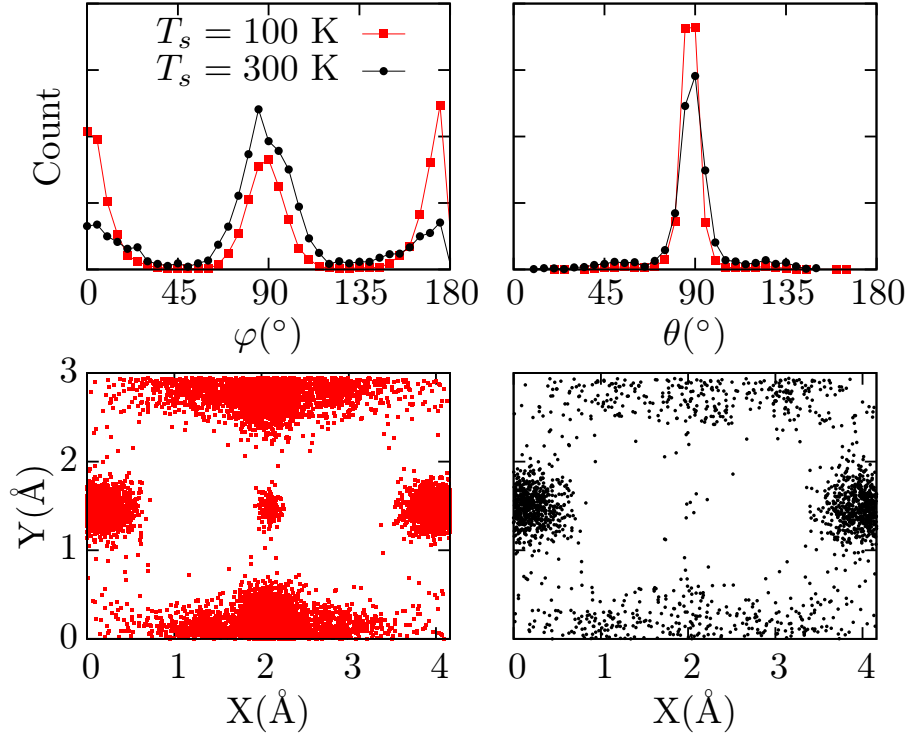
Figure 5.2: *Upper panels: Normalized angular distributions of the orientation of the adsorbed molecules for surface temperatures $T_s = 100$ K and 300 K. Left panel shows the φ distribution and right panel shows the θ distribution. Lower panels: Position of the center of mass of the adsorbed molecules over the surface unit cell for $T_s = 100$ K (left panel) and $T_s = 300$ K (right panel). The X and Y axis correspond to the [001] and [1$\bar{1}$0] directions, respectively. Initial translational energy of the molecules is $E_i = 0.3$ eV.*

is the most populated one with 61% of the adsorbed molecules, followed by the short bridge site (37%) and the hollow site (1%). Most of the molecules have the molecular axis parallel to the surface ($\theta = 90°$) and, as expected for adsorption in the LB well, they are oriented along the [001] direction ($\varphi = 0°$). The rest of the molecules are oriented along the [1$\bar{1}$0] direction ($\varphi = 90°$), which is consistent with adsorption in the SB well. At $T_s = 300$ K the number of molecules in the LB well (also in H001 and H110) decreases substantially (to 31% of the adsorbed

molecules) in comparison to the molecules adsorbed in the SB well (which in this case amounts to 61% of the adsorbed molecules). These results cannot be fully understood in terms of the adsorption energies of the wells (see Table 3.1). Based on purely energetics arguments a direct correlation between the depth of the wells and its population would be expected. However, the deepest SB well is the most populated adsorption site only at $T_s = 300$ K. Moreover, the population in any of the hollow wells is smaller than that in the LB well, despite their similar E_a.

These results can be understood with the help of Fig. 5.3 in which we show the minimum energy of the PES as a function of the (X, Y) coordinates of the CM of the molecule. Figures 5.3(a)-(c) show the minimum potential energy for a fixed
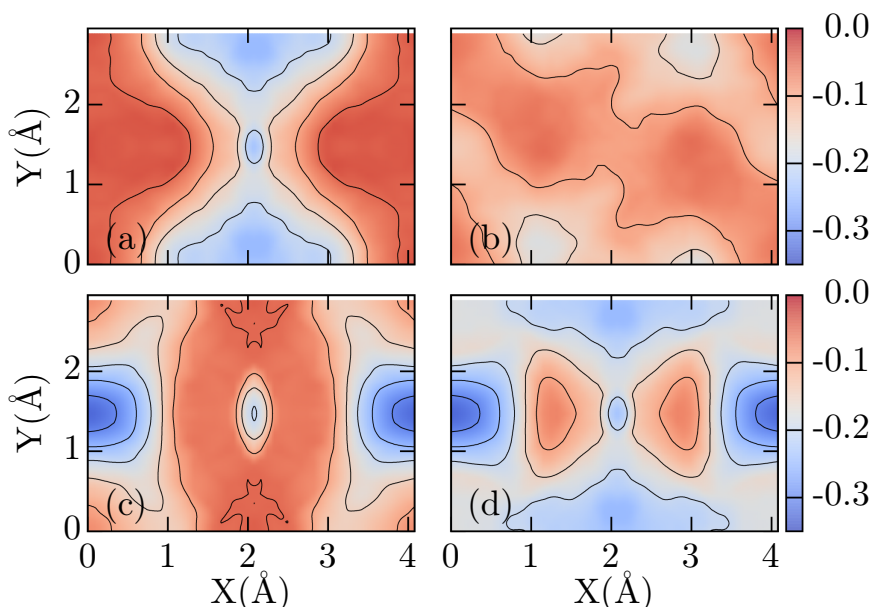
Figure 5.3: *Dependence of the minimum potential energy on the (X, Y) position of the CM of the molecule. In panels (a), (b) and (c) the minimum potential energy is calculated in the two dimensional (r, Z) configurational space for the following molecular orientations: (a) $\theta = 90°$ and $\varphi = 0°$, (b) $\theta = 90°$ and $\varphi = 45°$, (c) $\theta = 90°$ and $\varphi = 90°$. In panel (d) the minimum potential energy is calculated in the four dimensional (r, Z, θ, φ) configurational space. A color map is used to show the value of the minimum potential energies. The contour lines are separated by 50 meV. One unit cell is shown.*

orientation φ of the molecule parallel to the surface. Clearly, for molecules oriented along the [001] direction ($\varphi = 0°$) there is a small area of low potential energies associated with the hollow site and a large area of low potential energies

close to the long bridge site. Similarly, for molecules oriented along the [1$\bar{1}$0] direction ($\varphi = 90°$) there is a small area of low potential energies associated with the hollow site and a larger area of low potential energies related to the short bridge site. It is apparent that for the molecules adsorbed around the bridge sites there is a larger configurational space of low potential energies than for the molecules adsorbed around the hollow site. This explains why in our dynamics a large majority of the molecules adsorb in the LB and SB wells. In fact the (X, Y) distribution of minimum potential energies evaluated in the (r, Z, θ, φ) configurational space shown in Fig. 5.3(d) is very similar to the actual (X, Y) distributions of adsorbed molecules shown in the lower left panel of Fig. 5.2. The reason why at the low $T_s = 100$ K, more molecules are adsorbed on the LB site is clearly due to a larger configurational space of low potential energies around this site as shown in Fig. 5.3(d). However, at the larger $T_s = 300$ K adsorption in the LB well is reduced in favour of the SB well for which the adsorption energy is the highest.

We have checked that if the integration time is increased from 15 ps to 50 ps the adsorption probabilities do not significantly change. The only noticeable difference is that the molecules, having more time to exchange energy with the surface, are better localized at the bottom of the adsorption wells. Additional quasi-classical calculations that include in the O_2 initial incidence conditions the vibrational zero point energy and the rotational state J, with J ranging from 0 to 14, also show that the adsorption probabilities remain practically unaltered.

Evidently, it is not straightforward to relate our dynamics results with the observations of the molecular beam experiments. Our results for the adsorption probability as a function of the incidence energy show characteristics of a non-activated system that contrast with the available molecular beam experiments that suggest that the adsorption process is activated, as discussed in Ch. 3.1 (see also Fig. 4.6). More precisely, in our dynamics at $T_s = 100$ K and $E_i = 0.1$ eV the adsorption probability is ≈ 0.9 which should be compared with ≈ 0.02 in molecular beam experiments at similar conditions [19]. Let us mention that a similar discrepancy between experimental observations and theoretical calculations is also observed in the case of O_2 adsorption on Ag(001) [167, 180, 200]. One explanation of this disagreement could be that DFT-PBE fails to predict entrance barriers to the adsorption wells that exist in reality. Basis for such argument can be found in the previously studied dissociative adsorption of O_2 on Al(111), in which the lack of entrance energy barriers in DFT calculations was found to be the reason for disagreement between theoretical and experimental results [194, 201–

205]. The failure of DFT to predict the barrier was attributed to non-adiabatic spin effects [194, 203] or a flaw in the exchange-correlation functional [204, 205]. In Secs. 5.3 and 5.4 we discuss another possible explanation for the O_2/Ag(110) system.

Our dynamics also predict that most of the molecules adsorb in the bridge wells, from which there is a large dissociation barrier (> 2 eV) due to the repulsion by the Ag atoms (see Fig. 3.6). In none of the cases, the adsorption probability in the hollow wells (from which there is a lower dissociation barrier of 0.36 eV) is larger than 2%. In molecular beam experiments at $T_s = 300$ K the dissociation probability at $E_i = 0.7$ eV is almost 50%. Consequently, to achieve such large probabilities while still relying on DFT-PBE, a large portion of the molecules should migrate from the bridge wells to the hollow wells. For such migration to occur, relaxation of the surface may be important since in this case, the hollow wells become considerably deeper (see Table 3.1). This is precisely the subject of Sec. 5.3.

It is worth to mention that in thermal deposition experiments at $T_s = 25$ K the adsorption probability (in a physisorbed state) is close to 100% [16, 145]. In this respect, our dynamics results at low E_i could be representing this process. The incorrect large adsorption probabilities we obtain for low E_i even at $T_s = 300$ K could simply be due to the DFT-PBE overbinding of the bridge wells that was discussed in the previous Sec. 3.4. Unfortunately, to our knowledge, molecular beam experiments at $T_s < 80$ K have not been performed. Interestingly, our dynamics results agree with experimental observations which show that the [001] orientation of the molecular axis is preferred at low T_s, and that the [1$\bar{1}$0] orientation is preferred at higher T_s [16, 18, 134, 137, 143–146].

5.3 Transition barriers between the wells and surface relaxation effects

As noticed above, the GLO model has shown to be a valuable and computationally efficient approach to study surface temperature effects and gas-surface processes that are ruled by the energy exchange with the lattice. However, the GLO misses effects associated to the individual surface atoms displacements that might eventually alter the gas-surface dynamics. In the case of O_2 on Ag(110), Table 3.1 shows that surface relaxation results in an increase of the adsorption

energy in the hollow wells larger than 0.1 eV (see also Appendix A). We also note that when relaxed, the nearest Ag atoms around O_2 are displaced more than 0.1 Å from their equilibrium position in the clean surface. On the contrary, relaxation effects are negligible for adsorption in the bridge wells that are further away from the surface, as also shown in Table 3.1. These facts make it reasonable to assume that the adsorption dynamics is not going to be much influenced by relaxation effects in its initial stages. As already shown in Sec. 5.2 the configurational space available around the bridge wells is larger than the one around the hollow wells. Consequently, we expect that the bridge wells will still play a major role in the adsorption process by attracting a large portion of the molecules even in the case of allowing surface relaxation. Eventually the molecules may later move from the bridge wells to the hollow wells due to relaxation, inasmuch as the energy barriers connecting the wells allow the transition. This is what we explore next.

Table 5.1 shows the energy barriers for transitions between adsorption wells calculated with and without surface relaxation. Additionally, in Fig. 5.4 we show the energetics along the reaction path for each transition. First, we note that in all

Table 5.1: *Energy barriers between the adsorption wells of O_2 on Ag(110) obtained by the CI-NEB method allowing the surface atoms to relax ($B_{relax}(eV)$) and obtained with the frozen surface 6D PES ($B_{PES}(eV)$). The values are referred to the bottom of the initial well.*

Initial well	Final well	$B_{relax}(eV)$	$B_{PES}(eV)$
SB	H110	0.13	0.27
SB	H001	0.19	0.27
SB	LB	0.18	0.16
LB	H110	0.10	0.21
LB	H001	0.04	0.12
H110	H001	0.24	0.14

cases, these energy barriers are smaller in magnitude than the adsorption energies, which is also reflected in the negative values of the potential energies shown in Fig. 5.4. This means that for hot molecules, transition between adsorption wells will be more likely than desorption. Comparing the relaxed surface results with those obtained with the 6D PES, we observe that, as expected, relaxation hardly influences the transition energy barrier between the bridge wells. The energy
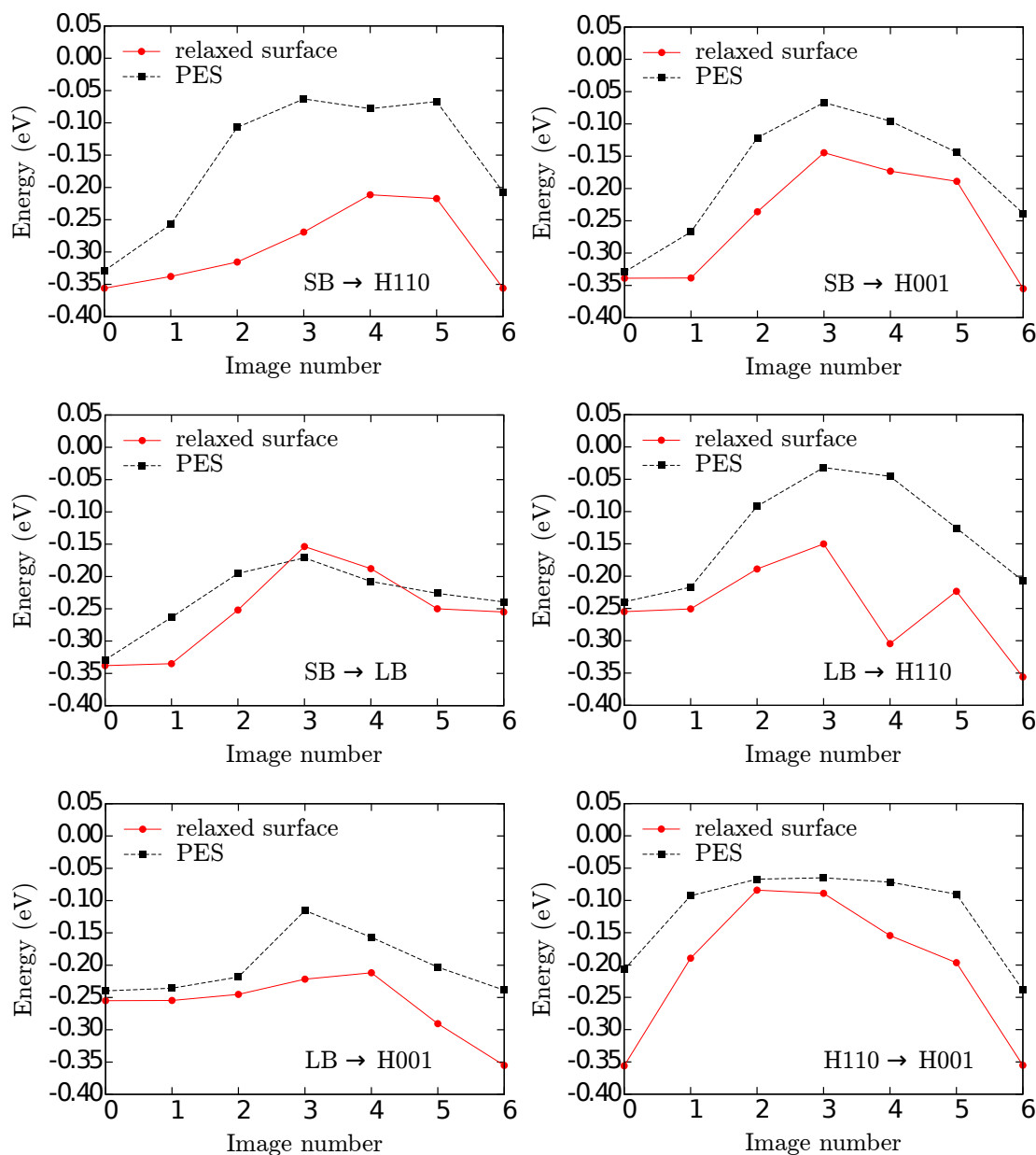
Figure 5.4: *Climbing-image nudged elastic band method results for the transitions between the adsorption wells. Black line represents results for the frozen surface (energy and forces are given by the PES). Red line represents results for the relaxed surface (energy and forces from VASP).*

barrier related to rotation between the two different geometries at the hollow site increases substantially in the relaxed surface case. As shown in Fig. 5.4, the reason for this is directly related to the larger adsorption energies at the hollow site

when surface relaxation is allowed. Last but not least, the transition energies between bridge and hollow wells are significantly reduced when relaxation effects are included. From the LB well the lowest energy barrier corresponds to the transition to the H001 well and its value is reduced from 0.12 eV obtained in the frozen surface PES to just 0.04 eV for the relaxed surface. Similarly, for the relaxed surface the lowest energy barrier from the SB well corresponds to the transition to the H110 well and amounts to 0.13 eV. This value should be compared to the value of 0.27 eV that is obtained in the frozen surface PES. Yet, none of such reduced values is negligible for molecules already thermalized with the surface at $T_s < 200$ K. Therefore, only hot molecules that still keep part of their initial E_i are expected to overcome these barriers and to be transferred from the bridge wells to the hollow wells.

All the above results allow us to suggest an alternative model for the adsorption dynamics of O_2 on Ag(110) that could explain the measured low adsorption probability at low incident energies in molecular beam experiments. In accordance to our dynamics simulations, molecules are expected to be adsorbed initially in the bridge sites because of their large and accessible configurational space that is not much altered by surface relaxation. Direct adsorption in the hollow wells is, thus, very unlikely. Now, considering that DFT-PBE is probably overestimating the adsorption energies on bridge, as TPD experiments suggest [135, 137], adsorption on the bridge wells would be unstable at the surface temperatures at which molecular beam experiments are performed. Thus, the molecules, being dynamically trapped on the attractive region around bridge will preferentially desorb at the lowest E_i because the configurational space leading to the hollow wells is very restrictive compared to the one towards desorption. However, as E_i increases more paths from bridge to hollow become accessible and the molecules can be efficiently transferred to the chemisorption hollow wells where desorption requires high T_s. In particular, an adsorption path in which the molecule is first attracted to the LB well and afterwards travels to the H001 well seems likely, based on the results of the dynamics study provided in Fig. 5.2 and the low transition energy barrier between the LB and H001 wells of 0.04 eV when relaxation is allowed.

Notice that the proposed model contrasts with the previous interpretation of the molecular beam experiments suggesting that there was no influence of the so-called physisorbed state. However, that assumption was based only on the low sticking probability measured at low E_i, which can alternatively be understood

as discussed above.

5.4 Full dimensional dynamics

In addition to the PES+GLO dynamics, we have performed AIMD simulations for a few E_i to confirm if the surface atom movement does indeed facilitate the transfer from the bridge to the hollow wells. We choose $E_i = 0.1, 0.3, 0.7$ eV as a representative set that covers most of the energy range of interest for molecular adsorption. This kind of calculations involve large computational requirements. Therefore, only a limited number of trajectories has been computed. In all cases we propagate each trajectory for approximately 5000 steps. We have run 21 trajectories with a time step of 1.5 fs for $E_i = 0.1$ eV, 34 trajectories with a time step of 1 fs for $E_i = 0.3$ eV, and 25 trajectories with a time step of 0.7 fs for $E_i = 0.7$ eV. The chosen time steps guarantee a stable integration in each case *. Due to the limited integration time, the calculated adsorption probabilities, especially at higher E_i, should be taken as upper limits. Nevertheless, as seen below, these restrictions do not affect the conclusions that we extract from our results.

In Fig. 5.5 we compare the adsorption probabilities obtained from our AIMD simulations to the results of molecular beam experiments. Similarly to the results of the dynamics performed using the PES+GLO model, the dependence of the adsorption probability on E_i shows the characteristics of a non-activated system. As before, for low E_i the calculations give a large adsorption probability that contrasts with the results of the molecular beam experiments.

It is interesting to look more carefully to the AIMD trajectories paying special attention to the final location of the molecule. For the highest analyzed energy $E_i = 0.7$ eV, at the end of the simulation time, most of the molecules are still moving between Ag(110) unit cells and we can not determine their final adsorption position. In the case of $E_i = 0.3$ eV, out of the 11 trajectories in which the molecule was adsorbed on the surface, we identified five of them to be adsorbed in the hollow wells, three of them to be adsorbed in the SB well, and three of them that have not clearly positioned in any of the four wells, after 6 ps. In the case of $E_i = 0.1$ eV we are able to determine the final adsorption well in all 15 trajectories

---

*We have experienced some difficulties related to an abrupt change of spin (from a magnetic to a non-magnetic state) which modifies the forces (and total energies) and makes the rest of the trajectory unusable. This situation is usually avoided using smaller time steps which is computationally more expensive.
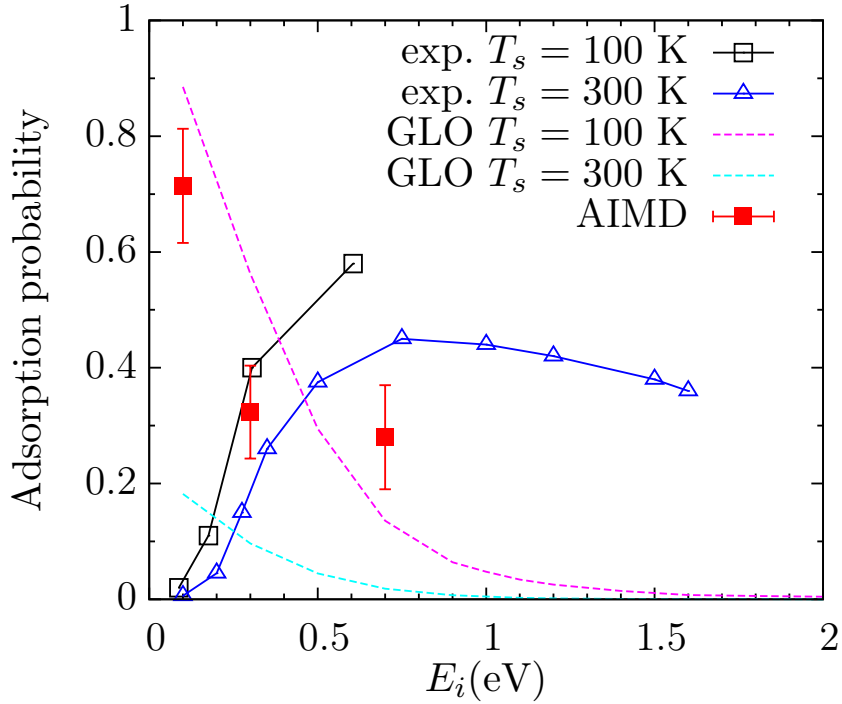
Figure 5.5: *Comparison of our dynamics results for the adsorption probability under normal incidence conditions as a function of the incidence energy E_i with molecular beam measurements of Refs. [19, 22]. GLO data are the same as in Fig. 5.1. Error bars for AIMD points represent the standard error of the binomial distribution.*

in which the molecules are adsorbed. 13 of these trajectories are adsorbed in the bridge wells and just 2 are adsorbed in the H001 well.

The above analysis shows that in AIMD simulations the adsorption probability in the hollow wells is significantly higher than the one predicted by the PES+GLO model ($\approx$ 45% versus $\approx$ 1% for E_i = 0.3 eV). This is a manifestation of the importance of surface relaxation in the adsorption of O_2 on Ag(110). Nevertheless, it is worth to remark that even in the cases in which the molecules finally adsorb in the hollow wells, a close inspection of their trajectories shows that they have previously visited a large portion of the configurational space and even spent a considerable amount of time around the bridge wells. This behaviour supports the considerations made in Sec. 5.3 regarding the initial attraction of the molecule to the bridge sites before it travels to its final adsorption well where it thermalizes. Still, at low E_i = 0.1 eV most of the molecules remain adsorbed in the bridge wells. The adsorption model proposed in Sec. 5.3 assumes that these

molecules would be desorbed under the experimental conditions, resulting in low adsorption probabilities at low E_i. However, due to the above mentioned DFT-PBE overestimation of the adsorption energy at the bridge wells this cannot be reproduced by the simulations.

Finally, it seems that at $E_i > 0.5$ eV DFT-PBE tends to underestimate the experimental adsorption probabilities both in the PES+GLO calculations and in the AIMD simulations. As in the latter case we did not apply any thermostat to the surface, one would expect that our AIMD results overestimate the adsorption probabilities for the given E_i compared to the thermalized surface. This is obviously not the case and thus it points out to a further difficulty in describing the adsorption of O_2 on Ag(110) with DFT-PBE.

5.5 Summary

In summary, we have performed a detailed, state of the art, theoretical study of the adsorption process of O_2 on Ag(110). Dynamics simulations performed using the PES+GLO model show characteristics of a nonactivated system, while the opposite was observed in the molecular beam experiments. This points out to a missing energy barrier for adsorption in the DFT-PBE PES. Moreover, in our calculations most of the molecules are adsorbed in the bridge wells due to the relatively large configurational space of attractive potential energies around them as compared to the hollow wells. However, surface relaxation effects are large for the hollow wells, which are the ones located close to the surface. This suggests that the PES+GLO model could be underestimating the adsorption in the hollow wells. We have calculated the energy barriers between the adsorption wells to study the possibility of transitions of the molecules initially adsorbed in the bridge wells to the hollow wells. Our results show that these transitions are only possible for molecules that still keep part of their initial kinetic energy.

Our AIMD simulations confirm the importance of surface relaxation, and suggest that the PES+GLO model overestimates the adsorption probability in the bridge wells. Individual AIMD trajectories confirm that adsorption in the hollow wells can proceed through initial adsorption in the bridge wells.

These results enable us to propose an alternative model for the adsorption dynamics in molecular beam experiments. We suggest that the experimentally observed activation barrier could be due to the transition barrier from the ph-

ysisorption like (bridge) wells to the chemisorption (hollow) wells. This hypothesis could be tested with molecular beam measurements at low surface temperatures $T_s < 40$ K for which high adsorption probabilities at the physisorption like wells would be expected. Unfortunately these experiments have not yet been performed.

All in all, we have shown that the adsorption of O_2 on Ag(110) involves a complicated dynamics and that for its description DFT-PBE has a limited accuracy. This leads us to suggest that further first principles electronic structure studies, involving other (more advanced) exchange-correlation functionals, may be needed to reproduce and elucidate the results of molecular beam experiments, which is the topic of the next chapter.

Search for an appropriate exchange-correlation functional to describe O$_2$ on Ag(110)

In previous chapters it has been shown that the standard PBE exchange-correlation functional can not provide a complete understanding of the molecular oxygen adsorption dynamics on Ag(110). In particular, the PBE description of the bridge wells is crucial. On the one hand, these wells have a large influence on the adsorption dynamics as basically all incoming molecules (with low incidence energies) are initially attracted to these wells. On the other hand, existence of such wells with the characteristics shown in Table 3.1 have not been observed experimentally. These wells have some similarities with the measured physisorption wells, but with much larger adsorption energies and lower O-O stretch vibrational frequencies. For these reasons, it is necessary to assess the accuracy of PBE description of the O$_2$/Ag(110) system.

Unfortunately, for most solid state systems there are no readily available theoretical "benchmark" methods to which DFT results can be compared. Currently, such methods exist for relatively small molecular systems, the so-called quantum chemistry methods (see Ch. 2.1). For solids, one could use quantum Monte Carlo methods, but only to a certain degree due to the high computational cost [206, 207]. Systems made of metals are usually especially hard to handle. This even worsens if one wants to treat a molecule on a metallic surface due to the associated increase of the system size. For these systems, there are ongoing developments of the so-called embedding approaches that in principle could provide benchmarking quality [205].

Due to the lack of well established benchmarking methods, we will take an alternative approach in this chapter. We will apply exchange-correlation functionals of increasing complexity and hopefully accuracy. The spread among the results obtained with different exchange-correlation functionals can give us information about the accuracy one should expect from a DFT calculation, in our

case the PBE calculation. Additionally, if the more advanced functionals tend to converge to the same value for some property, this can be a good indication that this value is close to reality.

A nice systematization of exchange-correlation functionals is the so-called Jacob's ladder of DFT [208]. On the way to "DFT heaven" (exact exchange-correlation functional) the first step, and the simplest approximation, is LDA, which is not considered here due to its well known deficiencies for gas surface systems. Next three steps include the exchange-correlation functionals that are considered in the next three sections. Namely, in Sec. 6.1 we consider GGA functionals, in Sec. 6.2 we consider meta-GGA functionals, and in Sec. 6.3 we consider hybrid functionals.

6.1 GGA

Due to their availability in all major DFT codes, relatively good accuracy and numerical stability, almost all first-principle gas-surface studies are based on the GGA exchange-correlation functionals. Many different GGA functionals exist, as discussed in Ch. 2.2.1. In this section we apply the most common ones to the O$_2$/Ag(110) system. The functionals we use are discussed in the following.

In addition to the above used PBE functional [45], the RPBE functional [48] is also commonly employed for gas-surface systems. The PBE functional is constructed such that it satisfies known quantum-mechanical limiting cases and for intermediate regions of the normalized density gradients it uses a sensible interpolation between limiting cases. The authors of the RPBE functional noticed that the PBE usually overbinds atoms and small molecules (NO, CO) both in vacuum (too large atomization energies) and on transitional metal surfaces (too large adsorption energies). They constructed the more repulsive RPBE functional by modifying the dependence of the exchange energy on the normalized density gradient. It was done in a way that the RPBE functional fulfilled the same physical limits as the PBE functional. With these changes much better energetics were obtained for the studied systems. However, this worsens the description of the solids and for other gas-surface systems RPBE gives too repulsive PESs [209, 210]. In fact, it has been observed that often experimental results lie in between the results obtained by PBE and RPBE and that their mixing can provide chemical accuracy for some systems [49, 211]. On the other hand, a better description of

solids properties than obtained from PBE can be obtained by reducing the PBE exchange interaction in the intermediate regions of the normalized density gradients. This gives rise to the PBEsol functional [212]. Note that this functional usually worsens results for molecules (compared to PBE) and that the PESs based on it are too attractive. In general it is hard to make GGAs more accurate for solids and molecules at the same time. GGA functionals can be coupled with van der Waals (vdW) corrections as discussed in Ch. 2.2.1. In this chapter effects of these corrections are also discussed.

Regarding the interaction of the oxygen molecule with silver surfaces, it has been shown that PBE performs better than RPBE for the $O_2/Ag(100)$ system [167]. Molecular beam experiments for the $O_2/Ag(111)$ system have been successfully simulated based on the PBE PES [168, 169]. This is one of the reasons why the 6D PES developed in this thesis is based on PBE.

To quantify effects of different exchange-correlation functionals on the PES of the $O_2/Ag(110)$ system, we concentrate on two characteristics:

- 1D $[V(Z)]$ effective PESs from vacuum to the adsorption wells

- adsorption energies of the molecule in each of the adsorption wells

The first characteristic gives us information on the accessibility of the wells from vacuum, especially whether adsorption wells are accessible without an energy barrier as in the case of PBE. The second one gives us information on the stability of each well and which adsorption well is expected to be more populated. In the construction of the 1D effective PESs with different exchange-correlation functionals we use the following procedure. First, the molecule is positioned parallel to the surface and above the hollow or bridge sites of the surface. Using each exchange-correlation functional, the interatomic distance of the molecule is then relaxed keeping the surface and other molecular degrees of freedom frozen. The procedure is repeated for several molecule-surface distances Z in order to obtain $V(Z)$. To calculate the adsorption energies, the molecule is positioned in the adsorption well and the molecular and surface degrees of freedom are relaxed using the different exchange-correlation functionals. The relaxed energy of the molecule in each of the wells is then subtracted from the energy of the molecule midway the two slabs, which gives the adsorption energy. The computational setup for DFT calculations is the same as the one used in Ch. 3 (see also Appendix A) unless noted otherwise.

The effective 1D PESs for the hollow (only H110) and bridge (only SB) configurations are shown in Fig. 6.1. Conclusions drawn in the following, based on the results for the H110 configuration, can also be applied to the H001 configuration, and similarly those for the SB configuration are applicable to the LB configuration. For each of the two configurations (H110 and SB) four 1D PESs are shown, calculated with the PBE, RPBE, PBEsol, and vdW corrected PBE functionals. For the vdW correction we use the recently proposed refinment [213] of the vdW-TS functional [62]. We use it due to its availability in the VASP code and its applicability to the spin polarised systems.

Comparing the PBE, RPBE, and PBEsol 1D PESs in Fig. 6.1 it can be seen, as expected, that RPBE is the most repulsive, PBEsol is the most attractive, and PBE is in between these two extremes. RPBE even predicts an entrance barrier to the well for the H110 configuration, but not for the SB configuration. Therefore, it is clear that the SB well is much more accessible than the H110 well in the RPBE description. Correcting the PBE functional with vdW contributions lowers the energies in the whole Z range. This effect is not surprising as the vdW corrections are always attractive. However, it is interesting to note that the correction is larger for the H110 configuration. The differences between the functionals in the important Z regions can be several hundred meVs. This spread is connected to the accuracy one should expect from a GGA calculation. The accuracy of several hundred meVs is not, unfortunately, good enough to treat gas-surface problems reliably.

In Table 6.1 we list the adsorption energies for each adsorption well. Again,

Table 6.1: *Adsorption energies (given in eV) for each adsorption well calculated with different exchange-correlation functionals. Negative adsorption energy means that the energy of the molecule in that adsorption well is higher than in vacuum. For these calculations we use a $5 \times 5 \times 1$ **k**-point Monkhorst-Pack gird.*

	H110	H001	SB	LB
PBE	0.42	0.38	0.35	0.29
RPBE	-0.02	-0.04	0.09	0.00
PBEsol	0.67	0.63	0.54	0.30
PBE+vdW corr.	0.57	0.52	0.42	0.36
vdW-DF-cx	0.58	0.54	0.44	0.37

the PBE results are in between the RPBE and PBEsol results. RPBE adsorption

Figure 6.1: *1D effective PES as a function of molecule-surface distance for H110 and SB configurations calculated with PBE (with and without vdW correction), RPBE, and PBEsol functionals. We use a Γ-centered $4 \times 4 \times 1$ **k**-point grid instead of the original shifted Monkhorst-Pack gird used before. The new grid includes more special **k**-points in the first Brilloiun zone, and therefore there are small differences in energies with respect to the original PBE results.*

energies are very close to the molecule-in-vacuum energies which clearly shows that this functional is too repulsive for this system and cannot be applied. Regarding the PBEsol results, although adsorption energies for all wells increase compared to the PBE results, it is worth noting that the increase is larger for the hollow wells than for the bridge wells (especially long bridge). As in the STM experiments only hollow adsorption wells are identified one might say that PBEsol point to the right direction of larger difference between the hollow and bridge adsorption energies. However, the adsorption energies of the bridge wells then clearly show that they cannot represent measured physisorption states. For this reason, using PBEsol one would certainly obtain large sticking probabilities at low incidence energies, in contrast with the molecular beam experiments. It is worth noting that it seems that mixing any two of these GGAs, the so-called "SRP functional" [49], that was successfully applied to other gas surface systems, would not be a successful approach.

We have also included in Table 6.1 the adsorption energies calculated with the above described vdW corrected PBE (of vdW-TS type) functional and with the vdW-DF-cx functional [214]*, which is a recent refinement of the vdW-DF functional [65]. Both functionals give very similar result. As in the case of PBEsol, these functionals also predict a larger difference between the hollow and bridge wells. However, since the adsorption energies for the bridge wells are too large in comparison to the measured physisorption states, the large sticking probability at low incidence energies problem would persist with vdW corrected GGAs.

6.2   Meta-GGA

I this section 1D PESs and adsorption energies are calculated with different meta-GGA functionals that, in addition to the density gradient, include information on the kinetic energy density, as discussed in Ch. 2.2.1. We use meta-GGA functionals that are implemented in the VASP code: TPSS [51], RTPSS [216], MS0 [217], MS1 [218], MS2 [218], and M06L [219]. The TPSS functional is constructed in a similar way to the PBE functional in the sense that it is constructed to match exact quantum-mechanical constraints without empirical parameters. These constrains are related to both one (or two) electron properties and electron gas properties.

---

*Spin polarised version of vdW-DF type of functionals are not available in current VASP code, so we use the QUANTUM ESPRESSO code [215]. Details of these calculations are those listed in Appendix A.

Hence, TPSS can describe well (better than PBE) at the same time molecules and solids. RTPSS is a refinement of TPSS in similar way as the PBEsol is of PBE, so that solid properties are even better described. However, the molecular properties remain well described. The MS0 functional features a simpler functional form than RTPSS, contains further constraints, and shows better predictions for simple molecules and solids than (R)TPSS. Its name comes from "made simple"-MS and "zero"-0 fitting parameters. MS1 and MS2 are functionals with one and two fitting parameters, respectively, which were fitted to a database of several measurements or high-quality quantum chemistry calculations. Finally, M06L is a functional with a large number of parameters fitted to a broad database. This functional typically performs better than the other meta-GGAs discussed here for systems similar to those included in the broad database that is used for the fitting. However, it is also much harder to handle as it is numerically less stable than the other mentioned meta-GGAs. Meta-GGAs are in general numerically trickier and to achieve self-consistency usually one has to start with converged GGA orbitals.

1D PESs calculated with these meta-GGAs are shown in Fig. 6.2. Due to the above mentioned numerical problems that can appear with meta-GGAs, we have used PBE interatomic distances for this figure. This approach is good enough for our purpose of checking how accessible the wells are from vacuum. It can be seen that differences between the curves are smaller than in the case of tested GGAs. A bit larger difference between the M06L functional and the others is probably due to the fact that this functional is also fitted to vdW bonded materials. All tested meta-GGA functionals predict that both H110 and SB wells are accessible without an energy barrier from vacuum.

The adsorption energies calculated with meta-GGAs are listed in Table 6.2. Both molecular and surface degrees of freedom are relaxed with each exchange-correlation functional, as in the previous section. All meta-GGAs predict the lowest adsorption energy for the LB well. However, which is the well with the highest adsorption energy is not that clear. Most of the meta-GGA functionals predict that the H110 well is the deepest, but MS0 and MS1 predict a larger adsorption energy for the SB well. Spread of the adsorption energies calculated with the selected meta-GGAs is smaller than the one obtained with the selected GGAs. The range of adsorption energies in the H110 well goes from 0.29 eV to 0.66 eV, while in the SB well it goes from 0.25 eV to 0.46 eV. This range of H110 adsorption energies seems plausible considering the measurements of the so-called chemisorbed state. However, the range of the SB adsorption energies seems too attractive to be
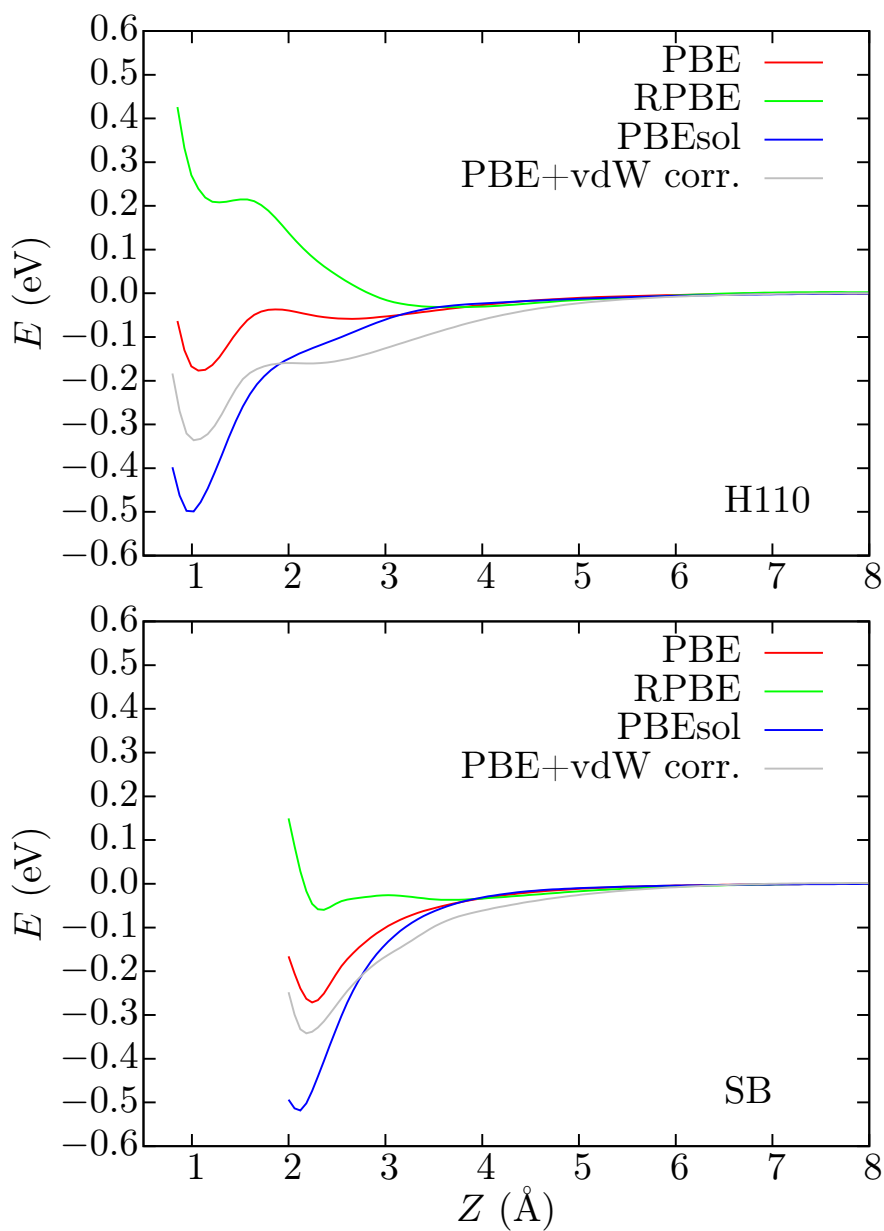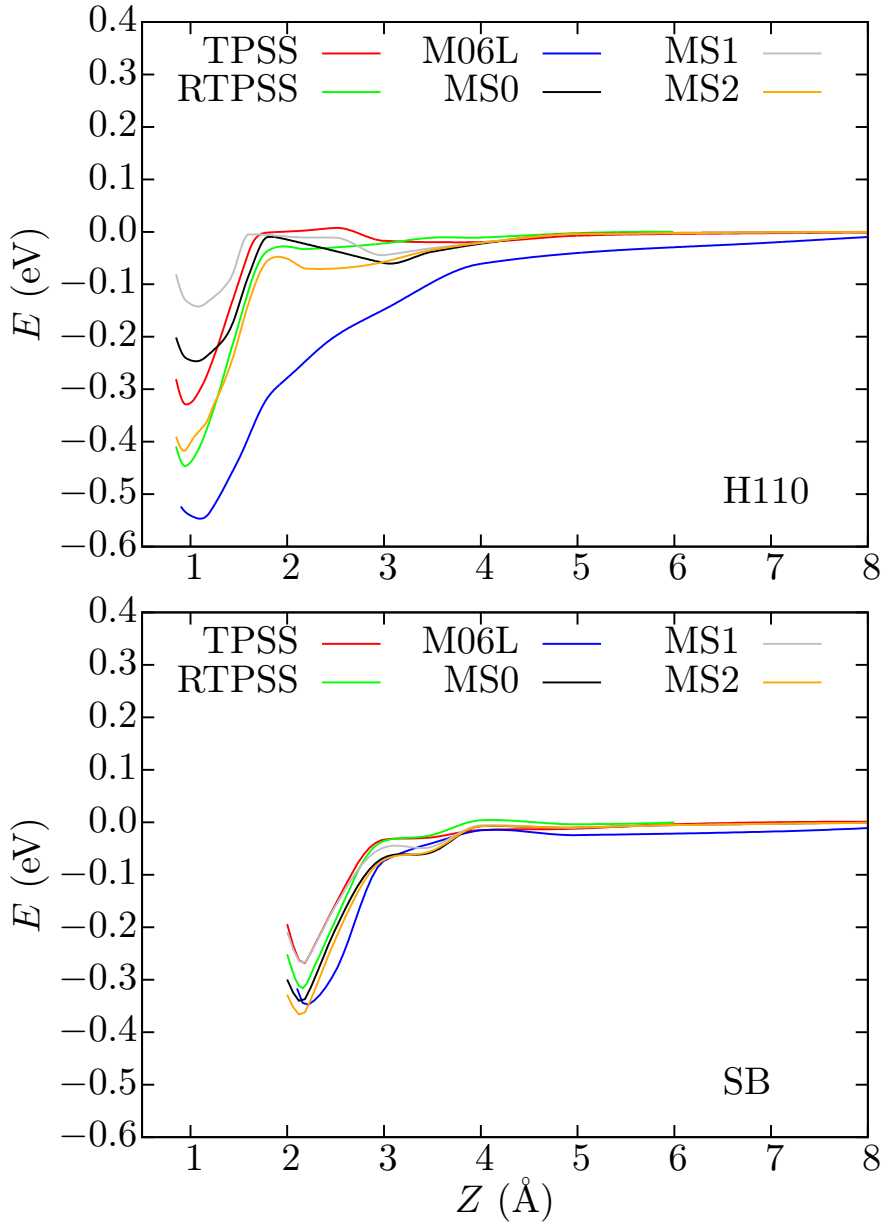
Figure 6.2: *1D effective PES as a function of molecule-surface distance for H110 and SB configurations calculated with different meta-GGA functionals. As in Fig. 6.1, we use a Γ-centered $4 \times 4 \times 1$ **k**-point grid. The energies are calculated for the PBE geometries of Fig. 6.1.*

consistent with the measurements of the so-called physisorbed state. Therefore it seems that the tested meta-GGAs also would not be significantly more successful

Table 6.2: *Adsorption energies (given in eV) for each adsorption well calculated with different meta-GGA exchange-correlation functionals. For these calculations we use a $5 \times 5 \times 1$ **k**-point Monkhorst-Pack gird.*

	H110	H001	SB	LB
TPSS	0.47	0.40	0.25	0.19
RTPSS	0.56	0.47	0.39	0.18
MS0	0.41	0.33	0.42	0.19
MS1	0.29	0.24	0.34	0.15
MS2	0.55	0.53	0.43	0.20
M06L	0.66	0.49	0.46	0.44

than PBE to describe molecular beam experiments. It seems that the bridge wells would still play an important role in the adsorption process. We expect that the sticking probability at low incidence energies and low temperatures would again be close to one, like in our PBE based PES+GLO and AIMD simulations.

6.2.1   Barriers to dissociation

Another difficulty with the DFT-PBE results is the fact that the energy required to desorb from the molecular adsorption well is smaller than the energy required to dissociate. Such results contrast with the experimental observations in which the large majority of molecules rather dissociate than desorb upon increasing T_s [17, 19, 20, 22, 140]. Therefore we have also calculated the dissociation barriers with two meta-GGAs (RTPSS and MS2) which are shown in Fig. 6.3. Calculations are performed using the same climbing-image nudged elastic band (CI-NEB) method that is already used in the previous chapter. Additionally, we have evaluated energies on the PBE transition path for other tested exchange-correlation functionals and aligned them with the corresponding adsorption energies. Comparing the lines evaluated in this way for RTPSS and MS2 with the actual CI-NEB calculations, one can see that this approximation is valid.

As shown in Fig. 6.3, RTPSS and MS2 predict, in contrast to PBE, a smaller energy barrier to dissociation than to desorption. Therefore, at least for this PES property these meta-GGAs perform better than PBE in comparison to experiments. In fact, the difference between the desorption and dissociation barriers of ≈ 0.1 eV agrees with the experimental value that is obtained from the decrease of sticking probability with surface temperature, as discussed in Sec. 3.1.
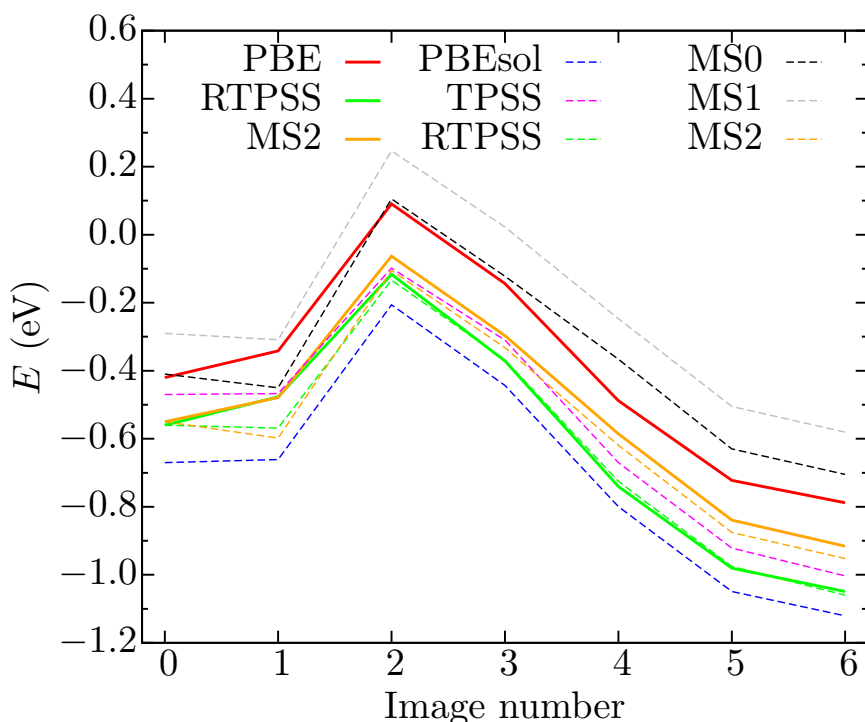
Figure 6.3: *Minimum energy path for dissociation calculated with different exchange correlation functionals. Image 0 corresponds to the H110 adsorption well and image 6 corresponds to the dissociated molecule with each of the atoms close to the LB site. Full lines are the results of CI-NEB calculations. Dashed lines are energies calculated with different exchange correlation functionals evaluated on the PBE minimum energy path and shifted to the adsorption energy of the corresponding functional.*

In general, for all tested GGAs and meta-GGAs in Fig. 6.3, it can be seen that the energy barrier to dissociation (measured from the bottom of the well) does not vary much between them. Therefore, the energetic preference for dissociation or desorption is mainly dependent on the description of the adsorption energy. The functionals that predict a relatively low adsorption energy for the H110 well give preference for desorption (MS0 and MS1), and those that predict a relatively high adsorption energy give preference to dissociation (the rest of meta-GGAs). It is interesting to note that the former also predict larger adsorption energies for the SB well than for the H110. PBEsol gives the largest adsorption energies of all tested functionals, and accordingly the largest energy preference for the dissociation over desorption. RPBE (not shown on the figure) gives the opposite extreme.

6.3   Hybrid functionals

In the previous section it has been shown that some meta-GGAs can reverse the PBE preference for desorption over dissociation. These meta-GGAs at the same time also favour energetically the adsorption in the hollow wells over the adsorption in the bridge wells. These results are in line with experimental observations. However, the bridge wells are still too attractive to be considered physisorption wells. Therefore, as they are available from vacuum without an energy barrier, it should be expected that the sticking probability at low incidence energies would be overestimated compared to experiments.

In light of these conclusions, it is worth to consider a possibility that measured low sticking probabilities at low incidence energies are due to entrance energy barriers to both hollow and bridge wells which are absent in the tested GGA and meta-GGA functionals. As discussed in Ch. 5.2, a missing entrance barrier is also the reason for the disagreement between molecular beam experiments and GGA based dynamics in the $O_2/Al(111)$ system. It has been shown in Ref. [204] that the entrance barrier can be recovered for that system if the hybrid (HSE and PBE0) exchange-correlation functionals are used. Therefore, in this section we apply hybrid functionals to the $O_2/Ag(110)$ system. Evaluations of these functionals are computationally very costly (see discussion in Ch. 2.2.1), so we will only consider a 1D effective PES calculated on PBE geometries shown in Fig. 6.4.

The first hybrid functional we consider is the screened hybrid functional HSE06 [59, 220]. It is based on the PBE functional and constructed such that 25% of the PBE exchange at short range is replaced by the exact exchange. At long range this functional is identical to the PBE. The good performance of this functional for both solids and small molecules is well established [60]. Interestingly, as shown in Fig. 6.4, this functional predicts an entrance energy barrier to both H110 and SB wells. Therefore, the low sticking probability at low incidence energies could be explained by the HSE06 functional. The barrier to the H110 well of 0.22 eV is much higher than the entrance barrier to the SB well of 0.04 eV. Due to this, it should be expected that, like in the PBE case, much more molecules are initially adsorbed in the SB well. Thus, even in this case the bridge wells would probably play an important role in the adsorption dynamics. Additionally, from the HSE06 energetics it seems that this functional predicts larger or similar adsorption energy for the SB well compared to the H110 well, taking into account that relaxation effects are typically not much larger than 0.2 eV for the H110 well
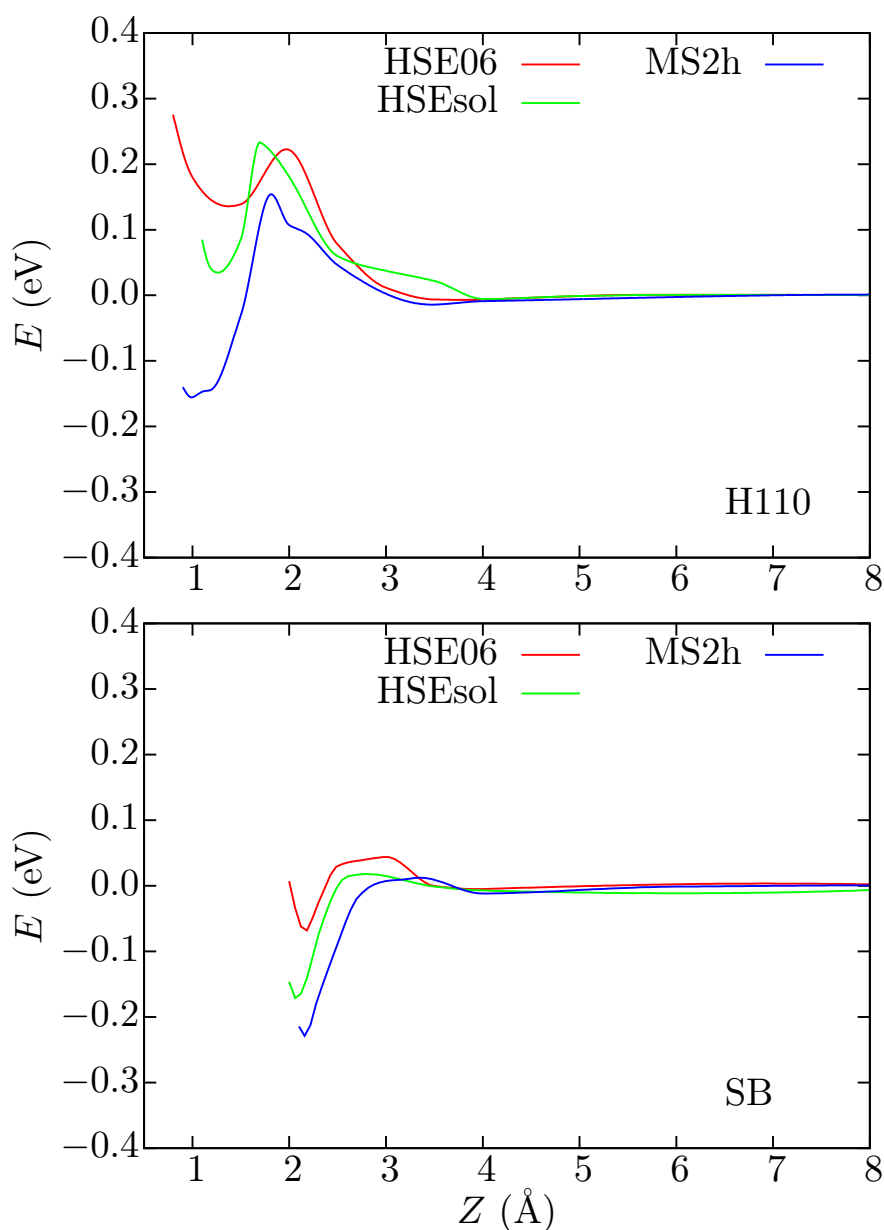
Figure 6.4: *1D effective PES as a function of molecule-surface distance for H110 and SB configurations calculated with different hybrid functionals. We use a $4 \times 4 \times 1$ **k**-point grid. The energies are calculated for the PBE geometries of Fig. 6.1.*

(compare Fig. 6.2 and Table 6.2). Therefore, HSE06 could fail in explaining why the bridge wells are not seen in the experiments. Furthermore, based on the H110 energetics and the discussion on the dissociation barriers from the previous sec-

tion, it seems that HSE06 would favour desorption over dissociation. For these reasons, it seems that HSE06 tends to be too repulsive close to the H110 well.

Next, we use the HSEsol hybrid functional [221]. The only difference between HSEsol and HSE06 is that PBEsol is used instead of PBE. This produces generally even better results for properties of the solids and a slightly worse results for the molecules [221]. Based on the comparison between PBE and PBEsol (see Table 6.1) one would expect that HSEsol would be more attractive than HSE, esprecially for the H110 configuration. Due to this, one might expect that some of the HS06 deficiencies for O_2/Ag(110) could be resolved. As shown in Fig. 6.4, indeed, HSEsol is more attractive than HSE06 in general. Unfortunately, above mentioned difficulties persist as the SB well is much more accessible from vacuum (with only a very small barrier of 0.02 eV compared to the barrier of 0.23 eV to access H110) and it looks like it has a larger or equal adsorption energy than the H110 well.

Finally, we use the MS2h meta hybrid functional made such that 9% of the MS2 exchange is replaced by the exact exchange [218]. To our knowledge this functional was not used for solids so far, but it has been shown to be very accurate for molecules [218]. It is interesting to consider this functional as in the previous section it has been shown that MS2 energetically favours adsorption on H110 over SB and dissociation over desorption. Unfortunately, in the VASP code meta hybrid functionals are not implemented. Therefore, our calculations are non-self-consistent and the energies reported here are obtained such that the ordinary self-consistent MS2 calculation is performed, and afterwards 9% of the MS2 exchange is replaced by the exact exchange energy calculated for the MS2 orbitals. 1D PESs obtained in this way with the MS2h functional are shown in Fig. 6.4. It can be seen that the entrance barrier to the H110 well of 0.15 eV is lower compared to the HSE and HSEsol values, while the entrance barrier to the SB well is very small (0.01 eV) and similar to the HSEsol value. It seems that MS2h predicts an increase of the adsorption energy of the SB well of around 0.05 eV compared to HSEsol and a much larger increase of the adsorption energy of the H110 well of around 0.2 eV compared to HSEsol. Therefore, MS2h would clearly energetically favour adsorption to the H110 well, although it is clear that the SB well will play an important role in the adsorption dynamics due to its accessibility from the vacuum. Based on these features, one might expect a better agreement between a MS2h adsorption dynamics and the molecular beam experiments. Namely, it can be expected that at least a good portion of the molecules

at low incidence energies would not stick to the surface due to existing energy barrier in the entrance channel. Molecules with higher incidence energies would overcome this barrier and stick to the surface. It seems that initially more of these molecules would be attracted toward the bridge wells. However, as the hollow wells are energetically more favourable, provided that the barriers between wells are small, molecules could finally adsorb in the hollow wells, as in experiments, where the dissociation barriers are small.

6.4   Summary

In this chapter we have studied how would the O_2/Ag(110) PES change if it is calculated with other exchange-correlation functional different from the PBE. We have concentrated on the adsorption energies and 1D PESs that show the potential energy as a function of the molecule-surface distance. We have used several popular GGAs, meta-GGAs and hybrid functionals.

Among GGAs, we have considered PBE, RPBE, PBEsol, and vdW corrected PBE functionals. We have shown that the O_2/Ag(110) interaction energetics vary extensively with respect to the used functional. On the one hand, the RPBE functional is very repulsive with very shallow adsorption wells (and larger adsorption energies for the bridge wells) which clearly can not explain experimental results. On the other hand, PBEsol is much more attractive and predicts larger adsorption energies for the hollow wells compared to the bridge wells, but as PBE it would fail in the reproduction of the low sticking probabilities at low incidence energies. This can not be resolved by inclusion of the vdW corrections to PBE because, as expected, they increase the attractiveness of the PES for all molecule-surface distances.

We have considered several meta-GGAs: TPSS, RTPSS, MS0, MS1, MS2, and M06L. The spread of the results is lower compared to the results of the considered GGAs. Meta-GGAs predict that both hollow and bridge wells are relatively easy to access from vacuum. All of the functionals predict too large adsorption energies for the bridge wells to consider these wells as candidates for the measured physisorption state. Therefore, meta-GGAs also do not seem to provide the solution to the problem of the low sticking probabilities at low incidence energies measured by the molecular beam experiments. However, most of the meta-GGAs (together with PBEsol) can solve the problem of the PBE energetic preference for

desorption over dissociation from the molecular adsorption well.

Inclusion of the exact exchange suggests that there might be an energy barrier from vacuum to the adsorption wells, which could explain the observed low sticking probabilities at low incidence energies. We have shown that advanced meta hybrid functionals like MS2h could potentially provide reasonable energetics, both regarding the entrance barrier, and also for the adsorption energies.

Obviously, further theoretical studies are necessary in order to reproduce the results of the molecular beam experiments. The study presented in this chapter have shown that exchange correlation functionals up to the fourth step of the Jacob's ladder of DFT suggest that the bridge wells should play an important role in the adsorption dynamics of $O_2/Ag(110)$, even though the experimental evidence for this is lacking. A more detailed study using advanced (meta) hybrid exchange-correlation functionals or embedding approaches [205] could provide a step forward to the solution. Due to the lack of benchmarking methods, it would be advantageous from the experimental side to have adsorption energies reliably measured, which can be achieved by, *e.g.*, microcalorimetry [222].

7

Femtosecond laser induced desorption of O_2 from Ag(110)

Laser driven photochemistry has proven to be a useful tool for promoting reactions at surfaces or even as a way to open new reaction channels not accessible by thermal activation [30, 223–226]. In particular, one important reaction is the photodesorption of a molecule from a metal surface. Generally, desorption on metals can be induced either by directly exciting the molecule (IR photons) or it can be substrate mediated (UV/Vis/NIR photons). Among substrate mediated processes, one usually distinguishes between desorption induced by electronic transitions (DIET) and desorption induced by multiple electronic transitions (DIMET) [227]. DIET is practically realized by using continuous wave or nanosecond-pulse lasers with low intensity, resulting in small desorption yields that increase linearly with the laser fluence. In DIET on metals, the adsorbate captures a hot electron and forms a short lived excited state (negative ion resonance). After decaying to the electronic ground state, the adsorbate may gain enough energy and desorb. On the contrary, DIMET, which is the subject of the present study, is realized by intense femtosecond laser pulses. Such pulses are short in comparison to typical relaxation times of adsorbate excited states and, consequently, they can produce multiple excitations of an adsorbate that lead to desorption. DIMET results in relatively large desorption yields that increase superlinearly with laser fluence [223].

Different methods have been used to model DIMET [224–226]. Several of them are the so-called excitation-deexcitation models, in which the system jumps between two or more electronic states (see review [224] for a complete list). However, these methods due to their complexity have only been applied to a reduced number of degrees of freedom. In this work, we use an alternative

---

This chapter is based on publications 2 and 3.

model [127, 228–230] that permits treating all the molecular degrees of freedom. Instead of treating excited states explicitly, in this model the nuclear motion is classical in the ground state potential and all the electronic degrees of freedom are included via friction and associated fluctuation forces. The friction force accounts for the dissipation of the adsorbate energy on the surface by creation of low energy electron-hole pairs, while fluctuation forces represent the inelastic scattering of hot electrons on the adsorbate nuclei. The magnitude of the fluctuation force is obtained in terms of the temperature of the laser-induced hot electrons. This electronic temperature can be estimated from the properties of the laser pulse and the metal substrate (see Ch. 2.5). The first important ingredient of this model is an accurate ground state potential. As discussed in Ch. 2, this potential can be modelled with a range of methods with increasing accuracy and theoretical, as well as, computational complexity, starting with simple two body potentials up to accurate quantum chemistry methods. Early works that used the molecular dynamics with electronic friction model to simulate the laser-induced desorption were based on empirical potentials [127, 228]. Nowadays, one can obtain better accuracy and predictability by state of the art non-empirical theoretical methods. Particularly, a good balance between accuracy and computational complexity is achieved by density functional theory (DFT). This method, already at its semi-local level, is able to capture reasonably well both metallic delocalized states and molecular localized states and their interaction.

Ab initio molecular dynamics, in which DFT is used at each integration step to calculate the forces, keeps both the DFT accuracy and the full dimensionality of the problem. However, it is still computationally too demanding to treat low probability processes or even to run long time (more than few ps) dynamics. In this chapter we are interested in phenomena that typically demand both large statistics and long time dynamics. Therefore, it is more advantageous to follow an alternative scheme that consists in constructing the adiabatic potential energy surface (PES) from a large set of DFT energies.

Recently, the laser-induced associative desorption of H_2 on Ru(0001) has been successfully modelled by using such DFT-based 6D PES [230]. In that work, the metal surface is kept frozen and the laser excitation is only modelled by a random scattering of hot electrons with the nuclei of the molecule. Here, we extend this model by allowing for lattice movement that enables us to incorporate laser-induced phonon excitations. The study of the effect of phonons in photodesorption, compared to that of electronic excitations, is one of the main objectives of

this chapter.

We will employ this methodology to study the laser-induced desorption of O_2 on Ag(110). As shown in previous chapters, the O_2 molecule can adsorb on Ag(110) on several adsorption sites that are characterized by different adsorption energies and electronic densities and, as such, it is an interesting model system. It gives us the possibility to investigate the importance of including the phonon excitations in the model for desorption from adsorption wells of different characteristics.

Photochemistry of O_2 on Ag(110) after substrate mediated photoexcitation under DIET conditions has been studied experimentally in Refs. [231–233]. Photodesorption, photodissociation, and also CO_2 formation were observed there. To our knowledge, no experimental studies under DIMET (femtosecond laser) conditions have been carried out so far. As such, our investigation has a predictive character.

The rest of the chapter is organized as follows. The implementation of the theoretical model is described in Sec. 7.1. Application of this model to the desorption of O_2 from Ag(110) is examined in the next three sections. Contributions of phonon and electron processes to desorption are studied in Sec. 7.2. Analysis of desorbed molecules is performed in Sec. 7.3 and the influence of initial surface temperature and laser characteristics on desorption is studied in Sec. 7.4. The main conclusions of the chapter are summarized in Sec. 7.5.

7.1   Implementation of the theoretical model

We start by solving the 2TM differential Eqs. (2.49)-(2.51) to obtain T_{el} and T_{ph} as a function of time for the specific surface and laser pulse properties of interest. The calculated time dependent electronic and phonon temperatures are saved on a grid (in practice in steps of 0.05 ps) and used as inputs in the molecular dynamics calculations [Eqs. (2.52)-(2.53)]. Another required input that is needed to obtain η_{el} is the electronic density of the bare surface $n(\mathbf{r})$. Here, $n(\mathbf{r})$ is calculated with DFT and saved on a real space grid.

We perform classical dynamics calculations that neglect the zero point energy of the adsorbate. Each trajectory starts with the molecule resting in one of the adsorption wells. The initial position of the surface $\mathbf{r}_s$ (and the corresponding momenta) are sampled by a conventional Monte Carlo procedure, such that they

correspond to the initial surface temperature. The dynamics equations (2.52), (2.43), and (2.44) are integrated with the Beeman algorithm [102] as implemented in Refs. [106, 234]. At each integration step, the corresponding T_{el} and T_{ph} are obtained by a cubic spline interpolation. The electronic density at the position of each atom in the molecule $n(\mathbf{r}_i)$ is obtained with a 3D cubic spline interpolation of the bare surface density calculated with DFT.

Using the same implementation that solves Eqs. (2.52), (2.43), and (2.44), one can also perform dynamics simulations that only include the electronic or the phonon contribution by setting, $\mathbf{r}_s = 0$ or $\eta_{el,i} = 0$, respectively. In the following, the three types of calculations will be denoted as, LDFA+GLO, when including both the electronic and phonon contributions, LDFA, when including only the electronic channel, and GLO, when only phonons are included.

Table 7.1: *Properties of the adsorption states of O$_2$ on Ag(110): Adsorption energy E_a, O$_2$-surface distance Z, and electronic density in which oxygen atoms are embedded (expressed in terms of the mean free electron radius r_s given in atomic units, a.u.).*

Site	E_a (eV)	Z (Å)	r_s (a.u.)
LB	−0.24	1.98	3.82
SB	−0.33	2.20	3.57
H001	−0.24	1.29	2.62
H110	−0.21	1.09	2.57

As shown in Ch. 3, our 6D PES predicts that the oxygen molecule on Ag(110) can adsorb in four adsorption wells. Table 7.1 summaries the main features of each adsorption well that are relevant for laser induced desorption. Namely, the adsorption energy E_a, the distance Z from the surface of the molecular center of mass (CM), and the value of the bare surface electron density at the position of each O atom, which is given in terms of the mean free electron radius r_s. Adequacy of the 6D PES presented in Ch. 3 to describe experimental observations for O$_2$ on Ag(110) is discussed in Chs. 5 and 6. There, several problems of the DFT description are identified. In spite of this, study in this chapter is meaningful since it still uses a state of the art PES for O$_2$ on Ag(110). Additionally, the use of a PES for a system that presents several adsorption sites with different characteristics is advantageous for a theoretical study over systems with just one adsorption site. Having one system with several wells gives us the opportunity to more clearly study the dependence of the results on the properties of the wells, such as the

adsorption energy, the distance from the surface, and thus, the electron density in which the molecule is embedded. In this respect, our results can be predictive for systems in which adsorption wells with similar characteristics exist.

Our simulations are performed for laser pulses of Gaussian shape with 800 nm wavelength, 130 fs of full width at half maximum (FWHM), and absorbed fluences in the range $F = 50 - 200$ J/m^2. Laser pulses with these properties were used in desorption experiments performed on other systems [30, 235]. The laser-induced T_{el} and T_{ph} are calculated using the following material constants for Ag: $C_{el} = 63.3$ J/m^{3}K, $\kappa = 429$ W/mK, $g = 2.5 \times 10^{16}$ W/m^{3}K, and $k = 5.29$ [236–238]. The phonon heat capacity C_{ph} is calculated in the Debye model, with Debye temperature $T_D(\text{Ag}) = 225$ K. The metal slab thickness d in Eq. (2.51) is set to 0.5 μm. We have checked that with this d-value the calculated T_{el} and T_{ph} are well converged.

The electronic friction coefficient entering Eqs. (2.52) and (2.53) as a function of the embedding density is given by

$$\eta_{el}(r_s) = 1.365 \, r_s^{-1.828} e^{-0.082 r_s} + 50.342 \, r_s^{0.491} e^{-2.704 r_s}, \tag{7.1}$$

where both r_s and η_{el} are in a.u. This function fits the friction coefficients of an oxygen atom calculated for embedding FEG densities varying in the range $r_s = 1 - 6$ a.u. This range covers all the electronic density values that are relevant in our dynamics. The GLO equations for the Ag(110) surface are solved using the same parameters as in Ch. 5.

To enable the thermalization of the molecule prior to the laser excitation, the laser pulse is turned on after 1.5 ps, thus keeping the initial temperature constant during this time interval. However, we have checked that the results of the dynamics (for the initial surface temperature of 100 K) do not depend on this thermalization time and that the laser pulse could be turned on at the beginning of the dynamics calculation without altering the final results. We have also checked that the largest integration step that can be used keeping the results of the dynamics stable is 1 fs. In all cases the integration time is 50 ps and the instant $t = 0$ corresponds to the start of the trajectory calculation.

As an outcome of our dynamics we consider that a molecule has been desorbed when its center of mass arrives at 6 Å from the surface and its velocity direction points away from the surface. We also distinguish another possible exit channel, dissociation, if the interatomic distance r is larger than 2.5 Å with positive radial velocity.

7.2   Electron and phonon mediated processes

Calculated desorption yields* Y as a function of the laser fluence F are shown in Fig. 7.1 for the four different adsorption wells. These values have been obtained from the number of desorption events out of 30 000 trajectory calculations performed for each laser fluence and initial adsorption position. Characteristic
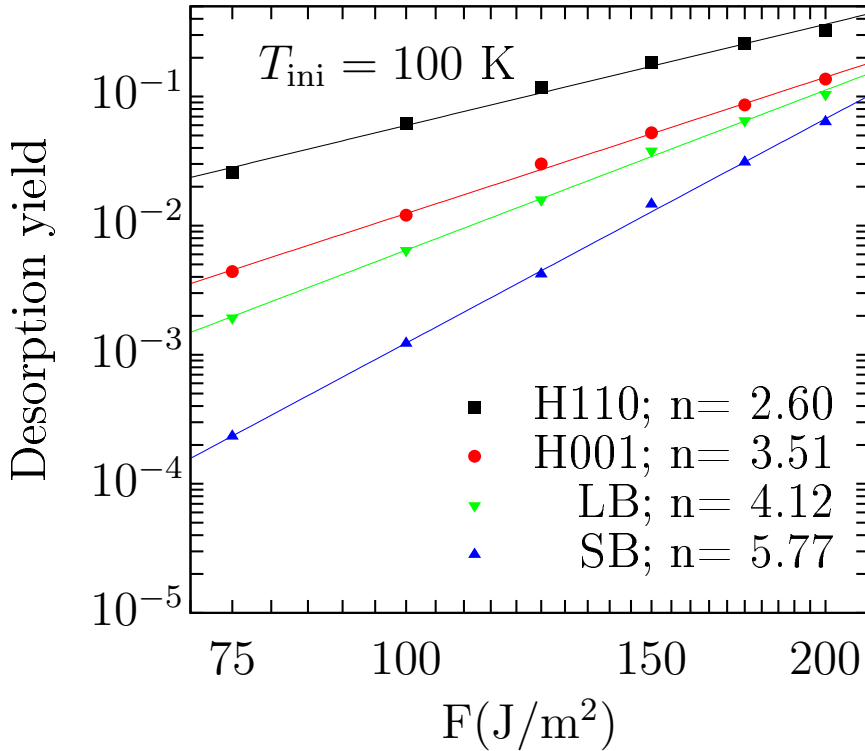
Figure 7.1: *Desorption yields Y from the four adsorption wells (shown with different symbols and colors) as a function of the laser fluence F. For each well the coefficient n is calculated by fitting the data to the equation $Y = aF^n$.*

super-linear desorption yields, which follow a power law $Y = aF^n$ with $n > 1$, are observed for the four wells. The values of the exponent n are in the range $2.6 - 5.8$. These values are similar to those obtained for other systems [224], such as CO/Cu(100) with $n = 5 - 8$ [228, 239], CO/Pd(111) with $n = 7 - 9$ [240], NO/Pt(111) with $n = 6$ [223, 241], O$_2$/Pt(111) with $n = 6$ [242, 243], O$_2$/Pd(111) with $n = 6 - 9$ [244], and associative desorption of H$_2$/Ru(0001) with $n =$

---

*The desorption yield is defined as the number of desorption events divided by the total number of trajectories.

3 [230, 235]. Independent of the considered laser fluence, the highest desorption yields are obtained for H110, followed by H001, LB, and SB. The exponent n of the power law is also different for each well, its value decreasing from $n = 5.8$ for desorption from the SB well down to $n = 2.6$ for desorption from the H110 well. Both results can be mostly related to the differences in the adsorption energies of the different wells (see E_a in Table 7.1). The highest desorption yield and lowest exponent correspond to the well with the lowest adsorption energy and vice versa. However, the adsorption energy itself is not the only property ruling the desorption process. The LB and H001 wells have the same adsorption energy (-0.24 eV), but the yields are consistently larger for desorption from the H001 well than for desorption from the LB well. As shown below, this effect is related to the different mechanisms that rule desorption from the hollow and the bridge sites.

Figure 7.2 shows the time dependence of T_{el} and T_{ph} as obtained from the 2TM for $F = 200$ J/m^2 in comparison with the time evolution of the desorption rate from each of the adsorption wells. There are remarkable differences between the bridge wells (LB and SB) and the hollow wells (H001 and H110) observed not only in the magnitude of the desorption rates, but also in their time evolution. The desorption rates for the hollow wells seem to follow the time evolution of T_{el}, but with a delay of around 3.5 ps. In contrast, the desorption rates from the bridge sites do not seem to be very much affected by the high increase of T_{el} at short times. In these cases, the highest values of the desorption rates occur at longer times, once T_{el} and T_{ph} are equilibrated. It is worth to mention that the desorption rate from SB seems to follow the time evolution of T_{ph}, but also with a certain delay. On the one hand, these observations suggest that desorption from the hollow sites is mainly an electron mediated effect, where the energy transfer from the electrons excited by the laser pulse to the adsorbed molecule plays a dominant role. On the other hand, these results also suggest that the heating of electrons is not that important for desorption from the bridge sites and that the laser mediated phonon excitation is the relevant mechanism in this case. In order to confirm these ideas and gain further insight in the relative importance of the electron and phonon mediated mechanisms, we have performed the two additional types of calculations described in Sec. 7.1 above, in which only the effect of either the heated electrons (LDFA) or heated phonons (GLO) is included in the desorption dynamics.

The desorption yields obtained from the four adsorption wells for two
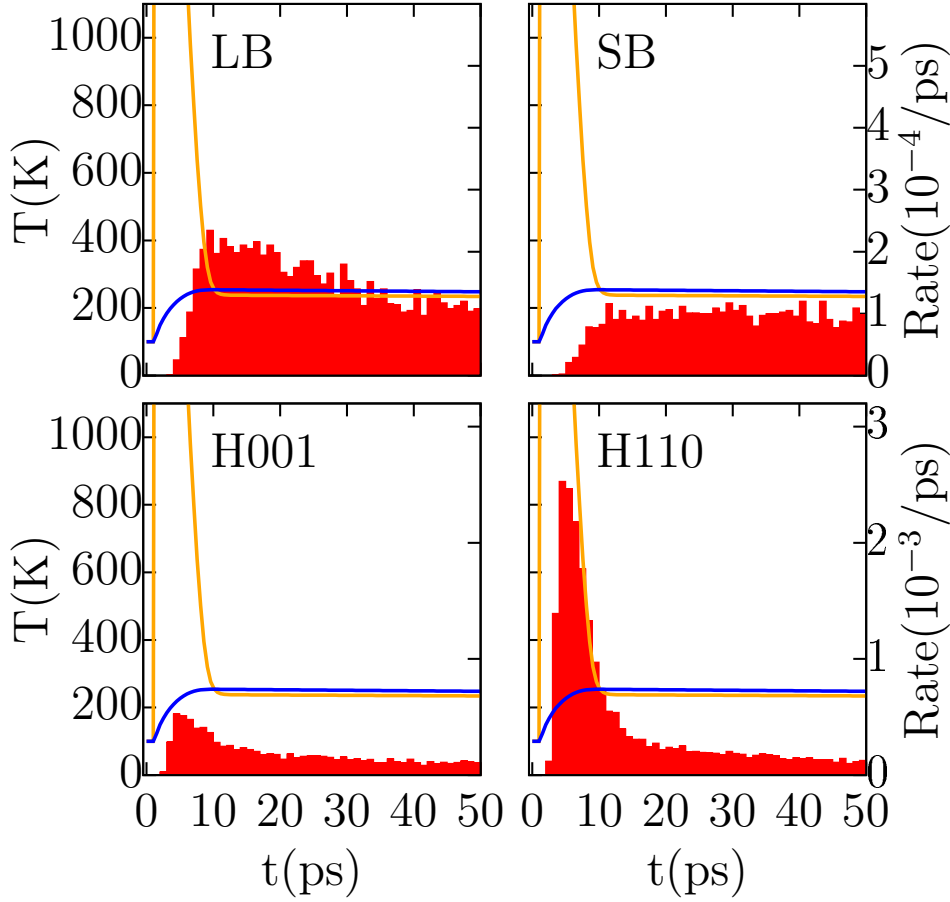
Figure 7.2: *Desorption rates as a function of time for $F = 200$ J/m² from the four adsorption sites (right ordinate). Note the different scales used for the bridge sites (upper panels) and the hollow sites (lower panels). Electron (orange line) and phonon (blue line) temperatures calculated from the 2TM are also shown (left ordinate). The electronic temperature peaks at values $T_{el} > 6000$ K (see Fig. 7.3). The histograms are obtained by counting desorption events in intervals of 1 ps.*

different laser fluences, using the three different models (LDFA, GLO, and LDFA+GLO), are given in Table 7.2. Additionally, the desorption rates for laser fluence $F = 200$ J/m² calculated with the LDFA and GLO models are shown in Figs. 7.3 and 7.4, respectively. The new LDFA and GLO results confirm the ideas inferred above. In the case of desorption from the hollow sites, the LDFA yields and rates are significantly larger than the GLO ones, while the opposite behavior is observed for desorption from the bridge wells although the differences between GLO and LDFA are smaller in these cases. Focusing on the LDFA cal-

Table 7.2: *Desorption yields from the four sites and for two different laser fluences calculated with the full model ($Y_{\mathrm{LDFA+GLO}}$), the model in which the surface is frozen (Y_{LDFA}), and the model in which electronic excitations are neglected (Y_{GLO}).*

$F = 100\,\mathrm{J/m^2}$				
model	LB	SB	H001	H110
$Y_{\mathrm{LDFA+GLO}}$	0.006	0.001	0.012	0.062
Y_{LDFA}	3×10^{-4}	6×10^{-5}	0.088	0.311
Y_{GLO}	0.007	7×10^{-4}	0.007	0.013

$F = 200\,\mathrm{J/m^2}$				
model	LB	SB	H001	H110
$Y_{\mathrm{LDFA+GLO}}$	0.104	0.064	0.136	0.325
Y_{LDFA}	0.023	0.011	0.369	0.740
Y_{GLO}	0.108	0.051	0.112	0.165

culations, it is clear that the desorption yields (Table 7.2) and rates for the bridge wells (Fig. 7.3) are reduced to marginal levels as compared to the ones obtained for the hollow sites. However, Fig. 7.4 and the GLO values in Table 7.2 show that the phonon-mediated contribution to desorption is rather similar among the four wells. In fact, the small differences we observe seem to be correlated with the differences in the adsorption energy. Thus, the lowest yield corresponds to the SB site, the one with the largest E_a, and the largest yield to the H110, the one with the lowest E_a. The intermediate cases represented by the LB and H001 sites, which have the same E_a, show very similar desorption yields. The absence of a similar one to one correspondence between E_a and the LDFA yields points to the electronic-mediated mechanism as the one responsible for removing that correlation in the LDFA+GLO yields, since in both cases the largest to lowest values for desorption follow the order H110, H001, LB, and SB. Yet, it remains to be understood what property (together with E_a) rules the efficiency of the electronic mechanism.

The electronic contribution to desorption is determined within the LDFA description by the value of the bare surface electron density at the position of each adsorbate (in our case the O atoms). The density profile along the plane normal to the surface that contains the molecule is shown in Fig. 7.5 for each of the adsorption configurations, together with the corresponding O atom positions. The inset
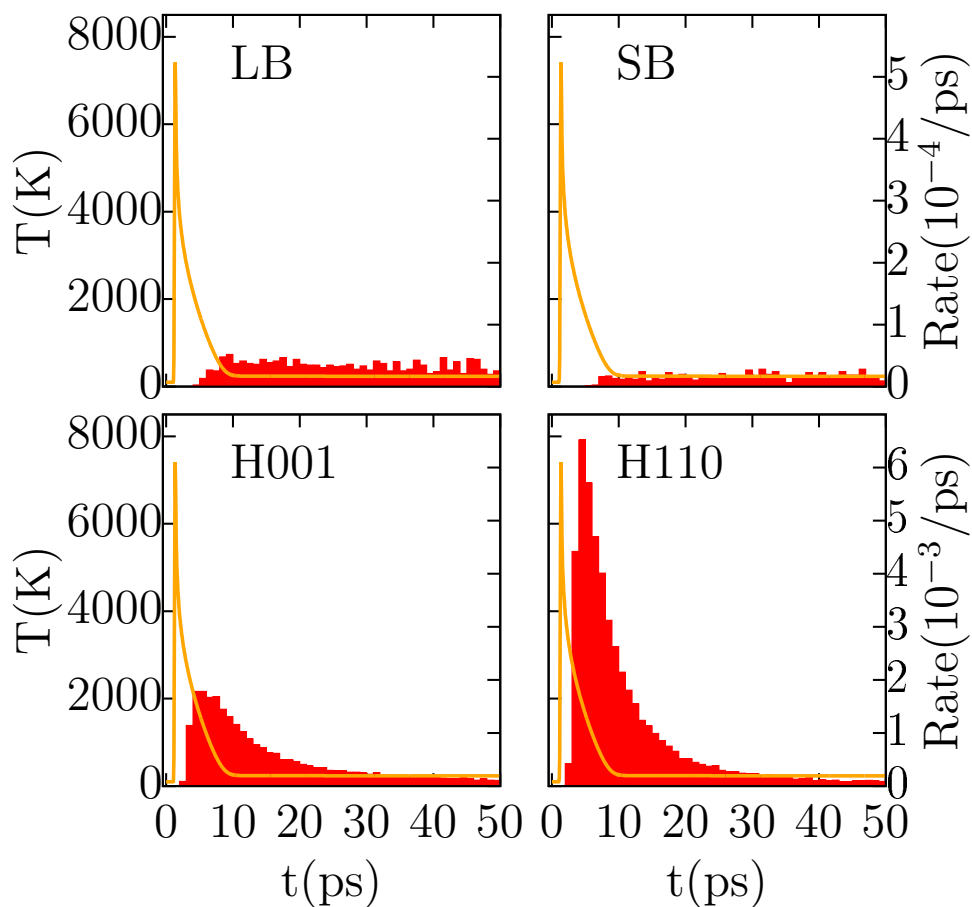
Figure 7.3: *Desorption rates as a function of time for F = 200 J/m^2 from the four adsorption sites calculated with the surface frozen (LDFA model) (right ordinate). Laser excitation of the surface is modelled only by the electronic temperature (orange line) given by the 2TM (left ordinate). Note the different scales used for the bridge sites (upper panels) and the hollow sites (lower panels).*

shows the friction coefficient of one O atom as a function of the electronic density. Clearly, the embedding electron density is higher when the molecule is adsorbed on the hollow wells than when it is adsorbed on the bridge wells (see also Table 7.1). This nicely fits with the results we have obtained. When T_{el} is high, the fluctuation forces acting on O$_2$ are correspondingly larger if the molecule is adsorbed on the hollow wells than if it is adsorbed on the bridge wells. Therefore, despite the similar adsorption energies of H001 and LB, desorption is more efficient from the former because of the larger embedding density.

Further insight regarding the competition between the electron- and phonon-
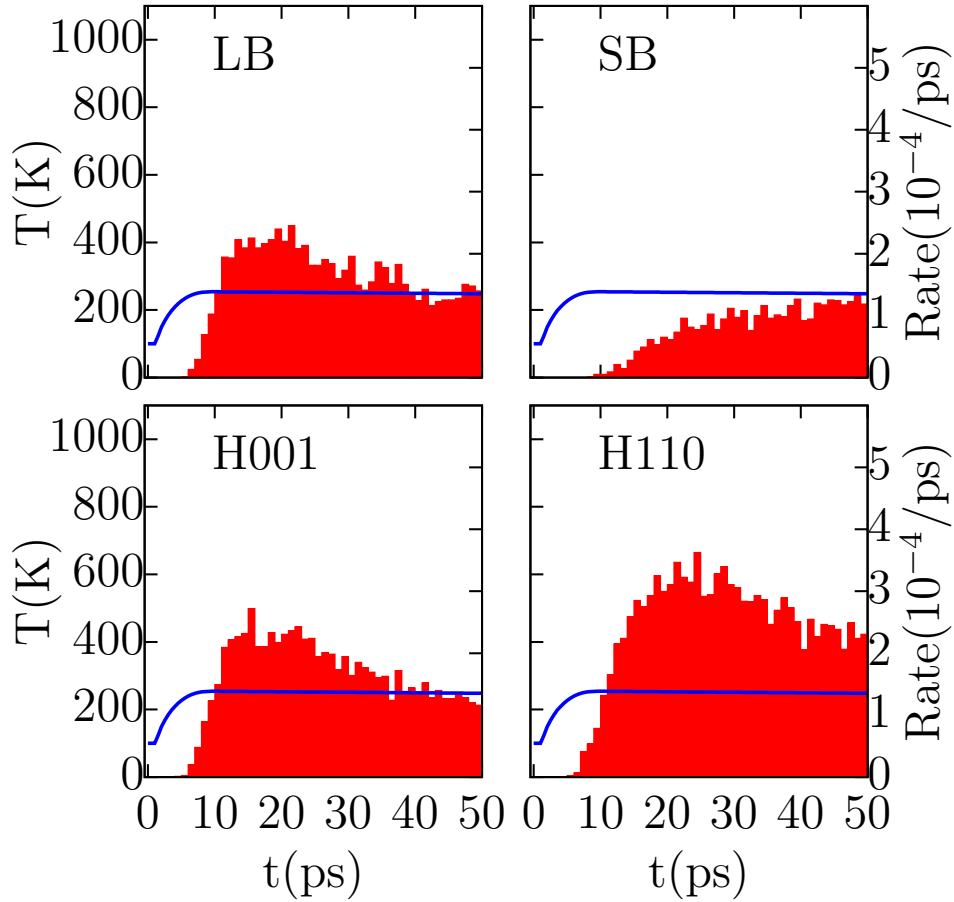
Figure 7.4: *Desorption rates as a function of time for $F = 200 \, J/m^2$ from the four adsorption sites calculated neglecting electronic excitations (GLO model) (right ordinate). Laser excitation of the surface is modelled only by the phonon temperature (blue line) as given by the 2TM (left ordinate).*

mediated mechanisms can be gained by comparing the LDFA and GLO results to those obtained with the LDFA+GLO simulations. First we observe that the LDFA model predicts larger yields for the electron-dominated desorption cases (H110, H001) than the LDFA+GLO. The reason is that the adsorbed O_2, being efficiently heated during the initial time interval in which T_{el} is high, reaches temperatures larger than T_{ph} at least during this period. Therefore, when surface motion is also included in the dynamics, the surface takes energy from the electronically heated molecule and the desorption probability is reduced in respect to the ideal case in which no surface motion is allowed. In the case of the GLO simulations, the yields are slightly larger than the LDFA+GLO ones for the LB site, suggesting
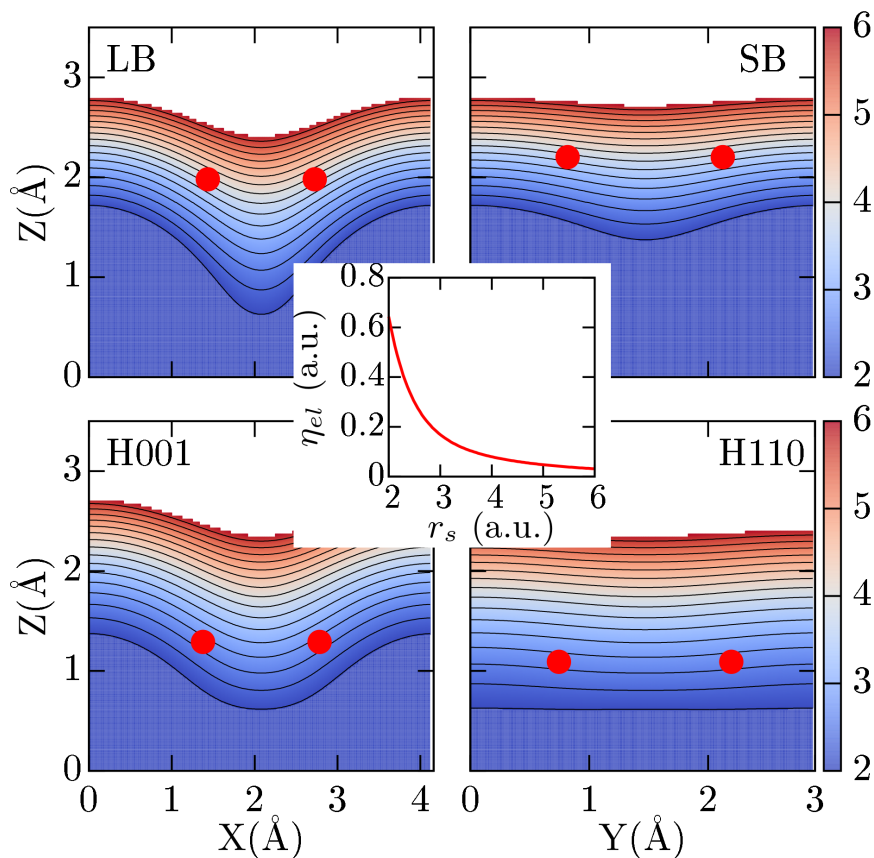
Figure 7.5: *Contour plot of electronic densities, expressed in terms of the mean free electron radius r_s, for the configurations of the four adsorption sites. Contour lines are separated by 0.25 a.u., in the range from 2 a.u. to 6 a.u. as shown by the color map. The positions of the oxygen atoms in the adsorption sites are shown with red dots. The inset shows the friction coefficient as a function of the electronic density given in terms of r_s.*

energy uptake by the electronic system, while for the SB well the LDFA+GLO yields almost coincide with the sum of the GLO and LDFA values.

7.3   Analysis of the desorbed molecules

In the following, we analyze the characteristics of the molecules desorbed from the different wells. The corresponding angular distributions of the desorbed molecules are shown in Fig. 7.6. These distributions are rather symmetrical around a desorbing angle of 45° relative to the surface normal for all the adsorption wells. Nevertheless, in the case of molecules desorbed from the H110 site a
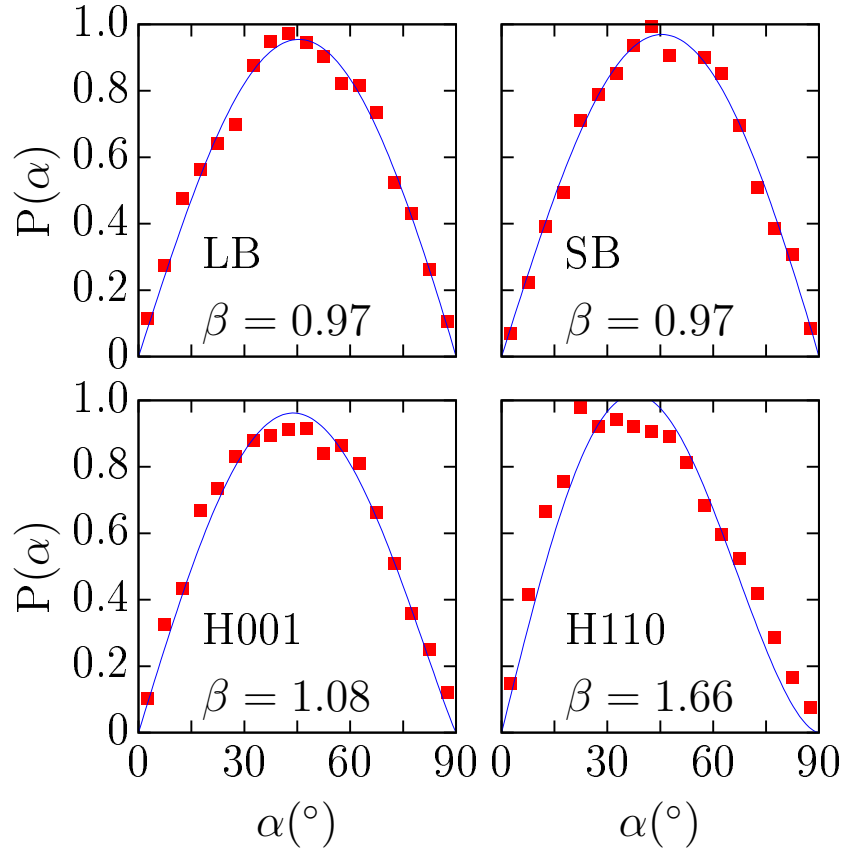
Figure 7.6: *Angular distribution of the molecules desorbed from the four adsorption wells for a laser fluence of $F = 200$ J/m^2. Red squares show the results of the dynamics. The blue line is obtained by fitting the data to the following function: $P(\alpha) = (\beta + 1)\sin\alpha\cos^\beta\alpha$.*

slight tendency to desorb into directions closer to the surface normal is observed. We fit the obtained angular distributionS to the velocity integrated flux-weighted Maxwell-Boltzmann distribution [230, 245] that gives $P(\alpha) = (\beta + 1)\sin\alpha\cos^\beta\alpha$. The parameter β is a measure of the alignment of the desorption flux. For large values of β the flux is aligned normal to the surface and the distribution is narrow, while $\beta = 1$ corresponds to a cosine distribution. As seen in Fig. 7.6, β is practically one for desorption from the H100, LB, and SB wells and it is somewhat larger than one for the H110 well. These (small) values contrast with the values $\beta \gtrsim 3$ obtained for the associative desorption of H$_2$ from Ru(0001) [230]. In that case, the deviation from the cosine distribution was explained by the presence of a late barrier towards desorption, causing a channelling effect and a narrow

angular distribution. However, in our case, the potential energy defining the molecule-surface interaction is monotonically increasing from the wells to the vacuum region (see Fig. 3.6), which results in $\beta \sim 1$.
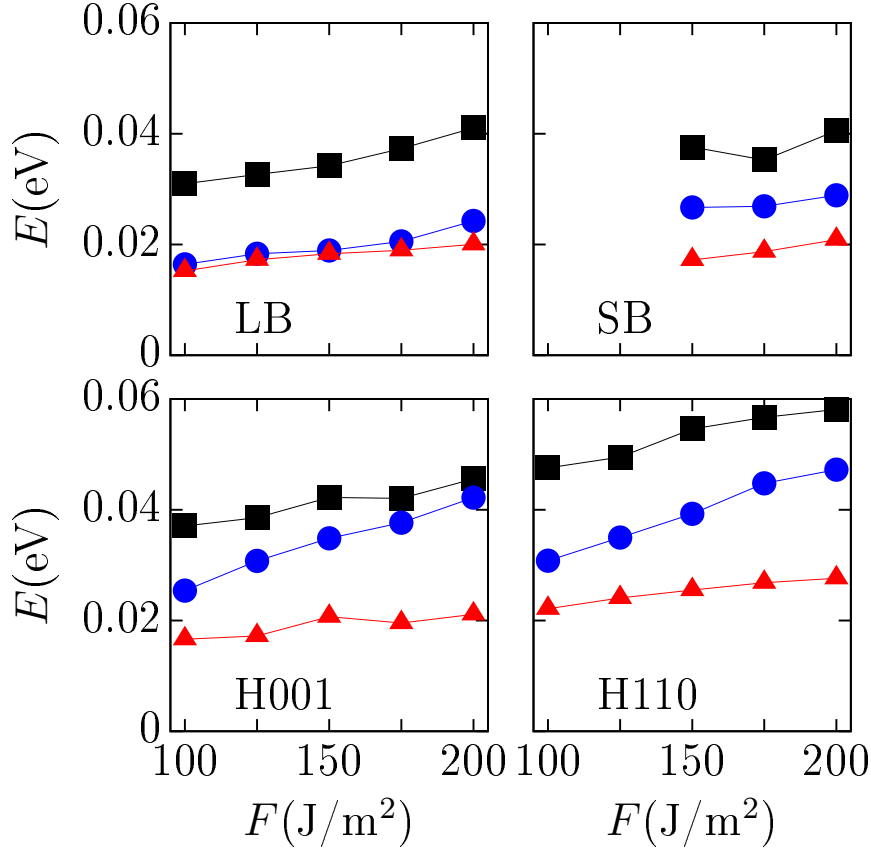
Figure 7.7: *Partition of the energy into translational (black squares), vibrational (blue circles), and rotational (red triangles) degrees of freedom of the molecules desorbed from the four wells as a the function of laser fluence F. Values for low fluences and SB well are not shown due to the poor statistics.*

Next, we analyze how the energy of the desorbing molecules are partitioned in translational and internal (vibrational and rotational) degrees of freedom. The dependence of the translational, vibrational, and rotational energies of the molecules desorbed from the four adsorption wells as a function of the laser fluence is shown in Fig. 7.7. Equipartition of energy between the different degrees of freedom of a free diatomic molecule means that the values of its translational, vibrational, and rotational energies are ordered according to the ratio 3 : 2 : 2 [246]. Figure 7.7 shows that only in the case of LB, where desorption is dominantly

phonon-mediated, the ideal thermal desorption is approximately fulfilled. Deviations from the ideal ratio are already observed for desorption from the SB well, which is also a phonon dominated process, and more clearly for H001 and H110 (both electron dominated). In these three cases, and for all the laser fluences, the translational energy is the largest and the rotational energy is the lowest. Within a good approximation, a linear increase with the laser fluence of the vibrational and translational energies of the desorbed molecules is observed. This is considered to be one of the hallmarks of DIMET [226].

Finally, it is worth noting that we also observe few dissociation events for molecules initially adsorbed in the H110 well. This is a very unlikely process that has only been observed at the highest fluences ($F > 175$ J/m^2) and with probabilities lower than 10^{-4}. In these conditions it is not possible to perform a more detailed analysis of the process. Still, the occurrence of dissociation events is an interesting result considering that the energy barrier from the bottom of the well to dissociation is 0.57 eV, significantly larger than the well depth of -0.21 eV.

7.4 Tuning desorption by modifying laser and surface properties

When studying laser induced desorption, given a molecule/surface system, only the initial surface temperature and the laser pulse parameters remain to be chosen (at least in the model presented above). The laser pulse parameters are: fluence, pulse width, and wavelength. The dependence of laser induced desorption on laser fluence is discussed above and in this section we study the influence of the other quantities that one can control, starting with the initial surface temperature.

Solutions of the 2TM for two different initial surface temperatures, $T_i = 50$ K and $T_i = 100$ K, are shown in Fig. 7.8. Clearly, the difference of 50 K in T_i causes a similar difference of around 50 K in the equilibrated temperatures (both T_{el} and T_{ph}), which are achieved after ~ 10 ps. However, the maximum of T_{el}, which is achieved in the wake of the laser pulse, is much reduced for the lower T_i (see the inset in Fig. 7.8). A reduction of T_i from 100 K to 50 K produces a reduction of the maximum of T_{el} that amounts to around 800 K (from 6300 K to 5500 K). In the following, we study how this influences the desorption yield.

Figure 7.9 shows that the desorption yield monotonically increases with increasing T_i. This is not surprising since, as we have already shown, increasing T_i
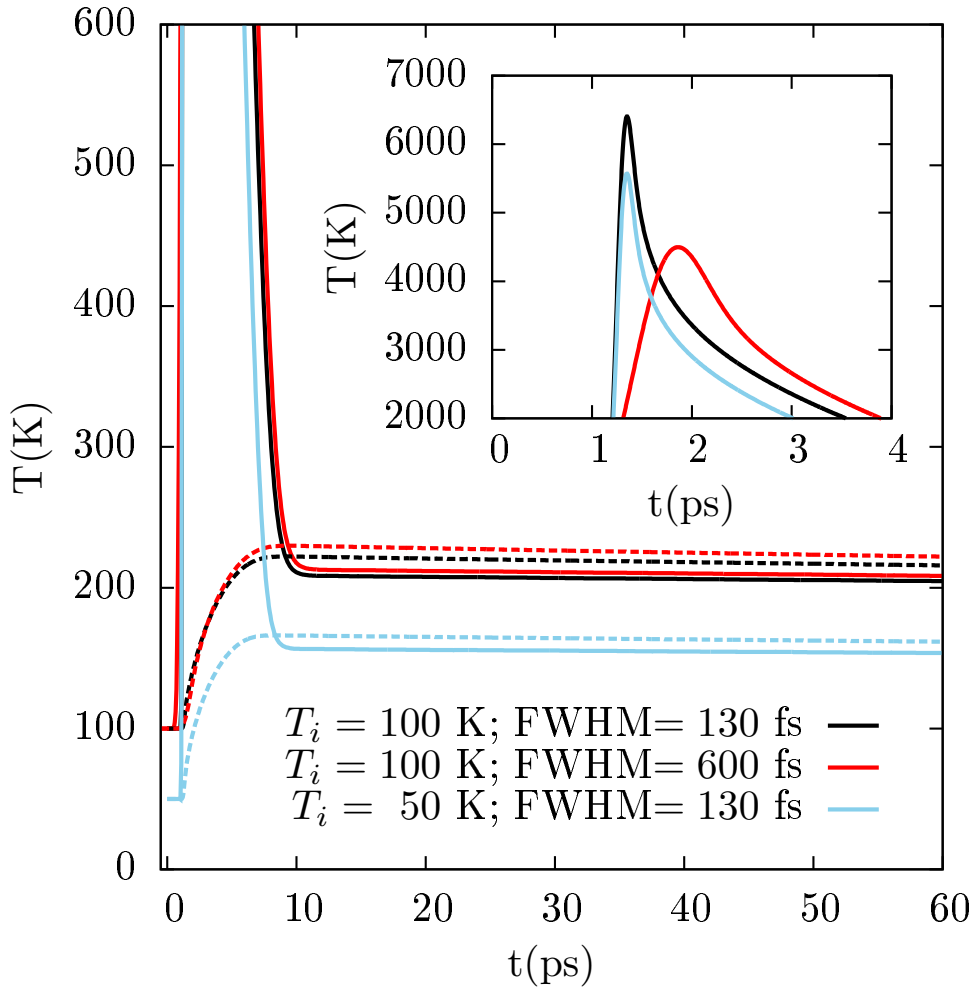
Figure 7.8: *Electronic (solid line) and phonon (dashed line) temperatures as a function of time calculated within the 2TM for different initial surface temperatures T_i and laser pulse widths (given as FWHM) with absorbed laser fluence $F = 150\,J/m^2$. Inset: detailed view of the maxima reached by T_{el} in each case.*

results in higher T_{el} and T_{ph}. For high initial surface temperatures, the desorption yield approaches 1 for all adsorption wells. The reason is that in the high initial surface temperature range, phonon temperatures are high enough to desorb all the molecules without any influence of the electronically mediated mechanism.

At low T_i, one could try to understand the rapid increase of the desorption yield with T_i using an Arrhenius-type expression [230, 247]. In the equilibrated regime ($t > 10$ ps in Fig. 7.8), the molecule is expected to be well thermalized with the surface at temperature T_{ph}. Since for the short bridge well desorp-

Figure 7.9: *Desorption yield (ordinate in logarithmic scale) from the four wells (represented by different symbols and colors) as a function of the initial surface temperature T_i. In all cases FWHM = 130 fs and F = 150 J/m^2. The inset shows the same data at $T_i <$ 200 K, plotted as a function of the inverse of the initial surface temperature T_i increased by 110 K and a corresponding linear fit.*

tion is almost purely phonon mediated, one may expect that the corresponding desorption rate at low T_i can be approximated by the Arrhenius expression $\sim \exp\left[-E_a / k_B T_{ph}(t)\right]$. As shown in Fig. 7.8, the equilibrated T_{ph} is around 110 K higher than T_i and it is almost constant with time (T_{ph} reduces only 3 K in the time period from 25 ps to 50 ps due to the diffusion term). This allows us to write the Arrhenius expression as $\sim \exp\left[-E_a / k_B (T_i + 110 \text{ K})\right]$. As this expression does not depend on time it is directly proportional to the desorption yield at low T_i. Indeed, the inset in Fig. 7.9 shows that the desorption yield increases exponentially with the negative inverse of $(T_i + 110$ K$)$. We fit the data for the desorption yield Y with the expression $Y = b \exp\left[-E_{\text{eff}} / k_B (T_i + 110 \text{ K})\right]$. Such a fit describes the data relatively good for all the wells with a very good fit obtained for the SB well.

Fitting to the data for $T_i < 100$ K gives: $E_{\text{eff}}(\text{SB}) = 0.25$ eV, $E_{\text{eff}}(\text{LB}) = 0.16$ eV, $E_{\text{eff}}(\text{H001}) = 0.11$ eV, and $E_{\text{eff}}(\text{H110}) = 0.07$ eV. The obtained values for E_{eff} are reasonable in comparison to E_a (see Table 7.1) for the bridge wells, especially for the SB well. Somewhat smaller E_{eff} in comparison to E_a is expected as in the dynamics most of the time molecules are not residing at the bottom of the well. For the hollow wells the poor agreement between E_{eff} and E_a is because T_{el} plays an important role for these wells. Since the dependence of T_{el} on T_i is more involved it is not straightforward to explain the observed exponential dependence of the desorption yield on T_i with the present simplified model.

It is interesting to look more closely at the H001 and LB wells, as they have the same adsorption energy but different dominant desorption mechanisms, electronic and phonon, respectively. Desorption from H001 is consistently higher. However, the ratio of the desorption yields is decreasing from $Y_{\text{H001}}/Y_{\text{LB}} = 3$ at $T_i = 50$ K to $Y_{\text{H001}}/Y_{\text{LB}} = 1$ at $T_i \geq 200$ K. This leads to the conclusion that if electronically mediated desorption is desired, it is necessary to have a low T_i.

The effect of the laser pulse FWHM on T_{el} and T_{ph} is also shown in Fig. 7.8. In the long time regime, when the temperatures are equilibrated, we observe that T_{el} and T_{ph} are only slightly modified by varying the FWHM. In fact, when the FWHM is increased from 130 fs to 600 fs, the change in the equilibrated temperatures amounts to just ≈ 5 K. This effect is, therefore, much less pronounced than the one we observed when varying T_i. However, we observe that when the FWHM is increased from 130 fs to 600 fs, the T_{el} curve broadens and the maximum value is reduced by ≈ 2000 K.

The way these changes in T_{el} affect the desorption yields is shown in Fig. 7.10. As in previous cases, the largest desorption yields are obtained from H110, the well with the lowest adsorption energy, followed by H001, LB, and SB. There is a slight increase of the desorption yield values with increasing the FWHM. In case of the bridge wells, for which desorption is dominated by phonons, this can be easily understood due to the small increase of the equilibrated T_{ph} with the FWHM. However, it is not straightforward to understand the observed behaviour in case of the hollow wells for which the electronic mechanism dominates, due to the more complicated behaviour of T_{el}. On the one hand, since increase of the FWHM results in somewhat larger equilibrated temperatures, it is expected that this increase has a positive contribution to the part of desorption induced by phonons, as in the case of the bridge wells. On the other hand, just from desorption yields, it is not clear what the contribution of the electronic channel is,

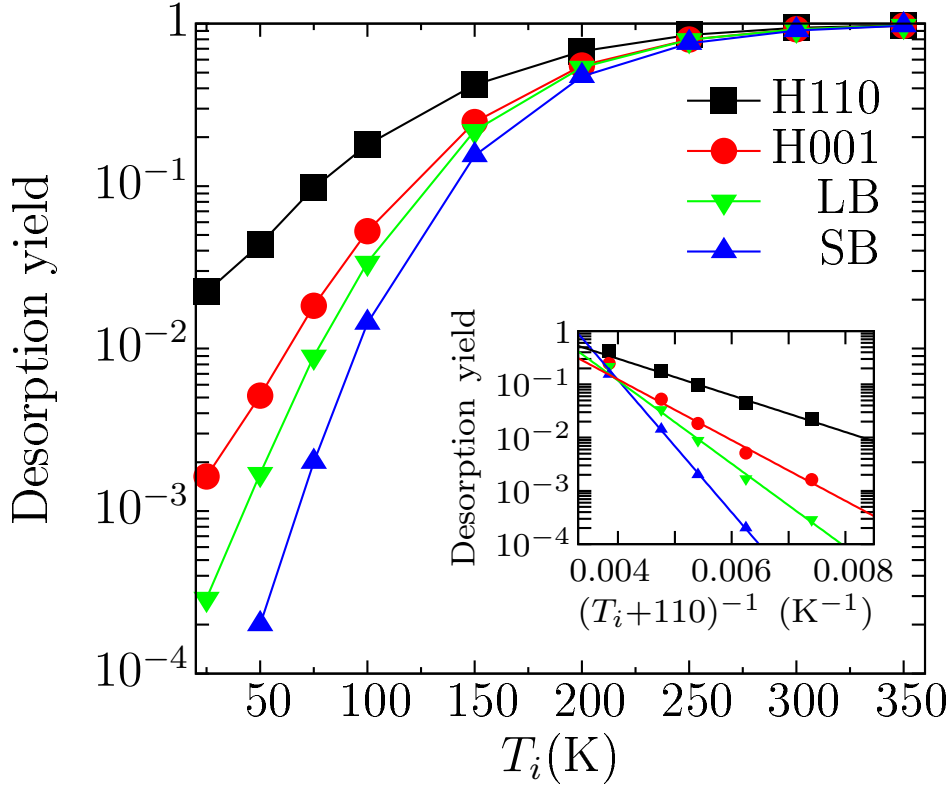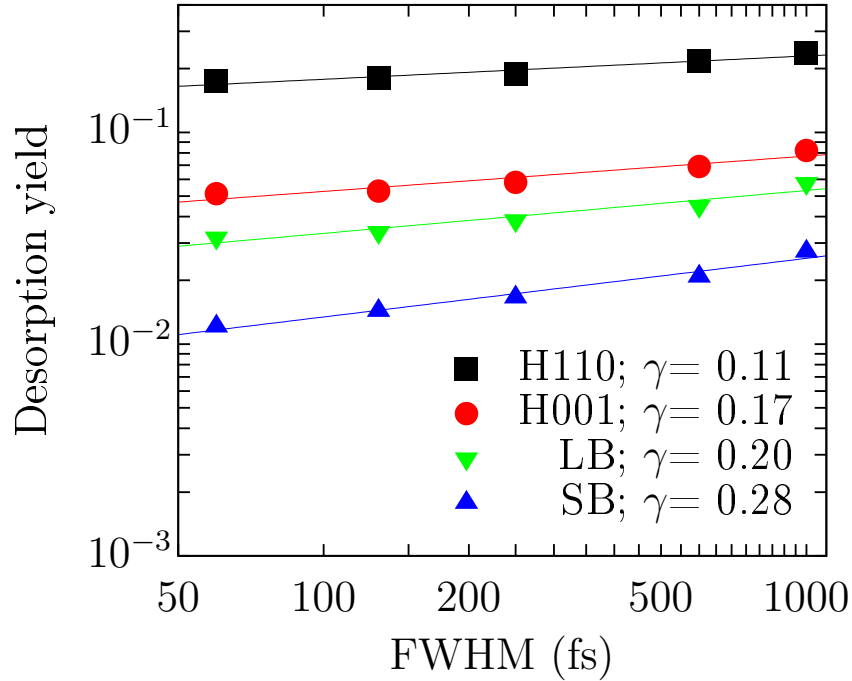**Figure 7.10:** *Desorption yield from the four wells (represented by different symbols and colors) as a function of the laser pulse FWHM (log-log scale). Data are fitted with a function $Y = c \, \text{FWHM}^{\gamma}$. In all cases $T_i = 100$ K and $F = 150$ J/m^2.*

as the peak maximum of T_{el} is considerably reduced, but the peak is broadened.

To gain a better insight on this issue we plot in Fig. 7.11 the desorption rates as a function of time, for two different laser pulse FWHMs. For the bridge wells, as expected, the desorption rates increase with the FWHM due to the larger phonon temperatures in the equilibrated regime. Interestingly, electron mediated desorption from the hollow wells in the wake of the laser pulse is also increased. This shows that in order to promote desorption via the electronic mechanism (under the studied conditions) larger desorption is obtained by increasing the time interval in which T_{el} is high than by increasing the maximum value of T_{el}.

As shown in Fig. 7.10, the increase of the desorption yields with the laser pulse FWHM can be also fitted with a power law in which exponents are smaller than 1. This contrasts with the power law that describes the dependence on laser fluence in which exponents are larger than 1. The values of exponents range from $\gamma = 0.11$ for the H110 well to $\gamma = 0.28$ for the SB well, which approximately correspond to the 10-th and the 4-th root of the FWHM, respectively. The ratio
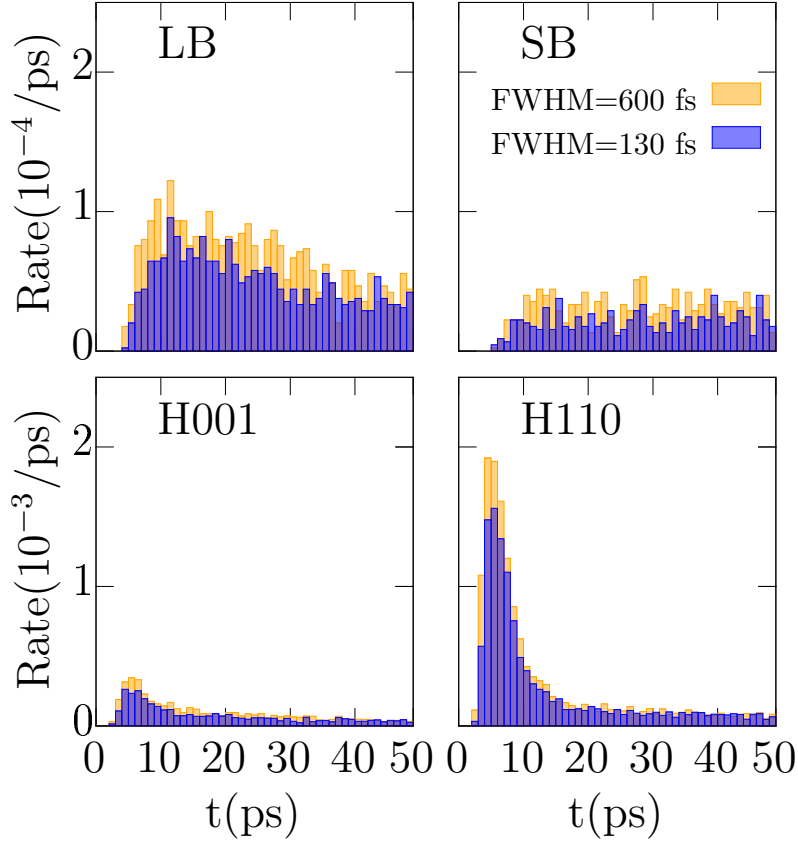
Figure 7.11: *Desorption rates from the four wells for two different laser pulse widths, FWHM = 600 fs (orange boxes) and FWHM = 130 fs (blue boxes). Note the different scales in upper and lower panels. In all cases F = 150 J/m^2 and T$_i$ = 100 K.*

between desorption yields from different wells does not significantly depend on the FWHM. This means, that tuning of the FWHM can not be used to favour either electron or phonon mediated processes, at least in the range of FWHM = 60 − 1000 fs that is explored here.

Finally, we discuss the effect of the laser wavelength λ, which enters Eq. (2.49) through the optical penetration depth $\alpha^{-1} = \lambda/(4\pi k)$, where k is the imaginary part of the refractive index (also called extinction coefficient) of the surface. For wavelengths $\lambda > 360$ nm, the extinction coefficient k of Ag increases linearly with λ [248, 249], so that α^{-1} remains constant, resulting in the same T_{el} and T_{ph}, and consequently, the same desorption dynamics. All the results presented above correspond to this range of λ. Practically the same value of α^{-1} is also obtained for UV light with $\lambda < 260$ nm. Additionally, since silver is much less reflective at

this low wavelengths, in experimental realizations larger absorbed fluences *F* can be obtained. The optical penetration depth is a few times larger for wavelengths around $\lambda = 320$ nm due to a dip in k associated with the plasma frequency of silver. However, we have checked that even in these cases the results do not change considerably.

7.5 Summary

In summary, we have extended the approach of Ref. [230] to simulate the multidimensional dynamics of a molecule adsorbed on a metal surface excited by an ultrashort laser pulse by including surface movement (phonons) via the GLO model. This allows us to treat simultaneously the laser induced electron and phonon excitations and their effect on the dynamics of the eventually desorbing molecule.

Using this new approach we have studied the laser induced desorption of O_2 from Ag(110). An interesting feature of this system is that it possesses four distinct molecular adsorption wells. This enables us to study how the desorption mechanisms are connected to the properties of the adsorption configuration. In general, we find that the effect of the laser-heated phonons in this system cannot be disregarded. Importantly, the phonon contribution to the desorption yield can be either positive or negative depending on the adsorption site. More precisely, when the molecule is initially adsorbed on the bridge sites inclusion of phonons increases the desorption probability. In fact, for these sites, coupling of the molecule to the phonon excitations constitutes the main desorption mechanism. However, for molecules adsorbed on the hollow sites not only the electronic channel is the dominant mechanism, but inclusion of phonons reduces the desorption probabilities because they take energy from the excited molecule. The subsequent reductions of the desorption yields can be rather high, in the range of a factor $2 - 7$, depending on the laser fluence. These observations are rationalized in terms of the distances from the surface at which the adsorption sites are located and the subsequent values of the electronic density in their surroundings. Hollow sites are closer to the surface than bridge sites and, consequently, in regions of higher electronic density. For this reason the electron channel dominates desorption in the former and the phonon channel in the latter.

Our results also suggest which desorption mechanism will be dominant in

systems that present both physisorbed and chemisorbed species. Since physisorbed molecules are located in low electronic density regions their desorption behavior is expected to be similar to the one we obtain for the bridge sites, whereas for chemisorbed states our findings for hollow sites apply.

We have shown that the initial surface temperature is an important parameter that greatly affects the desorption yields. The largest ratios of the desorption yields among the four wells are obtained for low initial surface temperatures. At high initial surface temperatures desorption yields from the four wells (and the ratios of desorption yields among them) saturate to one as all molecules become desorbed. As the desorption from the hollow wells, which is electronically induced, is always higher than the desorption from bridge wells, low initial surface temperatures can be used to favour the electronically induced process.

We have also shown that the effect of changing the laser pulse width or wavelength has only a modest influence on desorption. In general, desorption from the four wells increases as m-th root of the laser pulse width, with $m = 4 - 10$. However, this does not result in a significant change in the desorption yield ratios among the four wells.

8

Scattering and sticking dynamics of CO on Ru(0001)

8.1 Introduction

Besides O_2/Ag, one of the most studied gas-surface systems is the interaction of CO with different transition metal surfaces. The scientific interest for such system arises from its relative simplicity and technological importance; *e.g.* two important reactions are the catalytic oxidation of CO (important for automotive exhaust catalytic converters) and the Fischer-Tropsch process. In this chapter the interaction of CO with ruthenium will be addressed, a metal which is known to be the most efficient catalyst for the latter reaction [5]. Due to this, it was used in several experimental studies (see Refs. [250–261]). In general, it is well established that CO bonds to the Ru(0001) surface on a top site in upright position with the C atom down and with a chemisorption energy of 1.65 eV [262–264].

Molecular beam studies of the CO/Ru(0001) system have been performed in Refs. [23–25, 265]. These experiments showed that for low incidence beam energies the sticking probabilities are close to unity, but consistently lower than this value. With increasing incidence energies the sticking probabilities decrease slowly. The dependence of the sticking probability on surface temperature in the range $T = 85$–390 K is measured to be very small. These results are consistent with a deep chemisorption well accessible from vacuum without an energy barrier.

Similar, high sticking probabilities (but lower than unity) that slowly decrease with incidence energy and are independent of the surface temperature were observed for other transition metal surfaces: Ir(110) [266], Ni(100) [267], Ni(111) [268], Pt(111) [269], and Pd(111) [270].

Molecular beam measurements of scattering angle and energy loss distributions of CO molecules scattered from Ru(0001) showed surprising results [25].

The measured angular distribution width is too narrow for a system with a deep chemisorption well. For these systems one would expect a broad angular distribution as molecules are deflected toward the surface and scattered from a corrugated potential [271].

The aim of this chapter is to theoretically reproduce the results of the molecular beam experiments and thus provide its microscopical elucidation. In particular, it is important to explain how in spite of the presence of a deep chemisorption well the angular distributions are so narrow and also, why the sticking probabilities, although close to unity, are still noticeably lower than it (the differences being of the order of 5%). The latter fact is also unexpected since with a chemisorption well of 1.65 eV one would expect that molecules with low initial kinetic energies (of 0.1 eV) once accelerated by the well would transfer large portion of its normal kinetic energy to the surface atoms and internal degrees of freedom. As a result, after the collision the remaining normal kinetic energy would be lower than the desorption barrier and all molecules would stick to the surface.

We will show that this aim can be fulfilled by simulating the experiments with molecular dynamics calculations performed on a recently developed six-dimensional (6D) potential energy surface (PES) [272]. The PES is based on density functional theory (DFT) calculations using the RPBE functional [48] with D2 dispersion corrections [61]. Although for Ru the well-known CO adsorption site puzzle [273–275] is not that significant, inclusion of the van der Waals correction gives a good adsorption energy (1.69 eV) compared to experiments (1.65 eV), thus it improves the description of the energetics in comparison to the pure RPBE (1.43 eV) [272]. We will also discuss the relative importance of the energy loss of the molecule to excitations of surface phonons and low energy electron-hole pairs.

The rest of the chapter is organized as follows: In Sec. 8.2 we describe the methods we use. Results and their discussion concerning the sticking probabilities are presented in Sec. 8.3. Results for the scattering angle and energy loss distributions are discussed in Sec. 8.4. In Sec. 8.5 we discuss the vibrational deexcitation of vibrationally excited molecules upon collision with the surface. Finally, Sec. 8.6 concludes and summarizes the chapter.

8.2 Methods

To simulate the above mentioned molecular beam experiments [23–25, 265] we perform (quasi-)classical trajectory calculations (see Ch. 2.4). The interaction of CO with Ru(0001) is described by the recently constructed 6D PES [272] that is further improved as described in Ref. [32]. Next we give a brief description of the PES, while the full details can be found in Refs. [32, 272].

8.2.1 The potential energy surface

The PES is obtained via a CRP interpolation [83] of 80 000 van der Waals corrected semi-local DFT energies. These energies correspond to a grid that contains different molecular orientations and positions over the 2×2 Ru unit cell (see Fig. 8.1). The grid is composed of six irreducible lateral (X, Y) symmetrical positions on
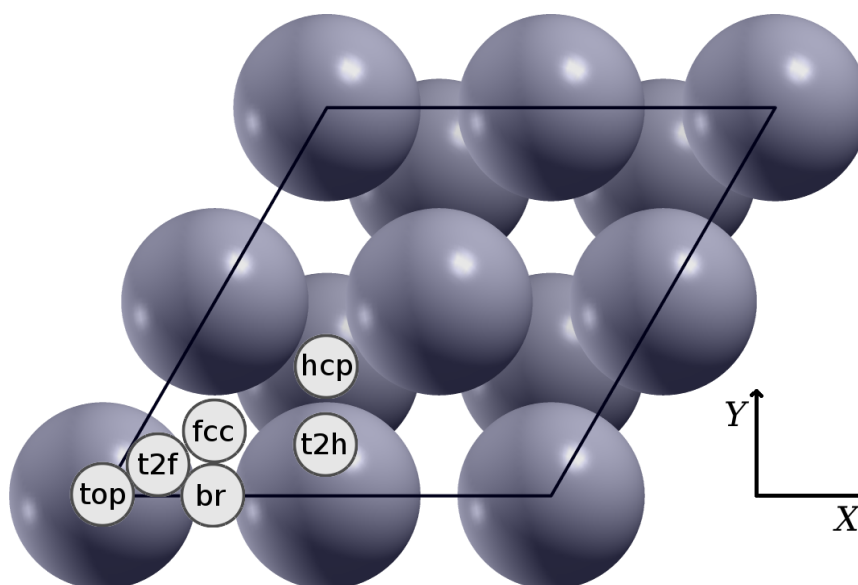
Figure 8.1: 2×2 *Ru(0001) unit cell that is used in the construction of the 6D PES. Labels inside the circles mark the six irreducible sites on the surface that compose the lateral (X, Y) grid: top, bridge (br), fcc, hcp, between top and fcc (t2f), and between top and hcp (t2h).*

the surface as shown in Fig. 8.1. For each of these (X, Y) positions, molecular orientations (θ, φ) are sampled in grid spacings of $\Delta\theta = \Delta\phi = \pi/6$. The coordinate system is chosen such that θ is the angle between the surface normal and

the molecular axis, and $\theta = 0°$ corresponds to the C atom pointing to the surface (C-down orientation). φ is the angle between the projection of the molecular axis to the surface plane and the X axis (see Fig. 8.1). For each (X, Y, θ, φ) position and orientation, 2D (r, Z) cuts are sampled with a 17×29 grid of points that span $r \in [0.725, 2.725]$ Å and $Z \in [0.9, 5.1]$ Å intervals.

DFT calculations are performed using the plane wave basis set VASP code [170, 171]. Standard projector-augmented wave (PAW) pseudopotentials are used and a kinetic energy cutoff of 400 eV is employed. The Brillouin zone is sampled by a $9 \times 9 \times 1$ Γ-centered Monkhorst-Pack grid of **k**-points. The gradient-corrected RPBE functional [48] is used together with Grimme D2 dispersion corrections [61] which are applied only to the molecule and first layer Ru atoms, as suggested in Ref. [276].

In Fig. 8.2 we show three 2D cuts of the 6D PES at the top site of the surface for different angles between the molecular axis and the surface θ. Left panel of
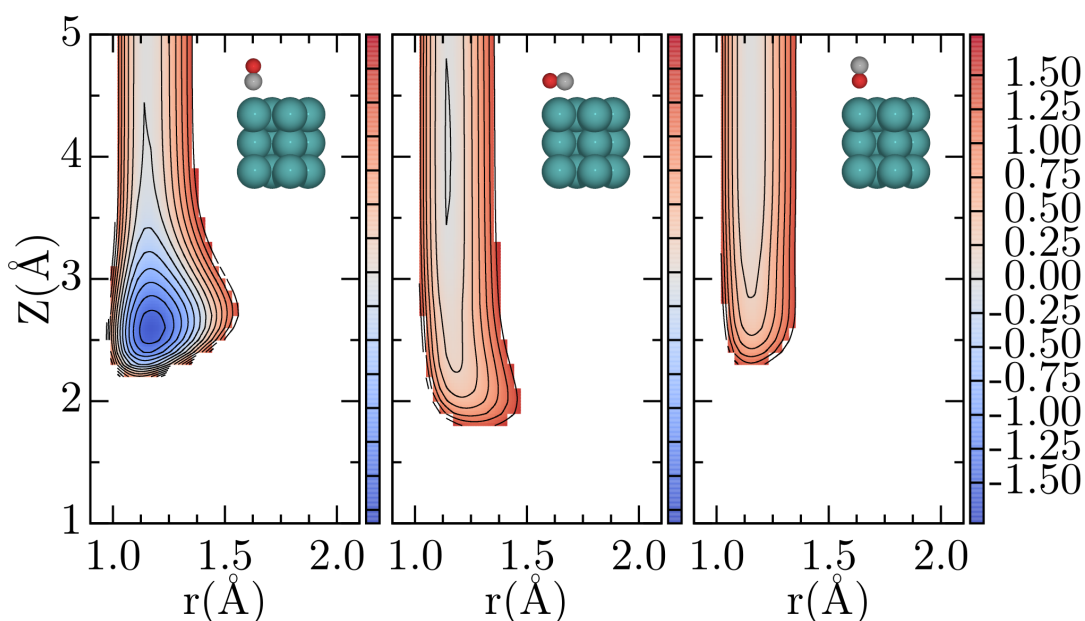
Figure 8.2: *2D (r, Z) cuts of the CO/Ru(0001) 6D PES over the top site of the surface for three orientations of the molecule: C-down ($\theta = 0°$), parallel to the surface ($\theta = 90°$, $\varphi = 0°$), and O-down ($\theta = 180°$). Contours are separated by 0.25 eV and their values are given on the color bar. Left panel shows the chemisorption well with the adsorption energy of 1.69 eV.*

Fig. 8.2 shows the chemisorption well in which the molecule is in upright position on top of a Ru atom with the C atom down. The distance between the center of

mass of the molecule and the surface is $Z = 2.59$ Å, the interatomic distance is $r = 1.17$ Å, and the chemisorption energy is 1.69 eV. In the middle and right panels of the figure it can be seen that the PES is almost purely repulsive for the parallel to the surface and O-down configurations.

8.2.2 Computational details

In addition to the adiabatic force given by the 6D PES, our simulations also include energy loss of the molecule to the surface phonons and to the low energy electron-hole pair excitations. This is achieved by using the same theoretical approach as it was previously used in Ch. 7.

In this approach the energy loss of the molecule to surface movement as well as surface temperature effects are described using the generalized Langevin oscillator model (GLO) [103, 104, 106]. Keeping the notation as before we use $\omega_x = \omega_y = 8.45 \times 10^{-4}$ a.u. (atomic units) and $\omega_z = 7.35 \times 10^{-4}$ a.u. for the Ru(0001) oscillator frequencies [277]. The coefficient η_{ph} (see Ch. 2.4.2) is obtained from the Debye temperature of Ru $T_D = 555$ K.

Energy dissipation to electron-hole pair excitations is modelled by a friction force proportional to the velocity of each atom in the molecule (so called molecular dynamics with electronic friction - MDEF) as explained in Ch. 2.4.3. In MDEF simulations of CO/Ru(0001) we use the following analytical expressions for the friction coefficients η_{el}

$$\eta_{el}(r_s) = 3.83407 r_s^{-2.58871} e^{0.155048 r_s}, \qquad (8.1)$$

for the C atom, and

$$\eta_{el}(r_s) = 5.07895 r_s^{3.73291} e^{0.251941 r_s}, \qquad (8.2)$$

for the O atom (both η_{el} and r_s are in a.u.). These expressions fit the calculations of Ref. [278].

From a theoretical point of view it is interesting to analyse the impact on the dynamics of either surface movement or electronic friction separately. Due to this, we consider the following models. The full model that includes both phonon and electronic energy loss channels is denoted MDEF-GLO. The model in which only the phonon energy loss channel is included is denoted MD-GLO. The model in which only the electronic energy loss channel is included is denoted MDEF. Finally, the model that does not include energy loss channels (constant energy calculation) is denoted MD.

In line with previous chapters, the initial conditions are chosen such that at the start of each trajectory calculation the center of mass (CM) of the molecule is positioned at $Z_i = 7$ Å above the surface. At this distance, by construction of the PES, there is no interaction of the molecule and the surface. The initial momentum of the molecular CM is calculated according to a given initial incidence energy E_i and incidence polar angle Θ_i. The initial lateral positions of the molecular CM (X_i, Y_i) in the unit cell are sampled by a conventional Monte-Carlo procedure. Unless otherwise stated, the orientation of the molecular axis (θ_i, φ_i) is chosen according to a random sampling of the solid angle. Most of our results are obtained within the so-called quasi-classical trajectory calculations. As explained in Ch. 2.4.1, in these calculations the vibrational energy of the molecule E_0 is the one corresponding to its zero point energy. The vibrational levels E_v of the molecule are obtained by solving the radial Schrödinger equation for the potential energy $E(r)$ of the molecule in vacuum. The initial interatomic distances r_i and the corresponding momenta are sampled by a classical microcanonical distribution such that they correspond to E_0. Similarly one can also simulate molecules that are initially in vibrationally excited states $v > 0$. For testing purposes we also performed classical trajectory calculations in which the molecule initially rests at the bottom of the radial potential energy $E(r)$.

Equations of motion are integrated using the Velocity-Verlet based Ermak-Buckholtz algorithm [279] with a time step of 0.05 fs that ensures stable integration. To obtain sticking probabilities with a monochromatic beam we calculate at least 5000 trajectories for each incidence condition. In order to obtain scattering distributions we perform 500 000 trajectory calculations for each incidence condition. In the case of beams with a distribution of energies we have calculated at least 10^6 trajectories.

8.3 Sticking probabilities

8.3.1 Experiments vs theory

Figure 8.3 shows the initial sticking probability S_0 as a function of the molecule incidence energy E_i calculated with the MDEF-GLO model (monochromatic beam) for two surface temperatures T. These results are compared with the results of molecular beam experiments of Kneitz *et al.* [23, 24] and Riedmüller *et al.* [25]. In both experiments sticking probabilities were determined by the method of King
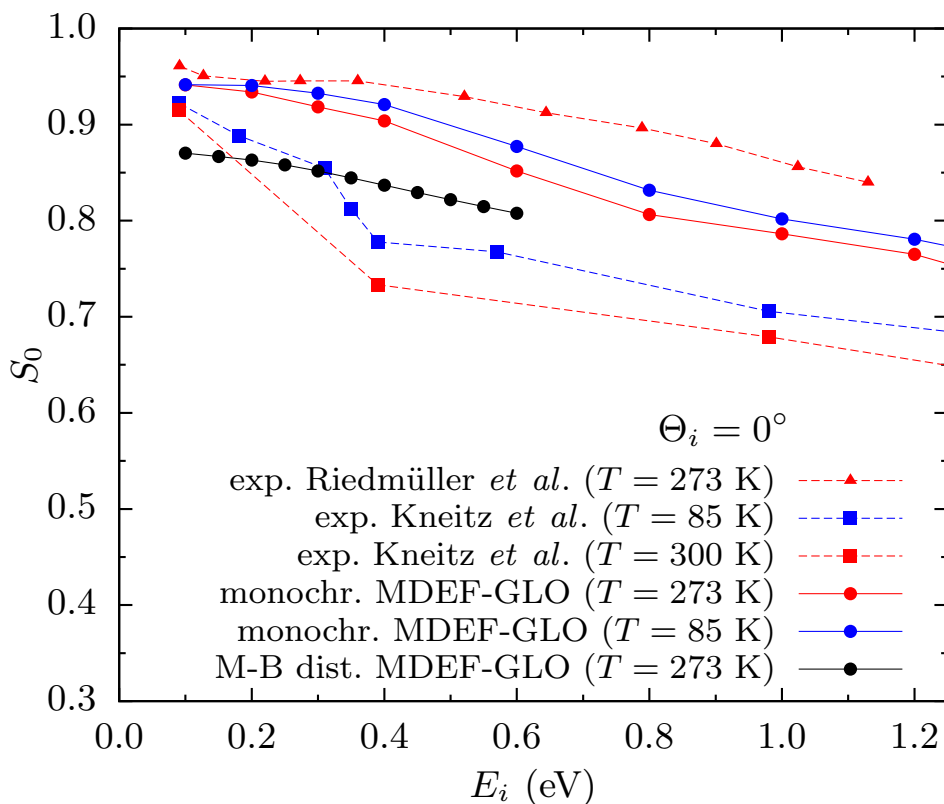
Figure 8.3: *Calculated sticking probabilities with a monochromatic beam (solid lines and circles) compared to the experimental results (dashed lines) of Kneitz et al. [23] (squares) and Riedmüller et al. [25] (triangles). Values for the lower temperature T = 85 K are in blue and values for the higher temperature T = 273-300 K are in red. Black line corresponds to a beam with molecule energies distributed according to a M-B distribution.*

and Wells that is known to give accurate sticking probabilities. Qualitatively and partly quantitatively our calculations and both experiments agree. Quantitative agreement is obtained for low E_i for which the sticking probability reaches almost unity thought it is clearly below it. With increasing E_i our results and both experiments show slowly decreasing sticking probabilities, however, quantitative differences are apparent. Our results lie between the two experimental results (see red lines in Fig. 8.3), somewhat closer to the ones of Riedmüller *et al.* [25] that give sticking probabilities that are consistently larger than our theoretical ones. As both experiments use similar techniques and there was only a short time between the publications we can not determine superiority of either experiment.

As can be seen in Fig. 8.3, the sticking probability depends only slightly on the

surface temperature (compare red and blue lines). The small decrease of S_0 with T is similar in both our calculations and the results of Kneitz *et al.* [23]. In an earlier work, Pfnür and Menzel came to the same conclusion [265]. As mentioned in Sec. 8.1, the small dependence of the sticking probability on T was also observed for other CO/transition metal systems [266, 267]. This behaviour is attributed to the non-existence of a precursor state in the adsorption process. If the precursor state existed, one would expect that desorption from this state would compete with conversion to the chemisorbed state, a mechanism that would strongly depend on the surface temperature. In our PES such precursor state does not exist, so the obtained results are expected.

Truly monochromatic beams are not experimentally available. Different energy distributions of the beams could result in differences in the measured sticking probabilities. Therefore, in the following, we try to quantify the effect of the incidence energy distributions. As we could not find the exact distributions of the molecule kinetic energies in the beams of Refs. [23–25] we used an ideal Maxwell-Boltzmann (M-B) distribution with a stream velocity corresponding to 50 meV. Our procedure is the same as in Ref. [280]. As shown in Fig. 8.3, in this case there is a non-negligible decrease in the sticking probability which amounts to ≈ 0.07 at low E_i. Therefore beam properties do have influence on the results for the studied system. However, it seems that differences between the two experiments can not be explained only by the possible differences in beam properties. Note that using a M-B distribution that features a rather broad energy tail should be looked at as an extreme case. The supersonic beams used in Refs. [23–25] typically have much narrower distributions. If we would have used in our simulations the unknown experimental distributions we would expect to obtain results that would lie between the two extreme cases that we have simulated (monochromatic and M-B distribution). Therefore, considering the information that can be extracted from actual experiments, we can conclude that our model describes the sticking probabilities reasonably well.

Given the initial energy and incidence angle, we have identified the initial polar orientation of the molecule θ_i as the single most important initial condition that is decisive for the sticking or not of a given molecule. We have checked that the other molecular degrees of freedom do not play a significant role. The only exception is that some correlation between the initial (X, Y) position and the sticking probability is observed for low E_i, as discussed below. Figure 8.4 shows the distributions of θ_i for adsorbed and scattered trajectories. Clearly, most of the
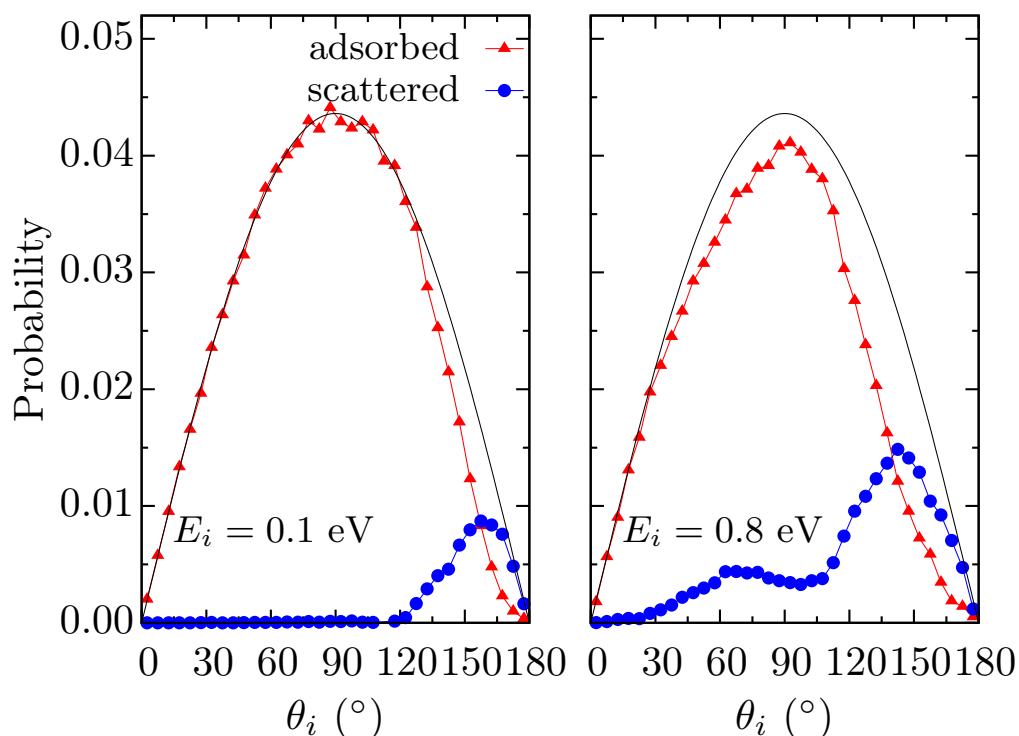
Figure 8.4: *Initial orientation (polar angle) θ_i of scattered (blue circles) and adsorbed (red triangles) molecules. The black line represents the ideal distribution of θ_i for all molecules. The shape of this distribution is due to the sampling of the solid angle.*

scattered molecules have large initial polar angles, which in our coordinate system means that the oxygen atom is roughly pointing to the surface. The reason is that the PES is purely repulsive for this CO orientation (see right panel of Fig. 8.2). At the lowest $E_i = 0.1$-0.3 eV, the distribution of θ_i for the scattered molecules is localized only at the largest θ_i. For larger E_i, more broad θ_i distributions like the one shown in the right panel of Fig. 8.4 are obtained.

Our results explain why in the experiments, though the sticking probabilities for low E_i are very large, they are never exactly one. This is due to the inability of molecules with θ_i close to $180°$ to reorientate and accommodate in the adsorption well. However, note that, as shown in Fig. 8.4, the number of molecules in the beam with this kind of orientations is very small. On the other hand, molecules in the most probable orientations, $\theta_i \approx 90°$, are able to reorientate rather efficiently and stick to the surface. These facts explain the observed large sticking probabilities.

We investigate the rotational anisotropy further by performing trajectory calculations with fixed θ_i. As shown in Fig. 8.5, the dependence of the sticking prob-
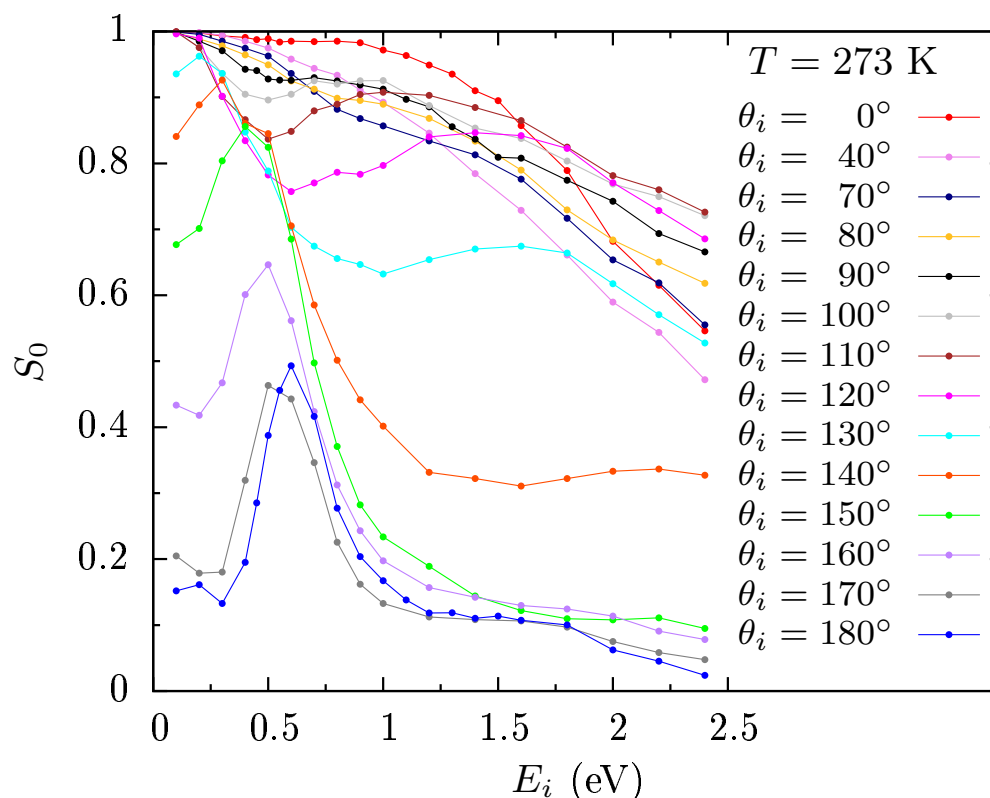
Figure 8.5: *Sticking probabilities for different fixed initial orientations (polar angle) θ_i calculated with the MDEF-GLO model.*

ability on E_i is completely different for $\theta_i \approx 180°$ compared to the $\theta_i \approx 90°$ and $\theta_i \approx 0°$ initial configurations. Sticking probabilities for the latter configurations are truly one in the low E_i range, gradually decreasing as E_i is increased, and in general are larger than the ones obtained when a Monte Carlo sampling of θ_i is used (see Fig. 8.3). On the contrary, for $\theta_i \approx 180°$ at low E_i the sticking probabilities are much lower, and show a resonance shape.

The above presented results can be understood by looking at Figs. 8.6 and 8.7. In these figures we show 2D (θ, Z) cuts of the potential energy of the molecule above two sites of the surface (top and t2h, see Fig. 8.1) with the other degrees of freedom relaxed (r, φ). We show the 2D PES for two sites instead of showing it for just one because we observe some correlation between the initial (X_i, Y_i) position of the molecule and the sticking probability. Namely, we observe that
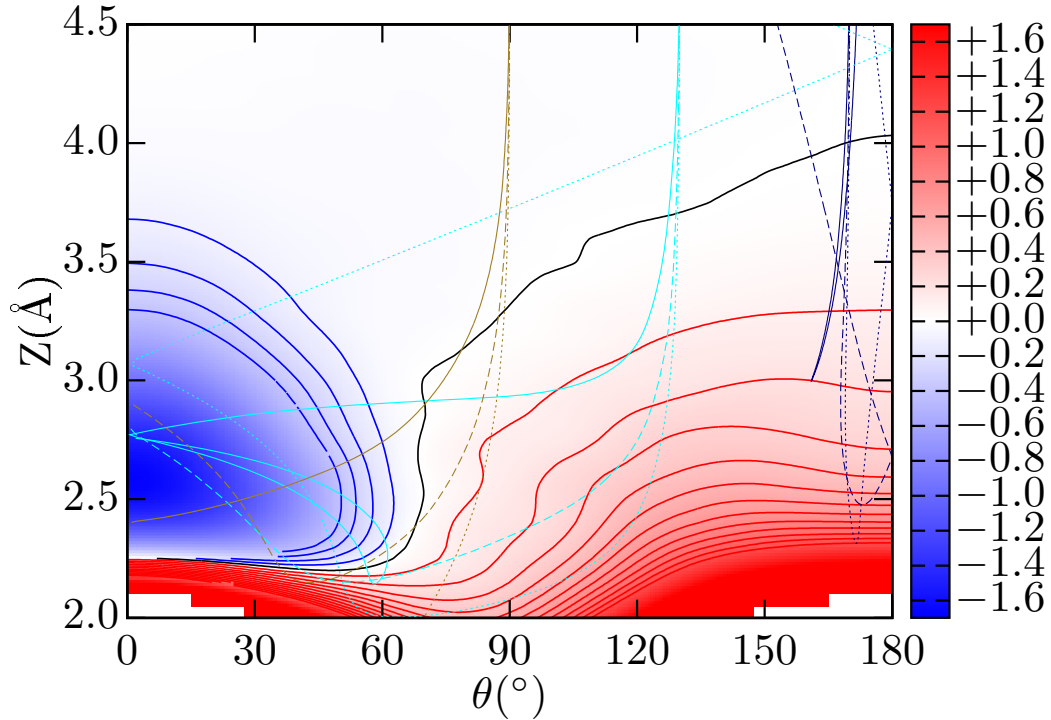
Figure 8.6: *The color map shows the PES of the molecule with the center of mass above the top site as a function of the distance from the surface and the angle between the surface normal and the molecular axis with the other degrees of freedom relaxed. The contours are separated by 0.1 eV (blue for negative potential values, black for zero, and red for positive values). Trajectories for three different initial orientations (marked with different colors) and three different energies (marked with full line for $E_i = 0.2$ eV, dashed line for $E_i = 0.6$ eV, and dotted line for $E_i = 1.2$ eV) are shown.*

for $\theta_i \approx 180°$ the sticking probability is smaller if the molecule impacts on the top site than if it impacts on the t2h site. Additionally, as discussed below, the two PESs are needed to explain the resonance in the sticking probability for $\theta_i \approx 180°$.

Overall, the PESs from Figs. 8.6 and 8.7 are similar. For C-down orientations, *i.e.* small θ ($\theta = 0°$ for Fig. 8.6 and $\theta = 30°$ for Fig. 8.7) there is a deep chemisorption well at $Z \approx 2.5$ Å. On the contrary, for $\theta > 90°$ as the molecule approaches the surface the PES becomes gradually more and more repulsive. Before discussing the differences between the two 2D PESs, we can use them to discuss the sticking probabilities we obtain in our dynamics. Obviously, the molecules with small θ_i are directly attracted to the chemisorption well and the sticking probability depends only on the ability of the molecule to lose enough translational energy.
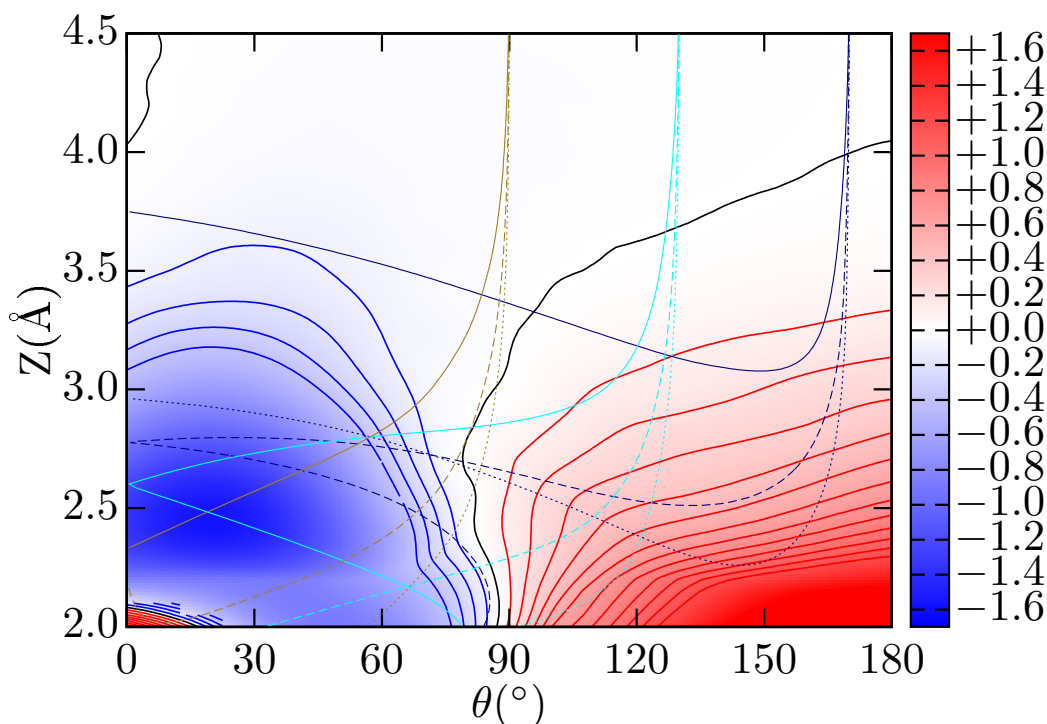
Figure 8.7: *The same as in Fig. 8.6 for molecule with center of mass above the top-hcp site.*

This is easily achievable at low E_i. Therefore, as already seen in Fig. 8.5, for these initial orientations the sticking probabilities are truly one at low E_i. As seen in the 2D PESs, for molecules that are initially roughly parallel to the surface ($\theta_i \approx 90°$) there are relatively large reorientation forces toward the C-down orientation. For this reason, it easy to imagine that the large majority of the molecules with such initial orientation will end up in the chemisorption region. To demonstrate this more transparently we have performed 2D Newtonian dynamics on the 2D PESs of Figs. 8.6 and 8.7 with three different E_i. For the lowest chosen energy value $E_i = 0.2$ eV, the trajectories with $\theta_i = 90°$ (golden lines in Figs. 8.6 and 8.7) and $\theta_i = 130°$ (cyan lines) show clearly an efficient reorientation of the molecule toward the chemisorption well. For higher E_i, even though the molecules reorientate they do not necessarily stick to the surface because they may not be able to lose enough energy to the surface before being reflected.

On the other hand, the situation for initially O-down oriented molecules ($\theta_i \approx 180°$) is completely different. As shown in the 2D cuts, the nature of the repulsive wall hardly depends on θ for $\theta > 140°$. For this reason the reorientation forces are

relatively small. Therefore, even molecules with low E_i are not able to reorientate easily in this case. This is clearly demonstrated by the trajectories in Figs. 8.6 and 8.7 for $E_i = 0.2$ eV and $\theta_i = 170°$ (solid dark blue lines). Both trajectories are scattered. Note that at $E_i = 0.2$ eV the sticking probability for this orientation is around 0.15 as shown in Fig. 8.5.

Molecules with higher E_i can probe more repulsive regions of the PES where the reorientation forces acting on the molecules are larger. The nature of the repulsive regions of the PES depends somewhat on the lateral X_i, Y_i position of the molecule. The differences are easily visible for large θ_i in Figs. 8.6 and 8.7. Namely, at the top site (Fig. 8.6) for $\theta_i > 130°$ the repulsive wall is either completely independent of θ, or even it can generate orientational forces toward the $\theta_i = 180°$ orientation. On the contrary, at the t2h site (Fig. 8.7) relatively small but clearly present reorientation forces toward the C-down orientation exist. Due to this, for $E_i = 0.6$ eV (dark blue dashed lines) the top site trajectory suggests scattering while the t2h site trajectory suggests adsorption. Therefore, at these E_i for which the resonance in the sticking probability is observed in Fig. 8.5 some molecules are able to reorientate and others are not, depending on the impact site. For even higher $E_i = 1.2$ eV (dark blue dotted lines) at the top site the molecule is again scattered because there is no reorientation force acting. In contrast, at the t2h site the molecule reorientates toward the C-down configuration. However, the molecule is at the same time repelled from the repulsive wall and possibly it will continue rotating and finally it may well be scattered from the surface. As in our simplified 2D trajectories there are no energy loss channels, we can not be conclusive in this case. The above discussion nicely fits with the results presented in Fig. 8.5 and illustrates why the resonance is observed for large θ_i. Of course to obtain the exact sticking probabilities one should consider the whole configurational space, which we already did with the 6D dynamics.

Summing-up, by using the two 2D cuts of the PES from Figs. 8.6 and 8.7 and the accompanying dynamics one can understand why only the molecules with $\theta_i \approx 180°$ can not efficiently reorientate at low E_i. The existence of these configurations that cannot reorientate explains why the adsorption probabilities are lower than one even at the lowest incidence energies. Nevertheless, since such configurations are improbable in the sampling of the solid angle (see Fig. 8.4) the adsorption probabilities at low E_i are still very high (close to one). With these figures we also explain the observed resonance in the sticking probabilities of the molecules with initial O-down orientation.

Experimentally one could also study the observed enhancement or reduction of the adsorption probabilities depending on θ_i by orienting the molecules in the beam [281]. This kind of experimental studies have already been performed for NO on several metal surfaces [139, 282, 283]. For example, for the NO/Ni(100) system 10-15% larger/lower adsorption probabilities were observed for N-end/O-end collisions at low E_i compared to the unoriented beam adsorption probabilities [284]. For that system, unoriented beam adsorption probabilities are close to the average of N-down and O-down oriented beam adsorption probabilities. In the case of CO/Ru(0001), according to our calculations, the adsorption probabilities for the unoriented beam are different from the average of the probabilities for O-down and C-down oriented beams (see Figs. 8.3 and 8.5). Moreover, as shown in Fig. 8.5, the difference in the probabilities for oriented beams are much larger in the CO/Ru(0001) case than those reported for NO beams. Therefore, though the actual measured anisotropy would depend on the degree of alignment of the molecules in the beam, the rotational anisotropy in the CO/Ru(0001) system is expected to be much larger than the ones observed so far.

8.3.2 Effects of electronic excitations in the molecular adsorption

In Fig. 8.8 we show the sticking probabilities obtained with the three models: MDEF-GLO (dissipation to both electronic friction and phonons is included), MD-GLO (dissipation only to phonons), and MDEF (dissipation only to electronic friction). Clearly, large adsorption probabilities which are in agreement with experiments are obtained only when energy dissipation to phonons is included (via GLO model). Electronic friction (in the MDEF-GLO model) increases the sticking probabilities slightly but noticeably compared to the MD-GLO model. This increase is similar to the effect of decreasing the surface temperature from $T = 273$ K to $T = 85$ K. The small effect of electronic friction is due to the short interaction time before the first collision of the molecule with the surface [285]. Note that in this first collision it is decided whether the molecule sticks or not. Similar small increase in the sticking probabilities when friction is included was also observed for the CO/Cu(100) system [286].
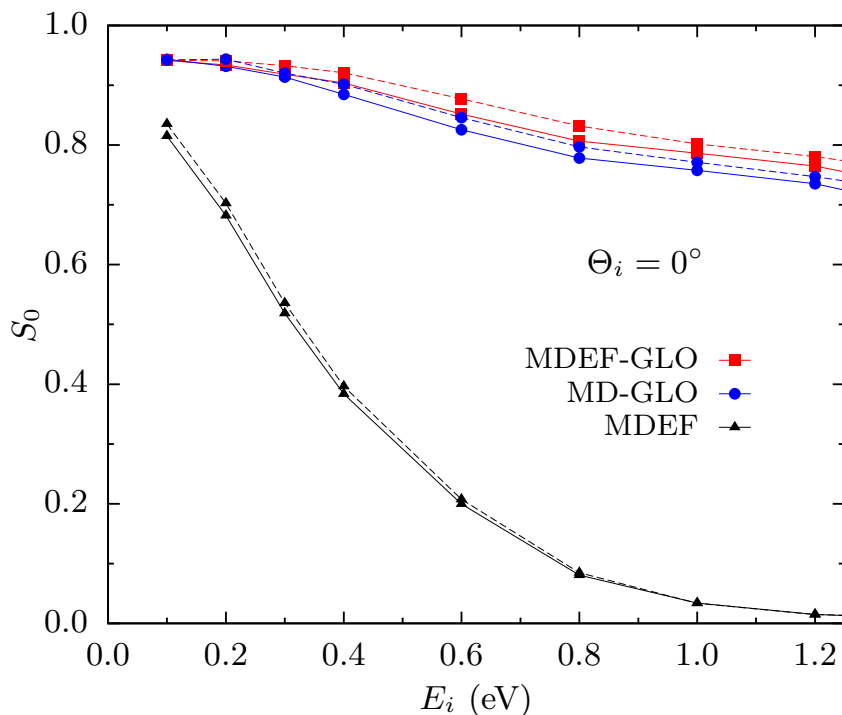
Figure 8.8: *Sticking probabilities at normal incidence calculated with different models (different energy loss channels included). Dashed lines are for $T = 85$ K and full lines are for $T = 273$ K.*

8.3.3 Classical vs quasi-classical calculations and excitations of internal degrees of freedom

All previous results are obtained from quasi-classical trajectory calculations in which the initial interatomic distances r_i and the corresponding momenta $p_{r,i}$ were set to correspond to the quantum vibrational ground state. In Fig. 8.9 we show the sticking probabilities obtained within classical trajectory calculations (r is equal to the equilibrium distance and $p_{r,i} = 0$) and for the first three vibrationally excited states. In general, differences are not very large. Sticking probabilities obtained from the classical and quasi-classical approaches are almost on top of each other for $E_i < 0.6$ eV. For larger E_i somewhat larger adsorption probabilities (up to 0.02) are obtained with the quasi-classical approach. Sticking probabilities of vibrationally excited molecules (with vibrational excitation up to $\nu = 3$) are also very similar regardless of the vibrational level. These results also point out to the conclusion that different populations of vibrationally excited molecules can not be the reason for differences in the experimental results of Ref. [23] and
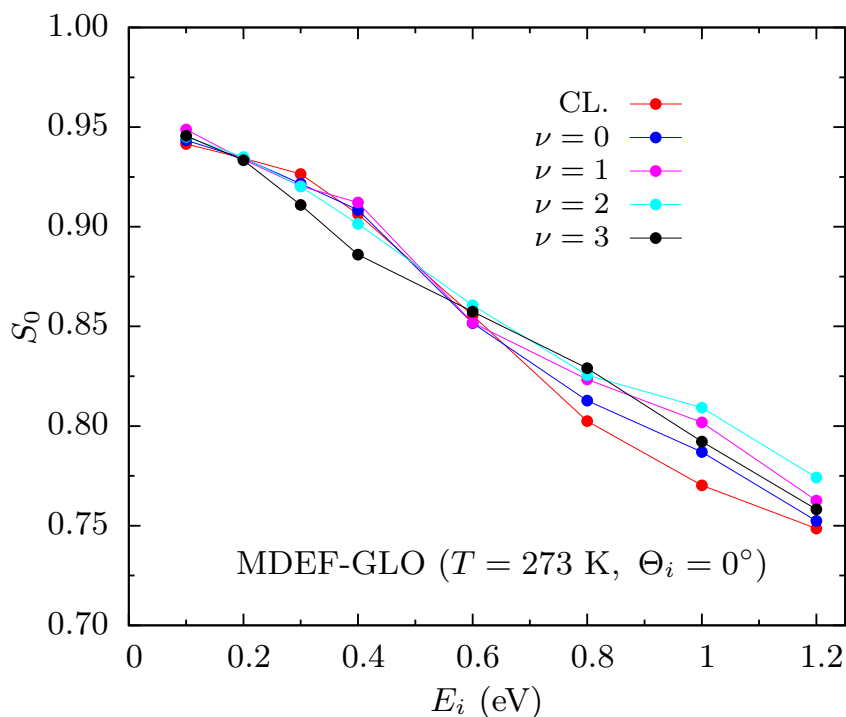
Figure 8.9: *Sticking probabilities obtained from classical trajectory calculations (neglecting zero point energy) and from quasi-classical trajectory calculations with vibrational excitation up to $\nu = 3$.*

Ref. [25].

Our results up to here were obtained for rotationally cold molecules ($J = 0$). Initial rotational state could also be important as sticking probabilities are highly dependent on the initial polar orientation of the molecule, as shown above. Due to this, one might expect that by excitation of rotational modes of the molecule the sticking probability would be modified. However, in Fig. 8.10 we show that the sticking probabilities for molecules in their first few rotational modes are very similar. This is due to the fact that rotational periods of these modes are long compared with typical interaction times before the first collision of the molecule with the repulsive wall of the PES. Excitation of higher rotational modes would make these time-scales commensurate, which could change the results we obtain. However, usually in supersonic beam experiments (as those of Ref. [23] or Ref. [25]) high rotational modes are not excited. Therefore, the rotational excitation also does not seem as a probable reason for the differences in the sticking probabilities obtained in the two different experiments.
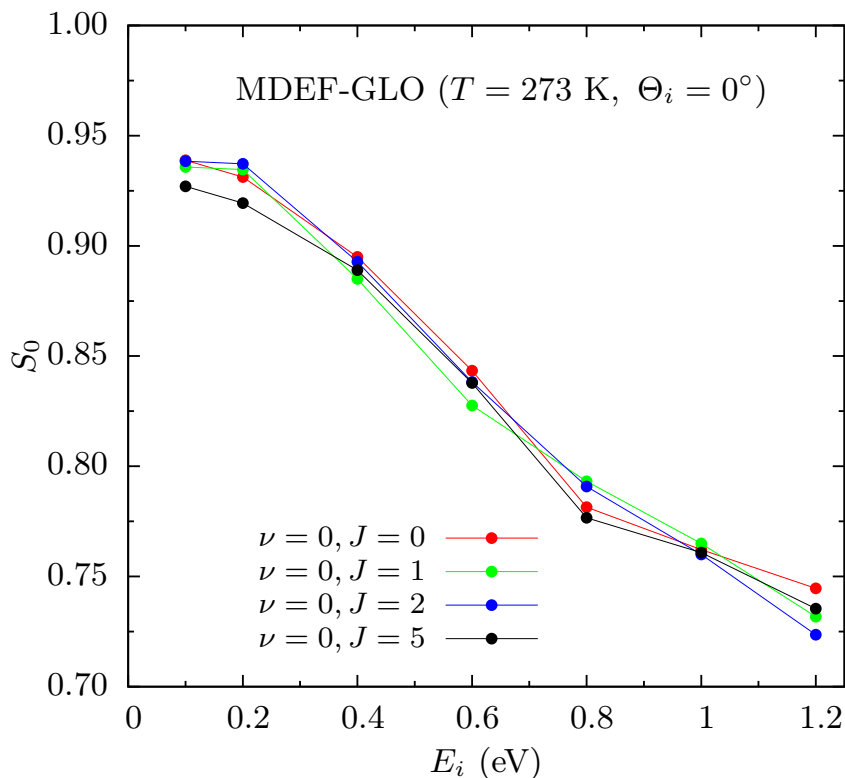
Figure 8.10: *Sticking probabilities calculated with rotational excitation up to J = 5.*

8.4 Scattering angle distributions and energy loss

8.4.1 Simulation of scattering angle distributions

Riedmüller *et al.* [25] also studied scattering angle distributions that are of interest due to their sensitivity to the PES corrugation. Experiments were performed for $E_i = 0.8$ eV, angle of incidence $\Theta_i = 60°$ and in the [11$\bar{2}$0] plane of incidence. We performed 500 000 trajectory calculations (per incidence condition) and used the procedure from Ref. [287] to extract the molecules scattered in the plane of incidence. Results of Ref. [25] are compared to our calculations in Fig. 8.11. Correspondence between the two results is clear. In accordance with the experiments, we observe a very small effect of the surface temperature and the superspecular peak at $\Theta_f \approx 70°$ (Θ_f is the scattering angle measured from the surface normal). At small scattering angles ($\Theta_f < 50°$) our calculations predict a broad shoulder which is absent in the experimental results. Below, in Sec. 8.4.3, we explain the origin of this shoulder, and here we focus on the $\Theta_f > 50°$ region.
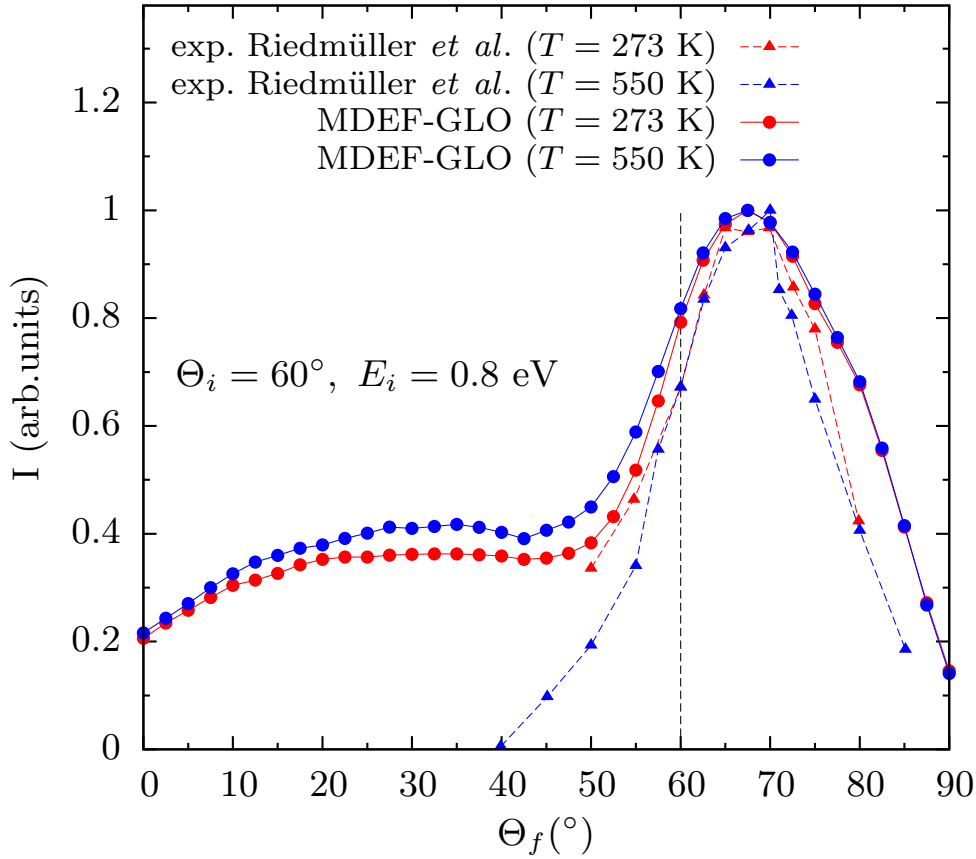
Figure 8.11: *Angular distribution of scattered molecules for an incidence angle of 60°
(marked by a vertical black dashed line). Our calulations (full line with circles) are com-
pared to experiments of Ref. [25] (dashed lines with triangles). We normalized our results
and the experimental ones to the same intensity at the maxima. Θ_f is the scattering angle
measured from the normal to the surface.*

As discussed in Ref. [25], the very small surface temperature effect can be ex-
plained by the choice of a high E_i. At such high E_i the incidence molecules are
very fast in comparison with the time scale of the surface movement, thus, in
practice, the molecules experience a quasi-static surface. The superspecular shift
can be explained by the conservation of parallel momentum. In other words,
mostly the normal momenta of the molecule is transferred to the surface, as dis-
cussed below.

The surprisingly narrow width of the angular distributions (with full width
at half maximum (FWHM) of 22° in experiments and 28° in our calculations) re-
mained unexplained in Ref. [25]. The surprise came from the fact that one would

expect a broader angular distribution due to the deep chemisorption well that exists in this system [271]. The reason for this expectation is that in the presence of a chemisorption well, molecules are deflected toward the surface where they scatter from a local repulsive wall. Due to the corrugation these walls are not oriented parallel to the surface which results in a broad angular distribution. In fact, as a good example, a broad distribution (with FWHM= 37°) was obtained in molecular beam experiments for the NO/Ru(0001) system [288]. Considering that NO is the molecule most similar to CO, and that the depth of chemisorption well on Ru(0001) is similar for both molecules, the observed narrow width of the angular distribution seems even more unusual. Furthermore, a broad angular distribution is also obtained for the CO/Ni(100) system [267].

In the following we show that our results on the rotational anisotropy in the sticking probability resolve these puzzling results. As shown in Fig. 8.4 molecules oriented such that the O atom points to the surface have a strong preference for being reflected. As the PES for such configuration does not have a deep chemisorption well (see Figs. 8.6 and 8.7), but only a repulsive wall, this explains the narrow angular distribution. A more detailed explanation on how the molecules with O-down orientation contribute to the narrow peak in the angular distribution is given in Secs. 8.4.2 and 8.4.3.

In addition to the scattering angle distributions, Riedmüller *et al.* [25] also measured the energy loss of the molecules as a function of the scattering angle. Figure 8.12 shows the comparison between these measurements and our calculations. The figure shows the angularly resolved ratio of final to initial translational energy for two different incidence angles. As can be seen in the figure, the agreement is rather good. However, in the experiments, the energy loss was measured to be somewhat smaller (up to 10%). In Sec. 8.4.3 we show that the agreement is even better if the experimental procedure is followed more closely.

Often two regimes of the energy loss, described by the following two simple models, are discussed in the scattering experiments [289, 290]:

- The hard cube model (also called parallel momentum conservation model) in which only the perpendicular momentum of the molecule can be transferred to the surface. In this model the ratio between the final E_f and the initial E_i translational energies is given as

$$\frac{E_f}{E_i} = \frac{\sin^2 \Theta_i}{\sin^2 \Theta_f}.$$

(8.3)

139

Figure 8.12: *Dependence of the translational energy loss (shown as the ratio between the initial and final translational energy of the molecule) on the scattering angle. Our results are shown with full lines and symbols. The corresponding experimental results are shown with dashed lines and empty symbols. We also show results of the hard cube model (dash-dotted line) and the binary collision model (dotted line).*

- The binary collision model (also called hard sphere scattering model) which originates from gas phase scattering and describes the collision of two spherical particles. In this model the ratio between the final E_f and the initial E_i translational energies is given as

$$\frac{E_f}{E_i} = \left[\frac{\sqrt{1 - (\frac{m}{M})^2 \sin^2(\Theta_i + \Theta_f)} - \frac{m}{M}\cos(\Theta_i + \Theta_f)}{1 + \frac{m}{M}} \right]^2, \qquad (8.4)$$

where m is the mass of the molecule and M is the mass of the surface atom.

Note that in both models the energy transfer to the internal degrees of freedom

is neglected. However, this is a crude approximation as shown in Sec. 8.5. The two models also assume only a single scattering event. We have checked that this is mostly true for molecules scattered in superspecular direction, however, for scattering in subspecular direction multiple collisions with the surface also occur. Additionally, in these models energy loss to the low energy electron-hole pairs is also neglected. However, in Sec. 8.4.4 we show that this effect is small.

It seems that these two models can be also applied to our system for some ranges of the scattering angle distribution. As shown in Fig. 8.12, the increase in energy loss (decrease of the ratio E_f/E_i) for high Θ_f (superspecular scattering) is reasonably well described by the parallel momentum conservation model (dash-dotted lines). On the other hand, the low Θ_f region of the distribution (subspecular scattering) shows similarities with the hard-sphere scattering model results. More insight into the two different regimes can be obtained if the energy loss is decoupled in contributions of initially C-down and O-down oriented molecules. This analysis is presented below in Sec. 8.4.2.

8.4.2   Angular distributions and energy loss: initial orientation of the molecule

In Sec. 8.3 we have shown that the adsorption probability is highly dependent on the initial orientation of the molecule. Therefore, it is natural to also explore its effect on the scattering angle distributions. In Fig. 8.13 we show the scattering angle distributions decomposed in contributions from initially O-down molecules ($\theta_i > 140°$) and the rest ($\theta_i < 140°$). We select $\theta_i = 140°$ to be a limiting angle as from Fig. 8.5 it seems that at this angle there is a crossover from molecules that dominantly stick to the surface and those that do not. The figure clearly shows that the narrow superspecular peak observed in the experiments is uniquely due to initially O-down orientations. Therefore, the narrow scattering peak is the result of molecules scattering from the repulsive wall without experiencing the chemisorption well, and due to this the narrowness of the peak is expected. On the other hand, it is clearly visible that molecules that visit the chemisorption region scatter with a broad distribution with a subspecular peak at $\Theta_f = 30°$ and FWHM $= 37°$. This is exactly the shoulder of the total scattering distribution.

The decomposition of the energy loss distributions in the contributions of molecules with different orientations gives an interesting insight as can be seen in Fig. 8.14. For superspecular scattering angles, the energy loss of initially O-down
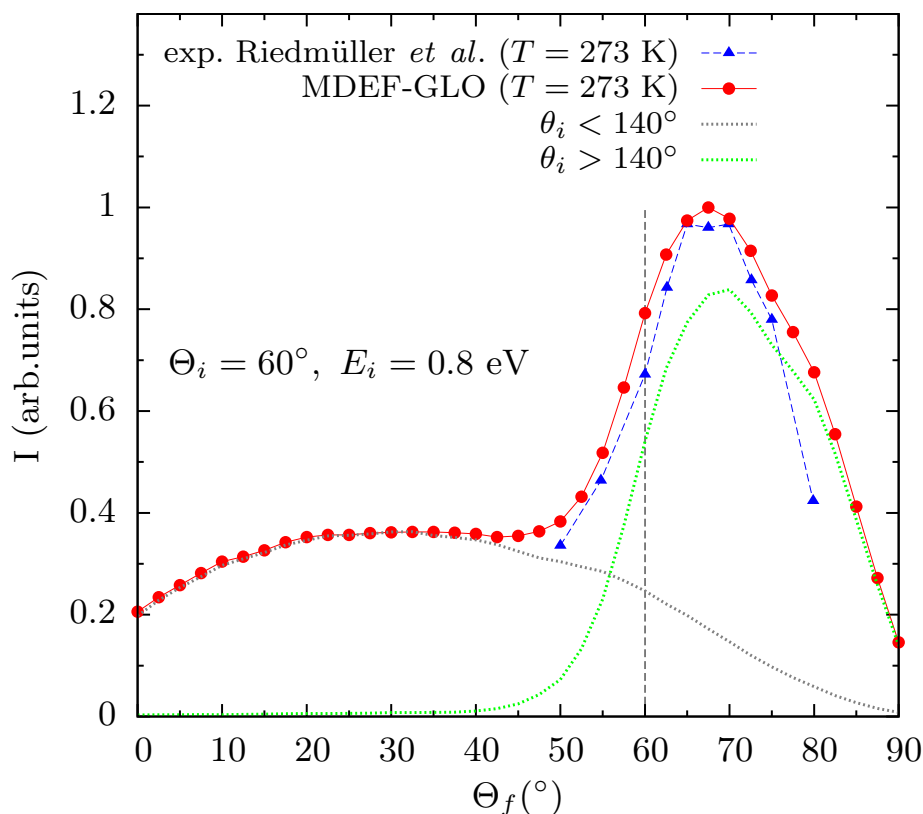
Figure 8.13: *Angular distribution of scattered molecules for an incidence angle of 60°
(marked by vertical black dashed line). Calculated total angular distribution (full red
line with circles) is separated in contribution of $\theta_i > 140°$ molecules (green dotted line)
and $\theta_i < 140°$ molecules (gray dotted line). Corresponding experiments of Ref. [25] are
also shown (dashed line with triangles).*

molecules ($\theta_i > 140°$) is somewhat smaller than the average energy loss obtained
for all orientations, and it is closer to the experimental results and the predic-
tions of the parallel momentum conservation model. It is not surprising that this
model works well in this case, as O-down molecules are scattered from a mostly
flat repulsive wall parallel to the surface. Due to this, only the normal component
of the translational energy is lost. In contrast, molecules with $\theta_i < 140°$ experi-
ence a much larger energy loss than measured in the experiments or obtained by
any of the simple models at these Θ_f. As discussed above these molecules visit
the chemisorption region where they can experience multiple scattering events.
These molecules also give almost all the contribution to the subspecular scatter-
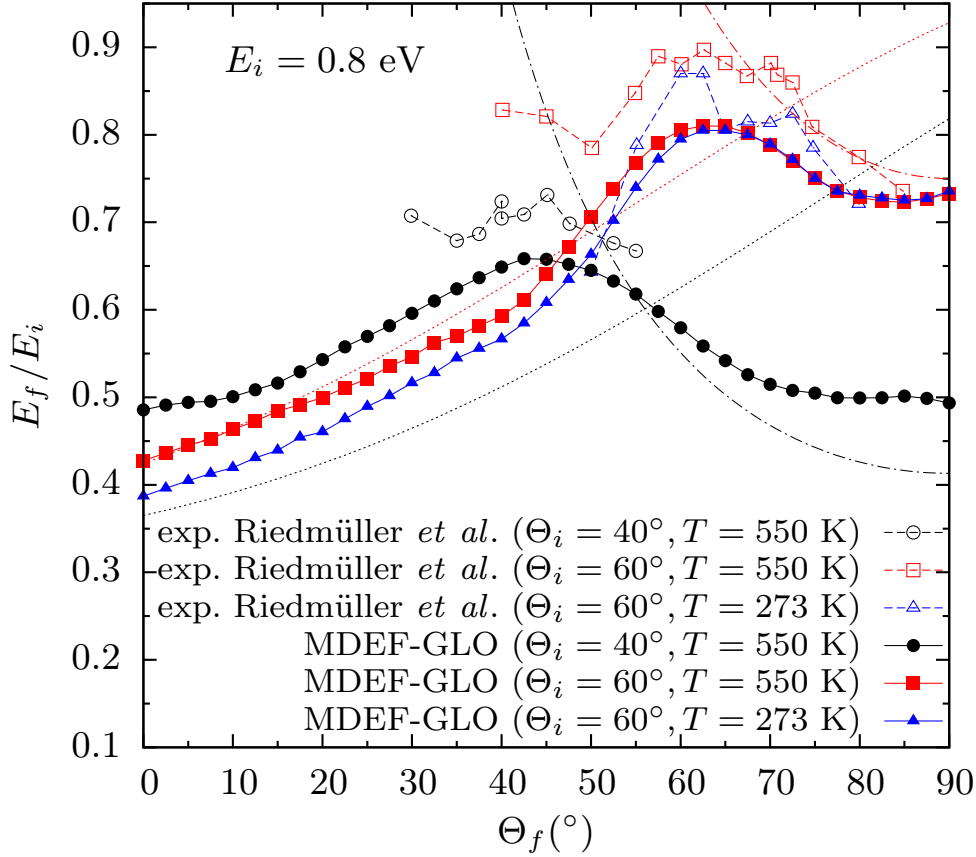ing angle region where, similarly, the energy loss is large.
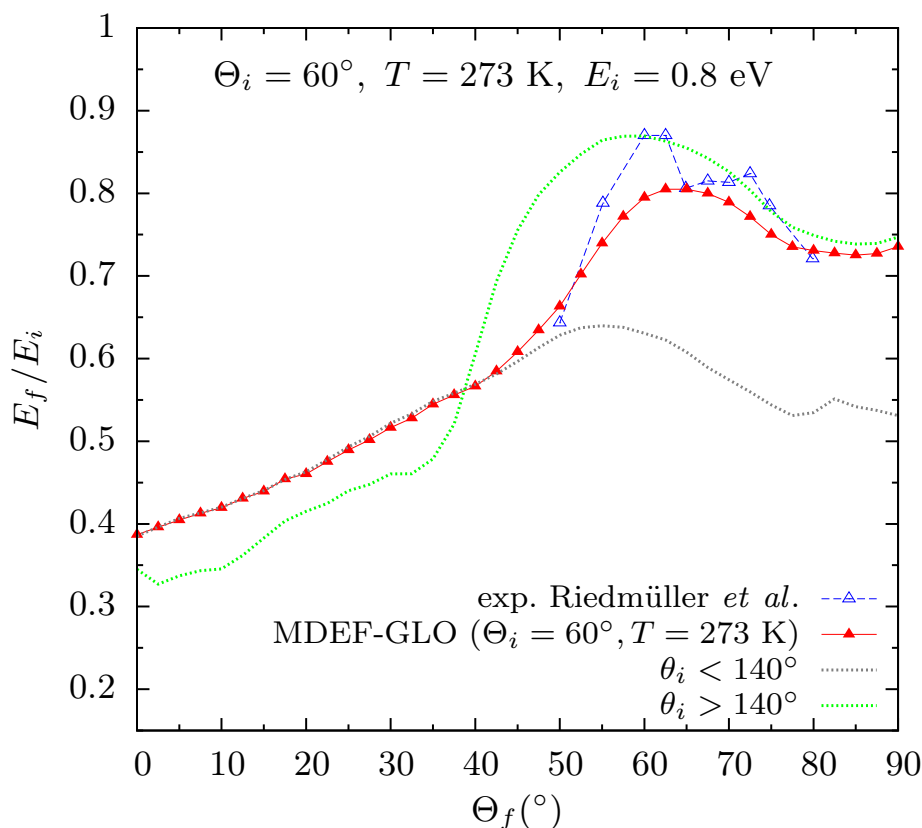
Figure 8.14: *Dependence of translational energy loss (shown as the ratio between initial and final translational energies of the molecule) on the scattering angle. Total results are shown with full lines and symbols. The corresponding experimental results are shown with dashed lines and empty symbols. Contribution of $\theta_i > 140°$ molecules is shown with a green dotted line and contribution of $\theta_i < 140°$ molecules is shown with a gray dotted line.*

8.4.3   Angular distributions and energy loss: time of flight

From the results of Sec. 8.4.2 it is apparent that the best agreement with the angular distributions measured in molecular beam experiments is obtained if only O-down molecules ($\theta_i > 140°$) are considered. With this in mind it is interesting to examine the fact that in the experiments of Riedmüller *et al.* [25] not all scattered molecules were taken into account when constructing the angular distributions, but only "directly inelastically backscattered molecules". Distinction between these and other molecules was based on the time of flight (TOF) spectra that shows two peaks. The left peak (shorter flight time - higher translational energy) was assigned to directly scattered molecules and the right peak (longer
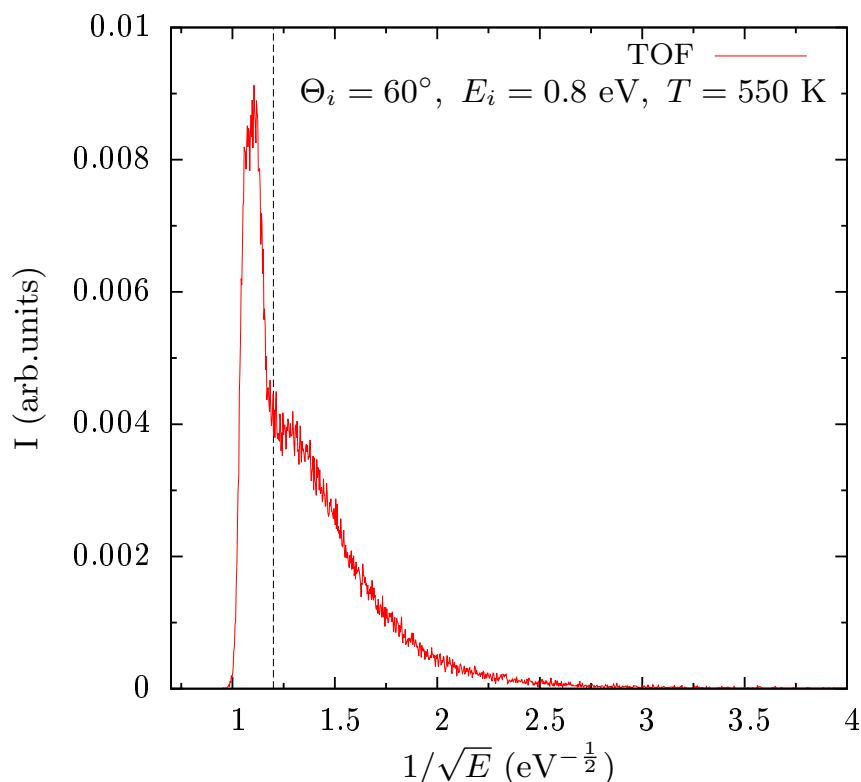
Figure 8.15: *Inverse square root of the translational energy of the scattered molecules that is proportional (with a constant) to the time of flight (TOF) of the molecule to the detector. Vertical dashed line separates* directly scattered molecules *(left peak) from* trapped molecules *(right peak).*

flight time - lower translational energy) was assigned to trapped molecules.

In Fig. 8.15 we show the equivalent of the TOF spectra obtained from our simulations. Interestingly, in our TOF spectra one can also distinguish two peaks. Therefore, it is worth to study the angular distributions constructed only from molecules that belong to the left peak. In the experiments the procedure to distinguish between the molecules from the two peaks is not given. Hence we simply define a cut-off between the two peaks as shown in Fig. 8.15. The angular distributions obtained from this procedure are shown in Fig. 8.16. We obtain similar results to those of previous Sec. 8.4.2 with an assignment of O-down molecules to the so-called directly scattered molecules and $\theta_i < 140°$ molecules to the so-called trapped molecules. Therefore, the shoulder that is absent in the experiments but exists in our simulations is due to the experimental construction of the scattering angle distributions that considered only directly scattered molecules. Note, how-
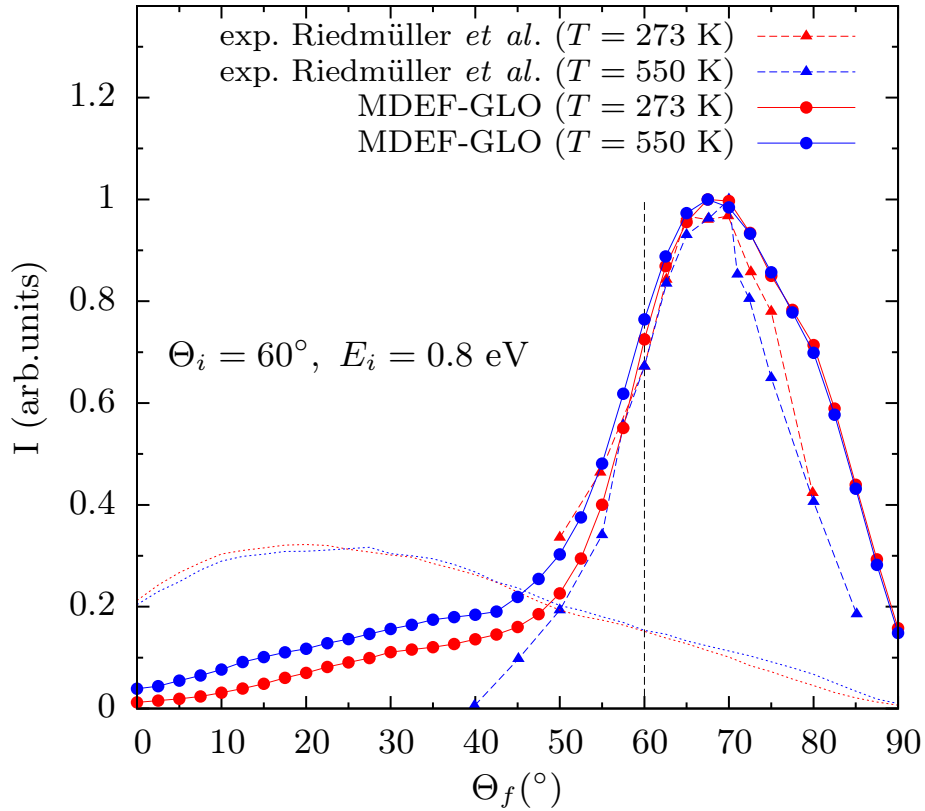
Figure 8.16: *Angular distribution of directly scattered molecules (left of cut-off line in Fig. 8.15) for an incidence angle of 60° (marked by vertical black dashed line). Our results (full line with circles) are compared to experiments of Ref. [25] (dashed lines with triangles). The distribution corresponding to scattered molecules to the right of the cut-off line in Fig. 8.15 is shown with dotted lines.*

ever, that our simple cut-off procedure still leaves some scattered molecules in the shoulder. Possibly in the experiments a somewhat different method is used to discriminate between directly scattered and trapped molecules more efficiently. Nevertheless, already with this procedure the agreement of our simulations with experiments is more than satisfying.

We employed the same procedure to obtain the angularly resolved energy loss which is shown in Fig. 8.17. There is a clear improvement in the agreement between our simulations and the experimental results. In fact, except for the two lowest experimental Θ_f points at $T = 273$ K our results are almost on top of the experimental results. Moreover, these are the only points in which there is a large surface temperature dependence in experiments. Due to this and the small scat-
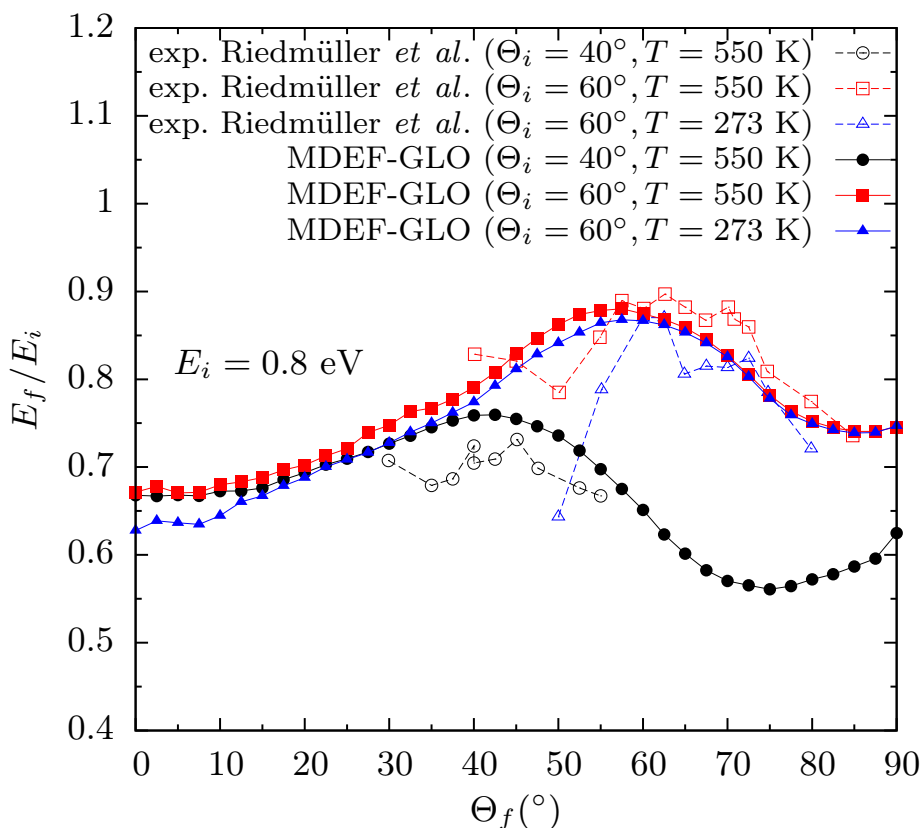
Figure 8.17: *The same as in Fig. 8.12, but only molecules to the left of the cut-off line in Fig. 8.15 are taken into account.*

tering intensities at these Θ_f, the experimental data could be noisy. All in all, our simulations seem to accurately describe the energy loss processes. Considering that the surface movement is described by the GLO model that involves several approximations this result is quite fascinating.

8.4.4 Effect of the energy loss to phonon and electron-hole pair excitations in the scattering angle distributions

Next we analyze the contributions of different energy loss channels to the scattering angle distributions. In Fig. 8.18 we show angular distributions calculated with the four models (which include different energy loss channels). Similarly to our conclusions for the sticking probabilities, inclusion of energy loss to phonons is fundamental for an accurate modelling of the CO scattering from the Ru(0001). Models which do not include energy loss to phonons predict too large proba-
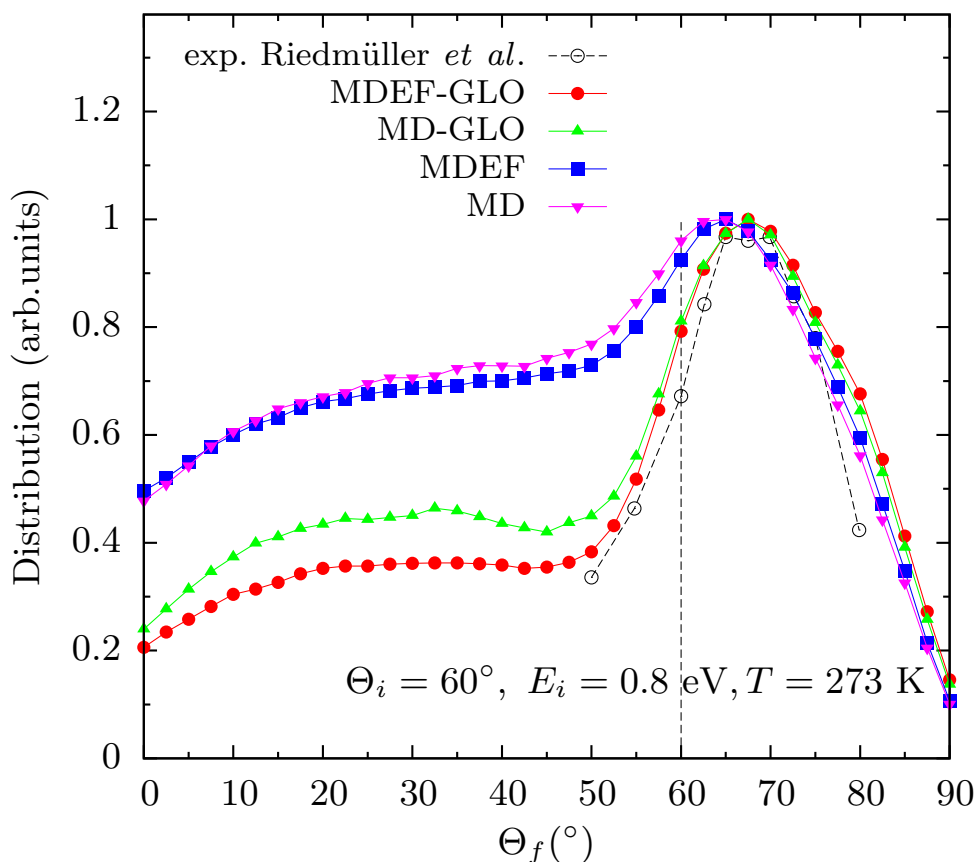
Figure 8.18: *Angular distributions calculated with different models.*

bilities for subspecular scattering angles and a peak that is shifted towards the specular angle. The much broader distribution in the cases when energy loss to phonons is not included is due to the fact that in these models the sticking probabilities are much smaller and even initially C-down oriented molecules are reflected. Therefore, effects of rotational anisotropy are small and broad angular distributions characteristic of a deep chemisorption well are obtained. Comparing the MDEF-GLO and MD-GLO models shows which is the importance of electronic energy loss in the scattering dynamics. At superspecular scattering angles the two curves are on top of each other which means that electronic excitations are not important. This is not surprising as the superspecular peak is mostly due to O-down molecules that directly scatter and have a very short interaction with the surface electronic density. In contrast, for molecules that scatter in subspecular directions MDEF-GLO gives reduced scattering probabilities as compared with MD-GLO. The reason is that these molecules have visited the chemisorption

region and there they have had enough time to lose part of their energy to excitation of low energy electron-hole pairs. As a result, the adsorption probabilities increase somewhat for these molecules when electronic excitations are included.

In Fig. 8.19 we study the angularly resolved energy loss calculated with the models that include different energy loss channels. At superspecular angles we
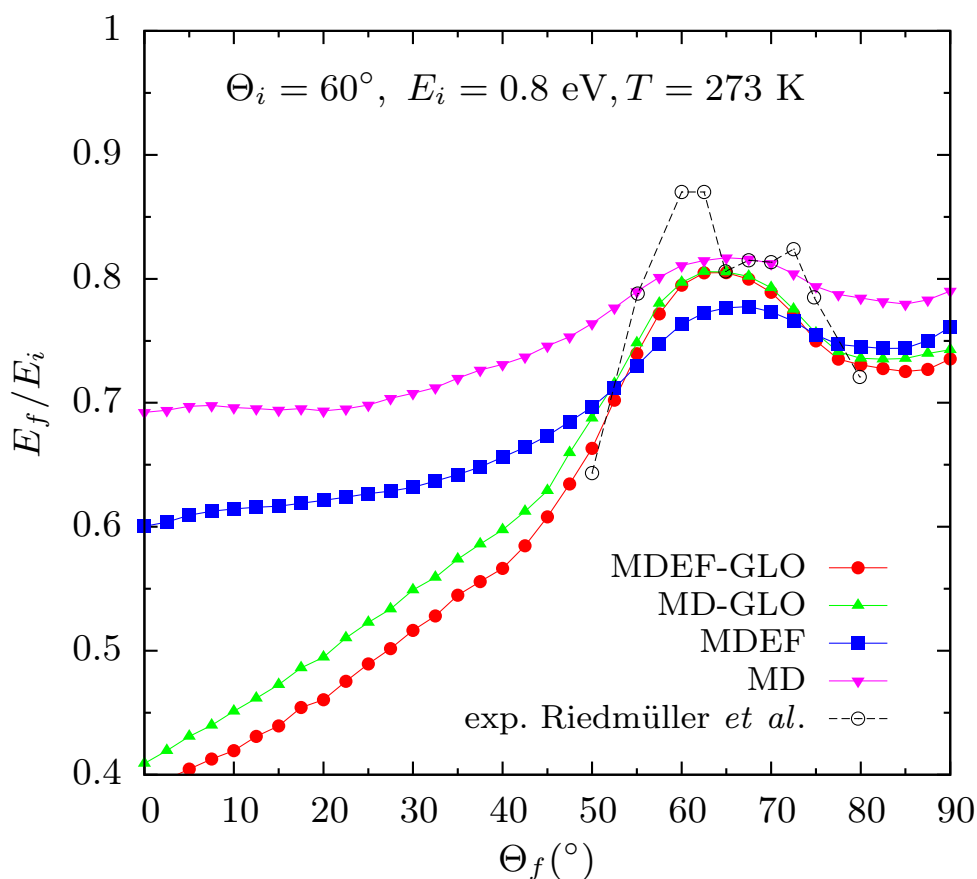
Figure 8.19: *Dependence of the translational energy loss on the scattering angle calculated with different models.*

obtain a similar energy loss regardless of the model used. No difference between the MDEF-GLO and MD-GLO models is expected as noted above due to the short interaction time. However, the small difference among all models is interesting as in the MD and MDEF models the surface is kept frozen. In fact in the MD model the total energy of the molecule is conserved. This shows that there is a large transfer of energy to the internal degrees of freedom and that at these large scattering angles this is the main contribution to the translational energy loss.

On the contrary, at subspecular scattering angles there is a large difference between the results of the different models. Obviously, the MD and MDEF models predict too low energy loses as in these models there is no transfer of energy to the surface movement. As explained above, the somewhat larger energy loss in the MDEF-GLO model compared to the MD-GLO model is due to the long interaction time of the molecule with the surface electron density for this range of scattering angles.

8.5   Vibrational deexcitation

Several experimental studies on the final internal states of initially vibrationally excited NO molecules scattered from noble metal surfaces have been performed [291–294]. In these works it has been observed that the large vibrational deexcitation is mainly due to the nonadiabatic coupling of the molecular motion to electronic excitations of the metal surface. Theoretical works including nonadiabatic effects via the independent electron surface hopping method [112] and the electronic friction method [295] have been partially successful in reproducing the experiments. The topic is still of interest and similar CO scattering experiments are worth performing [296, 297]. Therefore in this section we simulate the final vibrational distributions of scattered CO molecules that are initially in excited vibrational states. We will compare the results of the models that include nonadiabatic effects (electronic friction) and the ones that do not, in order to quantify the importance of these effects for the CO/Ru(0001) system.

In Figs. 8.20, 8.21, 8.22, and 8.23 we show final vibrational state distributions of scattered molecules that are initially in given vibrational states $\nu = 0$–7 calculated by the MDEF-GLO, MD-GLO, MDEF and MD models, respectively.

The binning of final vibrational states ν_f is performed such that for each scattered molecule we calculate its classical rovibrational energy and associate it with the rovibrational state ν, J closest in energy. Rovibrational states ν, J are obtained by solving the radial Schrödinger equation as described in Sec. 8.2.

As can be seen in Figs. 8.20, 8.21, 8.22, and 8.23 all models give similar probabilities of vibrational deexcitation (and excitation). This is especially true when comparing the MDEF-GLO and MD-GLO models as in this case the differences are subtle. The MDEF-GLO model predicts a little bit larger vibrational deexcitation. The largest differences between the probabilities of the MDEF-GLO and
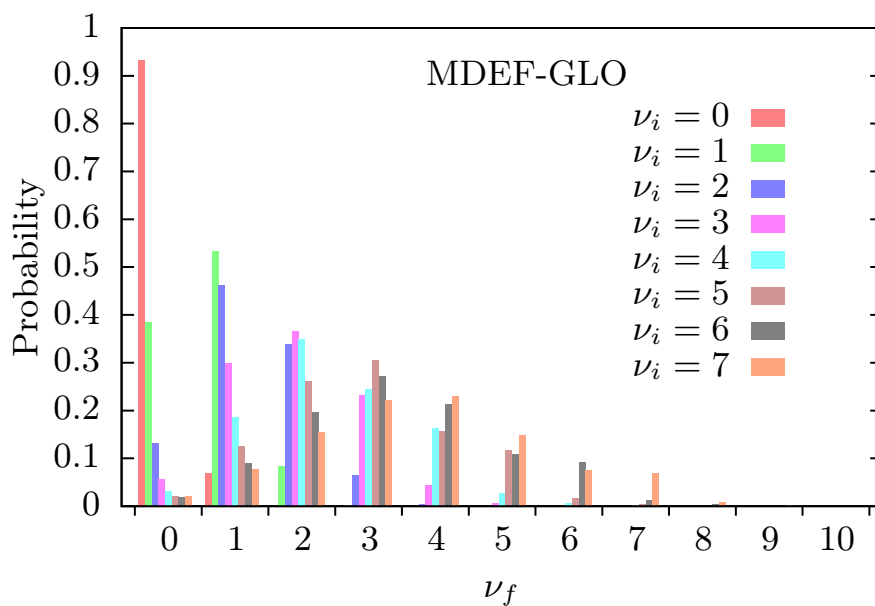
Figure 8.20: *Distribution of final vibrational states ν_f of scattered molecules with $E_i = 0.8$ eV calculated by the MDEF-GLO model. Different colors correspond to different initial vibrational states ν_i.*
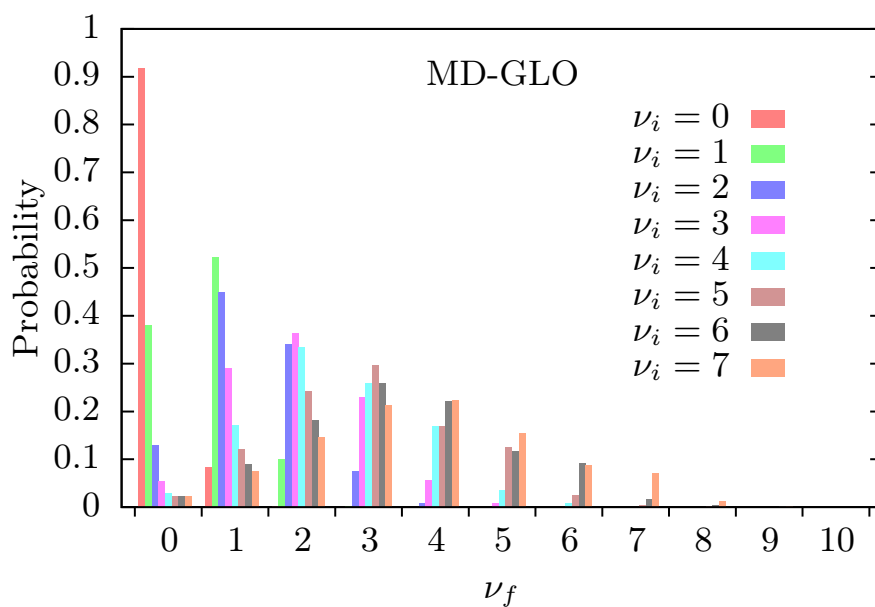
Figure 8.21: *Distribution of final vibrational states ν_f of scattered molecules with $E_i = 0.8$ eV calculated by the MD-GLO model. Different colors correspond to different initial vibrational states ν_i.*
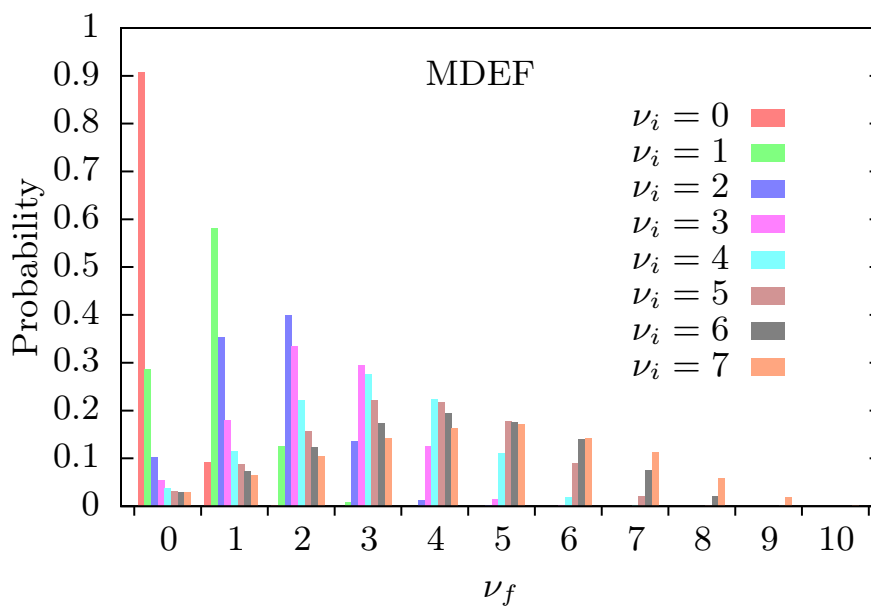
Figure 8.22: *Distribution of final vibrational states ν_f of scattered molecules with $E_i =$ 0.8 eV calculated by the MDEF model. Different colors correspond to different initial vibrational states ν_i.*
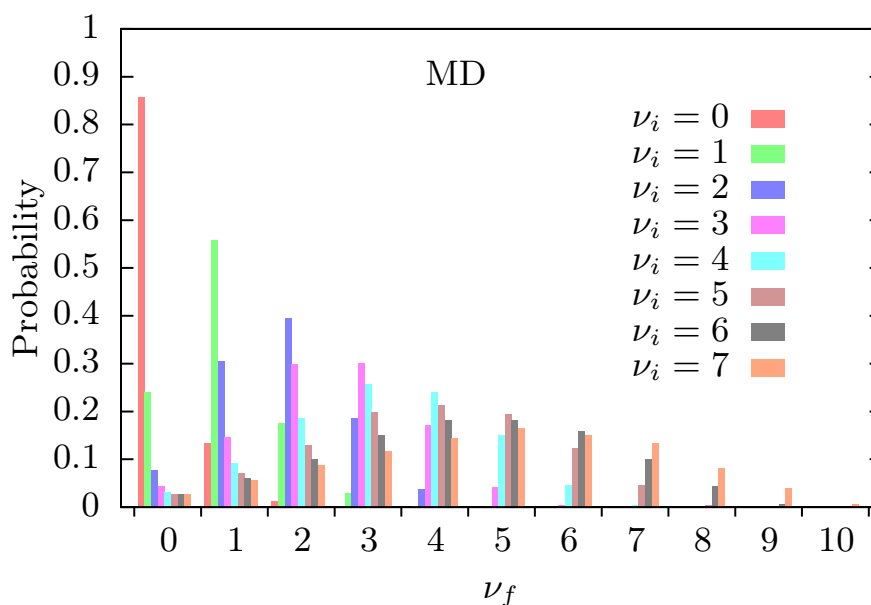
Figure 8.23: *Distribution of final vibrational states ν_f of scattered molecules with $E_i =$ 0.8 eV calculated by the MD model. Different colors correspond to different initial vibrational states ν_i.*

MD-GLO models shown in Figs 8.20 and 8.21 are of the order of 2%. However, when comparing these two models to the MDEF and MD models differences are more pronounced and clearly visible. The MDEF and MD models underestimate vibrational deexcitation, as the probabilities of finding the molecule in lower vibrational states is consistently smaller than in models that include surface movement. Accordingly, higher vibrational states have larger probabilities in the MDEF and MD models than in the MDEF-GLO model. Therefore, for vibrational deexcitation, as in the cases of the sticking probability and the scattering angle distributions, we arrive to the conclusion that the inclusion of surface movement and phonon excitations is fundamental for the description of the CO scattering from Ru(0001). On the other hand, the excitation of electron-hole pairs accounts only for a small but noticeable change in the results. Interestingly, even the MD
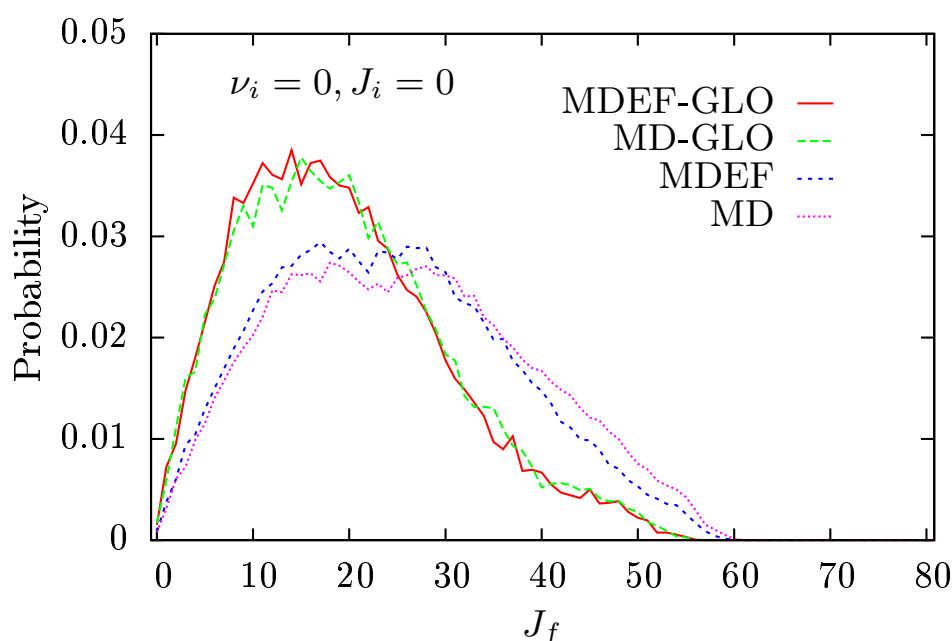
Figure 8.24: *Distribution of final rotational states J_f of scattered molecules with $E_i = 0.8$ eV calculated by the four models.*

model that does not include energy loss to either phonons or electron-hole pair excitations, that is the model in which energy of the molecule is conserved, is not that inaccurate in predicting the vibrational deexcitation. Therefore, the energy transfer between the vibrational motion to rotational and translational motion is efficient and constitutes the main channel for vibrational deexcitaiton.

In Fig. 8.24 we show the final rotational mode distribution calculated with the

four models for molecules initially in the $v_i = 0$, $J_i = 0$ state. In line with previous conclusions, MDEF-GLO and MD-GLO models give similar distributions that are distinct from the distributions obtained by MDEF and MD models. Models that include surface movement predict smaller rotational excitation.

8.6 Summary

In summary, we have performed molecular dynamics simulations to understand the results of molecular beam experiments in the CO/Ru(0001) system. In particular, two observations of these experiments were not previously understood. The first one is that around 5% of the incoming molecules with low incidence energies do not stick to the surface (kept at temperatures as low as 85 K). This is surprising as one would expect that all molecules stick to the surface due to the deep chemisorption well accessible without barrier from vacuum. The second one is the unusually narrow scattering angle distribution. In a system with a deep chemisorption well it is expected (and usually observed) that molecules are attracted to the well and thus deflected toward the surface where they scatter from a corrugated wall resulting in broad angular distributions. We have shown that both unusual observations are due to the rotational anisotropy of the molecule-surface potential. Namely, molecules with initially O-down orientation are scattered from a purely repulsive potential without feeling the chemisorption well. For O-down orientation, reorientation forces toward the well are small and therefore inefficient. The fact that only around 5% of the molecules are scattered at low incidence energies is due to the geometrically low probability of the O-down orientation in the total configurational space of molecular orientations. Once it is known that scattered molecules have not been attracted to the well the narrow scattering angle distribution is expected as molecules are scattered from the flat repulsive wall.

We have also studied adsorption probabilities of an oriented beam and predicted much larger differences between initially O-down and C-down orientations than previously reported for the similar NO molecule. Additionally, we have shown that non-adiabatic effects due to the excitation of low energy electron-hole pairs in Ru are small.

Furthermore, we have studied the translational energy loss of the scattered molecules and compared the results to the experiments. The agreement between

our results and the experiments is quite satisfactory. This shows that even the simple GLO model can capture the transfer of energy from the molecule to the surface quite accurately.

Finally, we have studied the transfer of vibrational energy to the internal degrees of freedom, surface movement and excitation of electron-hole pairs. Our results show that the energy loss channel to electron-hole pairs does not have a significant influence.

9

Conclusions and outlook

This thesis aimed at giving a contribution to the understanding of dynamics of small (gas) molecules on metal surfaces. In particular, two systems, $O_2/Ag(110)$ and $CO/Ru(0001)$, that are relevant for important catalytic processes have been studied.

Current knowledge about adsorption dynamics of O_2 on Ag(110) relies on several molecular beam experiments. A simple model based on these experiments has been proposed, but a full understanding is missing. With the purpose of filling this gap, we have performed state of the art molecular dynamics calculations. As a starting point, we have constructed a six dimensional potential energy surface based on first principles electronic structure calculations and demonstrated its high quality. Four adsorption wells have been identified in the potential energy surface which are accessible from vacuum without an energy barrier. The lowest barrier to dissociation is positioned on the hollow site of the surface. This barrier is considerably lower than the dissociation barriers calculated for the Ag(100) and Ag(111) surfaces which is consistent with the measured much higher reactivity of Ag(110). Dynamics simulations of the molecular adsorption process, both on the potential energy surface and "on the fly", have shown characteristics of a nonactivated system, while the opposite was observed in the molecular beam experiments. Moreover, most of the molecules are adsorbed in the bridge wells from which dissociation barriers are large. Several possible reasons for discrepancies between our simulations and experiments have been identified. We have recalculated the main features of the potential energy surface with different exchange-correlation functionals. Although, some experimental facts can be better understood with these functionals, still it seems that difficulties persist in order to reproduce the experimental results. In conclusion, we have proven that state of the art first principles methods can not fully explain the dynamics of this system and we suggest this system to serve as a challenging test for the theoretical

approaches that are yet to appear.

We have also presented a theoretical model to simulate the multidimensional dynamics of a molecule on a metal surface excited by an ultrashort laser pulse that includes surface movement. This approach allows to treat simultaneously the laser induced electron and phonon excitations and their effect on the dynamics of the molecule. As an example we have studied the laser induced desorption of O_2 from Ag(110). Our results suggest which desorption mechanism will be dominant in systems that present both physisorbed and chemisorbed species. Since physisorbed molecules are located in low electronic density regions their desorption behavior is expected to be phonon dominated, whereas desorption from chemisorbed states is expected to be hot electron dominated. Our study also shows that it would be of interest to perform an experimental study of the femtosecond laser induced dynamics of O_2 on Ag(110).

Our molecular dynamics simulations of the CO/Ru(0001) system have allowed to explain surprisingly narrow scattering angular distributions and incomplete adsorption at low incidence energies. We have shown that these unusual observations of molecular beam experiments are due to the rotational anisotropy of the molecule-surface potential. Namely, molecules with initially O-down orientation are scattered from a purely repulsive potential without feeling the chemisorption well. Therefore, not all molecules can stick to the surface at low incidence energies and narrow scattering angle distributions are obtained as molecules are scattered from the flat repulsive wall. We have also studied the vibrational energy loss of scattered molecules. Our results predict that the energy loss channel to electron hole pairs is not significant under the studied incidence conditions. As our model proved to be accurate for the molecules in the vibrational ground state, it would be interesting to compare our predictions with the corresponding experiments.

In this thesis some open questions have been closed and other have been opened which will hopefully serve as a tiny step forward in the quest for rational material design.

Appendices

<div align="right">

$\mathcal{A}$

</div>

Convergence analysis for the O$_2$/Ag(110) system

We perform a convergence study of the properties of adsorption wells of O$_2$ on Ag(110) for several DFT calculation parameters. The properties that we investigate are: the adsorption energy (E_a), the interatomic distance in the molecule (r_{O-O}), the vertical distance of the molecular center of mass to the surface (Z_{O-Ag}), and the spin polarisation (Sp) of the system. We define E_a as a difference between the energy of the system with the molecule in the well and the energy of the system with the molecule in the middle of the vacuum region ($Z_{O-Ag} \approx 9$ Å). This contrasts with the definition we use in the construction of 6D PES, where the zero potential energy is defined at $Z_{O-Ag} = 6$ Å. Due to this, one may notice a minor (~ 0.02 eV) difference in the corresponding adsorption energies.

The convergence study provides insight in the precision one should expect from the calculations. It also helps to resolve the differences between previously published DFT results [153–160]. For most of the calculations presented here we use the VASP code [170, 171] which includes a set of projector augmented wave method (PAW) pseudopotentials (PP) [75, 76]. For oxygen there are two types of PAW-PP, a soft one with a suggested plane-wave basis set energy cutoff of $E_{\text{cut-off}} = 400$ eV and a hard one with a suggested $E_{\text{cut-off}} = 700$ eV. We also study the convergence with respect to the **k**-point mesh, cell size, and the number of Ag layers. In all cases the two uppermost surface layer atoms and the O$_2$ atoms are relaxed until the forces are smaller than 0.01 eV/Å. Additionally, for the sake of comparison we perform some calculations with the QUANTUM ESPRESSO code [215] using a GBRV [298] PP with $E_{\text{cut-off}} = 680$ eV, which is above the suggested $E_{\text{cut-off}} = 540$ eV [298].

Our results are presented in Tables A.1-A.6. In general, differences in r_{O-O}, Z_{O-Ag}, and Sp are very small regardless of the calculation parameters. Regarding Sp, we found that additional care has to be taken when obtaining the lowest energy state for the bridge wells. In practice we had to perform a constrained spin

calculation [we set spin to 2 μ_B (Bohr magnetons)] to obtain the initial wavefunctions for the unconstrained calculation. In our experience, if one proceeds with the default VASP calculation results such as those denoted SBnsp and LBnsp in Table A.3 are obtained. These results reproduce the values obtained in Ref. [160].

The differences obtained for E_a when modifying the calculation parameters are more pronounced. Regarding the **k**-point mesh, in most of the cases, already a $4 \times 4 \times 1$ mesh suffices. The largest differences are due to the different PPs. The harder VASP PP and GBRV PP generally reduce E_a in comparison to the softer VASP PP. This reduction is somewhat larger in the case of the hollow wells. Such results further increase the difficulty to explain why adsorption in the bridge wells is not observed in experiments. The unit cell parameters do not change results significantly.

Table A.1: *Convergence study of the adsorption wells properties with respect to the **k**-point sampling for the soft VASP oxygen PP and a 2×3 unit cell with 5 Ag layers.*

site	slab	PP	**k**-point mesh	E_a(eV)	r_{O-O}(Å)	Z_{O-Ag}(Å)	$Sp(\mu_B)$
H110	$2 \times 3 \times 5$	soft	4×4	-0.38	1.45	1.03	0.00
H001	$2 \times 3 \times 5$	soft	4×4	-0.38	1.42	1.21	0.00
SB	$2 \times 3 \times 5$	soft	4×4	-0.36	1.31	2.16	1.24
LB	$2 \times 3 \times 5$	soft	4×4	-0.27	1.30	1.96	1.21
O₂	$2 \times 3 \times 5$	soft	4×4	-	1.24	9.65	-1.95
H110	$2 \times 3 \times 5$	soft	5×5	-0.42	1.46	1.00	0.00
H001	$2 \times 3 \times 5$	soft	5×5	-0.38	1.42	1.21	0.00
SB	$2 \times 3 \times 5$	soft	5×5	-0.35	1.31	2.15	1.20
LB	$2 \times 3 \times 5$	soft	5×5	-0.29	1.30	1.94	1.17
O₂	$2 \times 3 \times 5$	soft	5×5	-	1.24	9.65	-1.95
H110	$2 \times 3 \times 5$	soft	8×8	-0.38	1.46	1.01	0.00
H001	$2 \times 3 \times 5$	soft	8×8	-0.37	1.42	1.21	0.00
SB	$2 \times 3 \times 5$	soft	8×8	-0.34	1.31	2.16	1.26
LB	$2 \times 3 \times 5$	soft	8×8	-0.29	1.30	1.96	1.22
O₂	$2 \times 3 \times 5$	soft	8×8	-	1.24	9.65	-1.95
H110	$2 \times 3 \times 5$	soft	12×12	-0.39	1.46	1.00	0.00
H001	$2 \times 3 \times 5$	soft	12×12	-0.39	1.42	1.22	0.00

site	slab	PP	k-point mesh	E_a(eV)	r_{O-O}(Å)	Z_{O-Ag}(Å)	$Sp(\mu_B)$
SB	$2 \times 3 \times 5$	soft	12×12	-0.35	1.31	2.16	1.25
LB	$2 \times 3 \times 5$	soft	12×12	-0.29	1.30	1.95	1.21
O_2	$2 \times 3 \times 5$	soft	12×12	-	1.24	9.65	1.95

Table A.2: Convergence study of the adsorption wells properties with respect to the k-point sampling for the hard VASP oxygen PP and a 2×3 unit cell with 5 Ag layers.

site	slab	PP	k-point mesh	E_a(eV)	r_{O-O}(Å)	Z_{O-Ag}(Å)	$Sp(\mu_B)$
H110	$2 \times 3 \times 5$	hard	4×4	-0.26	1.45	1.00	0.00
H001	$2 \times 3 \times 5$	hard	4×4	-0.26	1.41	1.24	0.00
SB	$2 \times 3 \times 5$	hard	4×4	-0.29	1.30	2.18	1.28
LB	$2 \times 3 \times 5$	hard	4×4	-0.20	1.29	1.96	-1.24
O_2	$2 \times 3 \times 5$	hard	4×4	-	1.22	9.65	-1.96
H110	$2 \times 3 \times 5$	hard	5×5	-0.30	1.45	1.00	0.09
H001	$2 \times 3 \times 5$	hard	5×5	-0.27	1.41	1.24	0.00
SB	$2 \times 3 \times 5$	hard	5×5	-0.28	1.30	2.17	-1.24
LB	$2 \times 3 \times 5$	hard	5×5	-0.22	1.29	1.95	1.21
O_2	$2 \times 3 \times 5$	hard	5×5	-	1.22	9.65	-1.94
H110	$2 \times 3 \times 5$	hard	8×8	-0.26	1.45	1.01	0.02
H001	$2 \times 3 \times 5$	hard	8×8	-0.26	1.41	1.24	0.00
SB	$2 \times 3 \times 5$	hard	8×8	-0.28	1.30	2.18	-1.29
LB	$2 \times 3 \times 5$	hard	8×8	-0.22	1.29	1.94	1.24
O_2	$2 \times 3 \times 5$	hard	8×8	-	1.22	9.65	-1.94

Table A.3: Convergence study of the adsorption wells properties with respect to the k-point sampling for the soft VASP oxygen PP and a 3×4 unit cell with 5 Ag layers.

site	slab	PP	k-point mesh	E_a(eV)	r_{O-O}(Å)	Z_{O-Ag}(Å)	$Sp(\mu_B)$
H110	$3 \times 4 \times 5$	soft	4×4	-0.40	1.46	1.04	0.00
H001	$3 \times 4 \times 5$	soft	4×4	-0.38	1.42	1.26	0.00
SB	$3 \times 4 \times 5$	soft	4×4	-0.35	1.31	2.20	1.25
LB	$3 \times 4 \times 5$	soft	4×4	-0.29	1.30	2.01	1.25
O_2	$3 \times 4 \times 5$	soft	4×4	-	1.24	9.09	-1.93
H110	$3 \times 4 \times 5$	soft	5×5	-0.39	1.46	1.05	0.00

H001	$3 \times 4 \times 5$	soft	5×5	-0.38	1.42	1.26	0.00
SB	$3 \times 4 \times 5$	soft	5×5	-0.36	1.31	2.20	1.19
LB	$3 \times 4 \times 5$	soft	5×5	-0.30	1.30	2.01	1.24
O$_2$	$3 \times 4 \times 5$	soft	5×5	-	1.24	9.10	-1.93
SBnsp	$3 \times 4 \times 5$	soft	5×5	-0.10	1.34	2.06	-0.07
LBnsp	$3 \times 4 \times 5$	soft	5×5	-0.11	1.33	1.84	0.01
H110	$3 \times 4 \times 5$	soft	8×8	-0.41	1.46	1.04	0.00
H001	$3 \times 4 \times 5$	soft	8×8	-0.38	1.42	1.25	0.00
SB	$3 \times 4 \times 5$	soft	8×8	-0.36	1.31	2.20	1.21
LB	$3 \times 4 \times 5$	soft	8×8	-0.30	1.30	2.01	1.23
O$_2$	$3 \times 4 \times 5$	soft	8×8	-	1.24	9.10	-1.93

Table A.4: *Convergence study of the adsorption wells properties with respect to the* **k***-point sampling for the hard VASP oxygen PP and a 2×3 unit cell with 5 Ag layers.*

site	slab	PP	**k**-point mesh	E_a(eV)	r_{O-O}(Å)	Z_{O-Ag}(Å)	$Sp(\mu_B)$
H110	$3 \times 4 \times 5$	hard	4×4	-0.29	1.45	1.00	0.00
H001	$3 \times 4 \times 5$	hard	4×4	-0.27	1.41	1.25	0.00
SB	$3 \times 4 \times 5$	hard	4×4	-0.28	1.30	2.18	-1.28
LB	$3 \times 4 \times 5$	hard	4×4	-0.22	1.29	2.00	-1.27
O$_2$	$3 \times 4 \times 5$	hard	4×4	-	1.23	9.10	1.95
H110	$3 \times 4 \times 5$	hard	5×5	-0.28	1.45	1.01	0.00
H001	$3 \times 4 \times 5$	hard	5×5	-0.28	1.41	1.25	0.00
SB	$3 \times 4 \times 5$	hard	5×5	-0.29	1.30	2.17	-1.23
LB	$3 \times 4 \times 5$	hard	5×5	-0.24	1.29	2.01	-1.31
O$_2$	$3 \times 4 \times 5$	hard	5×5		-1.23	9.10	1.95
H110	$3 \times 4 \times 5$	hard	8×8	-0.30	1.45	1.01	0.00
H001	$3 \times 4 \times 5$	hard	8×8	-0.28	1.41	1.25	0.00
SB	$3 \times 4 \times 5$	hard	8×8	-0.29	1.30	2.17	-1.24
LB	$3 \times 4 \times 5$	hard	8×8	-0.23	1.29	1.96	-1.26
O$_2$	$3 \times 4 \times 5$	hard	8×8		1.23	9.10	1.95

Table A.5: *Convergence study of the adsorption wells properties with respect to the **k**-point sampling for the soft VASP oxygen PP and a 2 × 3 unit cell with 10 Ag layers.*

site	slab	PP	**k**-point mesh	E_a(eV)	r_{O-O}(Å)	Z_{O-Ag}(Å)	$Sp(\mu_B)$
H110	$2 \times 3 \times 10$	soft	4×4	-0.35	1.45	1.05	0.22
H001	$2 \times 3 \times 10$	soft	4×4	-0.38	1.42	1.24	0.00
SB	$2 \times 3 \times 10$	soft	4×4	-0.38	1.31	2.14	1.23
LB	$2 \times 3 \times 10$	soft	4×4	-0.31	1.30	1.96	1.24
O$_2$	$2 \times 3 \times 10$	soft	4×4	-	1.24	9.09	-1.95
H110	$2 \times 3 \times 10$	soft	5×5	-0.42	1.45	1.05	0.01
H001	$2 \times 3 \times 10$	soft	5×5	-0.42	1.42	1.24	0.00
SB	$2 \times 3 \times 10$	soft	5×5	-0.37	1.31	2.14	1.21
LB	$2 \times 3 \times 10$	soft	5×5	-0.33	1.30	1.95	1.22
O$_2$	$2 \times 3 \times 10$	soft	5×5	-	1.24	9.10	-1.95
H110	$2 \times 3 \times 10$	soft	8×8	-0.42	1.45	1.05	0.00
H001	$2 \times 3 \times 10$	soft	8×8	-0.43	1.42	1.24	0.00
SB	$2 \times 3 \times 10$	soft	8×8	-0.38	1.31	2.14	1.19
LB	$2 \times 3 \times 10$	soft	8×8	-0.33	1.30	1.95	1.23
O$_2$	$2 \times 3 \times 10$	soft	8×8	-	1.24	9.13	-1.95

Table A.6: *Convergence study of adsorption wells properties with respect to the **k**-point sampling for the GBRV [298] PPs and a 2 × 3 unit cell with 5 Ag layers calculated with the QUANTUM ESPRESSO code [215].*

site	slab	PP	**k**-point mesh	E_a(eV)	r_{O-O}(Å)	Z_{O-Ag}(Å)	$Sp(\mu_B)$
H110	$2 \times 3 \times 5$	GBRV	4×4	-0.22	1.45	1.02	0.00
H001	$2 \times 3 \times 5$	GBRV	4×4	-0.21	1.42	1.21	0.00
SB	$2 \times 3 \times 5$	GBRV	4×4	-0.27	1.30	2.18	1.30
LB	$2 \times 3 \times 5$	GBRV	4×4	-0.20	1.29	2.01	1.32
O$_2$	$2 \times 3 \times 5$	GBRV	4×4	-	1.23	9.00	1.96
H110	$2 \times 3 \times 5$	GBRV	5×5	-0.26	1.45	1.00	0.00
H001	$2 \times 3 \times 5$	GBRV	5×5	-0.26	1.42	1.22	0.00
SB	$2 \times 3 \times 5$	GBRV	5×5	-0.27	1.30	2.18	1.30
LB	$2 \times 3 \times 5$	GBRV	5×5	-0.22	1.29	2.01	1.30

O$_2$	$2 \times 3 \times 5$	GBRV	5×5	-	1.23	9.00	1.96
H110	$2 \times 3 \times 5$	GBRV	8×8	-0.23	1.45	1.00	0.00
H001	$2 \times 3 \times 5$	GBRV	8×8	-0.23	1.42	1.22	0.00
SB	$2 \times 3 \times 5$	GBRV	8×8	-0.26	1.30	2.18	1.31
LB	$2 \times 3 \times 5$	GBRV	8×8	-0.21	1.29	2.01	1.31
O$_2$	$2 \times 3 \times 5$	GBRV	8×8	-	1.23	9.00	1.96
H110	$2 \times 3 \times 5$	GBRV	12×12	-0.24	1.45	1.00	0.00
H001	$2 \times 3 \times 5$	GBRV	12×12	-0.23	1.42	1.22	0.00
SB	$2 \times 3 \times 5$	GBRV	12×12	-0.26	1.30	2.18	1.30
LB	$2 \times 3 \times 5$	GBRV	12×12	-0.21	1.29	2.01	1.31
O$_2$	$2 \times 3 \times 5$	GBRV	12×12	-	1.23	9.00	1.96

B

Interpolation details

B.1 Three dimensional atomic potential energy surface of O on Ag(110)

The interaction of the O atom with the frozen Ag(110) surface is described with a three-dimensional (3D) adiabatic potential energy surface (PES) that depends on the position $\mathbf{R}$ of the O atom over the surface. This 3D PES is simply used as an auxiliary utility to reduce the corrugation of the 6D O_2/Ag(110) PES as described in Ch. 3. As in the 6D PES case the Ag(110) surface is kept frozen.

The 3D PES $V^{3D}(\mathbf{R})$ is constructed by interpolating with the 3D CRP [83] method the spin-polarized DFT energy grid described in Ch. 3 of the thesis. In the 3D CRP, the function I^{3D} to be interpolated is calculated as

$$I^{3D}(\mathbf{R}) \;=\; V^{3D}(\mathbf{R}) - \sum_{i=1}^{n} V^{1D}(|\mathbf{R} - \mathbf{R}_i|). \tag{B.1}$$

where V^{1D} is a one-dimensional potential energy describing the interaction between the O atom and the ith-Ag atom that is located at $\mathbf{R}_i$. In our case, we use the potential energy of the O atom on the top site of Ag(110) for V^{1D}. The summation in Eq. (B.1) runs over first and second layer atoms that give a non zero contribution to V^{1D}. Compared to V^{3D}, the resulting I^{3D} is a less corrugated function that can be easily interpolated over X, Y and Z through a cubic spline interpolation in three dimensions [83].

The dependence of the O/Ag(110) PES on the distance Z between the atom and the surface is shown in Fig. B.1 for the top site, which is used to evaluate V^{1D}, and for other high-symmetry sites. In all cases the interaction of O with Ag(110) along the Z direction is characterized by an adsorption well followed by a repulsive wall. The systematic inspection of the (X, Y)-cuts of the 3D PES at fixed distances Z allows us to determine which sites are truly minima in 3D.

From this analysis we confirm that there is a minimum at the long-bridge site with the O atom 0.56 Å above the surface and a well depth of 3.09 eV. However, the absolute minimum corresponds to the atom located at ($X = 1.41$ Å, $Y = 1.47$ Å, $Z = 0.78$ Å) with an adsorption energy of 3.13 eV. It is worth to remark that surface relaxation may alter these results for O adsorption. Finally, we note that in common with the O_2/Ag(110) PES, none of the calculated sites show energy barriers in the entrance channel.
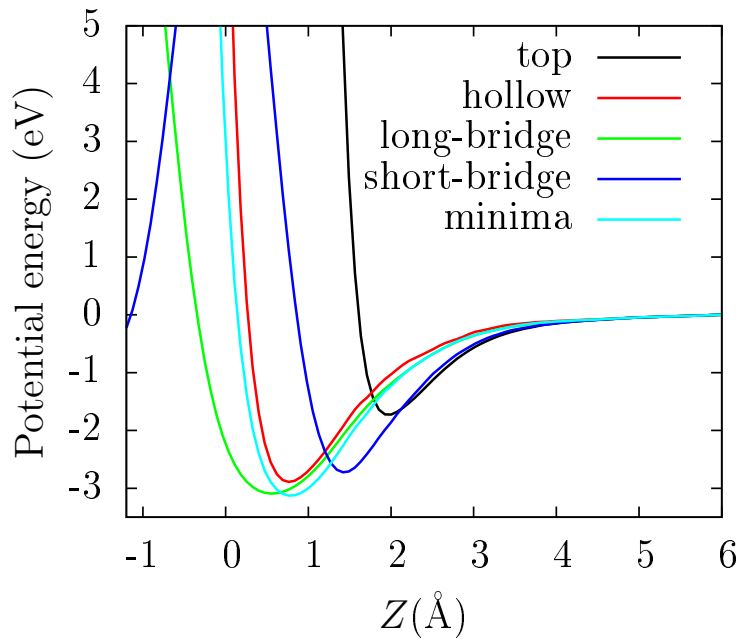
Figure B.1: *Dependence of the 3D atomic PES on distance Z of the oxygen atom from the Ag(110) for the most symmetric sites on the surface and for the site where the absolute minima of the 3D PES is located (see text).*

B.2 Six dimensional O_2/Ag(110) potential energy surface interpolation details

In this part of the Appendix B we describe in more detail the interpolation steps followed to obtain the value of the 6D PES at any point of the configurational space, *i.e.*, $V^{6D}(X, Y, Z, r, \theta, \varphi)$.

Once the (r_i, Z_i)-cuts of the 34 configurations ($X_0, Y_0, \theta_0, \varphi_0$) that conform the DFT energy grid described in Ch. 3 of the manuscript are calculated, we start ob-

taining the corresponding (r_i, Z_i)-cuts of the interpolation function I^{6D} for each of these configurations. This is done by subtracting the 3D potential V^{3D} as indicated in Eq. (2.32). Next, a conventional 2D cubic spline algorithm [299] (as employed in Ref. [83]) is used to interpolate the (r_i, Z_i)-cuts of each $I^{6D}(X_0, Y_0, \theta_0, \varphi_0)$ for the requested values (r, Z). The latter are then interpolated over φ and θ with Fourier expansions that take into account the symmetry of every site (X_0, Y_0). In particular, the Fourier functions used are as follows:

a) The configurations calculated on top site $(X = 0, Y = 0)$ and hollow site $(X = a/2, Y = a/(2\sqrt{2}))$ (both sites have the same symmetry) are: (1) $\theta = 0°$; (2) $\theta = 45°$ and $\varphi = 0°$; (3) $\theta = 45°$ and $\varphi = 35.26°$; (4) $\theta = 45°$ and $\varphi = 90°$; (5) $\theta = 90°$ and $\varphi = 0°$; (6) $\theta = 90°$ and $\varphi = 35.26°$; (7) $\theta = 90°$ and $\varphi = 90°$. In the following the notation $I(j)$ refers to the value of the interpolation function I^{6D} at the orientation conditions of item (j) above. Then, the Fourier functions $I_\theta(\varphi)$ for the interpolation over φ on top and hollow sites and $\theta = 0°, 45°, 90°$ are:

$$I_0(\varphi) = I(1) \tag{B.2}$$

$$
\begin{aligned}
I_{45}(\varphi) = \frac{1}{16}[2I(2) + 9I(3) + 5I(4) + 8(I(2) - I(4))\cos 2\varphi \\
+ (6I(2) - 9I(3) + 3I(4))\cos 4\varphi]
\end{aligned}
\tag{B.3}
$$

$$
\begin{aligned}
I_{90}(\varphi) = \frac{1}{16}[2I(5) + 9I(6) + 5I(7) + 8(I(5) - I(7))\cos 2\varphi \\
+ (6I(5) - 9I(6) + 3I(7))\cos 4\varphi]
\end{aligned}
\tag{B.4}
$$

The Fourier function for the interpolation over θ on top (T) and hollow (H) sites is:

$$
\begin{aligned}
I_{T,H}(\theta, \varphi) = \frac{1}{4}[(I_0(\varphi) + 2I_{45}(\varphi) + I_{90}(\varphi) \\
+ 2(I_0(\varphi) - I_{90}(\varphi))\cos 2\theta \\
+ (I_0(\varphi) - 2I_{45}(\varphi) + I_{90}(\varphi))\cos 4\theta]
\end{aligned}
\tag{B.5}
$$

b) The configurations calculated on long-bridge site $(X = a/2, Y = 0)$ and short-bridge site $(X = 0, Y = a/(2\sqrt{2}))$ (both sites have the same symmetry) are: (1) $\theta = 0°$; (2) $\theta = 45°$ and $\varphi = 0°$; (3) $\theta = 45°$ and $\varphi = 90°$; (4) $\theta = 90°$ and

$\varphi = 0°$; (5) $\theta = 90°$ and $\varphi = 90°$. The Fourier functions of the interpolation over φ on long-bridge and short-bridge sites are:

$$I_0(\varphi) = I(1) \tag{B.6}$$

$$I_{45}(\varphi) = \frac{1}{2}(I(2) + I(3)) + \frac{1}{2}(I(2) - I(3))\cos 2\varphi \tag{B.7}$$

$$I_{90}(\varphi) = \frac{1}{2}(I(4) + I(5)) + \frac{1}{2}(I(4) - I(5))\cos 2\varphi \tag{B.8}$$

The Fourier function for the interpolation over θ on long-bridge (LB) and short-bridge (SB) sites is:

$$\begin{aligned} I_{LB,SB}(\theta, \varphi) = \frac{1}{4}[&(I_0(\varphi) + 2I_{45}(\varphi) + I_{90}(\varphi) \\ &+ 2(I_0(\varphi) - I_{90}(\varphi))\cos 2\theta \\ &+ (I_0(\varphi) - 2I_{45}(\varphi) + I_{90}(\varphi))\cos 4\theta] \end{aligned} \tag{B.9}$$

c) The configurations calculated on the non-symmetrical top-hollow site ($X = a/4, Y = a/(4\sqrt{2})$) are: (1) $\theta = 0°$; (2) $\theta = 45°$ and $\varphi = 35.26$; (3) $\theta = 45°$ and $\varphi = 90°$; (4) $\theta = 45°$ and $\varphi = 144.74°$; (5) $\theta = 45°$ and $\varphi = 215.26°$; (6) $\theta = 45°$ and $\varphi = 270°$; (7) $\theta = 45°$ and $\varphi = 324.74°$; (8) $\theta = 90°$ and $\varphi = 35.26°$; (9) $\theta = 90°$ and $\varphi = 90°$; (10) $\theta = 90°$ and $\varphi = 144.74°$. The Fourier functions of the interpolation over φ on the top-hollow site are:

$$I_0(\varphi) = I(1) \tag{B.10}$$

$$a_0 = \frac{1}{16}(3(I(2) + I(4) + I(5) + I(7)) + 2(I(3) + I(6)))$$

$$a_1 = \frac{\sqrt{6}}{8}(I(2) - I(4) - I(5) + I(7))$$

$$a_2 = \frac{3}{16}(I(2) + I(4) + I(5) + I(7) - 2(I(3) + I(6)))$$

$$b_1 = \frac{1}{32\sqrt{3}}(9(I(2) + I(4) - I(5) - I(7)) + 10\sqrt{3}(I(3) - I(6)))$$

$$b_2 = \frac{3\sqrt{2}}{16}(I(2) - I(4) + I(5) - I(7))$$

$$b_3 = \frac{3}{32}(\sqrt{3}(I(2) + I(4) - I(5) - I(7)) + 2(I(6) - I(3)))$$

$$I_{45}(\varphi) = a_0 + a_1 \cos\varphi + a_2 \cos 2\varphi + b_1 \sin\varphi + b_2 \sin 2\varphi + b_3 \sin 3\varphi \tag{B.11}$$

$$I_{135}(\varphi) = a_0 - a_1 \cos\varphi + a_2 \cos 2\varphi - b_1 \sin\varphi + b_2 \sin 2\varphi - b_3 \sin 3\varphi \tag{B.12}$$

$$I_{90}(\varphi) = \frac{1}{8}[3I(8) + 3I(10) + 2I(9) + 3\sqrt{2}(I(8) - I(10))]\sin 2\varphi$$
$$+ 3[I(8) + I(10) - 2I(9))\cos 2\varphi] \tag{B.13}$$

The Fourier function for the interpolation over θ on the top-hollow (T-H) site is:

$$I_{T-H}(\theta, \varphi) = \frac{1}{4}[(I_0(\varphi) + I_{45}(\varphi) + I_{90}(\varphi) + I_{135}(\varphi))$$
$$+ (I_0(\varphi) - I_{45}(\varphi) + I_{90}(\varphi) - I_{135}(\varphi))\cos 4\theta]$$
$$+ \frac{1}{2}[(I_0(\varphi) - I_{90}(\varphi))\cos 2\theta + (I_{45}(\varphi) - I_{135}(\varphi))\sin 2\theta] \tag{B.14}$$

Once the (r,Z,θ,φ) interpolation is performed, one is left with one I^{6D} value for each of the five sites that conform the DFT energy grid: top I_T, hollow I_H, long-bridge I_{LB}, short-bridge I_{SB} and top-hollow I_{T-H}. Then, we use the 2D scattered cubic spline interpolation from Ref. [300] to get values in between each of top, hollow, long bridge and short bridge sites giving us a rectangular grid of nine values. On this grid we use a 2D periodic cubic spline [299] as in Ref. [301] to get the final value $I^{6D}(X,Y,Z,r,\varphi,\theta)$ from which we finally get the intended $V^{6D}(X,Y,Z,r,\varphi,\theta)$ by adding the corresponding V^{3D} values.

Bibliography

[1] U. Dingerdissen, A. Martin, D. Herein, and H. J. Wernicke, *The Development of Industrial Heterogeneous Catalysis*, in *Handbook of Heterogeneous Catalysis*, Wiley, 2008. (Cited on page 1.)

[2] J. W. Erisman, M. A. Sutton, J. Galloway, Z. Klimont, and W. Winiwarter, *How a century of ammonia synthesis changed the world*, Nature Geoscience **1**, 636 (2008). (Cited on page 1.)

[3] S. Rebsdat and D. Mayer, *Ethylene Oxide*, in *Ullmann's Encyclopedia of Industrial Chemistry*, Wiley, 2000. (Cited on page 1.)

[4] G. van der Laan and A. Beenackers, *Kinetics and Selectivity of the Fischer–Tropsch Synthesis: A Literature Review*, Catal. Rev. **41**, 255 (1999). (Cited on page 2.)

[5] H. Schulz, *Short history and present trends of Fischer–Tropsch synthesis*, Appl. Catal. A Gen. **186**, 3 (1999). (Cited on pages 2 and 121.)

[6] I. Chorkendorff and J. W. Niemantsverdriet, *Concepts of modern catalysis and kinetics*, John Wiley & Sons, 2006. (Cited on page 2.)

[7] R. Rioux, editor, *Model Systems in Catalysis*, Springer Science, 2010. (Cited on page 2.)

[8] B. Gates and H. Knözinger, editors, *Impact of Surface Science on Catalysis*, Elsevier, 2000. (Cited on page 2.)

[9] R. Díez Muiño and H. F. Busnengo, editors, *Dynamics of Gas-Surface Interactions*, Springer Berlin Heidelberg, 2013. (Cited on pages 3 and 23.)

[10] *Top500.org - Performance Development*, `http://www.top500.org/statistics/perfdevel`, Accessed: 11.11.2016. (Cited on page 3.)

[11] A. Groß, *Theoretical Surface Science*, Springer Nature, 2009. (Cited on pages 3 and 23.)

[12] A. Jain, S. P. Ong, G. Hautier, W. Chen, W. D. Richards, S. Dacek, S. Cholia, D. Gunter, D. Skinner, G. Ceder, and K. A. Persson, *Commentary: The Materials Project: A materials genome approach to accelerating materials innovation*, APL Mater. **1**, 011002 (2013). (Cited on page 3.)

[13] G.-J. Kroes, *Toward a Database of Chemically Accurate Barrier Heights for Reactions of Molecules with Metal Surfaces*, J. Phys. Chem. Lett. **6**, 4106 (2015). (Cited on page 3.)

[14] C. T. Campbell and M. T. Paffett, *Model studies of ethylene epoxidation catalyzed by the Ag(110) surface*, Surf. Sci. **139**, 396 (1984). (Cited on page 4.)

[15] C. T. Campbell, *Surface science study of selective ethylene epoxidation catalyzed by the Ag(110) surface: Structural sensitivity*, J. Vac. Sci. Technol. A **2**, 1024 (1984). (Cited on page 4.)

[16] K. Prince, G. Paolucci, and A. Bradshaw, *Oxygen adsorption on silver (110): Dispersion, bonding and precursor state*, Surf. Sci. **175**, 101 (1986). (Cited on pages 4, 38, and 74.)

[17] C. T. Campbell, *Atomic and molecular oxygen adsorption on Ag(111)*, Surf. Sci. **157**, 43 (1985). (Cited on pages 4, 36, 37, 51, and 91.)

[18] R. Guest, B. Hernnäs, P. Bennich, O. Björneholm, A. Nilsson, R. Palmer, and N. Mårtensson, *Orientation of a molecular precursor: a NEXAFS study of O_2/Ag(110)*, Surf. Sci. **278**, 239 (1992). (Cited on pages 4, 38, and 74.)

[19] L. Vattuone, M. Rocca, C. Boragno, and U. Valbusa, *Initial sticking coefficient of O_2 on Ag(110)*, J. Chem. Phys. **101**, 713 (1994). (Cited on pages 4, 35, 36, 37, 48, 49, 62, 63, 64, 69, 73, 79, and 91.)

[20] L. Vattuone, C. Boragno, M. Pupo, P. Restelli, M. Rocca, and U. Valbusa, *Azimuthal dependence of sticking probability of O_2 on Ag(110)*, Phys. Rev. Lett. **72**, 510 (1994). (Cited on pages 4, 35, 49, 63, 64, and 91.)

[21] L. Vattuone, M. Rocca, C. Boragno, and U. Valbusa, *Coverage dependence of sticking coefficient of O_2 on Ag(110)*, J. Chem. Phys. **101**, 726 (1994). (Cited on pages 4 and 35.)

[22] A. Raukema, D. A. Butler, and A. W. Kleyn, *The interaction of oxygen with the Ag(110) surface*, J. Phys.: Condens. Matter **8**, 2247 (1996). (Cited on pages 4, 35, 36, 48, 49, 62, 63, 64, 69, 79, and 91.)

[23] S. Kneitz, J. Gemeinhardt, and H.-P. Steinrück, *A molecular beam study of the adsorption dynamics of CO on Ru(0001), Cu(111) and a pseudomorphic Cu monolayer on Ru(0001)*, Surf. Sci. **440**, 307 (1999). (Cited on pages 4, 121, 123, 126, 127, 128, 135, and 136.)

[24] S. Kneitz, J. Gemeinhardt, H. Koschel, G. Held, and H.-P. Steinrück, *Energy and temperature dependent sticking coefficients of CO on ultrathin copper layers on Ru(001)*, Surf. Sci. **433-435**, 27 (1999). (Cited on pages 4, 121, 123, 126, and 128.)

[25] B. Riedmüller, I. Ciobîcă, D. Papageorgopoulos, B. Berenbak, R. van Santen, and A. Kleyn, *The dynamic interaction of CO with Ru(0001) in the presence of adsorbed CO and hydrogen*, Surf. Sci. **465**, 347 (2000). (Cited on pages 4, 121, 123, 126, 127, 128, 136, 137, 138, 139, 142, 143, and 145.)

[26] M. A. Fox and M. T. Dulay, *Heterogeneous photocatalysis*, Chem. Rev. **93**, 341 (1993). (Cited on page 4.)

[27] S. Linic, P. Christopher, and D. B. Ingram, *Plasmonic-metal nanostructures for efficient conversion of solar to chemical energy*, Nat. Mat. **10**, 911 (2011). (Cited on page 4.)

[28] P. Christopher, H. Xin, and S. Linic, *Visible-light-enhanced catalytic oxidation reactions on plasmonic silver nanostructures*, Nat. Chem. (2011). (Cited on page 4.)

[29] A. Marimuthu, J. Zhang, and S. Linic, *Tuning Selectivity in Propylene Epoxidation by Plasmon Mediated Photo-Switching of Cu Oxidation State*, Science **339**, 1590 (2013). (Cited on page 4.)

[30] M. Bonn, S. Funk, C. Hess, D. N. Denzler, C. Stampfl, M. Scheffler, M. Wolf, and G. Ertl, *Phonon- Versus Electron-Mediated Desorption and Oxidation of CO on Ru(0001)*, Science **285**, 1042 (1999). (Cited on pages 4, 99, and 103.)

[31] C. Frischkorn and M. Wolf, *Femtochemistry at Metal Surfaces: Nonadiabatic Reaction Dynamic*, Chem. Rev. **106**, 4207 (2006). (Cited on page 4.)

[32] R. Scholz, G. Floß, P. Saalfrank, G. Füchsel, I. Lončarić, and J. I. Juaristi, *Femtosecond-laser induced dynamics of CO on Ru(0001): Deep insights from a hot-electron friction model including surface motion*, Phys. Rev. B **94**, 165447 (2016). (Cited on pages 5 and 123.)

[33] H. Shull and G. G. Hall, *Atomic Units*, Nature **184**, 1559 (1959). (Cited on page 9.)

[34] M. Born and R. Oppenheimer, *Zur Quantentheorie der Molekeln*, Ann. Phys. **389**, 457 (1927). (Cited on page 10.)

[35] F. Jensen, *Introduction to computational chemistry*, John Wiley & Sons, 2013. (Cited on page 12.)

[36] P. Hohenberg and W. Kohn, *Inhomogeneous Electron Gas*, Phys. Rev. **136**, B864 (1964). (Cited on page 12.)

[37] W. Kohn and L. J. Sham, *Self-Consistent Equations Including Exchange and Correlation Effects*, Phys. Rev. **140**, A1133 (1965). (Cited on pages 13 and 15.)

[38] R. M. Martin, *Electronic structure: basic theory and practical methods*, Cambridge university press, 2004. (Cited on pages 15, 16, and 20.)

[39] D. M. Ceperley and B. J. Alder, *Ground State of the Electron Gas by a Stochastic Method*, Phys. Rev. Lett. **45**, 566 (1980). (Cited on page 16.)

[40] S. H. Vosko, L. Wilk, and M. Nusair, *Accurate spin-dependent electron liquid correlation energies for local spin density calculations: a critical analysis*, Can. J. Phys. **58**, 1200 (1980). (Cited on page 16.)

[41] J. P. Perdew and A. Zunger, *Self-interaction correction to density-functional approximations for many-electron systems*, Phys. Rev. B **23**, 5048 (1981). (Cited on page 16.)

[42] J. P. Perdew and Y. Wang, *Accurate and simple analytic representation of the electron-gas correlation energy*, Phys. Rev. B **45**, 13244 (1992). (Cited on page 16.)

[43] R. O. Jones and O. Gunnarsson, *The density functional formalism, its applications and prospects*, Rev. Mod. Phys. **61**, 689 (1989). (Cited on page 16.)

[44] K. Burke, *Perspective on density functional theory*, J. Chem. Phys. **136**, 150901 (2012). (Cited on page 17.)

[45] J. P. Perdew, K. Burke, and M. Ernzerhof, *Generalized Gradient Approximation Made Simple*, Phys. Rev. Lett. **77**, 3865 (1996). (Cited on pages 17, 40, and 84.)

[46] A. D. Becke, *Density-functional exchange-energy approximation with correct asymptotic behavior*, Phys. Rev. A **38**, 3098 (1988). (Cited on page 17.)

[47] C. Lee, W. Yang, and R. G. Parr, *Development of the Colle-Salvetti correlation-energy formula into a functional of the electron density*, Phys. Rev. B **37**, 785 (1988). (Cited on page 17.)

[48] B. Hammer, L. B. Hansen, and J. K. Nørskov, *Improved adsorption energetics within density-functional theory using revised Perdew-Burke-Ernzerhof functionals*, Phys. Rev. B **59**, 7413 (1999). (Cited on pages 17, 84, 122, and 124.)

[49] C. Díaz, E. Pijper, R. A. Olsen, H. F. Busnengo, D. J. Auerbach, and G. J. Kroes, *Chemically Accurate Simulation of a Prototypical Surface Reaction: H_2 Dissociation on Cu(111)*, Science **326**, 832 (2009). (Cited on pages 17, 84, and 88.)

[50] M. A. Marques, M. J. Oliveira, and T. Burnus, *Libxc: A library of exchange and correlation functionals for density functional theory*, Comput. Phys. Commun. **183**, 2272 (2012). (Cited on page 17.)

[51] J. Tao, J. P. Perdew, V. N. Staroverov, and G. E. Scuseria, *Climbing the Density Functional Ladder: Nonempirical Meta-Generalized Gradient Approximation Designed for Molecules and Solids*, Phys. Rev. Lett. **91**, 146401 (2003). (Cited on pages 18 and 88.)

[52] R. Peverati and D. G. Truhlar, *Quest for a universal density functional: the accuracy of density functionals across a broad spectrum of databases in chemistry and physics*, Phil. Trans. R. Soc. A **372** (2014). (Cited on pages 18 and 19.)

[53] J. Sun, M. Marsman, G. I. Csonka, A. Ruzsinszky, P. Hao, Y.-S. Kim, G. Kresse, and J. P. Perdew, *Self-consistent meta-generalized gradient approximation within the projector-augmented-wave method*, Phys. Rev. B **84**, 035117 (2011). (Cited on page 18.)

[54] E. Clementi and S. J. Chakravorty, *A comparative study of density functional models to estimate molecular atomization energies*, J. Chem. Phys. **93**, 2591 (1990). (Cited on page 18.)

[55] A. D. Becke, *A new mixing of Hartree-Fock and local density-functional theories*, J. Chem. Phys. **98**, 1372 (1993). (Cited on page 18.)

[56] J. P. Perdew, M. Ernzerhof, and K. Burke, *Rationale for mixing exact exchange with density functional approximations*, J. Chem. Phys. **105**, 9982 (1996). (Cited on page 18.)

[57] P. J. Stephens, F. J. Devlin, C. F. Chabalowski, and M. J. Frisch, *Ab Initio Calculation of Vibrational Absorption and Circular Dichroism Spectra Using Density Functional Force Fields*, J. Phys. Chem **98**, 11623 (1994). (Cited on page 19.)

[58] A. D. Becke, *Density-functional thermochemistry. III. The role of exact exchange*, J. Chem. Phys. **98**, 5648 (1993). (Cited on page 19.)

[59] J. Heyd, G. E. Scuseria, and M. Ernzerhof, *Hybrid functionals based on a screened Coulomb potential*, J. Chem. Phys. **118**, 8207 (2003). (Cited on pages 19 and 93.)

[60] J. Paier, M. Marsman, K. Hummer, G. Kresse, I. C. Gerber, and J. G. Ángyán, *Screened hybrid density functionals applied to solids*, J. Chem. Phys. **124**, 154709 (2006). (Cited on pages 19 and 93.)

[61] S. Grimme, *Semiempirical GGA-type density functional constructed with a long-range dispersion correction*, J. Comput. Chem. **27**, 1787 (2006). (Cited on pages 19, 122, and 124.)

[62] A. Tkatchenko and M. Scheffler, *Accurate Molecular Van Der Waals Interactions from Ground-State Electron Density and Free-Atom Reference Data*, Phys. Rev. Lett. **102**, 073005 (2009). (Cited on pages 19 and 86.)

[63] S. Grimme, J. Antony, S. Ehrlich, and H. Krieg, *A consistent and accurate ab initio parametrization of density functional dispersion correction (DFT-D) for the 94 elements H-Pu*, J. Chem. Phys. **132**, 154104 (2010). (Cited on page 19.)

[64] W. Liu, J. Carrasco, B. Santra, A. Michaelides, M. Scheffler, and A. Tkatchenko, *Benzene adsorbed on metals: Concerted effect of covalency and van der Waals bonding*, Phys. Rev. B **86**, 245405 (2012). (Cited on page 19.)

[65] M. Dion, H. Rydberg, E. Schröder, D. C. Langreth, and B. I. Lundqvist, *Van der Waals Density Functional for General Geometries*, Phys. Rev. Lett. **92**, 246401 (2004). (Cited on pages 19 and 88.)

[66] K. Berland, V. R. Cooper, K. Lee, E. Schröder, T. Thonhauser, P. Hyldgaard, and B. I. Lundqvist, *van der Waals forces in density functional theory: a review of the vdW-DF method*, Rep. Prog. Phys. **78**, 066501 (2015). (Cited on page 19.)

[67] P. Hyldgaard, K. Berland, and E. Schröder, *Interpretation of van der Waals density functionals*, Phys. Rev. B **90**, 075148 (2014). (Cited on page 19.)

[68] A. Ambrosetti, A. M. Reilly, R. A. DiStasio, and A. Tkatchenko, *Long-range correlation energy calculated from coupled atomic response functions*, J. Chem. Phys. **140**, 18A508 (2014). (Cited on page 20.)

[69] I. Lončarić and V. Despoja, *Benchmarking van der Waals functionals with non-contact RPA calculations on graphene-Ag(111)*, Phys. Rev. B **90**, 075414 (2014). (Cited on page 20.)

[70] F. Bloch, *Über die Quantenmechanik der Elektronen in Kristallgittern*, Z. Physik **52**, 555 (1929). (Cited on page 20.)

[71] H. J. Monkhorst and J. D. Pack, *Special points for Brillouin-zone integrations*, Phys. Rev. B **13**, 5188 (1976). (Cited on pages 21 and 40.)

[72] D. R. Hamann, M. Schlüter, and C. Chiang, *Norm-Conserving Pseudopotentials*, Phys. Rev. Lett. **43**, 1494 (1979). (Cited on page 21.)

[73] N. Troullier and J. L. Martins, *Efficient pseudopotentials for plane-wave calculations*, Phys. Rev. B **43**, 1993 (1991). (Cited on page 21.)

[74] K. Laasonen, R. Car, C. Lee, and D. Vanderbilt, *Implementation of ultrasoft pseudopotentials in ab initio molecular dynamics*, Phys. Rev. B **43**, 6796 (1991). (Cited on page 21.)

[75] P. E. Blöchl, *Projector augmented-wave method*, Phys. Rev. B **50**, 17953 (1994). (Cited on pages 21, 40, and 159.)

[76] G. Kresse and D. Joubert, *From ultrasoft pseudopotentials to the projector augmented-wave method*, Phys. Rev. B **59**, 1758 (1999). (Cited on pages 21, 40, and 159.)

[77] S. Sato, *On a New Method of Drawing the Potential Energy Surface*, J. Chem. Phys. **23**, 592 (1955). (Cited on page 23.)

[78] M. Karplus, R. N. Porter, and R. D. Sharma, *Exchange Reactions with Activation Energy. I. Simple Barrier Potential for (H, H_2)*, J. Chem. Phys. **43**, 3259 (1965). (Cited on page 23.)

[79] L. Martin-Gondre, C. Crespos, P. Larrégaray, J. Rayez, B. van Ootegem, and D. Conte, *Is the LEPS potential accurate enough to investigate the dissociation of diatomic molecules on surfaces?*, Chem. Phys. Lett. **471**, 136 (2009). (Cited on page 23.)

[80] L. Martin-Gondre, C. Crespos, P. Larrégaray, J. Rayez, D. Conte, and B. van Ootegem, *Detailed description of the flexible periodic London–Eyring–Polanyi–Sato potential energy function*, Chem. Phys. **367**, 136 (2010). (Cited on page 23.)

[81] M. S. Daw and M. I. Baskes, *Embedded-atom method: Derivation and application to impurities, surfaces, and other defects in metals*, Phys. Rev. B **29**, 6443 (1984). (Cited on page 23.)

[82] O. Bünermann, H. Jiang, Y. Dorenkamp, A. Kandratsenka, S. M. Janke, D. J. Auerbach, and A. M. Wodtke, *Electron-hole pair excitation determines the mechanism of hydrogen atom adsorption*, Science **350**, 1346 (2015). (Cited on page 23.)

[83] H. F. Busnengo, A. Salin, and W. Dong, *Representation of the 6D potential energy surface for a diatomic molecule near a solid surface*, J. Chem. Phys. **112**, 7641 (2000). (Cited on pages 23, 39, 43, 123, 165, and 167.)

[84] C. Crespos, M. Collins, E. Pijper, and G. Kroes, *Multi-dimensional potential energy surface determination by modified Shepard interpolation for a molecule–surface reaction: H_2 + Pt(111)*, Chem. Phys. Lett. **376**, 566 (2003). (Cited on page 23.)

[85] J. Behler, *Neural network potential-energy surfaces in chemistry: a tool for large-scale simulations*, Phys. Chem. Chem. Phys. **13**, 17930 (2011). (Cited on page 23.)

[86] M. Hestenes and E. Stiefel, *Methods of conjugate gradients for solving linear systems*, J. Res. Nat. Bur. Stand. **49**, 409 (1952). (Cited on page 26.)

[87] D. C. Liu and J. Nocedal, *On the limited memory BFGS method for large scale optimization*, Math. Prog. **45**, 503 (1989). (Cited on page 26.)

[88] E. Bitzek, P. Koskinen, F. Gähler, M. Moseler, and P. Gumbsch, *Structural Relaxation Made Simple*, Phys. Rev. Lett. **97**, 170201 (2006). (Cited on page 26.)

[89] D. J. Wales and J. P. K. Doye, *Global Optimization by Basin-Hopping and the Lowest Energy Structures of Lennard-Jones Clusters Containing up to 110 Atoms*, J. Phys. Chem. A **101**, 5111 (1997). (Cited on page 26.)

[90] S. Goedecker, *Minima hopping: An efficient search method for the global minimum of the potential energy surface of complex molecular systems*, J. Chem. Phys. **120**, 9911 (2004). (Cited on page 26.)

[91] S. Baroni, S. de Gironcoli, A. Dal Corso, and P. Giannozzi, *Phonons and related crystal properties from density-functional perturbation theory*, Rev. Mod. Phys. **73**, 515 (2001). (Cited on page 26.)

[92] B. Fornberg, *Generation of finite difference formulas on arbitrarily spaced grids*, Math. Comp. **51**, 699 (1988). (Cited on page 27.)

[93] M. L. Mckee and M. Page, *Computing Reaction Pathways on Molecular Potential Energy Surfaces*, in *Rev. Comp. Ch.*, pages 35–65, Wiley-Blackwell, 2007. (Cited on page 28.)

[94] G. Henkelman, G. Jóhannesson, and H. Jónsson, *Methods for Finding Saddle Points and Minimum Energy Paths*, in *Theoretical Methods in Condensed Phase Chemistry*, pages 269–302, Springer, 2002. (Cited on page 28.)

[95] G. Henkelman, B. P. Uberuaga, and H. Jónsson, *A climbing image nudged elastic band method for finding saddle points and minimum energy paths*, J. Chem. Phys. **113**, 9901 (2000). (Cited on pages 28 and 68.)

[96] G. Henkelman and H. Jónsson, *Improved tangent estimate in the nudged elastic band method for finding minimum energy paths and saddle points*, J. Chem. Phys. **113**, 9978 (2000). (Cited on pages 28 and 68.)

[97] D. J. Tannor, *Introduction to quantum mechanics*, University Science Books, 2007. (Cited on page 29.)

[98] P. Ehrenfest, *Bemerkung über die angenäherte Gültigkeit der klassischen Mechanik innerhalb der Quantenmechanik*, Z. Phys. A **45**, 455 (1927). (Cited on page 29.)

[99] H. Busnengo, E. Pijper, M. Somers, G. Kroes, A. Salin, R. Olsen, D. Lemoine, and W. Dong, *Six-dimensional quantum and classical dynamics study of H_2 (v= 0, J= 0) scattering from Pd (111)*, Chem. Phys. Lett. **356**, 515 (2002). (Cited on pages 29 and 30.)

[100] D. A. McCormack and G.-J. Kroes, *Accuracy of trajectory methods for activated adsorption of H_2 on Cu (100)*, Chemical physics letters **296**, 515 (1998). (Cited on pages 29 and 30.)

[101] L. Verlet, *Computer "Experiments" on Classical Fluids. I. Thermodynamical Properties of Lennard-Jones Molecules*, Phys. Rev. **159**, 98 (1967). (Cited on page 29.)

[102] D. Beeman, *Some multistep methods for use in molecular dynamics calculations*, J. Comput. Phys. **20**, 130 (1976). (Cited on pages 29, 54, 68, and 102.)

[103] S. A. Adelman and J. D. Doll, *Generalized Langevin equation approach for atom / solid-surface scattering: General formulation for classical scattering off harmonic solids*, J. Chem. Phys. **64**, 2375 (1976). (Cited on pages 30, 67, and 125.)

[104] J. C. Tully, *Dynamics of gas-surface interactions: 3D generalized Langevin model applied to fcc and bcc surfaces*, J. Chem. Phys. **73**, 1975 (1980). (Cited on pages 30, 31, 67, and 125.)

[105] H. F. Busnengo, W. Dong, and A. Salin, *Trapping, Molecular Adsorption, and Precursors for Nonactivated Chemisorption*, Phys. Rev. Lett. **93**, 236103 (2004). (Cited on pages 30, 31, and 67.)

[106] H. F. Busnengo, M. A. Di Césare, W. Dong, and A. Salin, *Surface temperature effects in dynamic trapping mediated adsorption of light molecules on metal surfaces: H_2 on Pd(111) and Pd(110)*, Phys. Rev. B **72**, 125411 (2005). (Cited on pages 30, 31, 67, 102, and 125.)

[107] B. Gergen, H. Nienhaus, W. H. Weinberg, and E. W. McFarland, *Chemically Induced Electronic Excitations at Metal Surfaces*, Science **294**, 2521 (2001). (Cited on page 31.)

[108] D. Krix, R. Nünthel, and H. Nienhaus, *Generation of hot charge carriers by adsorption of hydrogen and deuterium atoms on a silver surface*, Phys. Rev. B **75**, 073410 (2007). (Cited on page 31.)

[109] A. C. Luntz and M. Persson, *How adiabatic is activated adsorption/associative desorption?*, J. Chem. Phys. **123**, 074704 (2005). (Cited on page 31.)

[110] M. Lindenblatt, J. van Heys, and E. Pehlke, *Molecular dynamics of nonadiabatic processes at surfaces: Chemisorption of H/Al(111)*, Surf. Sci. **600**, 3624 (2006). (Cited on page 31.)

[111] J. I. Juaristi, M. Alducin, R. Díez Muiño, H. F. Busnengo, and A. Salin, *Role of Electron-Hole Pair Excitations in the Dissociative Adsorption of Diatomic Molecules on Metal Surfaces*, Phys. Rev. Lett. **100**, 116102 (2008). (Cited on pages 31 and 32.)

[112] N. Shenvi, S. Roy, and J. C. Tully, *Dynamical Steering and Electronic Excitation in NO Scattering from a Gold Surface*, Science **326**, 829 (2009). (Cited on pages 31 and 149.)

[113] M. Timmer and P. Kratzer, *Electron-hole spectra created by adsorption on metals from density functional theory*, Phys. Rev. B **79**, 165407 (2009). (Cited on page 31.)

[114] P. Echenique, R. Nieminen, and R. Ritchie, *Density functional calculation of stopping power of an electron gas for slow ions*, Solid State Commun. **37**, 779 (1981). (Cited on page 32.)

[115] P. M. Echenique, R. M. Nieminen, J. C. Ashley, and R. H. Ritchie, *Nonlinear stopping power of an electron gas for slow ions*, Phys. Rev. A **33**, 897 (1986). (Cited on page 32.)

[116] H. Winter, J. I. Juaristi, I. Nagy, A. Arnau, and P. M. Echenique, *Energy loss of slow ions in a nonuniform electron gas*, Phys. Rev. B **67**, 245401 (2003). (Cited on page 32.)

[117] J. I. Juaristi, A. Arnau, P. M. Echenique, C. Auth, and H. Winter, *Charge State Dependence of the Energy Loss of Slow Ions in Metals*, Phys. Rev. Lett. **82**, 1048 (1999). (Cited on page 32.)

[118] L. Martin-Gondre, M. Alducin, G. A. Bocan, R. Díez Muiño, and J. I. Juaristi, *Competition between Electron and Phonon Excitations in the Scattering of Nitrogen Atoms and Molecules off Tungsten and Silver Metal Surfaces*, Phys. Rev. Lett. **108**, 096101 (2012). (Cited on pages 32 and 68.)

[119] I. Goikoetxea, J. I. Juaristi, M. Alducin, and R. Díez Muiño, *Dissipative effects in the dynamics of N_2 on tungsten surfaces*, J. Phys.: Condens. Matter **21**, 264007 (2009). (Cited on page 32.)

[120] J. C. Tremblay, S. Monturet, and P. Saalfrank, *Electronic damping of anharmonic adsorbate vibrations at metallic surfaces*, Phys. Rev. B **81**, 125408 (2010). (Cited on page 32.)

[121] M. Blanco-Rey, J. Juaristi, R. Díez Muiño, H. Busnengo, G. Kroes, and M. Alducin, *Electronic Friction Dominates Hydrogen Hot-Atom Relaxation on Pd(100)*, Phys. Rev. Lett. **112**, 103203 (2014). (Cited on pages 32 and 33.)

[122] P. Saalfrank, J. I. Juaristi, M. Alducin, M. Blanco-Rey, and R. Díez Muiño, *Vibrational lifetimes of hydrogen on lead films: An ab initio molecular dynamics with electronic friction (AIMDEF) study*, J. Chem. Phys. **141**, 234702 (2014). (Cited on page 32.)

[123] O. Galparsoro, R. Pétuya, J. I. Juaristi, C. Crespos, M. Alducin, and P. Larrégaray, *Energy Dissipation to Tungsten Surfaces upon Eley–Rideal Recombination of N_2 and H_2*, J. Phys. Chem. C **119**, 15434 (2015). (Cited on page 32.)

[124] R. Feynman, *Forces in Molecules*, Phys. Rev. **56**, 340 (1939). (Cited on page 33.)

[125] P. H. Hünenberger, *Thermostat Algorithms for Molecular Dynamics Simulations*, in *Advanced Computer Simulation*, pages 105–149, Springer, 2005. (Cited on page 33.)

[126] S. I. Anisimov, B. L. Kapeliovich, and T. L. Perel'man, *Electron emission from metal surfaces exposed to ultrashort laser pulses*, JETP **39**, 375 (1974). (Cited on page 33.)

[127] C. Springer, M. Head-Gordon, and J. C. Tully, *Simulations of femtosecond laser-induced desorption of CO from Cu(100)*, Surf. Sci. **320**, L57 (1994). (Cited on pages 34 and 100.)

[128] H. Engelhardt and D. Menzel, *Adsorption of oxygen on silver single crystal surfaces*, Surf. Sci. **57**, 591 (1976). (Cited on page 36.)

[129] M. Bowker, M. Barteau, and R. Madix, *Oxygen induced adsorption and reaction of H_2, H_2O, CO and CO_2 on single crystal Ag(110)*, Surf. Sci. **92**, 528 (1980). (Cited on page 36.)

[130] M. Barteau and R. Madix, *The adsorption of molecular oxygen species on Ag(110)*, Surf. Sci. **97**, 101 (1980). (Cited on pages 36 and 37.)

[131] C. Backx, C. D. Groot, and P. Biloen, *Adsorption of oxygen on Ag(110) studied by high resolution ELS and TPD*, Surf. Sci. **104**, 300 (1981). (Cited on pages 36 and 37.)

[132] C. T. Campbell and M. T. Paffett, *The interactions of O_2, CO and CO_2 with Ag(110)*, Surf. Sci. **143**, 517 (1984). (Cited on pages 36 and 37.)

[133] M. Canepa, M. Salvietti, M. Traverso, and L. Mattera, *Surface reconstruction and thermal desorption: OAg(110) an experimental study*, Surf. Sci. **331-333**, 183 (1995). (Cited on page 36.)

[134] F. Bartolucci, R. Franchy, J. C. Barnard, and R. E. Palmer, *Two Chemisorbed Species of O_2 on Ag(110)*, Phys. Rev. Lett. **80**, 5224 (1998). (Cited on pages 36, 37, 50, and 74.)

[135] F. Bartolucci, *Negative Ionen-Resonanz von adsorbierten Molekülen*, PhD thesis, Forschungszentrum Jülich, 1998. (Cited on pages 36, 37, 51, and 77.)

[136] R. Franchy, F. Bartolucci, F. B. de Mongeot, F. Cemic, M. Rocca, U. Valbusa, L. Vattuone, S. Lacombe, K. Jacobi, K. B. K. Tang, R. E. Palmer, J. Villette, D. Teillet-Billy, and J. P. Gauyacq, *Negative ion resonances of O_2 adsorbed on Ag surfaces*, J. Phys.: Condens. Matter **12**, R53 (2000). (Cited on pages 36, 37, and 38.)

[137] I. I. Rzeźnicka, J. Lee, and J. T. Yates, *Electron-Stimulated Desorption Study of Oxygen Adsorbed on Ag(110). Observation of Inclined Physisorbed Species*, J. Phys. Chem. C **111**, 3705 (2007). (Cited on pages 36, 37, 38, 51, 74, and 77.)

[138] J. E. Klobas, M. Schmid, C. M. Friend, and R. J. Madix, *The dissociation-induced displacement of chemisorbed O_2 by mobile O atoms and the autocatalytic recombination of O due to chain fragmentation on Ag(110)*, Surf. Sci. **630**, 187 (2014). (Cited on pages 36, 37, 50, and 51.)

[139] U. Heinzmann, S. Holloway, A. W. Kleyn, R. E. Palmer, and K. J. Snowdon, *Orientation in molecule - surface interactions*, J. Phys.: Condens. Matter **8**, 3245 (1996). (Cited on pages 37 and 134.)

[140] L. Vattuone, M. Rocca, P. Restelli, M. Pupo, C. Boragno, and U. Valbusa, *Low-temperature dissocation of O_2 on Ag(110): Surface disorder and reconstruction*, Phys. Rev. B **49**, 5113 (1994). (Cited on pages 37 and 91.)

[141] K. B. K. Tang, P. J. Rous, and R. E. Palmer, *Energy and lifetime of the σ resonance of oriented O_2 physisorbed on Ag(110)*, Phys. Rev. B **52**, 12395 (1995). (Cited on page 38.)

[142] K. Tang, J. Villette, D. Teillet-Billy, J. Gauyacq, and R. Palmer, *Angular distributions in resonance electron scattering by oriented physisorbed molecules: O_2/Ag(110)*, Surf. Sci. **368**, 43 (1996), Vibrations at Surfaces. (Cited on page 38.)

[143] D. A. Outka, J. Stöhr, W. Jark, P. Stevens, J. Solomon, and R. J. Madix, *Orientation and bond length of molecular oxygen on Ag(110) and Pt(111): A near-edge x-ray-absorption fine-structure study*, Phys. Rev. B **35**, 4119 (1987). (Cited on pages 38 and 74.)

[144] J. Pawela-Crew, R. J. Madix, and J. Stöhr, *The effect of subsurface oxygen on the orientation of molecular oxygen on Ag(110)*, Surf. Sci. **339**, 23 (1995). (Cited on pages 38 and 74.)

[145] K. Prince, G. Paolucci, A. Bradshaw, K. Horn, and C. Mariani, *Oxygen adsorption on Ag(110): observation of a precursor state*, Vacuum **33**, 867 (1983). (Cited on pages 38 and 74.)

[146] K. Bange, T. Madey, and J. Sass, *The adsorption of oxygen on Ag(110): a new view of structure and bonding*, Chem. Phys. Lett. **113**, 56 (1985). (Cited on pages 38 and 74.)

[147] J. V. Barth, T. Zambelli, J. Wintterlin, R. Schuster, and G. Ertl, *Direct observation of mobility and interactions of oxygen molecules chemisorbed on the Ag(110) surface*, Phys. Rev. B **55**, 12902 (1997). (Cited on page 38.)

[148] J. R. Hahn, H. J. Lee, and W. Ho, *Electronic Resonance and Symmetry in Single-Molecule Inelastic Electron Tunneling*, Phys. Rev. Lett. **85**, 1914 (2000). (Cited on pages 38, 39, and 50.)

[149] T. Zambelli, J. V. Barth, and J. Wintterlin, *Thermal dissociation of chemisorbed oxygen molecules on Ag(110): an investigation by scanning tunnelling microscopy*, J. Phys.: Condens. Matter **14**, 4241 (2002). (Cited on page 38.)

[150] J. R. Hahn and W. Ho, *Chemisorption and dissociation of single oxygen molecules on Ag(110)*, J. Chem. Phys. **123**, 214702 (2005). (Cited on pages 38, 39, 50, and 51.)

[151] J. R. Hahn and W. Ho, *Orbital specific chemistry: Controlling the pathway in single-molecule dissociation*, J. Chem. Phys. **122**, 244704 (2005). (Cited on page 38.)

[152] M. Smerieri, L. Savio, L. Vattuone, and M. Rocca, *O_2 dissociation before the onset of added row nucleation on Ag(110): an atomistic scanning tunnelling microscopy view*, J. Phys.: Condens. Matter **22**, 304015 (2010). (Cited on page 38.)

[153] P. Gravil, J. White, and D. Bird, *Chemisorption of O_2 on Ag(110)*, Surf. Sci. **352-354**, 248 (1996). (Cited on pages 38, 48, 49, and 159.)

[154] P. A. Gravil, D. M. Bird, and J. A. White, *Adsorption and Dissociation of O_2 on Ag(110)*, Phys. Rev. Lett. **77**, 3933 (1996). (Cited on pages 38, 48, 49, 51, and 159.)

[155] D. Bird and P. Gravil, *First-principles calculations of molecular dissociation at surfaces*, Surf. Sci. **377-379**, 555 (1997). (Cited on pages 38, 39, 48, 49, 51, and 159.)

[156] M. Alducin, D. Sánchez-Portal, A. Arnau, and N. Lorente, *Mixed-Valency Signature in Vibrational Inelastic Electron Tunneling Spectroscopy*, Phys. Rev. Lett. **104**, 136101 (2010). (Cited on pages 38, 39, 49, 50, and 159.)

[157] S. Monturet, M. Alducin, and N. Lorente, *Role of molecular electronic structure in inelastic electron tunneling spectroscopy: O_2 on Ag(110)*, Phys. Rev. B **82**, 085447 (2010). (Cited on pages 38, 39, 49, 50, and 159.)

[158] F. Olsson, N. Lorente, and M. Persson, *STM images of molecularly and atomically chemisorbed oxygen on silver*, Surf. Sci. **522**, L27 (2003). (Cited on pages 38, 39, 49, and 159.)

[159] S. Roy, V. Mujica, and M. A. Ratner, *Chemistry at molecular junctions: Rotation and dissociation of O_2 on the Ag(110) surface induced by a scanning tunneling microscope*, J. Chem. Phys. **139**, 074702 (2013). (Cited on pages 38, 39, 48, 49, 51, and 159.)

[160] T. B. Rawal, S. Hong, A. Pulkkinen, M. Alatalo, and T. S. Rahman, *Adsorption, diffusion, and vibration of oxygen on* Ag(110), Phys. Rev. B **92**, 035444 (2015). (Cited on pages 38, 39, 49, 50, 159, and 160.)

[161] V. I. Pazzi and G. F. Tantardini, *Dynamics of oxygen adsorption on Ag(110): surface motion effects*, Surf. Sci. **377-379**, 572 (1997). (Cited on pages 38 and 39.)

[162] V. I. Pazzi, P. H. T. Philipsen, E. J. Baerends, and G. F. Tantardini, *Oxygen adsorption on Ag(110): density functional theory band structure calculations and dynamical simulations*, Surf. Sci. **443**, 1 (1999). (Cited on pages 38 and 39.)

[163] V. I. Pazzi and G. F. Tantardini, *Dynamical simulations of the oxygen adsorption on the Ag(110) surface*, J. Mol. Catal. A-Chem. **119**, 289 (1997). (Cited on page 38.)

[164] P. van Den Hoek and E. Baerends, *Chemisorption and dissociation of O_2, on Ag(110)*, Surf. Sci. **221**, L791 (1989). (Cited on page 38.)

[165] H. Nakatsuji and H. Nakai, *Theoretical study on molecular and dissociative chemisorptions of an O_2 molecule on an Ag surface: dipped adcluster model combined with symmetry-adapted cluster-configuration interaction method*, Chem. Phys. Lett. **174**, 283 (1990). (Cited on page 38.)

[166] M. R. Salazar, J. D. Kress, and A. Redondo, *Dissociation of molecular oxygen on unpromoted and cesium promoted Ag(110) surfaces*, Surf. Sci. **469**, 80 (2000). (Cited on page 38.)

[167] M. Alducin, H. F. Busnengo, and R. Díez Muiño, *Dissociative dynamics of spin-triplet and spin-singlet O_2 on Ag(100)*, J. Chem. Phys. **129**, 224702 (2008). (Cited on pages 39, 49, 53, 55, 62, 63, 73, and 85.)

[168] I. Goikoetxea, J. Beltrán, J. Meyer, J. I. Juaristi, M. Alducin, and K. Reuter, *Non-adiabatic effects during the dissociative adsorption of O_2 at Ag(111)? A first-principles divide and conquer study*, New J. Phys. **14**, 013050 (2012). (Cited on pages 39, 49, 53, 55, 62, 63, and 85.)

[169] I. Goikoetxea, J. Meyer, J. I. Juaristi, M. Alducin, and K. Reuter, *Role of Physisorption States in Molecular Scattering: A Semilocal Density-Functional Theory Study on O_2/Ag(111)*, Phys. Rev. Lett. **112**, 156101 (2014). (Cited on pages 39, 68, and 85.)

[170] G. Kresse and J. Furthmüller, *Efficiency of ab-initio total energy calculations for metals and semiconductors using a plane-wave basis set*, Comput. Mater. Sci. **6**, 15 (1996). (Cited on pages 40, 124, and 159.)

[171] G. Kresse and J. Furthmüller, *Efficient iterative schemes for ab initio total-energy calculations using a plane-wave basis set*, Phys. Rev. B **54**, 11169 (1996). (Cited on pages 40, 124, and 159.)

[172] R. Wyckoff, *Crystal Structures*, Crystal Structures, Interscience Publishers, 1963. (Cited on page 40.)

[173] M. Methfessel and A. T. Paxton, *High-precision sampling for Brillouin-zone integration in metals*, Phys. Rev. B **40**, 3616 (1989). (Cited on page 40.)

[174] Y. Kuk and L. C. Feldman, *Oscillatory relaxation of the Ag(110) surface*, Phys. Rev. B **30**, 5811 (1984). (Cited on page 40.)

[175] D. R. Lide, editor, *CRC Handbook of Chemistry and Physics*, American Chemical Society (ACS), 86 edition, 2005. (Cited on pages 40 and 41.)

[176] S. Klüpfel, P. Klüpfel, and H. Jónsson, *The effect of the Perdew-Zunger self-interaction correction to density functionals on the energetics of small molecules*, J. Chem. Phys. **137** (2012). (Cited on page 41.)

[177] S. R. Bahn and K. W. Jacobsen, *An object-oriented scripting interface to a legacy electronic structure code*, Comput. Sci. Eng. **4**, 56 (2002). (Cited on pages 45 and 68.)

[178] M. Spruit and A. Kleyn, *Dissociative adsorption of O_2 on Ag(111)*, Chem. Phys. Lett. **159**, 342 (1989). (Cited on pages 49, 53, and 62.)

[179] F. de Mongeot, U. Valbusa, and M. Rocca, *Oxygen adsorption on Ag(111)*, Surf. Sci. **339**, 291 (1995). (Cited on pages 49 and 53.)

[180] F. de Mongeot, M. Rocca, and U. Valbusa, *Energy and angle dependence of the initial sticking coefficient of O_2 on Ag(001)*, Surf. Sci. **363**, 68 (1996). (Cited on pages 49, 53, 62, 63, and 73.)

[181] F. de Mongeot, M. Rocca, and U. Valbusa, *Isothermal desorption of O_2 from Ag(001)*, Surf. Sci. **377-379**, 691 (1997). (Cited on page 49.)

[182] G. Henkelman, A. Arnaldsson, and H. Jónsson, *A fast and robust algorithm for Bader decomposition of charge density*, Comput. Mater. Sci. **36**, 354 (2006). (Cited on page 49.)

[183] E. Sanville, S. D. Kenny, R. Smith, and G. Henkelman, *Improved grid-based algorithm for Bader charge allocation*, J. Comp. Chem. **28**, 899 (2007). (Cited on page 49.)

[184] W. Tang, E. Sanville, and G. Henkelman, *A grid-based Bader analysis algorithm without lattice bias*, J. Phys.: Condens. Matter **21**, 084204 (2009). (Cited on page 49.)

[185] I. Goikoetxea, M. Alducin, R. Díez Muiño, and J. I. Juaristi, *Dissociative and non-dissociative adsorption dynamics of N_2 on Fe(110)*, Phys. Chem. Chem. Phys. **14**, 7471 (2012). (Cited on pages 55, 60, and 68.)

[186] I. Goikoetxea, J. I. Juaristi, R. Díez Muiño, and M. Alducin, *Surface Strain Improves Molecular Adsorption but Hampers Dissociation for* N_2 *on the* Fe/W(110) *Surface*, Phys. Rev. Lett. **113**, 066103 (2014). (Cited on pages 55 and 68.)

[187] J. C. Polanyi and W. H. Wong, *Location of Energy Barriers. I. Effect on the Dynamics of Reactions A+BC*, J. Chem. Phys. **51**, 1439 (1969). (Cited on page 59.)

[188] M. J. Murphy, J. F. Skelly, A. Hodgson, and B. Hammer, *Inverted vibrational distributions from N_2 recombination at Ru(001): Evidence for a metastable molecular chemisorption well*, J. Chem. Phys. **110**, 6954 (1999). (Cited on page 59.)

[189] R. R. Smith, D. R. Killelea, D. F. DelSesto, and A. L. Utz, *Preference for Vibrational over Translational Energy in a Gas-Surface Reaction*, Science **304**, 992 (2004). (Cited on page 59.)

[190] C. Díaz and R. A. Olsen, *A note on the vibrational efficacy in molecule-surface reactions*, J. Chem. Phys. **130**, 094706 (2009). (Cited on page 59.)

[191] B. Jiang, X. Ren, D. Xie, and H. Guo, *Enhancing dissociative chemisorption of H_2O on Cu(111) via vibrational excitation*, PNAS **109**, 10224 (2012). (Cited on page 59.)

[192] A. Raukema, D. A. Butler, F. M. Box, and A. W. Kleyn, *Dissociative and non-dissociative sticking of O_2 at the Ag(111) surface*, Surf. Sci. **347**, 151 (1996). (Cited on pages 62 and 63.)

[193] G. Katz, Y. Zeiri, and R. Kosloff, *Nonadiabatic charge transfer processes of oxygen on metal surfaces*, Isr. J. Chem. **45**, 27 (2005). (Cited on page 62.)

[194] J. Behler, B. Delley, S. Lorenz, K. Reuter, and M. Scheffler, *Dissociation of O_2 at Al(111): The Role of Spin Selection Rules*, Phys. Rev. Lett. **94**, 036104 (2005). (Cited on pages 62, 73, and 74.)

[195] F. Nattino, O. Galparsoro, F. Costanzo, R. Díez Muiño, M. Alducin, and G.-J. Kroes, *Modeling surface motion effects in N_2 dissociation on W(110): Ab initio molecular dynamics calculations and generalized Langevin oscillator model*, J. Chem. Phys. **144**, 244708 (2016). (Cited on page 68.)

[196] G. Bracco, L. Bruschi, L. Pedemonte, and R. Tatarek, *Temperature dependence of the Ag(110) surface phonons*, Surf. Sci. **377-379**, 325 (1997). (Cited on page 68.)

[197] S. Narasimhan, *Ab initio lattice dynamics of Ag(110)*, Surf. Sci. **496**, 331 (2002). (Cited on page 68.)

[198] D. Sheppard, R. Terrell, and G. Henkelman, *Optimization methods for finding minimum energy paths*, J. Chem. Phys. **128**, 134106 (2008). (Cited on page 68.)

[199] D. Sheppard and G. Henkelman, *Paths to which the nudged elastic band converges*, J. Comput. Chem. **32**, 1769 (2011). (Cited on page 68.)

[200] L. Vattuone, U. Burghaus, U. Valbusa, and M. Rocca, *Breakdown of normal energy scaling at high impact energy for O_2 on Ag(001)*, Surf. Sci. **408**, L693 (1998). (Cited on page 73.)

[201] K. Honkala and K. Laasonen, *Oxygen Molecule Dissociation on the Al(111) Surface*, Phys. Rev. Lett. **84**, 705 (2000). (Cited on page 73.)

[202] Y. Yourdshahyan, B. Razaznejad, and B. I. Lundqvist, *Adiabatic potential-energy surfaces for oxygen on Al(111)*, Phys. Rev. B **65**, 075416 (2002). (Cited on page 73.)

[203] J. Behler, K. Reuter, and M. Scheffler, *Nonadiabatic effects in the dissociation of oxygen molecules at the Al(111) surface*, Phys. Rev. B **77**, 115421 (2008). (Cited on pages 73 and 74.)

[204] H.-R. Liu, H. Xiang, and X. G. Gong, *First principles study of adsorption of O_2 on Al surface with hybrid functionals*, J. Chem. Phys. **135**, 214702 (2011). (Cited on pages 73, 74, and 93.)

[205] F. Libisch, C. Huang, P. Liao, M. Pavone, and E. A. Carter, *Origin of the Energy Barrier to Chemical Reactions of O_2 on Al(111): Evidence for Charge Transfer, Not Spin Selection*, Phys. Rev. Lett. **109**, 198303 (2012). (Cited on pages 73, 74, 83, and 97.)

[206] W. M. C. Foulkes, L. Mitas, R. J. Needs, and G. Rajagopal, *Quantum Monte Carlo simulations of solids*, Rev. Mod. Phys. **73**, 33 (2001). (Cited on page 83.)

[207] G. H. Booth, A. Grüneis, G. Kresse, and A. Alavi, *Towards an exact description of electronic wavefunctions in real solids*, Nature **493**, 365 (2012). (Cited on page 83.)

[208] J. P. Perdew and K. Schmidt, *Jacob's ladder of density functional approximations for the exchange-correlation energy*, AIP Conf. Proc. **577**, 1 (2001). (Cited on page 84.)

[209] G. A. Bocan, R. Díez Muiño, M. Alducin, H. F. Busnengo, and A. Salin, *The role of exchange-correlation functionals in the potential energy surface and dynamics of N_2 dissociation on W surfaces*, J. Chem. Phys. **128**, 154704 (2008). (Cited on page 84.)

[210] K. R. Geethalakshmi, J. I. Juaristi, R. Díez Muiño, and M. Alducin, *Non-reactive scattering of N_2 from the W(110) surface studied with different exchange-correlation functionals*, Phys. Chem. Chem. Phys. **13**, 4357 (2011). (Cited on page 84.)

[211] G.-J. Kroes, *Towards chemically accurate simulation of molecule-surface reactions*, Phys. Chem. Chem. Phys. **14**, 14966 (2012). (Cited on page 84.)

[212] J. P. Perdew, A. Ruzsinszky, G. I. Csonka, O. A. Vydrov, G. E. Scuseria, L. A. Constantin, X. Zhou, and K. Burke, *Restoring the Density-Gradient Expansion for Exchange in Solids and Surfaces*, Phys. Rev. Lett. **100**, 136406 (2008). (Cited on page 85.)

[213] T. Bučko, S. Lebègue, T. Gould, and J. G. Ángyán, *Many-body dispersion corrections for periodic systems: an efficient reciprocal space implementation.*, J. Phys. Condens. Matter **28**, 045201 (2016). (Cited on page 86.)

[214] K. Berland and P. Hyldgaard, *Exchange functional that tests the robustness of the plasmon description of the van der Waals density functional*, Phys. Rev. B **89**, 035412 (2014). (Cited on page 88.)

[215] P. Giannozzi et al., *QUANTUM ESPRESSO: a modular and open-source software project for quantum simulations of materials*, J. Phys.: Condens. Matter **21**, 395502 (19pp) (2009). (Cited on pages 88, 159, and 163.)

[216] J. P. Perdew, A. Ruzsinszky, G. I. Csonka, L. A. Constantin, and J. Sun, *Workhorse Semilocal Density Functional for Condensed Matter Physics and Quantum Chemistry*, Phys. Rev. Lett. **103**, 026403 (2009). (Cited on page 88.)

[217] J. Sun, B. Xiao, and A. Ruzsinszky, *Communication : Effect of the orbital-overlap dependence in the meta generalized gradient approximation*, J. Chem. Phys. **137**, 051101 (2012). (Cited on page 88.)

[218] J. Sun, R. Haunschild, B. Xiao, I. W. Bulik, G. E. Scuseria, and J. P. Perdew, *Semilocal and hybrid meta-generalized gradient approximations based on the understanding of the kinetic-energy-density dependence*, J. Chem. Phys. **138**, 044113 (2013). (Cited on pages 88 and 95.)

[219] Y. Zhao and D. G. Truhlar, *A new local density functional for main-group thermochemistry, transition metal bonding, thermochemical kinetics, and noncovalent interactions*, J. Chem. Phys. **125**, 194101 (2006). (Cited on page 88.)

[220] A. V. Krukau, O. A. Vydrov, A. F. Izmaylov, and G. E. Scuseria, *Influence of the exchange screening parameter on the performance of screened hybrid functionals*, J. Chem. Phys. **125**, 224106 (2006). (Cited on page 93.)

[221] L. Schimka, J. Harl, and G. Kresse, *Improved hybrid functional for solids: The HSEsol functional*, J. Chem. Phys. **134**, 024116 (2011). (Cited on page 95.)

[222] V. Fiorin, D. Borthwick, and D. A. King, *Surface Thermodynamics: Small Molecule Adsorption Calorimetry on Metal Single Crystals*, in *Model Systems in Catalysis: Single Crystals to Supported Enzyme Mimics*, edited by R. Rioux, pages 175–201, Springer New York, 2010. (Cited on page 97.)

[223] W. Ho, *Femtosecond laser-induced dynamical quantum processes on solid surfaces (DQPSS)*, Surf. Sci. **363**, 166 (1996). (Cited on pages 99 and 104.)

[224] P. Saalfrank, *Quantum Dynamical Approach to Ultrafast Molecular Desorption from Surfaces*, Chem. Rev. **106**, 4116 (2006). (Cited on pages 99 and 104.)

[225] H. Guo, P. Saalfrank, and T. Seideman, *Theory of photoinduced surface reactions of admolecules*, Prog. Surf. Sci. **62**, 239 (1999). (Cited on page 99.)

[226] P. Saalfrank, M. Nest, I. Andrianov, T. Klamroth, D. Kröner, and S. Beyvers, *Quantum dynamics of laser-induced desorption from metal and semiconductor surfaces, and related phenomena*, J. Phys.: Condens. Matter **18**, S1425 (2006). (Cited on pages 99 and 113.)

[227] J. A. Prybyla, T. F. Heinz, J. A. Misewich, M. M. T. Loy, and J. H. Glownia, *Desorption induced by femtosecond laser pulses*, Phys. Rev. Lett. **64**, 1537 (1990). (Cited on page 99.)

[228] C. Springer and M. Head-Gordon, *Simulations of the femtosecond laser-induced desorption of CO from Cu(100) at 0.5 ML coverage*, Chem. Phys. **205**, 73 (1996). (Cited on pages 100 and 104.)

[229] A. C. Luntz, M. Persson, S. Wagner, C. Frischkorn, and M. Wolf, *Femtosecond laser induced associative desorption of H2 from Ru(0001): Comparison of "first principles" theory with experiment*, J. Chem. Phys. **124**, 244702 (2006). (Cited on page 100.)

[230] G. Füchsel, T. Klamroth, S. Monturet, and P. Saalfrank, *Dissipative dynamics within the electronic friction approach: the femtosecond laser desorption of H_2/D_2 from Ru(0001)*, Phys. Chem. Chem. Phys. **13**, 8659 (2011). (Cited on pages 100, 105, 111, 114, and 119.)

[231] S. R. Hatch, X. Y. Zhu, J. M. White, and A. Campion, *Photoinduced pathways to dissociation and desorption of dioxygen on silver (110) and platinum (111)*, J. Phys. Chem. **95**, 1759 (1991). (Cited on page 101.)

[232] R. Pelak and W. Ho, *Low temperature surface photochemistry: O_2 and CO on Ag(110) at 30 K*, Surf. Sci. **321**, L233 (1994). (Cited on page 101.)

[233] Q.-S. Xin and X.-Y. Zhu, *Is localized collision responsible for O_2 photodesorption from Ag(110)?*, Surf. Sci. **347**, 346 (1996). (Cited on page 101.)

[234] J. C. Tully, G. H. Gilmer, and M. Shugard, *Molecular dynamics of surface diffusion. I. The motion of adatoms and clusters*, J. Chem. Phys. **71**, 1630 (1979). (Cited on page 102.)

[235] D. N. Denzler, C. Frischkorn, C. Hess, M. Wolf, and G. Ertl, *Electronic Excitation and Dynamic Promotion of a Surface Reaction*, Phys. Rev. Lett. **91**, 226102 (2003). (Cited on pages 103 and 105.)

[236] Z. Lin, L. V. Zhigilei, and V. Celli, *Electron-phonon coupling and electron heat capacity of metals under conditions of strong electron-phonon nonequilibrium*, Phys. Rev. B **77**, 075133 (2008). (Cited on page 103.)

[237] E. Majchrzak and J. Poteralska, *Two-temperature microscale heat transfer model. Part II: Determination of lattice parameters*, Scientific Research of the Institute of Mathematics and Computer Science **9**, 109 (2010). (Cited on page 103.)

[238] E. Palik, *Handbook of optical properties of solids*, Academic, 1985. (Cited on page 103.)

[239] L. M. Struck, L. J. Richter, S. A. Buntin, R. R. Cavanagh, and J. C. Stephenson, *Femtosecond Laser-Induced Desorption of CO from Cu(100): Comparison of Theory and Experiment*, Phys. Rev. Lett. **77**, 4576 (1996). (Cited on page 104.)

[240] P. Szymanski, A. L. Harris, and N. Camillone, *Temperature-Dependent Femtosecond Photoinduced Desorption in CO/Pd(111)*, J. Phys. Chem. A **111**, 12524 (2007). (Cited on page 104.)

[241] P. Saalfrank, G. Boendgen, K. Finger, and L. Pesce, *Photodesorption of NO from a metal surface: quantum dynamical implications of a two-mode model*, Chem. Phys. **251**, 51 (2000). (Cited on page 104.)

[242] F.-J. Kao, D. G. Busch, D. Cohen, D. Gomes da Costa, and W. Ho, *Femtosecond laser desorption of molecularly adsorbed oxygen from Pt(111)*, Phys. Rev. Lett. **71**, 2094 (1993). (Cited on page 104.)

[243] S. Gao, *Quantum kinetic theory of vibrational heating and bond breaking by hot electrons*, Phys. Rev. B **55**, 1876 (1997). (Cited on page 104.)

[244] P. Szymanski, A. L. Harris, and N. Camillone, *Adsorption-state-dependent subpicosecond photoinduced desorption dynamics*, J. Chem. Phys. **126**, 214709 (2007). (Cited on page 104.)

[245] F. M. Zimmermann and W. Ho, *State resolved studies of photochemical dynamics at surfaces*, Surf. Sci. Rep. **22**, 127 (1995). (Cited on page 111.)

[246] D. Oxtoby, H. Gillis, and L. Butler, *Principles of modern chemistry*, Cengage Learning, 2015. (Cited on page 112.)

[247] M. Brandbyge, P. Hedegård, T. F. Heinz, J. A. Misewich, and D. M. Newns, *Electronically driven adsorbate excitation mechanism in femtosecond-pulse laser desorption*, Phys. Rev. B **52**, 6042 (1995). (Cited on page 114.)

[248] S. Babar and J. H. Weaver, *Optical constants of Cu, Ag, and Au revisited*, Appl. Opt. **54**, 477 (2015). (Cited on page 118.)

[249] M. N. Polyanskiy, *Refractive index database*. (Cited on page 118.)

[250] H. Pfnür, D. Menzel, F. Hoffmann, A. Ortega, and A. Bradshaw, *High resolution vibrational spectroscopy of CO on Ru(001): The importance of lateral interactions*, Surf. Sci. **93**, 431 (1980). (Cited on page 121.)

[251] D. E. Starr and H. Bluhm, *CO adsorption and dissociation on Ru(0001) at elevated pressures*, Surf. Sci. **608**, 241 (2013). (Cited on page 121.)

[252] M. Dell'Angela et al., *Real-Time Observation of Surface Bond Breaking with an X-ray Laser*, Science **339**, 1302 (2013). (Cited on page 121.)

[253] H. Öström et al., *Probing the transition state region in catalytic CO oxidation on Ru*, Science **347**, 978 (2015). (Cited on page 121.)

[254] A. Böttcher, H. Niehus, S. Schwegmann, H. Over, and G. Ertl, *CO Oxidation Reaction over Oxygen-Rich Ru(0001) Surfaces*, J. Phys. Chem. B **101**, 11185 (1997). (Cited on page 121.)

[255] C. Stampfl and M. Scheffler, *Anomalous Behavior of Ru for Catalytic Oxidation: A Theoretical Study of the Catalytic Reaction* $CO + \frac{1}{2}O_2 \rightarrow CO_2$, Phys. Rev. Lett. **78**, 1500 (1997). (Cited on page 121.)

[256] S. Funk, M. Bonn, D. N. Denzler, C. Hess, M. Wolf, and G. Ertl, *Desorption of CO from Ru(001) induced by near-infrared femtosecond laser pulses*, J. Chem. Phys. **112**, 9888 (2000). (Cited on page 121.)

[257] W. F. Lin, P. A. Christensen, A. Hamnett, M. S. Zei, and G. Ertl, *The Electro-Oxidation of CO at the Ru(0001) Single-Crystal Electrode Surface*, J. Phys. Chem. B **104**, 6642 (2000). (Cited on page 121.)

[258] I. M. Ciobica and R. A. van Santen, *Carbon Monoxide Dissociation on Planar and Stepped Ru(0001) Surfaces*, J. Phys. Chem. B **107**, 3808 (2003). (Cited on page 121.)

[259] H. Xin et al., *Strong Influence of Coadsorbate Interaction on CO Desorption Dynamics on Ru(0001) Probed by Ultrafast X-Ray Spectroscopy and Ab Initio Simulations*, Phys. Rev. Lett. **114**, 156101 (2015). (Cited on page 121.)

[260] M. Beye et al., *Selective Ultrafast Probing of Transient Hot Chemisorbed and Precursor States of CO on Ru(0001)*, Phys. Rev. Lett. **110**, 186101 (2013). (Cited on page 121.)

[261] J. Gladh, T. Hansson, and H. Öström, *Electron- and phonon-coupling in femtosecond laser-induced desorption of {CO} from Ru(0001)*, Surf. Sci. **615**, 65 (2013). (Cited on page 121.)

[262] H. Over, W. Moritz, and G. Ertl, *Anisotropic atomic motions in structural analysis by low energy electron diffraction*, Phys. Rev. Lett. **70**, 315 (1993). (Cited on page 121.)

[263] H. Pfnür, P. Feulner, and D. Menzel, *The influence of adsorbate interactions on kinetics and equilibrium for CO on Ru(001). II. Desorption kinetics and equilibrium*, J. Chem. Phys. **79**, 4613 (1983). (Cited on page 121.)

[264] F. B. de Mongeot, M. Scherer, B. Gleich, E. Kopatzki, and R. Behm, *CO adsorption and oxidation on bimetallic Pt/Ru(0001) surfaces – a combined STM and TPD/TPR study*, Surf. Sci. **411**, 249 (1998). (Cited on page 121.)

[265] H. Pfnür and D. Menzel, *The influence of adsorbate interactions on kinetics and equilibrium for CO on Ru(001). I. Adsorption kinetics*, J. Chem. Phys. **79**, 2400 (1983). (Cited on pages 121, 123, and 128.)

[266] H. Steinrück and R. Madix, *The interaction of CO and Ar molecular beams with Ir(110)*, Surf. Sci. **185**, 36 (1987). (Cited on pages 121 and 128.)

[267] M. D'evelyn, H.-P. Steinrück, and R. Madix, *Precursors and trapping in the molecular chemisorption of CO on Ni(100)*, Surf. Sci. **180**, 47 (1987). (Cited on pages 121, 128, and 139.)

[268] S. L. Tang, J. D. Beckerle, M. B. Lee, and S. T. Ceyer, *Effect of translational energy on the molecular chemisorption of CO on Ni(111): Implications for the dynamics of the chemisorption process*, J. Chem. Phys. **84**, 6488 (1986). (Cited on page 121.)

[269] C. Campbell, G. Ertl, H. Kuipers, and J. Segner, *A molecular beam investigation of the interactions of CO with a Pt(111) surface*, Surf. Sci. **107**, 207 (1981). (Cited on page 121.)

[270] T. Engel, *A molecular beam investigation of He, CO, and O_2 scattering from Pd(111)*, J. Chem. Phys. **69**, 373 (1978). (Cited on page 121.)

[271] A. W. Kleyn, *Molecular beams and chemical dynamics at surfaces*, Chem. Soc. Rev. **32**, 87 (2003). (Cited on pages 122 and 139.)

[272] G. Füchsel, J. C. Tremblay, and P. Saalfrank, *A six-dimensional potential energy surface for Ru (0001)(2× 2): CO*, J. Chem. Phys. **141**, 094704 (2014). (Cited on pages 122 and 123.)

[273] P. Feibelman, B. Hammer, J. Nørskov, F. Wagner, M. Scheffler, R. Stumpf, R. Watwe, and J. Dumesic, *The CO/Pt(111) Puzzle*, J. Phys. Chem. B **105**, 4018 (2001). (Cited on page 122.)

[274] P. Lazić, M. Alaei, N. Atodiresei, V. Caciuc, R. Brako, and S. Blügel, *Density functional theory with nonlocal correlation: A key to the solution of the CO adsorption puzzle*, Phys. Rev. B **81**, 045401 (2010). (Cited on page 122.)

[275] J. Sun, M. Marsman, A. Ruzsinszky, G. Kresse, and J. P. Perdew, *Improved lattice constants, surface energies, and CO desorption energies from a semilocal density functional*, Phys. Rev. B **83**, 121410 (2011). (Cited on page 122.)

[276] E. R. McNellis, J. Meyer, and K. Reuter, *Azobenzene at coinage metal surfaces: Role of dispersive van der Waals interactions*, Phys. Rev. B **80**, 205414 (2009). (Cited on page 124.)

[277] R. Heid and K.-P. Bohnen, *Ab initio lattice dynamics of metal surfaces*, Phys. Rep. **387**, 151 (2003). (Cited on page 125.)

[278] M. J. Puska and R. M. Nieminen, *Atoms embedded in an electron gas: Phase shifts and cross sections*, Phys. Rev. B **27**, 6121 (1983). (Cited on page 125.)

[279] D. Ermak and H. Buckholz, *Numerical integration of the Langevin equation: Monte Carlo simulation*, J. Comput. Phys. **35**, 169 (1980). (Cited on page 126.)

[280] G. Füchsel, S. Schimka, and P. Saalfrank, *On the Role of Electronic Friction for Dissociative Adsorption and Scattering of Hydrogen Molecules at a Ru(0001) Surface*, J. Phys. Chem. A **117**, 8761 (2013). (Cited on page 128.)

[281] T. Schäfer, N. Bartels, N. Hocke, X. Yang, and A. M. Wodtke, *Orienting polar molecules without hexapoles: Optical state selection with adiabatic orientation*, Chem. Phys. Lett. **535**, 1 (2012). (Cited on page 134.)

[282] M. Brandt, H. Müller, G. Zagatta, O. Wehmeyer, N. Böwering, and U. Heinzmann, *Sticking and scattering of gas-phase oriented NO at Pt(100) as a function of the translational energy and of molecular orientation*, Surf. Sci. **331**, 30 (1995). (Cited on page 134.)

[283] E. W. Kuipers, M. G. Tenner, A. W. Kleyn, and S. Stolte, *Steric effects for NO/Pt(111) adsorption and scattering*, Phys. Rev. Lett. **62**, 2152 (1989). (Cited on page 134.)

[284] G. Fecher, N. Böwering, M. Volkmer, B. Pawlitzky, and U. Heinzmann, *Dependence of the sticking probability on initial molecular orientation: NO on Ni(100)*, Surf. Sci. **230**, L169 (1990). (Cited on page 134.)

[285] D. Novko, M. Blanco-Rey, J. I. Juaristi, and M. Alducin, *Ab initio molecular dynamics with simultaneous electron and phonon excitations*, Phys. Rev. B **92**, 201411 (2015). (Cited on page 134.)

[286] J. T. Kindt, J. C. Tully, M. Head-Gordon, and M. A. Gomez, *Electron-hole pair contributions to scattering, sticking, and surface diffusion: CO on Cu(100)*, J. Chem. Phys. **109**, 3629 (1998). (Cited on page 134.)

[287] L. Martin-Gondre, G. A. Bocan, M. Blanco-Rey, M. Alducin, J. I. Juaristi, and R. Díez Muiño, *Scattering of Nitrogen Atoms off Ag(111) Surfaces: A Theoretical Study*, J. Phys. Chem. C **117**, 9779 (2013). (Cited on page 137.)

[288] D. A. Butler, B. Berenbak, S. Stolte, and A. W. Kleyn, *Elastic Scattering in a Reactive Environment: NO on* $Ru(0001) - (1 \times 1)H$, Phys. Rev. Lett. **78**, 4653 (1997). (Cited on page 139.)

[289] A. Raukema, R. J. Dirksen, and A. W. Kleyn, *Probing the (dual) repulsive wall in the interaction of O_2, N_2, and Ar with the Ag(111) surface*, J. Chem. Phys. **103**, 6217 (1995). (Cited on page 139.)

[290] M. Bonfanti and R. Martinazzo, *Classical and quantum dynamics at surfaces: Basic concepts from simple models*, Int. J. Quantum Chem. (2016). (Cited on page 139.)

[291] Y. Huang, C. T. Rettner, D. J. Auerbach, and A. M. Wodtke, *Vibrational Promotion of Electron Transfer*, Science **290**, 111 (2000). (Cited on page 149.)

[292] C. Bartels, R. Cooper, D. J. Auerbach, and A. M. Wodtke, *Energy transfer at metal surfaces: the need to go beyond the electronic friction picture*, Chem. Sci. **2**, 1647 (2011). (Cited on page 149.)

[293] B. C. Krüger, N. Bartels, C. Bartels, A. Kandratsenka, J. C. Tully, A. M. Wodtke, and T. Schäfer, *NO Vibrational Energy Transfer on a Metal Surface: Still a Challenge to First-Principles Theory*, J. Phys. Chem. C **119**, 3268 (2015). (Cited on page 149.)

[294] B. C. Krüger, S. Meyer, A. Kandratsenka, A. M. Wodtke, and T. Schäfer, *Vibrational Inelasticity of Highly Vibrationally Excited NO on Ag(111)*, J. Phys. Chem. Lett. **7**, 441 (2016). (Cited on page 149.)

[295] S. Monturet and P. Saalfrank, *Role of electronic friction during the scattering of vibrationally excited nitric oxide molecules from Au(111)*, Phys. Rev. B **82**, 075404 (2010). (Cited on page 149.)

[296] T. Schafer, N. Bartels, K. Golibrzuch, C. Bartels, H. Kockert, D. J. Auerbach, T. N. Kitsopoulos, and A. M. Wodtke, *Observation of direct vibrational excitation in gas-surface collisions of CO with Au(111): a new model system for surface dynamics*, Phys. Chem. Chem. Phys. **15**, 1863 (2013). (Cited on page 149.)

[297] P. R. Shirhatti, J. Werdecker, K. Golibrzuch, A. M. Wodtke, and C. Bartels, *Electron hole pair mediated vibrational excitation in CO scattering from Au(111): Incidence energy and surface temperature dependence*, J. Chem. Phys. **141** (2014). (Cited on page 149.)

[298] K. F. Garrity, J. W. Bennett, K. M. Rabe, and D. Vanderbilt, *Pseudopotentials for high-throughput DFT calculations*, Comput. Mater. Sci. **81**, 446 (2014). (Cited on pages 159 and 163.)

[299] W. H. Press, S. Teukolsky, W. Vetterling, and B. Flannery, *Numerical recipes in FORTRAN (Cambridge*, Cambridge Univ. Press, 1992. (Cited on pages 167 and 169.)

[300] H. Akima, *Algorithm 761: Scattered-data Surface Fitting That Has the Accuracy of a Cubic Polynomial*, ACM Trans. Math. Softw. **22**, 362 (1996). (Cited on page 169.)

[301] M. Alducin, R. Díez Muiño, H. F. Busnengo, and A. Salin, *Low sticking probability in the nonactivated dissociation of N_2 molecules on W(110)*, J. Chem. Phys. **125**, 144705 (2006). (Cited on page 169.)

Resumen (Summary in Spanish)

La presente tesis está dedicada a la modelización teórica basada en primeros principios de la dinámica de sistemas gas-superficie que son relevantes para la catálisis heterogénea. La tesis se divide en nueve capítulos que se resumen a continuación:

En el primer capítulo se dan las motivaciones para el trabajo realizado y se introduce el tema de estudio. La relevancia de la catálisis heterogénea en nuestro mundo es enorme, por lo tanto el entender y el mejorar los catalizadores actuales es de gran interés. En esta tesis se estudian dos sistemas muy importantes en el campo de la catálisis heterogénea: O_2/Ag(110) y CO/Ru(0001). El primero es importante para entender la reacción catalítica de la epoxidación de etileno, que es la que produce el oxido de etileno, material de gran relevancia en la industria química. La importancia del segundo se relaciona con la del proceso Fischer-Tropsch y con la de la conversión catalítica de CO en CO_2. Por este motivo numerosos experimentos han sido realizados en estos sistemas. De particular interés son los experimentos con haces moleculares. Gran cantidad de información acerca de la interacción gas-superficie puede obtenerse de estos experimentos, especialmente cuando son realizados con moléculas con energías de incidencia (y en algunos casos, energías internas) bien definidas dispersadas por superficies planas. Tomando como referencia estos experimentos, en principio, se puede intentar comprender las características de la superficie de energía potencial que define la interacción. Sin embargo, a menudo es difícil realizar la conexión entre los resultados experimentales y los detalles microscópicos de la interacción. Por otro lado, estos últimos pueden obtenerse a partir de modelizaciones teóricas. En esta tesis realizamos simulaciones de dinámica molecular con el objetivo de entender los experimentos de haces moleculares. También se estudiará la dinámica de adsorbatos inducida por pulsos laser de femtosegundos.

En el segundo capítulo se presentan los modelos teóricos que se usan en esta tesis. Empezando desde la descripción cuántica completa del sistema, gradual-

mente llegamos a los modelos que se aplican a los sistemas gas-superficie particulares. En primer lugar se separan los grados de libertad electrónicos y nucleares. En segundo lugar, se discuten los métodos para resolver el problema de la estructura electrónica, mostrando la superioridad del formalismo del funcional de densidad respecto a los otros métodos. A continuación, se presenta una breve revisión del formalismo del funcional de densidad, se presentan las aproximaciones más comunes y se describe su uso en la práctica. En este punto, nos centramos en las superficies de energía potencial mostrando la forma en que se construyen y se exploran sus características. Seguidamente discutimos la dinámica de los grados de libertad nucleares en una superficie de energía potencial y realizamos la transición desde la dinámica cuántica a la clásica. También describimos como modelizar el movimiento de la superficie cuando la superficie de energía potencial sólo incluye los grados de libertad de la molécula y cómo incluir efectos no adiabáticos en la dinámica. Asimismo, introducimos la llamada dinámica molecular "on the fly". Finalmente, describimos la modelización de la dinámica inducida por pulsos láseres de femtosegundos.

El tercer capítulo es el primero que se dedica al $O_2/Ag(110)$. Por este motivo incluimos una revisión de los trabajos experimentales más relevantes y de trabajos teóricos previos en este sistema. A continuación describimos el procedimiento seguido para obtener la superficie de energía potencial de este sistema a partir de cálculos basados en la teoría del funcional de densidad. Mostramos que la superficie de energía potencial obtenida es de alta calidad. Se identifican cuatro pozos de adsorción que son accesibles desde el vacío sin barreras energéticas. Dos de las pozos de adsorción están situados en la posición "hueco" (hollow) de la superficie y aparentan ser consistentes con el estado de quimisorción descrito en los experimentos. Los otros dos pozos de adsorción están situados en las posiciones "puente" (bridge) de la superficie y presentan similitudes con los estados de fisisorción obtenidos experimentalmente, aunque están ligados a la superficie más fuertemente de lo que se esperaría a partir de las medidas experimentales. La barrera energética más baja hacia la disociación medida desde el vacío es de 0.36 eV y se haya situada en la posición "hueco" de la superficie. El valor de esta barrera energética es considerablemente más baja que las barreras calculadas en las superficies Ag(100) y Ag(111), lo que es consistente con el hecho de que la reactividad medida en la superficie Ag(110) es mucho más alta que en las otras dos.

En el cuarto capítulo se estudia la dinámica de la disociación de O_2 en Ag(110)

mediante simulaciones de dinámica molecular en la superficie de energía potencial obtenida para la superficie "congelada". Nuestros cálculos de dinámica clásica muestran que bajo condiciones de incidencia normal no se obtiene disociación para energías translacionales por debajo de 0.9 eV. Este valor contrasta con el calculado para la mínima barrera de energía para la disociación. Este hecho es una indicación de que el espacio de configuraciones que lleva a la disociación es muy reducido en este sistema. Los cálculos cuasiclásicos revelan que la energía vibracional es muy eficiente promoviendo la disociación. Incluyendo la energía del punto cero que es de sólo 90 meV, la energía de 0.9 eV necesaria para que haya disociación en el caso clásico se reduce hasta alrededor de 0.6 eV. Nuestros resultados para la disociación de O_2 son consistentes con la ausencia de disociación directa a bajas energías de incidencia en los diferentes experimentos de haces moleculares.

En el quinto capítulo introducimos el movimiento de la superficie en las simulaciones de dinámica molecular para estudiar la adsorción de O_2 en Ag(110). Las simulaciones se realizan tanto usando la superficie de energía potencial precalculada como "on the fly". Las simulaciones de la dinámica muestran las características de un sistema no activado, lo que contrasta con los resultados en los experimentos con haces moleculares en los que se observó lo contrario. Además, en nuestros cálculos la mayoría de las moléculas se adsorben en los pozos situados en las posiciones "puente". Esto es debido a que la región del espacio de configuraciones alrededor de ellos en la que la energía potencial es atractiva es más amplia que la de alrededor de los pozos de adsorción que se encuentran en las posiciones "hueco". Sin embargo, la barrera de energía hacia la disociación desde los pozos de adsorción "puente" es alta. Basándonos en estos resultados, se discuten las razones para las diferencias existentes entre nuestras simulaciones de dinámica molecular y los experimentos con haces moleculares. Se concluye que el funcional de canje y correlación estándar (el llamado PBE) no es capaz de explicar los resultados experimentales.

Las conclusiones obtenidas en el capítulo anterior nos llevan a explorar en el sexto capítulo si otras aproximaciones para el funcional de canje y correlación usado en los cálculos basados en la teoría del funcional de densidad pueden reproducir mejor los experimentos de haces moleculares. Con este objetivo se utilizan diferentes funcionales de canje y correlación de creciente complejidad para calcular las propiedades más relevantes del potencial de interacción del sistema O_2/Ag(110). En primer lugar mostramos que diferentes aproximaciones de gra-

diente generalizado (GGA) dan lugar a una gran dispersión en los resultados, pero que a pesar de todo, ninguna de ellas parece describir con precisión la interacción O_2/Ag(110). La dispersión de los resultados con funcionales meta-GGA es menor. Sin embargo, todos los funcionales meta-GGA predicen grandes probabilidades de adsorción a bajas energías de incidencia lo que no concuerda con las observaciones experimentales. Este problema podría ser resuelto mediante el uso de funcionales híbridos meta-GGA que son computacionalmente muy costosos.

En el capítulo séptimo se presenta el estudio de la desorción de O_2 inducida por laser desde la superficie Ag(110). En primer lugar se presenta una breve introducción de la modelización de la dinámica inducida por láseres de femtosegundo. El modelo incluye de forma novedosa tanto las excitaciones de fonones como de electrones inducidas por laser. A continuación calculamos los rendimientos y ritmos de desorción en función de la fluencia del laser desde cada uno de los cuatro pozos de adsorción. Encontramos que el efecto de los fonones excitados por el laser no puede despreciarse. De manera importante, encontramos que la contribución de los fonones al rendimiento de la desorción puede ser positiva o negativa dependiendo del pozo de adsorción. Más concretamente cuando la molécula está inicialmente adsorbida en las posiciones "puente" la inclusión de los fonones en el modelo aumenta la probabilidad de desorción. De hecho, para estos pozos de adsorción, el acoplo de la molécula a las excitaciones de fonones constituye el mecanismo principal de desorción. Por otro lado, para las moléculas inicialmente adsorbidas en las pociones "hueco", no sólo el mecanismo electrónico es el dominante, sino que la inclusión de los fonones reduce la probabilidad de desorción porque estos toman energía de la molécula. Estas observaciones son racionalizadas en términos de las distancias a la superficie en las que los sitios de adsorción se sitúan y de los correspondientes valores de la densidad electrónica en sus alrededores. Los sitios de adsorción "hueco" están más cerca de la superficie que los sitios "puente" y, por lo tanto, en regiones de mayor densidad electrónica. Por este motivo, el canal electrónico domina la desorción en el caso de los primeros y el canal de fonones lo hace en el caso de los segundos.

En el octavo capítulo se estudia la dinámica de dispersión y adsorción de CO en la superficie Ru(0001). En primer lugar, se presenta una revisión de los experimentos de haces moleculares más relevantes y se describe la superficie de energía potencial. A continuación, se realizan simulaciones de dinámica molecular en la citada superficie de energía potencial incluyendo el movimiento de la

superficie con el objetivo de reproducir los resultados de los experimentos de haces moleculares. Concretamente, dos de las observaciones realizadas en estos experimentos no eran previamente entendidas. La primera era que, manteniendo la superficie a una temperatura tan baja como 85 K, alrededor de un 5% de las moléculas incidentes a bajas energías no eran adsorbidas. Esto era sorprendente porque teniendo en cuenta el muy profundo pozo de adsorción al que las moléculas pueden acceder sin barreras energéticas desde el vacío, cabía esperar que todas las moléculas fueran adsorbidas. La segunda era la inusualmente estrecha distribución de ángulos de dispersión. En un sistema con un pozo de adsorción profundo es de esperar (y es frecuentemente observado) que las moléculas sean atraídas al pozo y a continuación deflectadas hacia la superficie, con su consiguiente dispersión en un muro energético corrugado, dando lugar a una distribución angular ancha. Nuestras simulaciones muestran que ambas observaciones inusuales son debidas a la anisotropía rotacional del potencial molécula-superficie. Más concretamente, las moléculas que están inicialmente con el átomo O apuntando hacia la superficie son dispersadas por un potencial puramente repulsivo sin sentir ningún efecto debido al pozo de adsorción. Para estas moléculas las fuerzas de reorientación hacia el pozo son pequeñas y, por lo tanto, ineficaces. El hecho de que sólo alrededor del 5% de las moléculas sean dispersadas a bajas energías de incidencia es debido a la baja probabilidad en términos geométricos que tiene la orientación con el átomo O apuntando hacia la superficie en relación al espacio de configuración total de orientaciones moleculares. Una vez entendido que las moléculas dispersadas no han sido atraídas por el pozo de adsorción, es esperable que la distribución de ángulos de dispersión sea estrecha ya que son dispersadas por un muro repulsivo plano de energía potencial. Se ha estudiado también la transferencia de energía vibracional a otros grados de libertad de la molécula, al movimiento de la superficie y a la excitación de electrones hueco. Nuestros resultados muestran que el canal de pérdida de energía correspondiente a la excitación de electrones huecos no tiene un efecto significativo.

Finalmente, el noveno capítulo resume los resultados más importantes y presenta una perspectiva para futuras investigaciones basadas en estos resultados. En particular, los resultados correspondientes a la dinámica de adsorción en el sistema $O_2/Ag(110)$ presentan problemas intrigantes que deberán ser resueltos por desarrollos teóricos futuros. En lo que se refiere a la modelización de las reacciones inducidas por laser, nuestros métodos y resultados son directa-

mente aplicables a otros sistemas. Finalmente, nuestros resultados para el sistema CO/Ru(0001) explican resultados, obtenidos en experimentos de haces moleculares, que parecían paradójicos.